Impact of CO_2 on alkali-rich explosive volcanism – Case studies from Saray Volcano, Iran and Laacher See Volcano, Germany

Dissertation zur Erlangung des Doktorgrades
an der Fakultät für Geowissenschaften
der Ludwig-Maximilians-Universität München

Vorgelegt von
Donjá Aßbichler

München
11. September 2019

Erstgutachter:	PD. Dr. Thomas Kunzmann
Zweitgutachterin:	PD. Dr. Bettina Scheu
Tag der mündlichen Prüfung:	22. Januar 2020

ABSTRACT

Saray Volcano, Northwest Iran, and Laacher See Volcano, Germany, erupted alkaline, potassic magmas, including carbonatite-bearing magmatic cumulates with trachytic to phonolitic composition. In addition, both contain felsic ejecta consisting mainly of sanidine. Aim of this thesis was to study the petrogenesis of the sanidine-rich rocks with focus on the role of CO_2 and to figure out the tipping point that initiated their explosive eruption. Whole-rock composition was analyzed with XRF and ICP-MS. Particular attention was set on the microtexture of the investigated samples. Polarizing light microscope and BSE-images as well as microchemical analysis (EMPA) were used to decipher the relationships and mineral reactions of the mineral assemblage. Photoluminescence helped to study zircon textures and generations. Microchemical analysis of volatile-bearing minerals and Raman spectroscopy of fluid inclusions and of volatile-bearing minerals were performed in order to constrain the reaction conditions of the investigated samples.

Of specific interest are “live” magmatic cumulates or bombs as they are directly extracted from their formation site in the magma chamber or the margin of it. In these samples, the reaction conditions and mineral relationships are immediately quenched during ejection due to rapid cooling. Special feature of the trachyte from Saray Volcano are sanidine megacrysts with up to 10 cm in size, embedded in a glass-rich to microlitic groundmass. Since Saray is a poorly studied volcano, all eruption products, trachytic lavas and bombs as well as lamprophyric dykes were sampled in order to understand their relationship. Thermobarometric calculations showed that the trachyte of Saray Volcano crystallized at a temperature of 980-1135°C and a pressure 11-16 kbar, which translates into a depth of ~ 40 km. Multiple resorption and crystallization events are reflected in pseudo-oscillatory zoning of sanidine due to varying Ba content. It was caused by continuous percolation of mantle derived CO_2, which transferred heat into the magma chamber and contributed to the temperature fluctuating around liquidus. This way, formation of sanidine megacrysts up to 10 cm was enabled by the suppression of groundmass nucleation. The influx of a CO_2-loaden lamprophyre into the magma chamber marks the tipping point for the eruption. The source of lamprophyre was estimated to be at a depth > 70 km. Based on the mantle xenolith cargo in lamprophyre, the ascent rate estimation yielded at least 3 m/s. Consequently, the contact time between trachyte and lamprophyre was very short and the interaction was limited to transfer of CO_2 including heat, carbonatite and Fe-Ti-Ba-F-phlogopite (phl-II) from lamprophyre into trachyte, and sanidine and hydrous, Mg-rich phlogopite megacrysts from trachyte into lamprophyre. The fast ascent and eruption quenched the mineral reactions, providing perfect conditions to study the partitioning behavior of Ba and F between the two types of phlogopite and sanidine in the different chemical environment of these two melts. Carbonate + quartz pseudomorphs after diopside prove an unusual high $X(CO_2) > 0.9$ in the top of the trachytic magma chamber and in felsic minette. The systematic of the microtextures in different samples enabled to decipher the chronology of the eruption event triggered by the accumulation of CO_2.

At Laacher See Volcano, focus was set on the formation of sanidinites, which are cumulates from the magma chamber roof. These felsic cumulates are holocrystalline and rich in cavities, which are typically filled with carbonate and a variety of euhedral crystals, specifically high field strength elements (HFSE) containing minerals.

Laacher See Volcano turned out to be a par excellence example to study carbothermal processes occurring in the volatile-rich part of the magma chamber. Cavities and minerals crystallizing in the open spaces document the existence of a free gas phase in the top of the magma chamber. The systematics of the different types of sanidinite documented in the change from haüyne to nosean reflect the respective fluid composition in the upper part of the magma chamber. The sodalite minerals haüyne and nosean are key indicators of changed reaction conditions. This study also showed that CO_2 leaches and extracts preferentially divalent elements and REE leading with time to a "purification" of specific minerals such as zircon. Carbothermal vapor depositions of carbonates fill part of the cavities. The formation of a gas-tight caprock by densification of the porous crystallized magma chamber roof enabled the formation of a CO_2-fluid cap in the rigid part of the magma chamber and thus the required conditions to generate a critical overpressure in the magma chamber.

In both cases, CO_2 played a key role, although the impact of CO_2 depends on external factors, such as temperature and depth of the magma chamber. At Saray Volcano, CO_2 percolation enabled the growth of sanidine megacrysts whereas at Laacher See Volcano, carbothermal processes are recorded in the cumulates of the magma chamber roof. In both cases, however, the tipping point of the eruption was caused by reaching a critical overpressure due to CO_2 accumulation. As a result, the brecciation by wall rock failure triggered the explosive expansion of CO_2.

ACKNOWLEDGEMENT

In 2013, I started with my PhD in Munich under the supervision of my former advisor Thomas (Tommi) Fehr. Topic was the solvothermal densification of zirconoxide ceramics as corrosion protection in municipal solid waste incineration (MSWI) plants. My task was to investigate solvothermal transport mechanisms of zirconium in natural samples, such as the sanidinites from Laacher See Volcano, and adapt these results to technical applications. Saray Volcano, I discovered by incidence. A friend of mine in Iran, Manijeh Asadpour, who heard that I was doing by PhD on sanidine-rich ejected cumulates, informed me about Saray Volcano, with large sanidine crystals, nearby the city Urumieh.

Tommi supported me immediately and encouraged me to study these cumulates in order to better understand solvothermal transport mechanism of HFSE. My successful application to the Beate-Mocek-Award of DMG provided me the opportunity to visit Saray Volcano. Once there, I immediately fell in love with this little volcano and its amazing eruption products such as the massive trachytic lava dome in the center, with sanidine megacrysts up to 10 cm in a bluish-green groundmass.

Unfortunately, Tommi passed away short time before the field trip and only one year after I started my PhD. However, I'm very grateful that Tommi asked me to come to Munich and introduced me to the world of solvothermal processes and into material science. He taught me that in science, there are no boundaries. His motto was always "Von der Natur lernen, heißt siegen lernen". Thank you, Tommi, for all your support! Chapter 4 is dedicated to you!

Special thanks goes also to Thomas Kunzmann who offered to be my new advisor. Thomas, I really appreciated the discussions with you and thank you so much for the freedom to develop my own thoughts. Thank you so much for your support! I also thank Don Dingwell for his support especially after the early death of my first advisor.

I would like to express the deepest appreciation to all my helper during the fieldwork

- Tommi Fehr and Ruppi Hochleiter were my first instructors to get the right view for the right samples. Ruppi, thank you for your time whenever I had a question. Thank you also for providing me a large collection of sanidinites from Laacher See Volcano
- Special thank goes also to Stefan Praschl, who helped me in the field trip to Laacher See Volcano and drove all the way home with a broken exhaust
- Manijeh Asadpour was my guide in Iran and showed me the places we should go. Eeeeeeeeeeebiiiiii carried tons of samples for me and was babysitter for my daughter Lily during the field campaign and thanks to the drivers, who didn't hesitate to drive me wherever I wanted to and for preparing our delicious meals. Our tea time with fresh barbari bread, cheese and dates on the carpet in the field was marvelous! And I want to thank my daughter Lily for helping Manijeh and me in the field, especially when she acted as a scale
- Thanks a lot also to Ulli Küppers, who helped me to interpret the field observations

For my analytics, I have received a great deal of support and assistance from many people. I want to thank all of you for your excellent cooperation

- Dirk Müller and Maren Kahl for technical support at the EMPA
- Christoph Lenz for carrying out the photoluminescence analysis
- Melanie Kaliwoda to introduce me into the Raman Spectroscopy and Kurt Krenn for helping me with the Raman measurements and interpretation of the CO_2 inclusions in nosean
- Eileen Eckmeier and Karin Maisburger for the possibility to measure C concentrations in the whole rock.
- Karin Paschert, Antonia Wimmer and Thomas Dorfner for their support in the chemistry lab, Namvar Jahanmehr for thin section preparation and Hilger Lohringer for the preparation of the samples for microprobe analysis
- Christina Plattner and Ludmilla Teixeira for doing the PCA-Analysis

Many people spent their time to discuss my observations. Without their passionate participation and input, my work could not have been successfully conducted.

- Maren Kahl and Cristina Decampos gave valuable hints and reviews of the Saray Volcano part at an early stage. The remarks of John Wolff and an anonymous reviewer helped me to improve the results
- Many thanks to Axel Schmitt for the discussions on Laacher See carbonatites and review of the Saray Volcano part. Special thanks also to Gerhard Wörner for the invitation to Göttingen and lively discussions. The possibility of microscopying his carbonatite-samples from Laacher See Volcano was of great importance to my research.
- Soraya Heuss-Aßbichler for all the inspiring discussions day and night
- Special thanks to Christoph Lenz; he was my personal Lenzipedia to answer mineralogical questions and to discuss microtextures and mineral reactions “und was die Erde im Innersten zusammen hält”.
- Emily Janots helped me a lot to interpret the microtextures of the sanidine crystals in sanidinites from Laacher See Volcano
- Soraya Heuss-Aßbichler, Fabian Dellefant, Werner Ertl-Ingrisch, Christoph Lenz, Stefanie Rieger, Dorothea Lowe and Roya Aßbichler - thank you for proof reading the thesis

I have greatly benefited from Miriam Dühnforth who was my mentor in the LMU mentoring program. Especially at the time, when my advisor passed away and one year later when I gave birth to my daughter she always encouraged me to continue. I had the support and encouragement of Anke Friedrich, who opened my eyes to understand processes on a geological scale. Anke, thank you so much, you have been extraordinarily tolerant and supportive to combine work, PhD-thesis and family.

I received generous support for my study. My thanks to

- Beate-Mocek Preis committee; without this award I would not have traveled to Saray Volcano
- LMU Mentoring program which financially supported several field trips and trips to conferences where I could discuss my results

Last, but not least, I want to thank my family. My highest thanks go to my mother Soraya for all the discussions and philosophical conversations, especially those late after midnight with a glass of wine and for always encouraging me to continue – even in the hardest times. My sister Roya and my father Franz for taking care of my daughter Lily especially in the afternoons when I had only a half-day child-care. And I want to thank my daughter Lily for being the best field and discussion assistant ☺ Short time prior to the submission of my thesis she asked me "why are you spending so much time on investigating volcanoes? The magma is stored in the crust, and once it is in a mood it rises up and erupts – that's it. Now come, and play with me!" And I want to thank Stefan for all his support and patience, even when my thesis turned me into a zombie-version. Thank you guys so much!!! All for one and one for all.

CONTENT

1 INTRODUCTION

At first glance, the two volcanoes, Saray Volcano (Northwest Iran) and Laacher See Volcano (Eifel, Germany), do not seem to have much in common. The relatively small Saray Volcano (NW Iran) is associated with a metasomatic mantle source formed by the subduction of the oceanic crust of the Neo-Tethys in Miocene times. It has a deep located trachytic magma chamber and the eruption involved dome formation, accompanied by explosive eruption stages. As a result, the eruption products occur in a relatively small, well-exposed area. In contrast, Laacher See Volcano (Germany) is an intraplate volcano with a magma chamber, located in the shallow crust. The products of the phreatomagmatic eruption were deposited over a large area with a well-defined and accessible stratigraphy.

On closer inspection however, the two volcanoes have several common features. Both volcanos erupted alkaline, potassic magmas, including carbonatite-bearing magmatic cumulates with trachytic/phonolitic composition consisting mainly of sanidine. Special feature of the trachyte from Saray Volcano are sanidine megacrysts with up to 10 cm in size, partly embedded in a glass-rich groundmass. In case of Laacher See Volcano, the cumulates, the so called “sanidinites”, are holocrystalline and rich in cavities. These cavities are typically filled with a variety of euhedral crystals, specifically high field strength element (HFSE) containing minerals. At both volcanos, there is evidence for a mafic magma recharge – lamprophyres in the case of the Saray Volcano and basanite in the case of the Laacher See Volcano. In both areas, high levels of CO_2 emissions are evident, and isotope data show that the CO_2 is mantle derived.

Tamburello et al. (2018) showed that CO_2 surface degassing correlates well with tectonic settings. Different sources of diffusive CO_2 degassing are arcs, rifts, and intraplate magmatism. Recent studies indicate that not the total magmatic CO_2 degasses through volcanic vents. The major quantity of magmatic CO_2 enters hydrothermal systems or escapes to the surface along fracture pathways of active faults (Hutchison et al. 2015, Jolie et al. 2016, Muirhead et al. 2016). In tectonically active regions, it is expected that CO_2 transport occurs through cracks and fractures formed by faulting. Overpressure due to accumulation of CO_2 in the crust results in enhanced seismic activity (Irwin and Barnes 1980, Tamburello et al. 2018). Formation of pathways in the crust leads to a feedback mechanism, where CO_2-induced fracturing facilitates the rise of deep fluids (Tamburello et al. 2018). CO_2 escapes also from volcanic vents, either via passive degassing or before, during and after eruptions. Consequently, CO_2 flux occurs also through magmatic bodies (Wallace et al. 2015).

In general, however, it is assumed that CO_2 plays a more passive role in the magmatic activity, although some studies address the role of CO_2 on eruption dynamics. The type of gas distribution in a magma during eruption can control the style and intensity of the eruptive activity (Eichelberger et al. 1986; Jaupart and Vergniolle 1988). Severe explosive eruptions are also discussed to be the effect of gas accumulation (Freda et al. 2011; Burton et al. 2013) as well as buoyancy effects in the magma chamber due to CO_2 bubbles (Burton et al. 2013).

CO_2 emanations dominate between and prior to eruptions, whereas strong melt-soluble volatiles, such as water (> 85 %), minor CO_2 and SO_2 (2-10%) and halogen gases (HF, HCl, CO) prevail when the magma reaches the surface

(Edmonds et al. 2015). Gas-monitoring of active volcanoes revealed that the gas flux of both, CO_2 and SO_2, is significantly lower before an eruption, followed by massive CO_2 degassing prior to high-explosive eruptions (e.g. Aiuppa et al. 2011; Allard et al. 1989). In case of Stromboli (Italy), high activity is related to the collapse of foam layers formed by the accumulation of gas (e.g. Jaupart and Vergniolle 1988; Menand and Phillips 2007). At Dieng volcano (Indonesia), the accumulation of CO_2 in the underplating mafic magma recharge was proposed (Allard et al. 1989). Nonetheless, these are just assumptions based on CO_2 emission monitoring; evidence from natural eruption products is missing so far.

In contrast to H_2O, CO_2 is in general considered to be dissolved in melts at high-pressure conditions (>10-20 kbar, depending on temperature of the magma). At lower pressures, CO_2 "degasses" and percolates upwards as a decoupled, free fluid phase. A major analytical challenge is therefore, that CO_2 – as a separate fluid phase – often leaves no or only cryptic traces in eruption products formed at crustal pressures. In consequence, little is known on the effects of a free CO_2 phase - besides its potential to influence eruption dynamics. Only a few studies may be found in the literature that focus on the impact of a free CO_2 gas phase on crystallization conditions. Giuffrida et al. (2017) investigated eruption products from Etna and experimentally showed that the presence of CO_2 gas suppresses the crystallization of plagioclase.

A remarkable common feature in trachytes of Saray Volcano and phonolite of Laacher See Volcano is the presence of carbonatite. The relationship between trachyte, carbonatite and lamprophyre, however, is still unclear. Therefore, the necessity of a detailed study of micro-textures and fluid inclusions in combination with microchemical and geochemical analyses is of utmost importance to detect and verify effects of CO_2 on the genesis of volcanic rocks. Aim of this thesis is to answer the following questions:

1) Does CO_2 gas interact with the magmatic system, or does it simply flush through the magma chamber without affecting the melt? What influence has CO_2 on the crystallization process?
2) Is there petrological evidence for the contribution of CO_2 to eruption dynamics in natural samples?
3) How did carbonatites form in the respective melt?

The focus of this study is to decipher the significance of CO_2 in course of melt evolution in the magma chamber by using petrographic texture analysis of the mineral assemblages, with special emphasis paid to textural features of mineral reactions in combination with measurements of fluid inclusions, micro-chemical analysis and whole-rock geochemistry.

Of specific interest are "live" magmatic cumulates/bombs as they are directly extracted from their formation position in the magma chamber or its margin and the reaction conditions and mineral relationships are immediately quenched during ejection due to rapid cooling. The study of the latter has great advantages in comparison to tephra, as there, the mineral relationships are lost due to fragmentation and vesiculation, or in comparison to lavas, which normally extrude too slowly to preserve mineral reactions. Only a combined, holistic investigation of all the eruption products may provide an overall picture of the processes in the magma chamber prior to the eruption and the consequences for the type of eruption mechanism.

Saray Volcano is a poorly studied volcano. Only a few studies on the geochemistry and/or geochronology of eruption products of this volcano can be found in the literature (e.g. Moayyed et al. 2008; Hajalilou et al. 2009; Pang et al. 2013; Moghadam et al. 2014). It produced a variety of eruption products including different types of carbonatite-bearing trachytic lavas and a lava dome, at least two block-and-ash flow deposits with trachytic blocks and bombs, in addition to associated lamprophyric plugs and dykes. In consequence, during this study all types of eruption products from the trachytic-lamprophyric eruption period of Saray Volcano were sampled in order to decipher the crystallization conditions of the trachytic magma chamber and to understand the relationship between trachyte and lamprophyre. First, a model for the magma chamber had to be developed, including thermobarometric calculations to define the boundary conditions of the trachytic magma chamber. Second, geochemical analysis together with microchemical investigations and a detailed study of the microtextures of the whole set of eruption products helped to understand the formation of sanidine megacrysts and the role of CO_2 in the eruption mechanism.

Laacher See Volcano is characterized by massive stratified tephra deposits containing nodules of magmatic cumulates. The felsic cumulates, consisting mainly of sanidine, and therefore called “sanidinites”, are subject of scientific research since at least 160 years. In the 19th century, Pater Theodor Wolf from the nearby Monastery Maria Laach realized that the characteristic minerals – nosean and haüyne – never occur within the same rock fragment, which was later used as major distinguishing feature. The sanidinites were always controversially discussed, as cognate with the phonolitic magma chamber, as pneumatolytic dykes or as rocks overprinted by a hot gas phase. Tait (1988) showed, however, that the sanidinites are part of a series of mafic, intermediate and felsic cumulates which accumulated at the magma chamber margin, with the sanidinites representing the magma chamber roof that forms a carapace surrounding the phonolitic magma body. The nosean-sanidinites are nowadays interpreted as carbonatite-bearing or carbonatitic syenites, which intruded in the upper magma chamber carapace, but with a close relationship to the phonolitic magma (Liebsch 1996; Schmitt et al. 2010). The relationship between carbonatite-bearing syenite and phonolite however is not yet understood (Schmitt et al. 2010). As the sanidinites represent the uppermost, rigid part of the magma chamber it is most likely, that an exsolved CO_2 gas phase penetrates this section (or accumulates there) on its way through to the country rock and further to the surface. Because of the latter assumption, a large variety of haüyne- and nosean-sanidinites was sampled and investigated in order to understand the impact of the exsolved CO_2 phase, specifically on the modification of the minerals, carbonate formation and its contribution to the eruption mechanism.

The whole-rock and mineral composition of all investigated samples was analyzed. In case of Laacher See, principle component analysis was used to extract the interrelationship of the felsic cumulates with the different eruption products. Particular attention was set on the microtextures of the investigated samples. Polarizing light microscope and BSE-images as well as microchemical analysis (EMPA) were used to decipher relationships and mineral reactions of the present mineral assemblage. For the samples from Laacher See Volcano, photoluminescence was used to investigate the textures of the zircon generations. Microchemical analysis of volatile-bearing minerals and Raman spectroscopy of fluid inclusions of volatile-bearing minerals were used to constrain the reaction conditions of the investigated samples.

2 METHODS

2.1 SAMPLING

For this study, a large range of trachytic lavas, bombs and associated lamprophyres from Saray Volcano and sanidinites (felsic cumulates) from Laacher See Volcano were investigated. The samples from Saray Volcano were collected in two field campaigns in spring 2014 and 2017. A broad variety of sanidinite samples from Laacher See was provided by the collection of Prof. Dr. Karl-Thomas Fehr and Dr. Rupert Hochleitner. Additional samples were collected in a field trip in summer 2014 to cover the whole spectrum of the very heterogeneous group of sanidinites.

2.2 ANALYTICAL METHODS

The whole set of samples (~ 150 samples from Saray Volcano and ~ 200 samples from Laacher See Volcano) was studied macroscopically and with the binocular microscope to select the appropriate samples for thin section preparation. In order to avoid misinterpretation, a large number of thin sections were prepared in order to obtain the widest possible variety of microtextures and thus to have a good base to work out the formation of these rocks. Thin sections were first studied by polarizing light microscope in order to select samples for further geochemical and microchemical analysis. The whole-rock composition was determined by WD-XRF and ICP-MS under consideration of volatiles (CO_2, SO_3, Cl and F); CO_2 was determined by a C/N analyzer. Main focus was set on the study of microtextures and mineral reactions using polarizing light microscope and BSE-imaging. Microchemical analysis was carried out with an electron microprobe after thorough study of the thin sections in BSE-image and qualitative determination of the elements contained in the minerals by EDX-analysis. Structurally bound H_2O and CO_2 and the composition of fluid inclusions was analyzed with Raman spectroscopy. For the samples from Laacher See Volcano, photoluminescence was used to investigate the textures of the zircon generations.

Whole rock analysis

WD-XRF analysis of the whole-rocks were measured with a Philips, MagiX Pro XRF spectrometer at the Department of Earth and Environmental Sciences (DEES) at the Ludwig-Maximilians-Universität (LMU) München. Sample powders were dried at 110 °C for more than 6 h and subsequently ignited at 1050 °C for more than 2 h to determine the loss on ignition (LOI). Major and minor elements were measured using glass beads prepared by fusion of 1 g ignited sample powder and 9 g SPECTROMELT A12 (66 % di-lithium tetraborate, 34 % lithium metaborate) in a PANalytical Eagon 2 furnace fusion system. SO_3 was measured by XRF analysis of powder tablets; these were prepared by mixing 8 g of the sample powder with 2 g of Merck Hoechst wax C micropowder ($C_{38}H_{76}N_2O_2$). Powder tablets were homogenized and pressed at P=15 bar for > 1 minute. The calibration was done using international certified standards. Independent test of the analytical precision of the calibration were done at the Actlab Laboratory, Canada. Analytical quality was ensured by analyzing USGS reference materials as

unknowns. Fe^{2+}/Fe^{3+} for samples from Saray Volcano was determined by titration. Titration was not carried out for samples from Laacher See Volcano as these samples have in general low iron contents. Trace element compositions of selected samples were obtained on 1 g of pulverized sample (> 200 g initial sample) sent to the ACME Lab in Vancouver (Bureau Veritas Minerals, Canada). After fusion in lithium borate, major and trace elements were measured by ICP-MS. Total carbon and nitrogen were determined at the soil laboratory of the Department of Geography at the Ludwig-Maximilians-Universität (LMU) München after the sample material was ground and homogenized. Measurements were conducted in duplicates by dry combustion with an elemental analyzer (Elementar Vario EL cube). The values for total organic carbon corresponded to the total carbon content because the samples did not contain carbonaceous material.

Backscattered electron (BSE) images and detailed, quantitative concentration profiles of major and minor elements were performed for sanidine, clinopyroxene, phlogopite/biotite, carbonate, nosean, haüyne, carbonate, magnetite, titanite, apatite, zircon, baddeleyite, pyrochlore and glass using a Cameca SX 100 WDX electron microprobe (EMP) analyzer at DEES, LMU München. Run conditions were 15 kV accelerating voltage and 20 nA beam current. Counting times for peak and background were 10 s for all minerals besides zircon, apatite, baddeleyite and pyrochlore. Analytical quality was ensured by analyzing the reference materials as unknowns and by mineral formula recalculation. Following conditions were used:

- Sanidine, plagioclase, clinopyroxene, nosean, haüyne
  focused beam with following standards: albite (Na), olivine (Mg, Fe), wollastonite (Si, Ca), orthoclase (Al, K), ilmenite (Mn), benitoite (Ba, Ti) and $SrSO_4$ (Sr)
- Phlogopite
  defocused beam (10 µm) using following standards: albite (Na), biotite (Si, Fe), wollastonite (Ca), orthoclase (Al, K), apatite (P, F), Cr_2O_3 (Cr), vanadinite (Cl), ilmenite (Ti, Mn), periclase (Mg) and benitoide (Ba)
- Calcite
  defocused beam (10 µm) using folling standards Calcite (Ca), dolomite (Ca, Mg), Fe_2O_3 (Fe)
- zircon, pyrochlore, apatite, baddeleyite
  albit (Na), almandine (Al), anhydrite (S), apatite (P), benitoite (Ti), bustamite (Mn), Ce-PO_4 (Ce), Dy-PO_4 (Dy), Er-PO_4 (Er), Fe_2O_3 (Fe), Gd-PO_4 (Gd), Ho-PO_4 (Ho), Hf (Hf), La-PO_4 (La), Nb (Nb), Nd-PO_4 (Nd), Pr-PO_4 (Pr), PbS (Pb), Sm-PO_4 (Sm), sphalerite (Zn), $SrSO_4$ (Sr), Ta (Ta), Th (ThO_2), UO_2 (U), wollastonite (Ca), Y-PO_4 (Y), Yb-PO_4 (Yb), zircon (Si, Zr)
  Peak-time of 5s for (Zr) 10s for (Ca, La, Ce, Mn,Hf, Fe, Er,Yb, Na, Si, Sr, Nb, P, S), 15s for (Ti), 20s (Pb, U) and 30s for (Pr, Ta, Sm, Gd, Dy, Ho)

Aqueous H_2O in phlogopite was identified by a Horiba Xplora confocal laser micro-Raman system of the Mineralogical State Collection Munich at the DEES, LMU, using a frequency-doubled Nd:YAG laser (532 nm). A 100x long distance objective was used to achieve an approximate spatial resolution of 1.2 µm (in x-y direction).

Confocal Raman spectra of CO_2-vapor inclusions in nosean were obtained with a HORIBA JOBIN YVON LabRam-HR800 Raman micro-spectrometer at the NAWI, Graz Geocenter, Department of Petrology and Geochemistry (University of Graz, Austria). Crystals within polished sections were excited at room temperatures with 532 nm emission line of a 100mW Nd-YAG laser through an OLYMPUS 100X objective (N.A. 0.9). The laser spot on the

surface had a diameter of approximately 1 µm and a power of about 20 mW. Light was dispersed by a holographic grating with 1800 grooves/mm. Spectral resolution of about 1.8 cm^{-1} was experimentally determined by measuring the Rayleigh line of a polished single crystal silicon-wafer. The dispersed light was collected by a 1024×256 open electrode CCD detector. Spectra were recorded unpolarized. Band shifts were calibrated by regularly adjusting the zero-order position of the grating and controlled by measuring the Rayleigh line. The detection range was between 100 cm^{-1} and 3800 cm^{-1}.

Laser-induced steady state photoluminescence (PL) measurements (single spectra and hyperspectral maps) were done using a Horiba LabRAM HR Evolution dispersive spectrometer at the Department of Mineralogy and Crystallograpy, University Vienna (Austria). This spectrometer system is coupled to an Olympus BX41 optical microscope and equipped with a Si-based, Peltier-cooled charge-coupled device detector. Photoluminescence of trace Dy^{3+} and Sm^{3+} was excited effectively using a 473 nm diode-pumped solid-state laser (9 mW at the sample surface). An Olympus 100× objective (numerical aperture 0.9) was used and the system operated in optimum confocal mode resulting in a lateral resolution of ~ 1 µm, and a depth resolution (with the beam being focused at the sample surface) of approx. 2 – 3 µm. The spectral resolution in the green spectral region was is ca. 3 cm^{-1} using a diffraction grating with 600 grooves per millimeter. Hyperspectral PL maps that consist typically of 60,000−80,000 single spectra, were obtained using a software-controlled x–y stage. PL maps with the integrated emission intensities of Dy^{3+} and Sm^{3+} given color-coded respectively, were produced from this data sets after background correction.

Saray Volcano Picture: Simon Prochaska – Fieldtrip 2018

3 PETROLOGICAL INVESTIGATION OF TRACHYTES AND LAMPROPHYRES OF SARAY VOLCANO

3.1 INTRODUCTION TO SARAY VOLCANO

Saray Volcano (SV) is a poorly studied, extraordinary ultrapotassic volcano, surrounded by calc-alkaline volcanoes of the Urumieh-Dokhtar magmatic arc (Figure 1). It formed by at least two major eruptive events in the Mid-Miocene: during the oldest known event, tephritic lavas and pyroclastics erupted. The second eruptive event produced trachytic lavas and pyroclastics including trachytic bombs and blocks and the lamprophyric plugs and dykes. The trachytic eruption is dated at 10.33 ± 0.1 Ma (Moghadam et al. 2014) and the lamprophyric intrusions are 10.35 ± 0.02 Ma old (Aghazadeh et al. 2015). A peculiarity is the high proportion of sanidine megacrysts with an average size of up to 6 cm, and occasionally even up to 10 cm, in the trachyte magma. This raises the question of how this magma was able to erupt.

The formation of K-feldspar megacrysts with sizes up to 20 cm is a common feature in plutonic rocks (Vernon 2018), whereas volcanic rocks with sanidine megacrysts are extremely rare (Vernon and Paterson 2008). A few examples are reported from the Rockeskyll volcanic complex, Germany (Riley and Bailey 2003), Mt. Amiata and Vico Volcano, Italy (Balducci and Leoni 1981; Perini et al. 2004; Johnson and Glazner 2010; Landi et al. 2019), the central Andes, specifically the Taapaca Volcano, Chile (Wegner et al. 2005; Zellmer and Clavero 2006; Higgins 2011) and Dangzishan volcano, Northeast China (Zhang et al. 1993).

The formation of megacrysts is still under debate. Two contrasting time settings are assumed for their formation: On the one hand, megacrysts are suggested to be products of porphyroblastic crystallization in the magma chamber under subsolidus conditions in a late crystallization stage (Johnson and Glazner 2010; Glazner and Johnson 2013). Repeated reheating and migration of water-rich fluids support textural coarsening by remelting of smaller groundmass crystal and preferential growth of phenocrysts (Glazner and Johnson 2013). On the other hand, several features argue for an early formation of K-feldspar megacrysts in a magma: euhedral shape of the crystals, internal oscillatory zoning, occurrence in a fine-grained, quenched groundmass of granitoids and incorporation of megacrysts into mafic magma replenishments (Vernon 2018 and references therein). Two main mechanisms are assumed for the free growth of megacrysts in a liquid: 1) a low nucleation/growth ratio at low degrees of undercooling (Berger and Roselle 2001), and 2) coarsening of smaller crystals after the principal of Ostwald ripening, where dissolution of smaller crystals occurs in favor of larger ones (Higgins 2000), e.g. due to fluctuation around the liquidus temperature (Higgins 2011).

Chemical growth zoning is typical for magmatic minerals. A common feature of K-feldspar megacrysts is Ba-zoning (Vernon 2018). K-feldspars in felsic plutons, be it megacryst or not, show often Ba zoning (Němec 1975; Long and Luth 1986; Gagnevin et al. 2005; Johnson and Glazner 2010; Słaby et al. 2011). There are also examples for Ba-zoning in sanidine of erupted magmas, like the Bishop Tuff (Anderson et al. 2000; Morgan and London 2003; Evans and Bachmann 2013; Chamberlain et al. 2014), the Bandelier Tuff (Wolff et al. 2015), the Lionato Tuff (Gaeta 1998) and the Laacher See tephra (Ginibre et al. 2004). However, Ba concentrations in sanidine

crystals of these locations rarely exceed 1 wt%, with exception of Lionato Tuff (Italy), where sanidine shows concentrations of up to 11.5 wt% BaO (Gaeta 1998). The high partitioning coefficient for Ba between K-feldspar and silicate melt promotes the incorporation of Ba in K-feldspar (Guo and Green 1990).

In plagioclase, Ca-Na zoning prevails over a long period due to the comparably slow Al-Si coupled diffusion (Brown and Parsons 1994). In contrast, zoning in K-feldspars is mostly absent due to fast K-Na diffusion (Smith and Brown 1988). The preserved Ba zoning including the oscillatory zoning in sanidine, however, can be explained by diffusion rates of Ba being six orders of magnitude slower compared with Na at the same temperature (Cherniak 2002). K-feldspar megacrysts have typically higher Ba concentrations in the core and lower concentrations towards the rim, which is assigned as normal zoning (Vernon 2018). Inverse Ba-zoning, however, is explained by coarsening processes as dissolution of Ba-bearing feldspar leads to a local enrichment of Ba in the melt (Bachmann and Bergantz 2006; Higgins 2011; Vernon 2018) . Shore and Fowler (1996) explained oscillatory Ba zoning in phenocrysts as a result of rapid growth. For plagioclase, various factors are considered that might cause oscillatory zoning patterns, e.g., changes in external reaction conditions including pressure and temperature (Brown and Parsons 1994), diffusion couples (Ghiorso 1987) or mechanisms of growth at disequilibrium conditions (Smith and Brown 1988). Multiple magma recharge represents another attempt to explain this phenomenon (Perugini et al. 2005; Słaby et al. 2011).

Lamprophyres are a heterogeneous group of alkali-rich to ultrapotassic porphyritic rocks (Rock 1977, 1987, 1991; Mitchell 1994). Common feature of all lamprophyres is their porphyritic texture with amphibole or biotite phenocrysts, the lack of felsic phenocrysts and olivine in the groundmass, high alkali content, and high amount of volatiles (H_2O and/or CO_2) (Rock 1977; Mitchell 1994). They occur mainly as dykes, and less frequently as plugs, silts and lava flows (Rock 1977, 1991) or are emplaced explosively (e.g. Tyrrell 1928; Bowes et al. 1964). In any case, their intrusion occurs always at a late stage of igneous activity, even terminating it (Ayres and Higgins 1939; Rock 1977). A subgroup of the lamprophyres are minettes. They are characterized, by definition, by the presence of biotite phenocrysts, an alkali-feldspar-rich groundmass and the absence of plagioclase and amphibole (Rock 1977) and are associated with alkaline rocks.

Various studies discussed the association of lamprophyric rocks with trachytes (Yanev et al. 2010) and with syenitoids (London 1997; Nardi et al. 2007; Soder et al. 2016). However, the relationship between these rocks is still under debate. The occurrence of anorthoclase crystals in lamprophyres, for example, are considered as xenocrysts (Chapman and Powell 1876) and are explained to be incorporated from more differentiated magmas such as phonolites or (nepheline-) syenites. Formation of minette is also discussed by mixing of lamproite with dacite magma (Prelevic et al. 2004). The role of carbonatite, which often accompanies these rocks, is also still unclear.

The aim of this study is to investigate the formation of sanidine megacrysts in trachyte, the relationship between trachyte and lamprophyre and their eruption mechanism(s). What enabled the eruption of magma with such large megacrysts and what role did the lamprophyres play? Therefore, a series of trachytic lavas and additional magmatic nodules (bombs) were collected as "living" documents of the magma chamber along with mafic and

felsic minette and carefully analyzed using geochemical, petrographic, and mineral chemistry methods, with particular emphasis on microtexture and mineral reactions.

3.2 GEOLOGICAL SETTING OF SARAY VOLCANO

Saray Volcano (SV) is located on Eslamy Peninsula (37°50'52.4"N, 45°29'53.1"E) in the middle between the two cities Urmia and Tabriz (Figure 1). Geologically it is located in the **Zagros collision zone,** which is part of the Alpine-Himalaya-Belt and trends along a NW-SE striking Arabian-Eurasian convergent plate boundary. The **Main Zagros Thrust** (MZT, Figure 1a) is a convergent plate boundary between the Arabic and the Eurasian Plate. It was dominated by the subduction of the Neo-Tethys with a suture zone well exposed as an ophiolite belt (Azizi and Moinevaziri 2009). After the closure of the Neo-Tethys, the regime changed to obduction processes and present-day collision.

Parallel to the MZT, on the East, the **Sanadaj-Sirjan zone** (SSZ, Figure 1), occurs with regional and contact metamorphic sediments (shale, sandstone and calcareous rocks) in addition to Jurassic igneous bodies. It is a magmatic arc caused by the subduction of the Neo-Tethys (Berberian and Berberian 1981; Khalaji et al. 2007; Azizi and Moinevaziri 2009; Deevsalar et al. 2017). However, recent studies question this interpretation (Hunziker et al. 2015; Azizi et al. 2018) because the geochemical characteristics of subduction related magmatism is missing. Azizi and Stern (2019) stated that the magmatic activity was brief however and propagated to the west. Based on the geochronology and geochemistry, the igneous rocks of the Sanandaj-Sirjan zone are discussed as the result of continental rifting. In consequence, the authors proposed that the subduction along the SW margin of Eurasia started after Jurassic (Azizi and Stern 2019).

To the East, the Tertiary to Quaternary **Urumieh-Dokhtar magmatic arc** (UDMA) rocks are exposed. It is approximately 150 km wide and expands for almost 2000 km from Northwest to the Southeast of Iran (Figure 1). The Urumieh-Dokhtar magmatic arc is related to the subduction of the Neotethys and is characterized by tholeiitic, calc-alkaline, and K-rich extrusive and intrusive rocks (Berberian and Berberian 1981; Moinvaziri 1985; Verdel et al. 2011; Ayati et al. 2013; Yeganehfar et al. 2013). Prominent volcanoes are Sahand, (3707 m) and Sabalan (4811 m) in Northwest (Figure 1), and Taftan (3940 m) and Bazman (3490 m) in Southeast of the Urumieh-Dokhtar magmatic arc. The oldest rocks of this magmatic belt are pre-Jurassic calc-alkaline intrusive rocks occurring in the Southeast. The exposed igneous rocks are from the Eocene with a climax of volcanic activity in the Middle Eocene (Berberian and King 1981), and it is assumed that several of these volcanoes are only dormant.

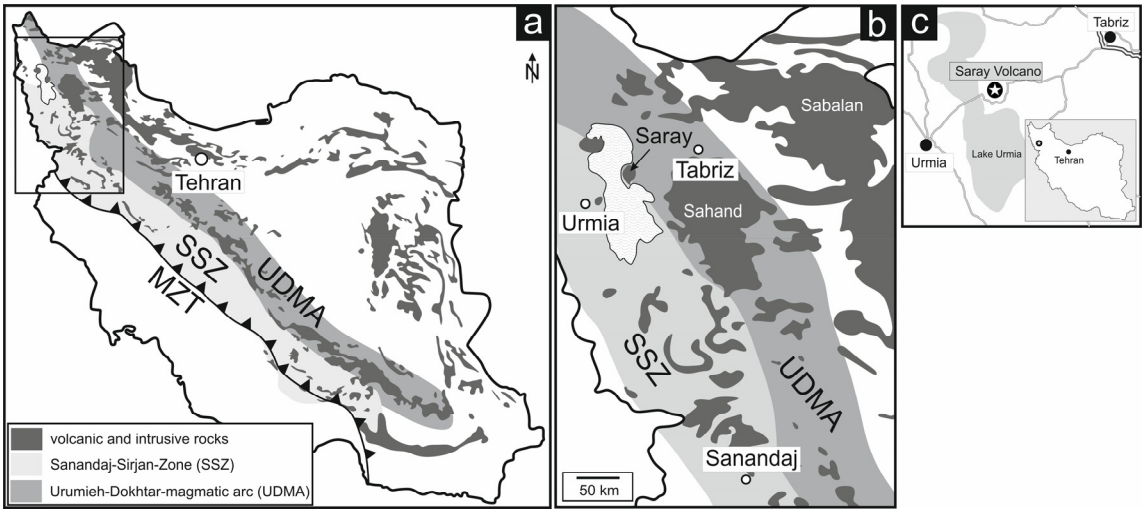

Figure 1: Simplified tectonic map a) of Iran showing the plate boundary, the Main Zagros thrust (MZT), the Sanandaj Sirjan zone (SSZ) and the Urumieh Dokhtar magmatic arc (UDMA); map simplified after Richards et al. (2006) and b) with the location of Sahand Volcano, Sabalan Volcano and Saray Volcano; map modified after Azizi et al. (2014) and c) map showing the position of Saray Volcano (37°50'52.4"N, 45°29'53.1") and the location of Saray Volcano on the road between Urmia and Tabriz

Saray Volcano is a stratovolcano with gentle slope flanks. It has a maximum elevation of ~2200 m (with a base level at 1300 m) and a surface area of only ~360 km². Accordingly, it is comparable in size with e.g. Mt. St. Helens (elevation = 2539, at a base level of ~1400 m, area = 450 km²), and much smaller than e.g. Mt. Etna (elevation = 3329 m, area = 1190 km²) or the prominent Sahand Volcano (elevation = 3707 m, area = 7200 km²) located ~ 50 km to the East. The morphology is dominated by (leucite-) basanite and (leucite-) tephrite lava flow sequences and related pyroclastic rocks (Figure 2). Trachyte lavas crop out in form of a huge lava dome in the center of Saray Volcano and smaller lava extrusions at the flanks (Figure 2). Related block-and-ash flow deposits containing sanidine-rich blocks and bombs are exposed in the Southwest part of the peninsula (Figure 2). Lamprophyric dykes crosscut the older units, or occur as plugs in the former crater area (Figure 2).

The first volcanic activity of Saray Volcano is dated to the late Miocene (~11 Ma, Pang et al. 2013) which coincides with the oldest ages for Sahand Volcano (11.7 Ma, Moinvaziri 1985). The most obvious difference between the two adjacent volcanoes is their chemistry: Sahand Volcano – like other volcanoes in the Urumieh-Dokhtar magmatic arc – consists mainly of calc-alkaline rocks, whereas Saray Volcano (SV) is characterized by shoshonitic to ultrapotassic eruption products.

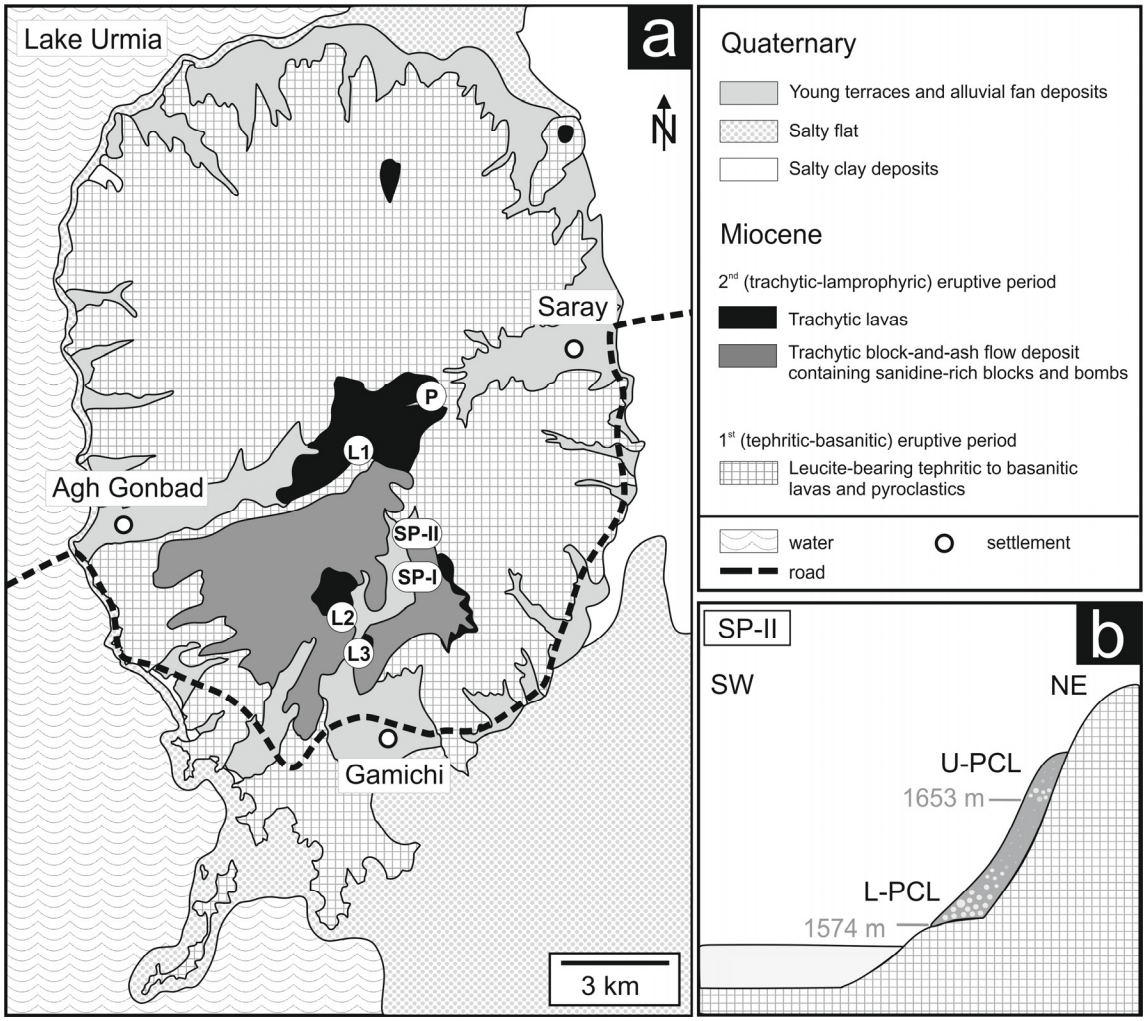

Figure 2: a) Geological map of Saray Volcano showing the sampling positions of the trachytic lavas (L1-3), the trachytic bombs from the block-and-ash flow deposit at sampling position I (SP-I) and position II (SP-II), the felsic minettes plugs sampled at (P) and the mafic minettes dykes sampled at (P) and (SP-II). b) Schematic section of sampling position II (SP-II) showing two layers of block-and-ash flow deposits; the lower pyroclastic layer (L-PCL) is at an elevation of 1574 m, the upper pyroclastic layer (U-PCL) at an elevation of 1653 m; both layers are characterized by abundant sanidine-rich blocks and bombs at the base and decreasing number and size towards the top

Below is a brief overview of the two main eruption activities of Saray Volcano:

(1) The base of the Saray Volcano was created by a leucite-bearing **basanitic-tephritic eruption** that started about 11 Ma ago (Pang et al. 2013). The lavas are overlain by basanitic to tephritic pyroclastic deposits indicating an increase in explosiveness during the last stage of the volcanic activity (Hajalilou et al. 2009). The heavily eroded pyroclastic unit crop out mainly in areas near Lake Urmia. The basanite lavas and pyroclastic rocks contain (altered) olivine phenocrysts, clinopyroxene and leucite with minor amount of apatite, phlogopite, Ba-bearing sanidine and Fe-Ti-oxides. In comparison, the sanidine content in the tephritic lavas and pyroclastics is higher and olivine is absent (Hajalilou et al. 2009).

(2) The younger, **trachytic-lamprophyric eruption event** is characterized by a period of trachytic effusive and explosive eruptions, dated 10.3 ± 0.1 Ma and 10.9 ± 0.1 Ma (Ar-Ar ages of biotite, Aghazadeh et al. 2015). In the center of Saray Volcano, a trachytic lava dome crops out, several smaller lava extrusions crop out at the

flanks. Block-and-ash flows are deposited between Gamichi valley and Agh Gonbad valley. The pyroclastic deposits are cut by various lamprophyric dykes, which are characterized by phlogopite phenocrysts (~ 4 cm) embedded in a fine-grained groundmass of K-feldspar and clinopyroxene. These dykes were dated to an age of 10.35 ± 0.02 Ma (Ar-Ar ages of biotite, (Aghazadeh et al. 2015)). The trachytic eruption products as well as the lamprophyric dykes contain xenoliths of glimmerite, pyroxenite and wherlite, which can reach a size of a few centimeters to a few decimeters.

3.3 RESULTS

3.3.1 FIELD OBSERVATIONS AND SAMPLE SELECTION

Field work campaigns took place in spring 2014 and 2017 with focus on the **trachytic-lamprophyric eruption event** of Saray Volcano. The outcrop conditions at Saray Volcano are excellent, because of deep erosion creating broad shallow valleys, which cut the pyroclastic deposits, providing an extensive view of the internal structure. This enables sampling throughout the entire pyroclastic deposit. Samples that have been exposed to the surface for a long time show severe signs of alteration. However, the intense physical erosion has the result that the outcrops constantly have fresh surfaces: Between the two field trips, a landslide caused the release of fresh, unaltered material in the pyroclastic unit, allowing the sampling of fresh material during the second campaign.

The **lava dome (L1)** represents the main part of the trachytic lava extrusion. It is located in the center of Saray Volcano on the south side of the former crater and faces the Agh Gonbad valley. The spread of trachytic blocks up to several meters in size in Agh Gonbad valley characterizes the main extrusion direction of the lava flow. Remarkable are sanidine megacrysts of up to 10 cm in length and plenty vapor bubbles with a general size of 0.5-1 cm which are embedded in a greenish-blue groundmass. At the base of the unit, sanidine crystals are mostly broken and swirled along the contact with the older layer. Above the contact, sanidine crystals are aligned and show a flow pattern (trachytic texture, Figure 3).

The **pyroclastic unit** is exposed in Gamichi valley (see Figure 2a). It is strongly eroded and only preserved at the flanks of the valley (see Figure 2b). A recent landslide in the Gamichi valley uncovered an unweathered part of the pyroclastic unit. Due to poorly sorted rocks, we can conclude that the products of a block-and-ash flow (BAF) were deposited at a short distance, about 4 to 6 km from the south side of the dome. From bottom to top, the frequency and size of the blocks and bombs changes. Due to the striking change in the properties in the middle of the profile, two different pyroclastic layers can be distinguished (see Figure 2b).

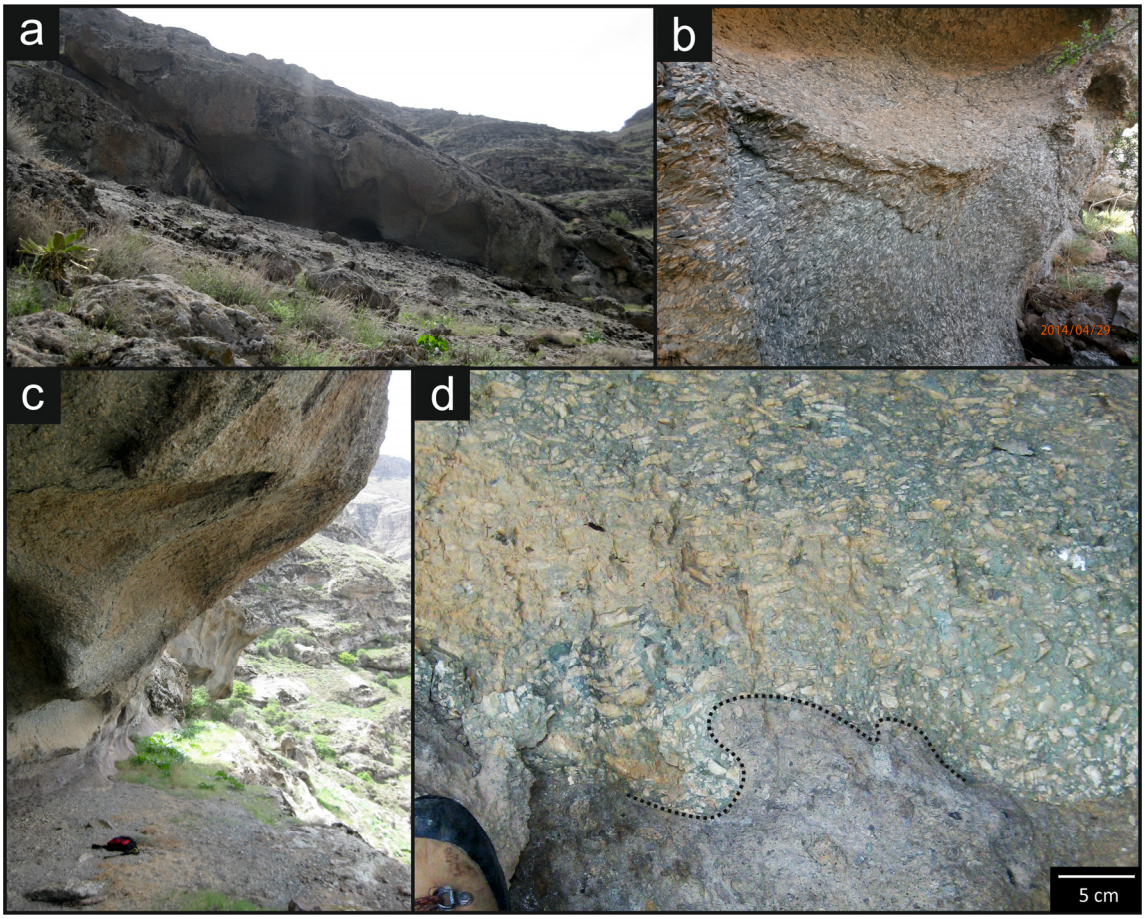

Figure 3: a) Outcrop of the trachytic lava dome (L1), b) alignment of sanidine crystals in the flow direction, c) outcrop showing the tearing edge of the extruding lava L1 d) trachyte lava at the contact to older pyroclastic material

The **lower pyroclastic layer (L-PCL)** has a thickness of ~50 m and is deposited discordantly on the pyroclastic deposit of the first older volcanic activity. Along the profile of the L-PCL, there is a continual change in clast size: At the bottom, sanidine-rich clasts with sizes ranging from 10 cm up to 1 m in diameter are abundant. They are all rounded and poorly sorted and contain sanidine phenocrysts with sizes up to 4 cm (Figures 4a and b). The smaller clasts (< 30 cm) have mostly a red, glassy groundmass, whereas the bigger clast appear grey, with a crystalline groundmass. Towards the top of the L-PCL the abundance and size of the clasts decreases (5-25 cm in average). The color of these clasts ranges from red-yellow-brown to grey. In the uppermost part of the layer, only small clasts < 15 cm are exposed. Sanidine phenocrysts occur only rarely within the uppermost clasts. The sudden appearance of blocks and bombs consisting of rounded and poorly sorted sanidine-rich clasts marks the beginning of a second **upper pyroclastic layer (U-PCL)** with ~7 m thickness (Figure 4b). Figure 4 shows the outcrop of the pyroclastic deposit with clear signs of salt induced erosion. The color of the clasts varies from yellow-brown to greenish-grey. The fact that no paleo-soils occur at the contact between the two pyroclastic layers indicates that the deposition occurred within a short time.

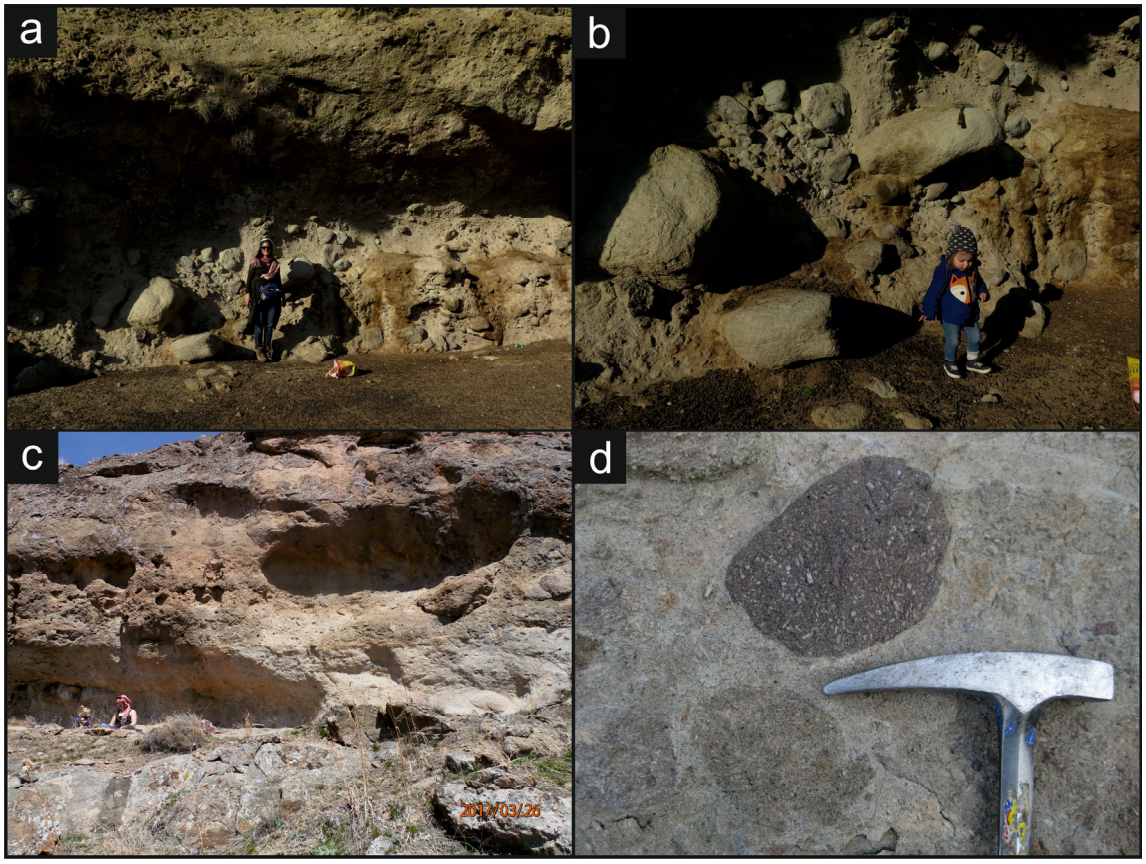

Figure 4: Field observations, a) and b) photos of the lower pyroclastic layer (L-PCL), b) photos of upper pyroclastic layer (U-PCL) showing salt induced erosion, size of the child ~80 cm, d) detail of bombs from the U-PCL

The extrusion of trachytic **lavas (L2, L3)** at the flanks of the volcano as well as the intrusion of lamprophyric plugs and dykes (sampled at P and SP-II in Figure 2) mark the youngest preserved volcanic activity. The trachytic lavas cross-cut the pyroclastic layers and crop out on the Northeastern (L2) and Southwestern (L3) side of Gamichi valley. Both lavas are fine- to medium-grained and exhibit sanidine phenocrysts (~ 1 cm). Their outcrops show typical signs of salt induced erosion, such as rounded surfaces and holes reminding of tafoni (Figure 5).

The **lamprophyres** occur mainly in Gamichi and Saray valleys in form of dykes and sills or crop out within the former crater in form of subvolcanic domes, plugs or dykes. The sills range from 0.5 to 2-3 m in diameter and are radially arranged, trending from the center of the volcano towards the shores of Lake Urmia, whereas the dykes crosscut vertically the pyroclastic layers. Typically, they contain phlogopite phenocrysts and are orthoclase (sanidine) dominated; plagioclase is absent. Therefore, the lamprophyres can be classified as “minette” (= phlogopite phenocryst-bearing lamprophyre); this term is used throughout this study.

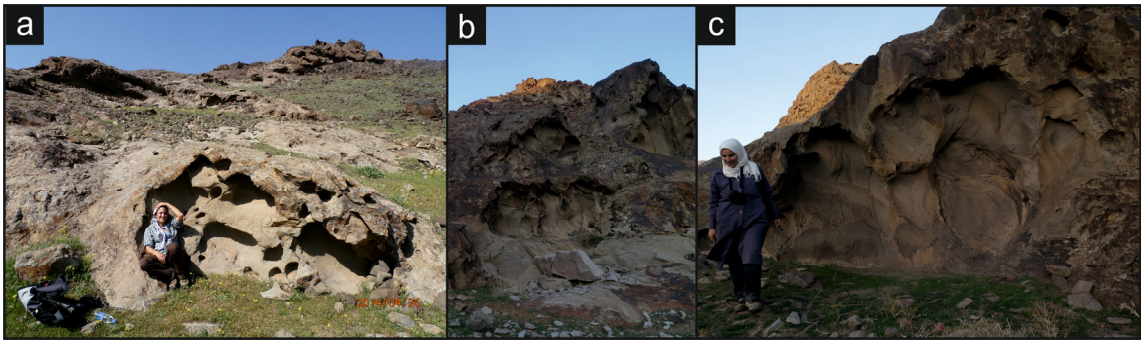

Figure 5: Field observations, photos of a) lava L2 and b-c) lava L3 from the flanks of the volcano; all of them showing salt induced corrosion

At Saray Volcano, two major types of minette can be distinguished: **Mafic minettes (M1-M3)**, characterized by their dark green to almost black color, and **felsic minettes (F1-F4)**, which are pinkish-grey in color. Both types of minette occur as single dykes or two separate units, side by side of each other. They are both characterized by abundant phlogopite phenocrysts up to 1 cm in size. Typical for the mafic and felsic minettes are xenoliths of **glimmerite (X-Gl)**, **pyroxenite (X-Px)** and **wherlite (X-Ol)** ranging in size from several millimeters to several decimeters. Sanidine phenocrysts occur only rarely in felsic minette.

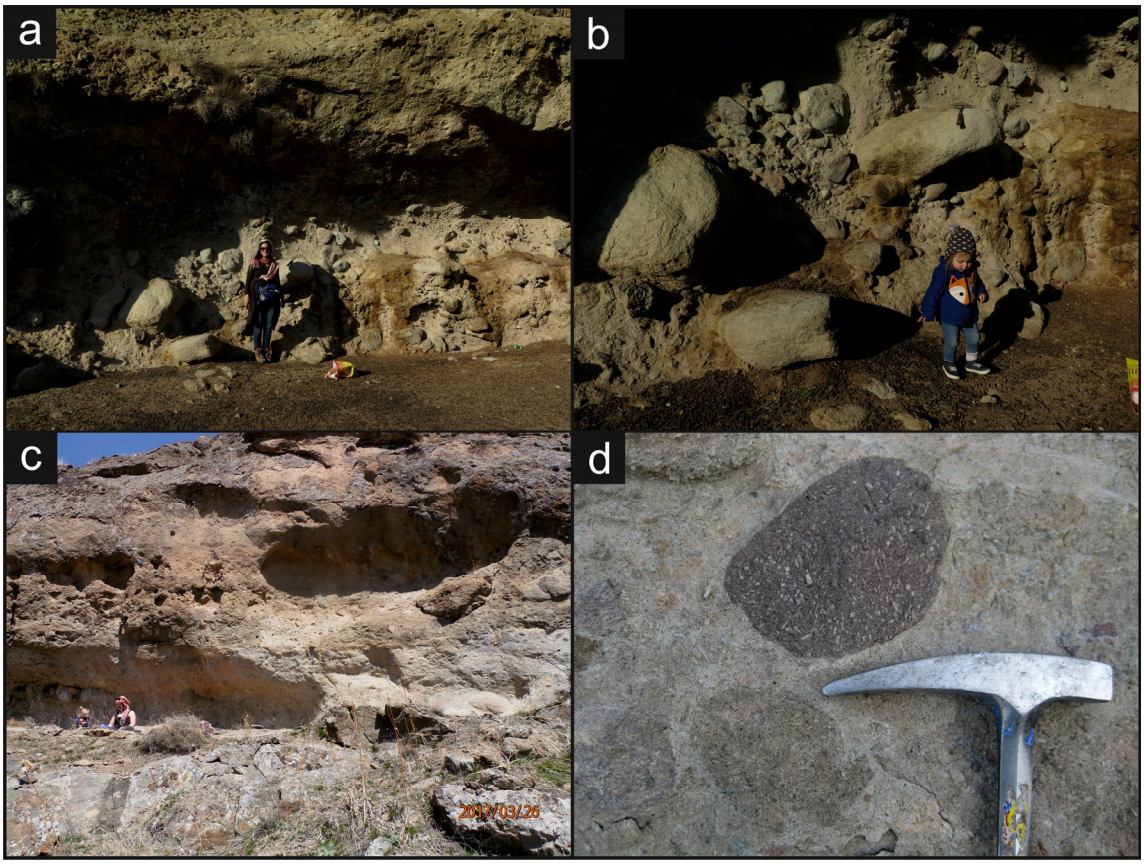

Figure 6: Field observations, a) felsic minette in contact to mafic minette, b) felsic minette with abundant gas bubbles, c) mafic minette with abundant centimeter sized glimmerite xenoliths and d) mafic minette with a glimmerite xenolith

In total, more than 150 samples were collected, focusing on the main trachytic lava and pyroclastic outcrops, as well as lamprophyric plugs found in the former crater of Saray Volcano and minette dykes. All selected samples were fresh and showed no signs of chemical weathering. Based on their macroscopic characteristics and their eruption type, the selected samples were divided into 5 groups, with (**L**) for trachytic lava rocks, (**B**) for bombs, (**F**) for felsic minettes, (**M**) for mafic minettes and (**X**) for xenoliths (Table 1). After initial macroscopic inspection, a set of samples was selected for geochemical and microscopic examination. According to microscopic observations and geochemical analysis, samples representing the main characteristics of each group were selected for further detailed microscopic and microchemical analysis.

Table 1 gives an overview of the selected samples. The three different trachytic **lava** extrusions are represented by L-samples: L1 reflects the samples ES83, ES84 and ES85, which were taken from the extrusive lava dome. L2 (samples ES61 and ES62) represents the trachytic lava extrusion at the western side *Gamichi* valley and L3 (GV-5-1) the lava extrusion on the eastern side of this valley (see Figure 2a).

In total seven different types of **bombs** were identified: In the lower pyroclastic layer (L-PCL) two major groups of bombs were distinguished: sanidine-rich bombs **B1** (samples ES35, ES36 and ES37, collected from sampling position I [SP-I]) and **B3** (sample ES113, collected from sampling position II [SP-II]) are characterized by a dark red glassy groundmass. The bombs summarized under **B2** (samples ES41, ES56 and ES57, collected from SP-I) represent the bombs with a grey, crystalline groundmass. The other bomb samples B4 (sample ES114), B5 (sample ES115), B6 (sample ES103) and B7 (sample ES105) were collected from the upper horizon U-PCL (sampling position [SP-II] at 1653 m; see Figure 2b).

In addition, four different **felsic minettes** were selected, represented by the samples **F1** (SV-2-1), **F2** (SV-4-1), **F3** (SV-7-2), **F4** (SV-8-1). They all crop out east of the trachyte dome, within the former crater. The **mafic minette dykes** from Gamichi valley and Saray valley crosscutting the trachytes are represented by following two samples: **M1** (GV-1-5) and **M2** (L6). Sample **M3** (SV-2-2) is a mafic minette adjacent to the felsic minette **F1**. In addition, different types of xenoliths occurring mainly in the plug samples and lamprophyres were collected: a glimmerite xenolith **X-Gl** (GV-0-2) collected in Gamichi valley (Figure 2a), an olivine-rich (peridotite) xenolith **X-Ol** (SV-7-1) and a pyroxenite **X-Px** (SV-1-1).

3.3.2 PETROGRAPHY

All investigated lava, bomb, plug and dyke samples show a porphyric texture. Table 1 shows the phenocryst assemblage in the samples, and Table 2 gives an overview of the minor and accessory mineral phases. **Sanidine** is the only feldspar in all samples; plagioclase is absent. Sanidine is the characteristic phenocryst of the trachytic eruption products, including lavas and bombs. The sanidine crystals are euhedral with a size of 1 to 6 cm; rare crystals reach a size up to 10 cm. It is the major phase forming the groundmass of all crystalline rocks. In the minette samples, sanidine is restricted to the groundmass.

Table 1: Overview of the samples selected for detailed microscopic and microchemical analyses

Type	Abbreviation	sample	Rock type	location
Lava	L1	ES 83	trachyte	Lava dome in the central part of Saray Volcano
		ES 84		
		ES 85		
	L2	ES 61		Lava on the eastern side of Gamichi valley
		ES 62		
	L3	GV-5-1		Lava on the western side of Gamichi valley
Bombs	B1	ES35	trachyte	L-PCL (SP-I)
		ES 36		
		ES 37		
	B2	ES 41		
		ES 56		
		ES 57		
	B3	ES 113		L-PCL (SP-II, 1674 m)
	B4	ES 114		U-PCL (SP-II, 1653 m)
	B5	ES 115		
		ES 103		
		ES 105		
Felsic minettes	F1	SV-2-1	felsic minette	Felsic minettes east of the trachyte dome, within the former crater
	F2	SV-4-1		
	F3	SV-7-2		
	F4	SV-8-1		
Mafic minettes	M1	GV-1-5	mafic minette	Mafic minette dyke from Gamichi valley crosscutting the trachytic pyroclastic depositis
	M2	L6		
	M3	SV-2-2		Mafic minette dyke occurring next to a felsic minette in the former crater
Xenoliths	X-Gl	GV-0-2	glimmerite	Occurring as xenoliths within felsic and mafic minettes and in trachyte
	X-Ol	SV-7-1	peridotite	
	X-Px	SV-1-1	pyroxenite	

Clinopyroxene microphenocrysts were observed in all trachytic and minette samples. They are mainly euhedral and appear light to dark green in the polarizing microscope. **Phlogopite** in micro- to megacrysts size occurs in almost all investigated rocks. In general, **olivine** macro- to megacrysts occur in minettes, lava L3 contains only rare individuals. **Carbonatite** is common feature in the groundmass of the felsic minettes. In addition, areas with carbonatite were observed within groundmass of the trachyte bomb samples B3 and B4 and lavas L1 and L2.

Accessory minerals are **magnetite** and **apatite** occurring in the groundmass of all samples (Table 2). Partly they can reach microphenocrysts size (≤ 0.5 cm). Some samples contain **titanite** (samples L1, L2 and B2) and **zircon** (samples L1 and B3) as accessories.

Notably minette contains **glimmerite**, **pyroxenite** and **peridotite** (wehrlite) xenoliths with sizes from a few millimeters up to 30 cm in diameter. Rare xenoliths of glimmerite with sizes < 5 mm were observed in trachyte.

3.3.2.1 TRACHYTES - LAVAS (L1–L3) AND BOMBS (B1-B7)

Macroscopic observations: All **trachytic lava** samples contain euhedral sanidine phenocrysts and clinopyroxene microphenocrysts, mostly aligned along a flow pattern (see Figure 3b). Vesicles up to several centimeters in size are present. In the central lava dome (L1) sanidine phenocrysts have an average size of 3 to 4 cm (Figure 7a); occasional megacrysts reach a maximum size up to 10 cm. There are subordinate clinopyroxene microphenocrysts. The microcrystalline, greenish-blue, porous groundmass consists of interlocked sanidine crystals (up to 200 µm). In the other lavas, which crop out at the flanks of Saray Volcano (L2 and L3) and in all bomb samples, sanidine phenocrysts are on average smaller than in L1, with the size varying between 0.5 and 2 cm (Figure 7b). Compared to L1, the groundmass sanidine crystals of L2 and L3 are larger, reaching a size up to 2 mm. Sanidine phenocrysts as well as groundmass crystals within lavas L2 and L3 are aligned in one direction (see Figure 3c). In lava L3, occasionally, olivine macro- to megacrysts (up to 1.5 cm). Macroscopically visible reactions rims around these olivine crystals suggest them to be xenocrysts in trachyte.

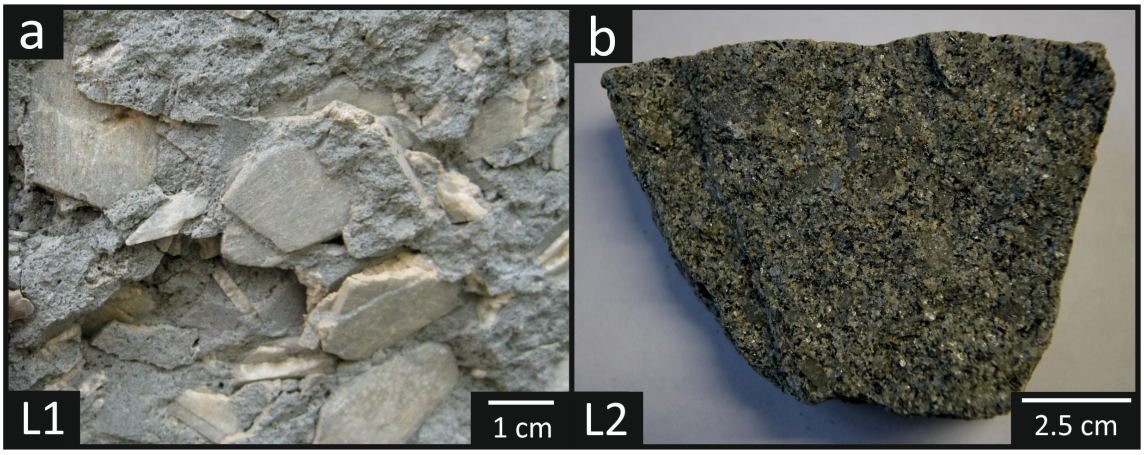

Figure 7: Photos of a) Lava sample L1 with sanidine megacrysts in a greenish-blue groundmass, b) lava sample L2 with sanidine macrocrysts in a coarse-grained groundmass

The **trachytic blocks and bombs** were deposited in a porous, welded ash groundmass with a beige color and macroscopically visible fragments of sanidine and pyroxene. Sanidine-rich blocks and bombs are often well-rounded and reach sizes between 20 cm and 1 m in diameter and occur preferentially at the bottom of the pyroclastic layer. Sanidine occurs always as isolated ~0.5 to 2 cm large macro- and megacrysts within the fine-grained crystalline to glassy groundmass (Figure 8). Similar to the trachytic lavas, the crystals are mostly aligned in one direction. The color of the groundmass of most bomb samples varies greatly between both pyroclastic layers. In the L-PCL, bombs typically appear dark red, which is mainly caused by the glass-rich groundmass. With increasing crystallinity, the color changes to orange-brown and grey in the L-PCL, and greenish-blue in the uppermost U-PCL, similar to the color of the lava dome samples.

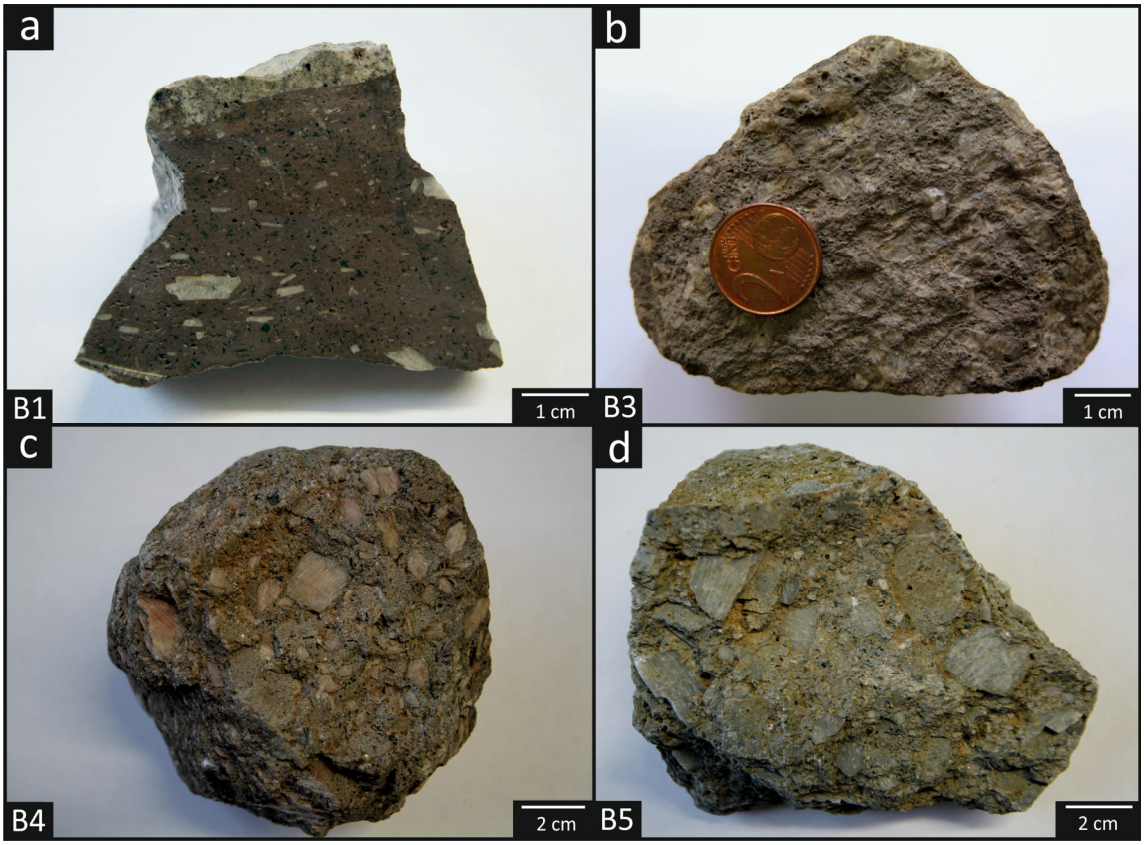

Figure 8: Photos of different trachytic bombs, a-b) with sanidine phenocrysts embedded in a glass-rich groundmass, c) sanidine phenocrysts embedded in a partly crystallized groundmass d) with sanidine phenocrysts embedded in a fully crystallized groundmass

Microscopic observations: Characteristic for all trachytic eruption products – lavas and bombs – are **sanidine** phenocrysts. Oscillatory zoning of the sanidine phenocrysts is visible under crossed polarizers (Figure 9). BSE images (and EMP-analyses, see Chapter 3.3.4. "Mineral chemistry") show that these zonings are mainly caused by changes in Ba content. All sanidine phenocrysts are almost free of inclusions; the few inclusions present consist of phlogopite, diopside, apatite and titanite. In lava L3, the sanidine phenocrysts show poikilitic growth rims (Figures 9b and c) entrapping frequently diopside and (often strongly resorbed) phlogopite. The samples B4 and B5 contain a large amount of bubbles trapped in the outermost rims of sanidine, occasionally including fluid inclusions.

Detailed investigations of BSE images reveal three different stages of resorption affecting the sanidine megacrysts:

- "**Weak resorption**": irregular or rounded surfaces at the end of each oscillatory cycle (yellow arrows in Figure 10a).
- "**Strong resorption**": invasive resorption that either truncates the previous compositional zoning or consumes it (white arrows in Figure 10a). The newly grown sanidine rim show no significant change in Ba.
- "**High-grade resorption**": irregular dissolution surfaces and embayments accompanied by significant changes in Ba of the newly grown sanidine rim (e.g. Figure 10c).

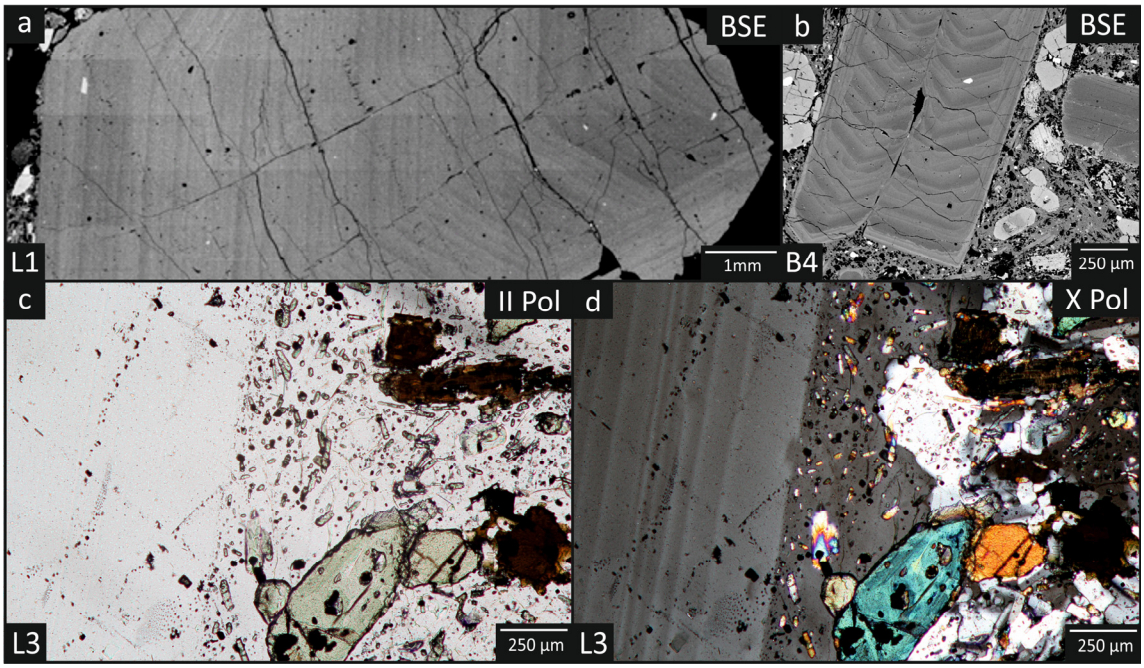

Figure 9: BSE images a) of an oscillatory-zoned sanidine megacryst from lava L1, and b) sanidine phenocrysts from bomb sample B4, and c-d) micro-photographs of a sanidine phenocryst (left) with a poikilitic rim entrapping diopside crystals c) with parallel polarizers and d) crossed polarizers showing the oscillatory zoning of the sanidine phenocryst

Clinopyroxene macro- to microphenocrysts are abundant with most of them having euhedral grain shapes. Characteristic are multiple resorption phenomena within one crystal, which are marked by rounded surfaces and dissolution embayments (Figure 11a). In lava sample L1, aegirine occurs as xenomorphic crystals in the groundmass or forms rims around diopside (Figure 11b). In addition, all clinopyroxene crystals show multiple oscillatory zoning, which is often already visible in the polarizing light microscope. Some clinopyroxene crystals contain inclusions of apatite, phlogopite or silicate melt. In sample B3, only pseudomorphs after diopside occur: Within the outline of the former pyroxene crystals, the mineral assemblage quartz + dolomite + calcite ± Fe-oxide ± apatite was identified (Figure 11).

The amount of **phlogopite** crystals in the lava samples varies largely, from almost absent (e.g. B1) to the third most prevalent phase after sanidine and diopside (e.g. L3). Detailed (microchemical) investigations showed that two different types of phlogopite, phl-I and phl-II, occur in these samples. They can be distinguished in BSE due to their brightness reflecting differences in chemical composition.

The “dark” **phl-I** is Mg-rich, generally free of inclusions, and shows no signs of dissolution. Hematite exsolution lamellae are rare and restricted to the area close to the rim. In some samples, phlogopite inclusions in cores of sanidine and diopside were identified as phl-I. In contrast, the “bright” **phl-II** is a Ba-, Ti-, Fe-rich F-phlogopite and contains often inclusions of minerals such as magnetite and apatite. Often it also shows both, silicic and carbonatite melt inclusions. In trachyte, phl-II exhibits uniformly distributed hematite exsolution lamellae, which cause the crystals to appear almost black under crossed polarizers. All observed phl-II crystals in the trachytic

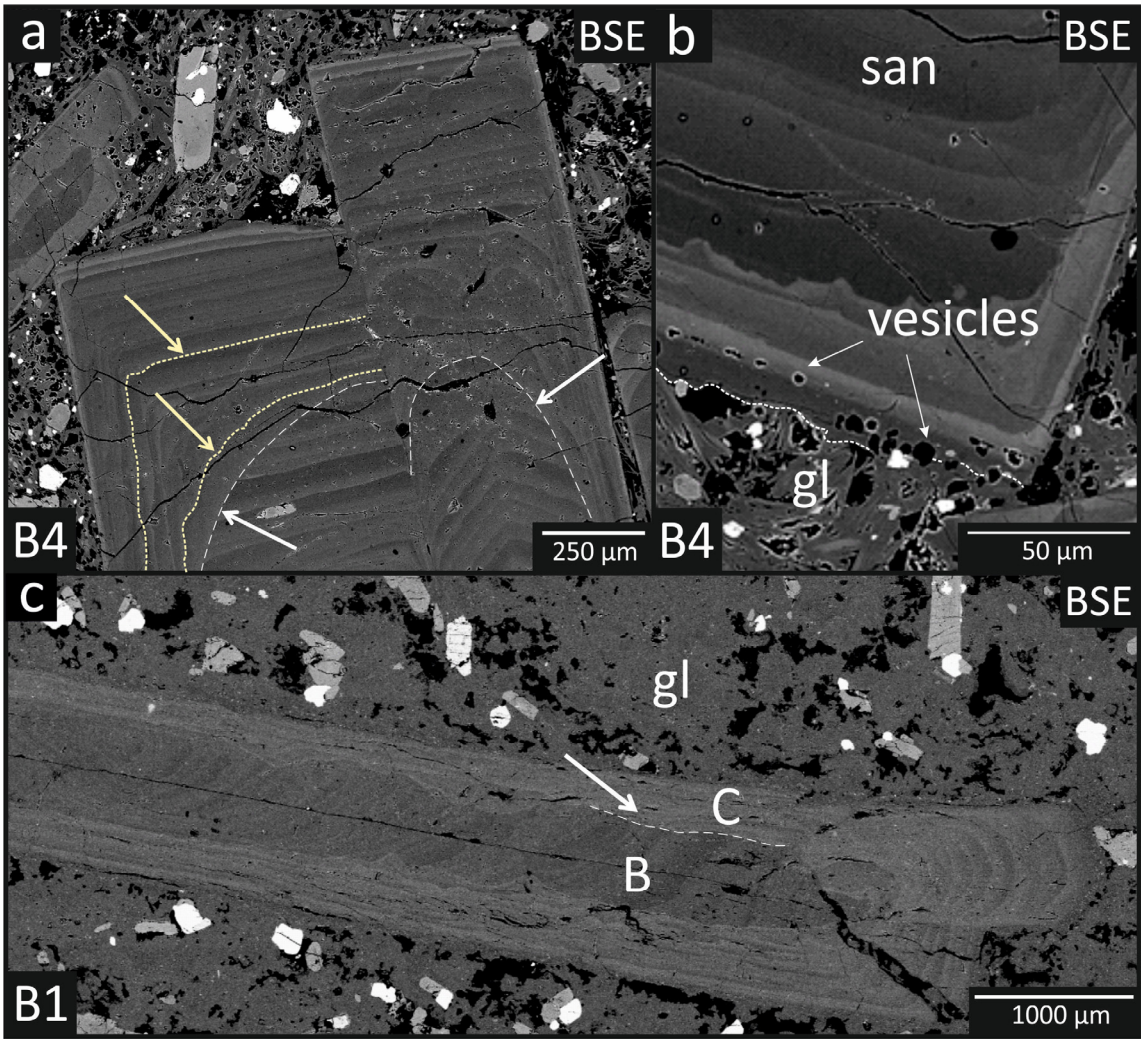

Figure 10: BSE images showing the different features of weak, strong and high-grade resorption of sanidine; weak resorption occurs at the end of each oscillatory cycle e.g. yellowish arrows in a; a) sanidine crystal in bomb sample B4 with strong resorption that either truncates the previous compositional zoning or consumes it (white arrows); b) sanidine crystal with vesicles at the boundary of the crystal to the groundmass in bomb sample B4, c) example for high-grade resorption (dashed line) separating growth zone B and C in bomb sample B1

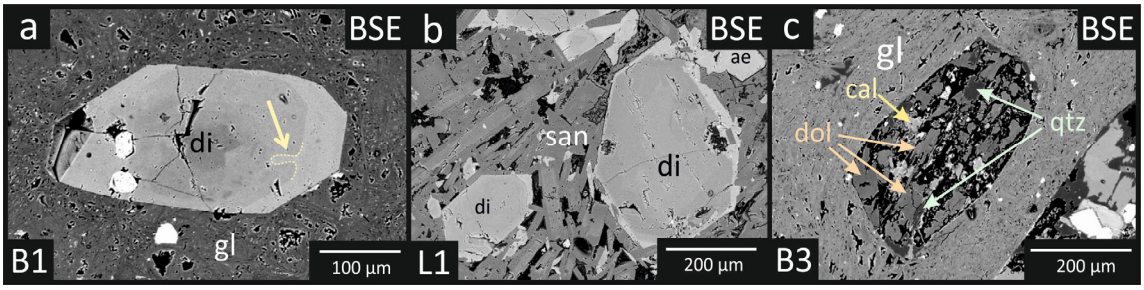

Figure 11: BSE image of clinopyroxene, a) diopside showing resorption (yellow arrow) with deep dissolution embayment (dashed line), b) diopside with aegirine-augite rim and c) a pseudomorph of calcite, dolomite and quartz after diopside

eruption products are strongly resorbed (Figure 12b). In general, they show clear signs of corrosion with jagged grain boundaries and dissolution holes. Notable, sample E4: Here both types of phlogopite (phl-I and phl-II) occur next to each other (Figure 12). Occasionally thin **kelyphytic rims** consisting of diopside surround both types of

phlogopite (Figures 12a and b). Phl-II entrapped in the outermost poikilitic rims of sanidine phenocrysts as well as the isolated groundmass phlogopite crystals show corroded surfaces. A special feature of the lava dome (L1) are accumulations of phlogopite with sizes < 1mm in diameter (remnants of glimmerite xenoliths). The rare glimmerites show strong dissolution features. Due to the small size of the phlogopite crystals and the high degree of dissolution, they can easily be overseen.

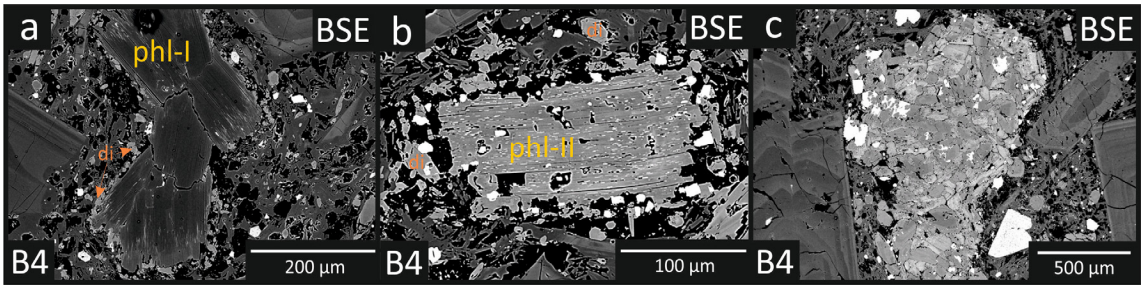

Figure 12: BSE images of phlogopite in bomb sample B4 of a) zoned phl-I crystal with a thin kelyphytic rim consisting of diopside, b) corroded phl-II crystal with hematite exsolution lamellae surrounded by diopside crystals, and c) glimmerite xenolith

The **groundmass** of the trachytic samples differs in various aspects: In **lava L1,** the randomly distributed small sanidine crystals (< 200 µm) form a porous structure (Figure 13a). In addition, abundant cavities with a diameter up to 1 cm are present, formed by gas bubbles or channels. In **lava samples L2 and L3** the sanidine crystals of the groundmass reach a size of up to 2 mm. In lava L2, sanidine laths (phenocrysts and groundmass) and clinopyroxene phenocrysts, aligned along the flow direction, often contain empty cavities between the crystals (Figure 13b). In contrast, lava L3 is the densest of the three lava types. Here, the crystalline matrix consist entirely of sanidine and contains no cavities.

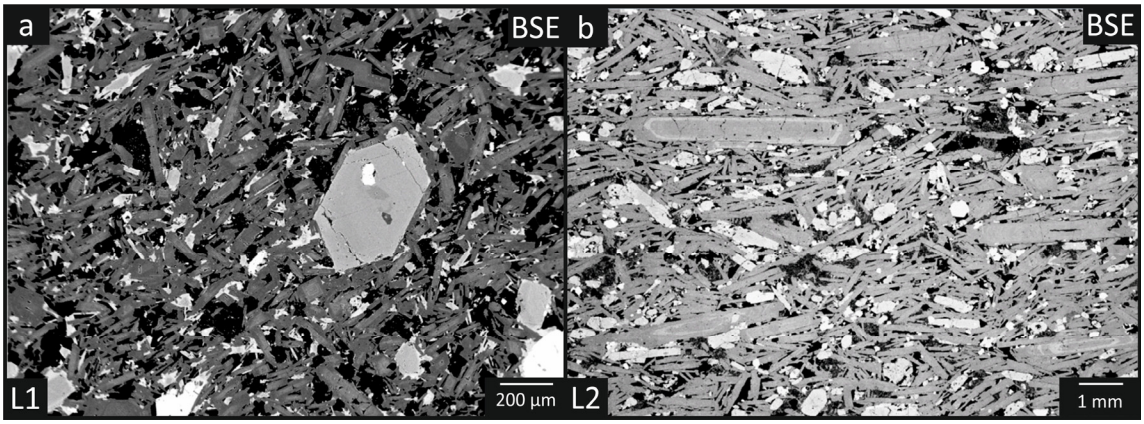

Figure 13: BSE images of a) the porous groundmass of lava L1 and b) the groundmass of lava L2 with sanidine and clinopyroxene aligned in one direction

Figure 14 shows the different textures of the groundmass of the sanidine-rich bombs. The groundmass of the bomb samples is vitric, with occasional microlites of Fe-Ti oxides, (B1, B3) to hypocrystalline (B2, B4). In the lower pyroclastic layer, bombs with a phenocryst/groundmass ratio < 50 % are widespread. In the upper pyroclastic layer, however, the groundmass is mostly crystalline, consisting mainly of sanidine microlites, followed by

clinopyroxene and phlogopite. These rocks are usually vesicular, the proportion of bubbles varies from low (B5) to high (B4).

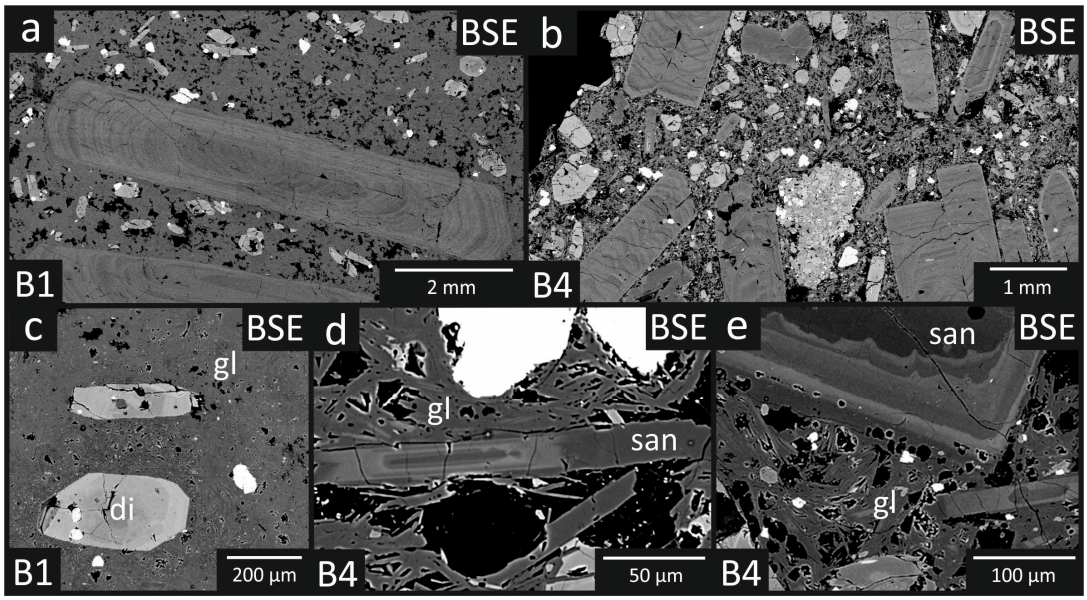

Figure 14: BSE images of the different textures of the groundmasses of the sanidine-rich bombs, a) sanidine megacryst in a glassy groundmass, b) sanidine megacrysts in partially crystalline groundmass, c) diopside crystal in a glassy groundmass, d) sanidine groundmass crystal in a partly crystallized groundmass, e) rim of a sanidine megacryst with entrapped fluid inclusions embedded in a vesicle-rich partly crystallized groundmass

A special feature of the trachytes of Saray Volcano is the occurrence of **carbonatite** in form of evenly distributed fine-grained carbonate crystals in the trachytic glass/melt groundmass of bomb B3 and B4. Carbonatite forms elongated areas or schlieren within the silicate matrix and is is also present as cloud-like elongated blobs or droplet within the silicate melt (lava L1 and sample B3). In L1, carbonatite occurs also in the pressure shadow of the gas-bubble cavities. Some of the carbonatite blobs contain euhedral phl-II crystals. Phl-II crystals embedded in the carbonatite matrix show no signs of dissolution whereas the crystals at the contact to the trachytic melt are moderately to strongly attacked and display hematite exsolution lamellae (Figure 15).

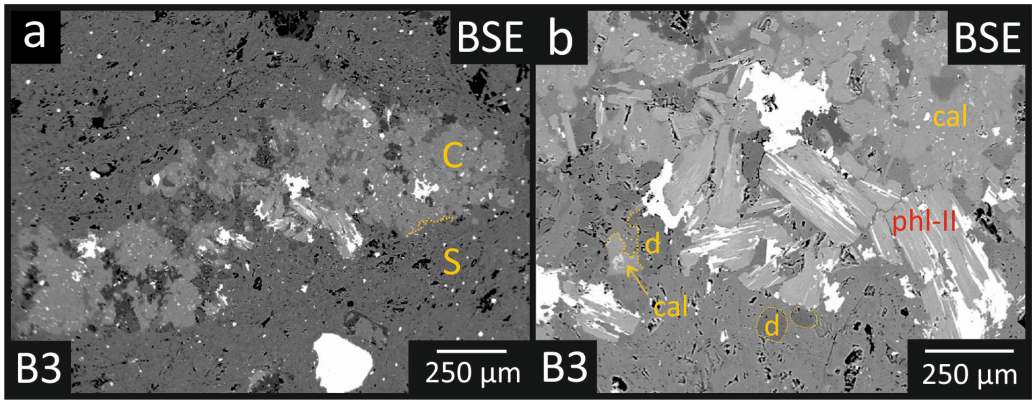

Figure 15: a) Carbonatite blobs (C) in the silicate glass (S) groundmass of bomb sample B3 b) detail shows that carbonate blob consist of calcite and dolomite. Phl-II in carbonatite is unaltered. Phl-II at the contact to silicate melt shows Fe-oxide formation

Accessories of the trachytic rocks are apatite and magnetite. Frequently titanite occurs (e.g. samples L1, L2 and B2). Apatite, magnetite and titanite show euhedral to subhedral grain shapes and reach sizes up to 500 µm. Notable, small euhedral apatite crystals (< 30 µm) in the groundmass of the bomb B4, which contain abundant fluid inclusions. Lava dome samples L1 contain euhedral to subhedral zircons with sizes up to 100 µm or occurs as inclusions in diopside (L1). In sample B3, zircon precipitates with sizes < 20 µm occur in the glassy groundmass.

3.3.2.2 FELSIC MINETTE (F1-F4)

Macroscopic observations: Felsic minette has a porphyritic texture with phlogopite crystals up to 1 cm in size embedded in a grey to pinkish-grey groundmass (Figure 16). Further phenocrysts are olivine (up to 1 cm in size), magnetite and apatite. Sanidine is in general restricted to the groundmass. Individual sanidine crystals up to 2 cm are however rare (Figure 16b). The plugs carry numerous xenoliths up to 25-30 cm in diameter consisting of pyroxenite, glimmerite and olivine-rich nodules. Sample F4 is characterized by centimeter-sized gas bubbles which often contain carbonates (Figure 16a).

Microscopic observations: The investigation of the phlogopite crystals by BSE imaging and chemical analyses (see chapter "Mineral chemistry") showed that only **phl-II** is present in felsic minette; phl-I was not identified in the investigated samples. Some larger crystals, free of inclusions, show darker cores in BSE (enriched in Mg and Cr; Figure 17a), whereas most phlogopite crystals lack distinct chemical zoning (Figure 17b). Phl-II occurs always together with carbonatite. In addition, phl-II contains silicic and carbonatitic melt inclusions (Figure 17c). Furthermore, inclusions of magnetite in phl-II are abundant, whereas apatite inclusions are rare.

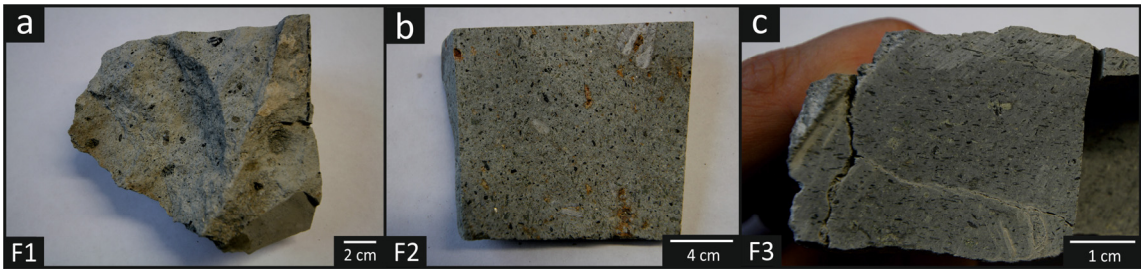

Figure 16: Photos of felsic minette samples a) F4 dark appearing phlogopite phenocrysts and glimmerite xenoliths in a grey groundmass consisting predominantly of sanidine, b) F2 with sanidine xenocrysts (white) c) F3 with clinopyroxene crystals (dark) showing an alignment in flow direction

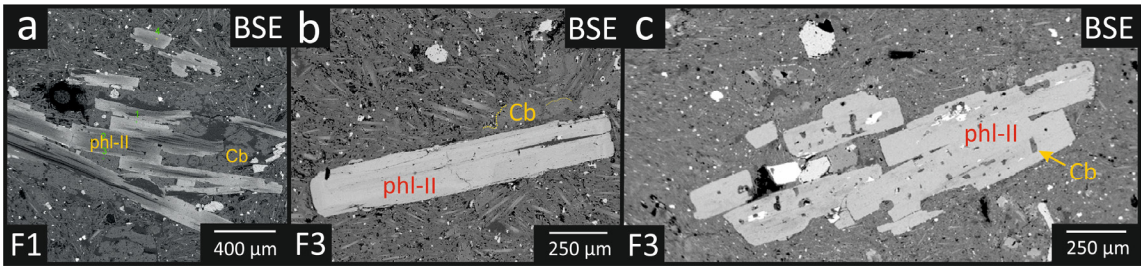

Figure 17: BSE images of phl crystals in felsic minette, always adjacent to carbonates. a) Chemically zoned phl-II adjacent to carbonate, b) unzoned phl-II crystals and c) phl-II with carbonatitic melt inclusions

Diopside per se is the second common phenocryst in the plug samples. Often, however, only the outlines of the former pyroxene crystals are preserved and replaced by the mineral assemblage quartz + dolomite (Figure 18). The reaction starts along the cracks (Figure 18c) and can lead to a complete replacement of diopside (Figures 18a and b). **Olivine** phenocrysts occur frequently in felsic minette. The crystals are often replaced by carbonate and talc. Accessory apatite and magnetite are in general euhedral to subhedral phenocrysts with sizes up to 600 µm.

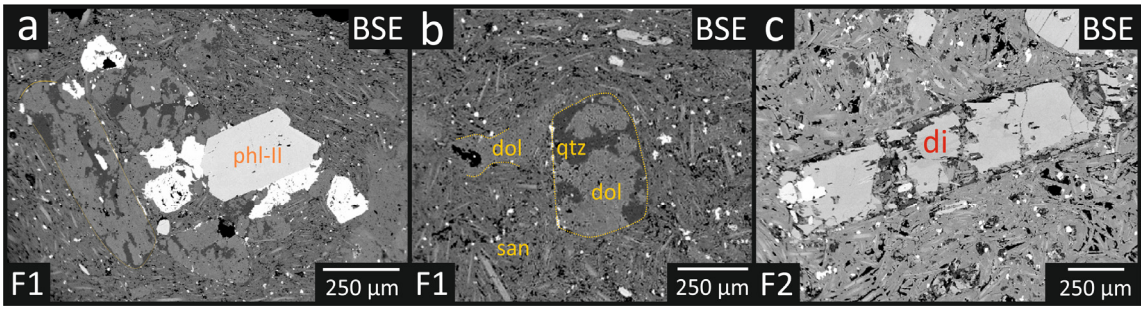

Figure 18: BSE images of pseudomorphic replacement after diopside in felsic minette showing a) completely replaced diopside crystals and a euhedral phl-II crystal surrounded by a groundmass of sanidine microlites and carbonatite and b) diopside crystals replaced by carbonate and quartz in a groundmass of sanidine microlites and carbonatite and c) diopside, partially replaced along the cracks by carbonate and quartz

Sanidine phenocrysts are rare in felsic minette. In general, the occurrence of sanidine is restricted to the groundmass. The few larger crystals (< 2 cm) observed in sample F2, are intensively resorbed. As shown in Figure 19, these grains show Ba-rich rims. Within these Ba-rich rims, individual barite inclusions (< 20 µm) were identified.

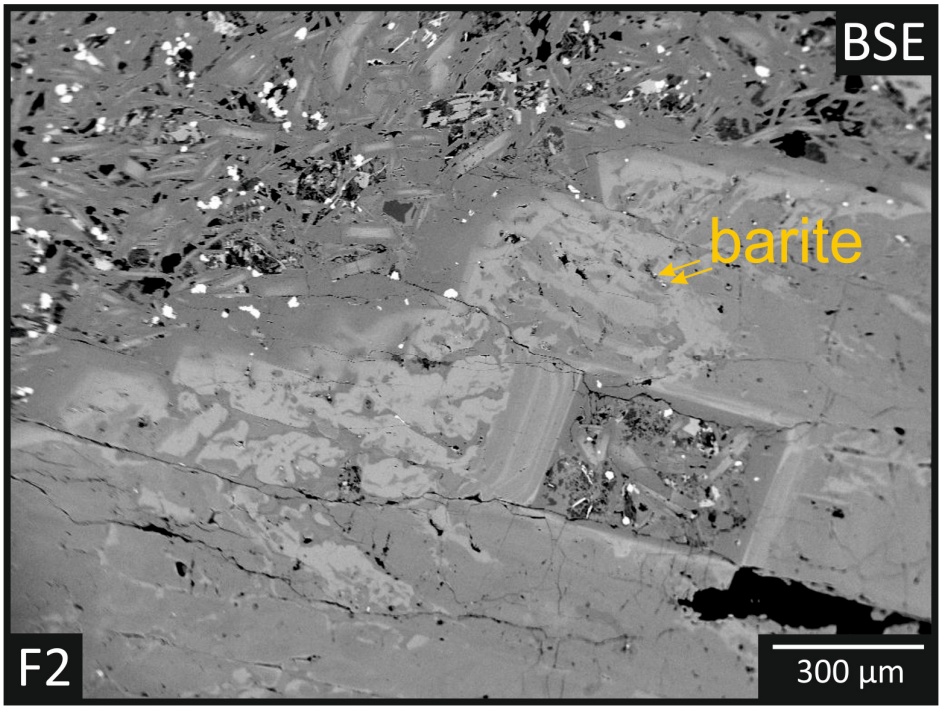

Figure 19: BSE image showing a sanidine xenocrysts in felsic minette F2 shows strong dissolution textures; notably barite was identified in pores of the sanidine crystal

The **groundmass** of felsic minette can be subdivided into two distinct parts: a siliceous and a carbonate dominated one. The siliceous part consists mainly of sanidine, mostly aligned along a flow direction. Carbonatite forms schlieren with several millimeter in size adjacent or surrounding small euhedral to subhedral phlogopite crystals. It occurs as small grains between the sanidine crystals or is contained as carbonatitic melt inclusions in phlogopite. Carbonate occurs also in the pseudomorphs after diopside (Figure 20).

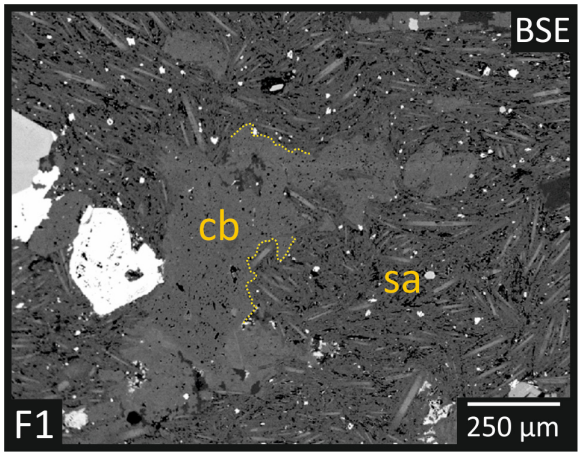

Figure 20: BSE image of a carbonatite blob in a groundmass consisting of sanidine microlites

3.3.2.3 MAFIC MINETTE (M1-M3)

Macroscopic observations: Typical for the dark green, mafic minette are macro- to megacrystic phlogopite crystals (up to 2 cm, Figure 22). Similar to felsic minette they carry pyroxenite, glimmerite and olivine-rich xenoliths (for further description see later in the text).

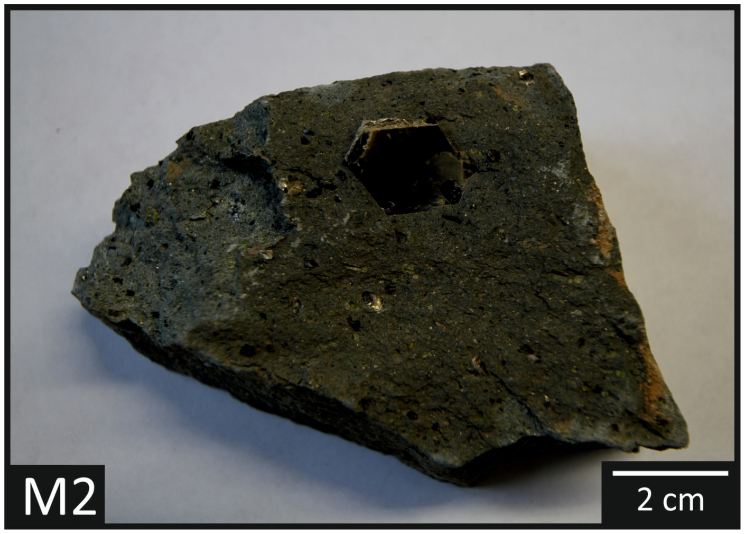

Figure 21: Photo of mafic minette sample with a euhedral phlogopite megacryst

Microscopic observations: Major phenocrysts in mafic minette is **phlogopite** with a size up to 1 cm followed by clinopyroxene, magnetite and apatite. In mafic minette both types of phlogopite, phl-I and phl-II, occur (Figure 22). **Phl-I** phenocrysts are large (up to 1 cm), but rather rare (only 2-3 per thin section) and show clear signs of mechanical stress such as cracks or broken crystals. These crystals are often twisted and show kink-band like textures (Figure 22d). The surface of the crystals is intensely resorbed leading to rounded shapes and dissolution embayment (Figure 22). **Phl-II** crystals are mostly smaller with sizes up to several millimeters or occur as fine-grained flakes within the groundmass. In contrast to phl-I, they contain abundant euhedral apatite inclusions.

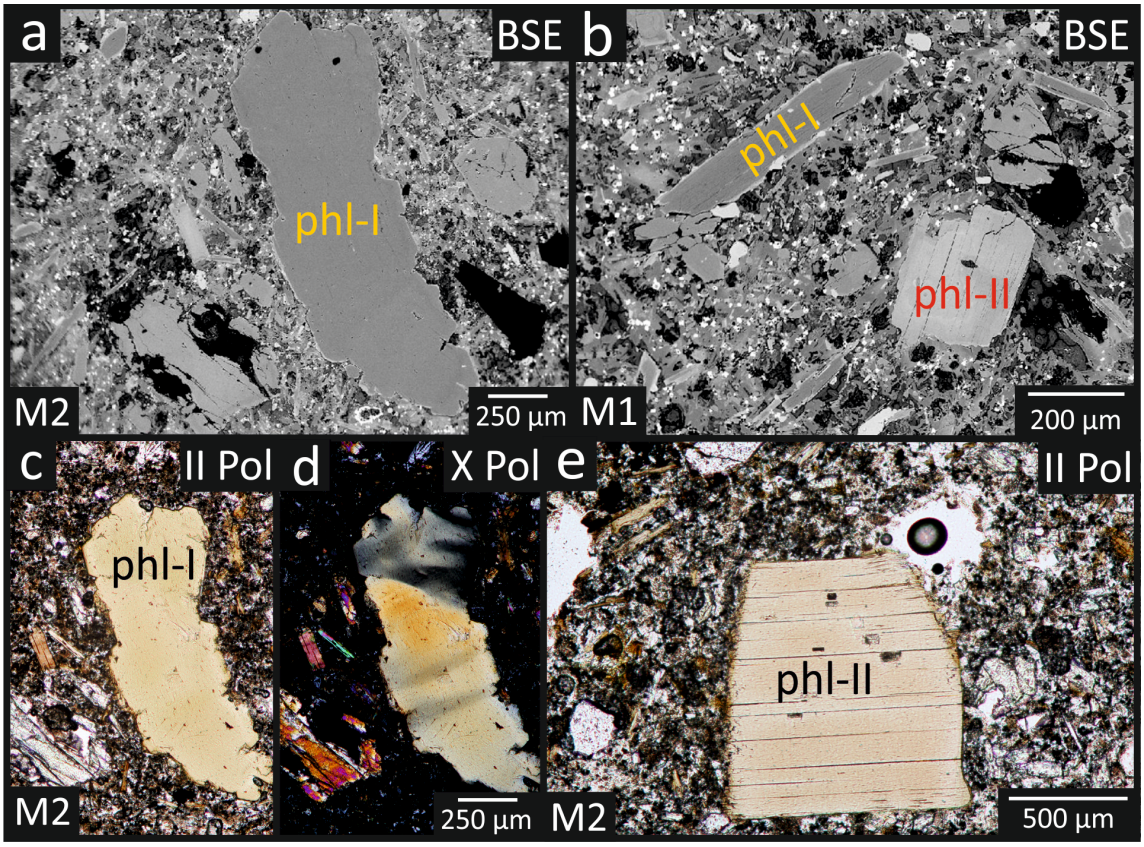

Figure 22: Mafic minette with phl-I showing irregular grain boundaries a) BSE image and c-d) polarized light microscope image with c) parallel and d) crossed polarizers, b) BSE image of phl-I with a Ba-rich rim and phl-II with a Mg-rich rim, e) phl-II with reactions rim to the glass matrix

Mafic minette contains euhedral **apatite** phenocrysts with sizes up to 1 mm (Figure 23a). Apatite is also abundant as inclusions in **clinopyroxene** crystals (Figure 23b). Clinopyroxene (diopside) crystals are all broken or show cracks. **Olivine** phenocrysts occur only occasionally and show often replacement by carbonates and talc. The groundmass of mafic minette consists of vesicular glass with fragments of phl-I and phl-II and abundant µm-sized Fe-Ti-oxides.

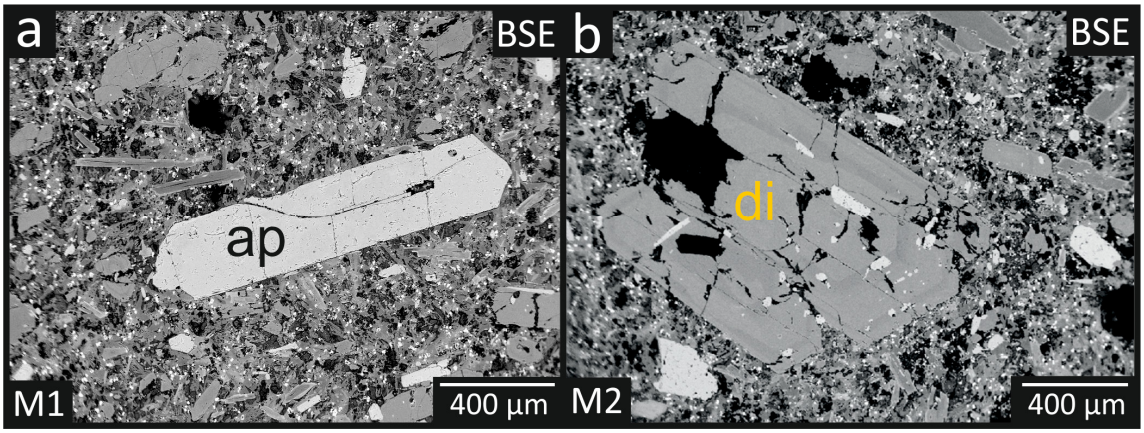

Figure 23: BSE images of mafic minette with a) a euhedral apatite phenocrysts and b) a broken diopside crystals with apatite inclusions

3.3.2.4 XENOLITHS (X-GL, X-OL AND X-PX)

Different types of xenoliths with a size from some millimeters up to 30 cm in diameter were observed in the felsic and mafic minette: peridotite (wherlite) xenoliths (X-Ol) and pyroxenite (X-Px) were only found in minette whereas glimmerite xenoliths (X-Gl) were also found in trachyte.

Peridotite (wherlite) xenolith (Figure 24): The main phase of peridotite xenoliths is olivine in a glass-rich groundmass. In contact to the melt, olivine shows often reaction rims consisting of diopside + Fe-Ti-oxides + phl-II. In some cases, olivine is altered to calcite and talc (Figures 24b and c). Euhedral phl-II crystals occur within the reaction rims around olivine as well as in the groundmass. Diopside crystals are often broken or twisted and contain abundant euhedral apatite inclusions. Remarkable are globules with diameters up to 1 mm in diameter, consisting of K-feldspar, albite and hyalophane (Figures 24c and d).

Glimmerite xenolith (Figure 25): A major phase in glimmerite xenoliths is phlogopite followed by clinopyroxene (diopside). BSE imaging showed that phl-II is the only phlogopite present (Figure 25). The proportion of phlogopite in glimmerite ranges from ~ 50 % up to ~ 80 %. Phlogopite and diopside crystals are intergrown with euhedral apatite and magnetite crystals or contain euhedral apatite inclusions. In addition, some of the phlogopite crystals contain carbonate melt inclusions (Figure 26b). Sometimes, the space between the phlogopite crystals is filled with interstitial melt (Figure 25e).

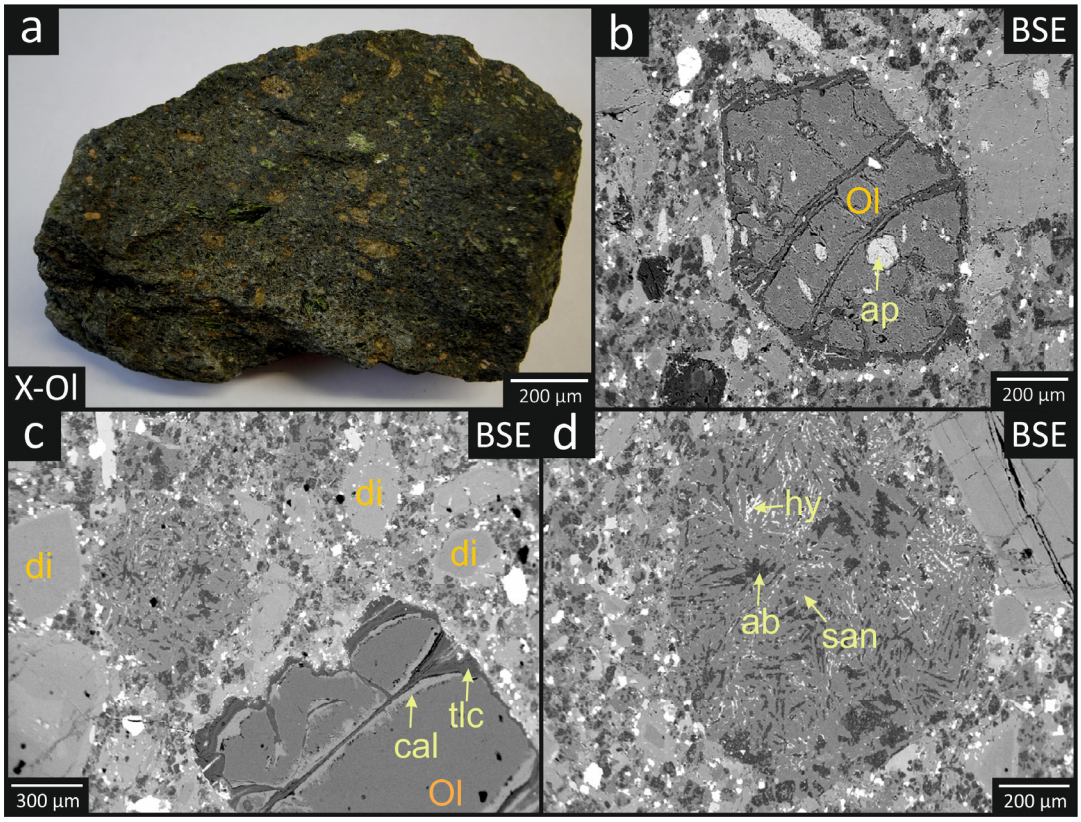

Figure 24: a) Photo of an peridotite xenolith (X-Ol), BSE images of b) an olivine crystal with apatite inclusions, c) an olivine crystal altered to calcite and talc, d) ocelli, consisting of albite, K-feldspar and hyalophane in X-Ol

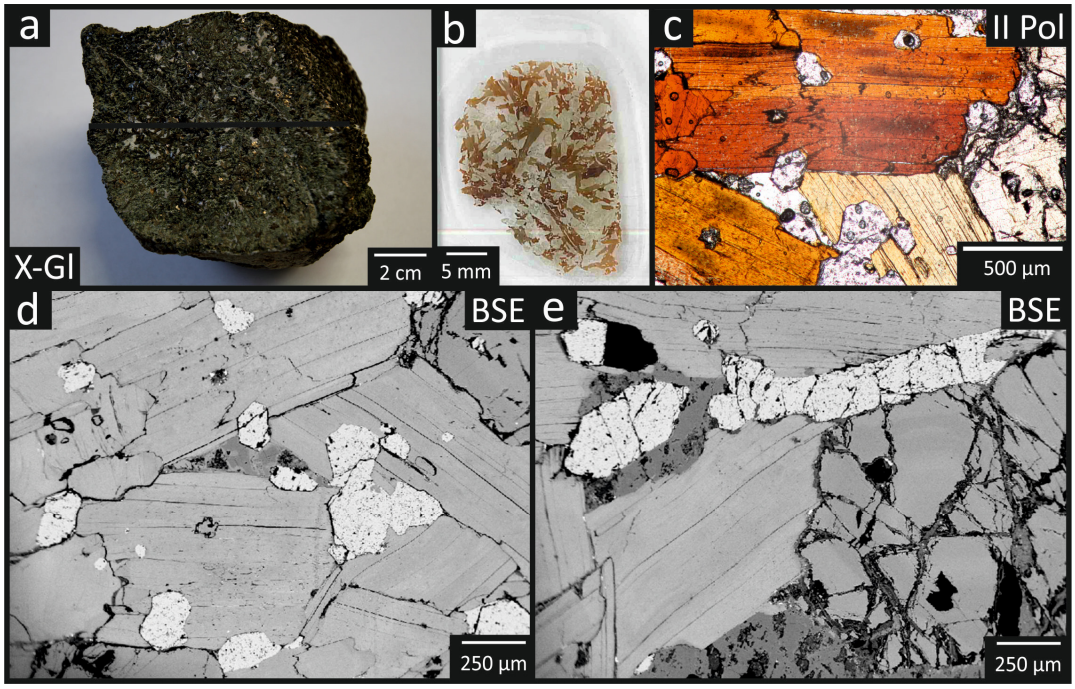

Figure 25: a) Photo of glimmerite xenolith (X-Ol), b) scan of the thin section, b) polarized light image of phlogopite with apatite, BSE images of c) phlogopite with euhedral apatite and d) phlogopite adjacent to a broken diopside and apatite, cavities are filled with glass

Notably, glimmerite xenoliths show different textures in different environments. In mafic minette, the largest glimmerite xenoliths have sizes up to 30 cm in diameter, with phlogopite crystals up to 1 cm (Figure 25). Besides cracks in diopside, they show no significant alteration. In glimmerite, contained in the felsic minette, all diopside crystals are replaced by carbonate and quartz (Figures 26a-b). In trachyte, only small glimmerite xenoliths (< 5 mm in diameter) occur. The phlogopite crystals in these glimmerites exhibit hematite exsolution lamellae. All glimmerite xenoliths show signs of dissolution and alteration at the contact to the trachytic melt. In some cases, the corrosion phenomena are only moderate (Figures 26c-d), whereas other glimmerite xenoliths are strongly attacked and can therefore, hardly be identified.

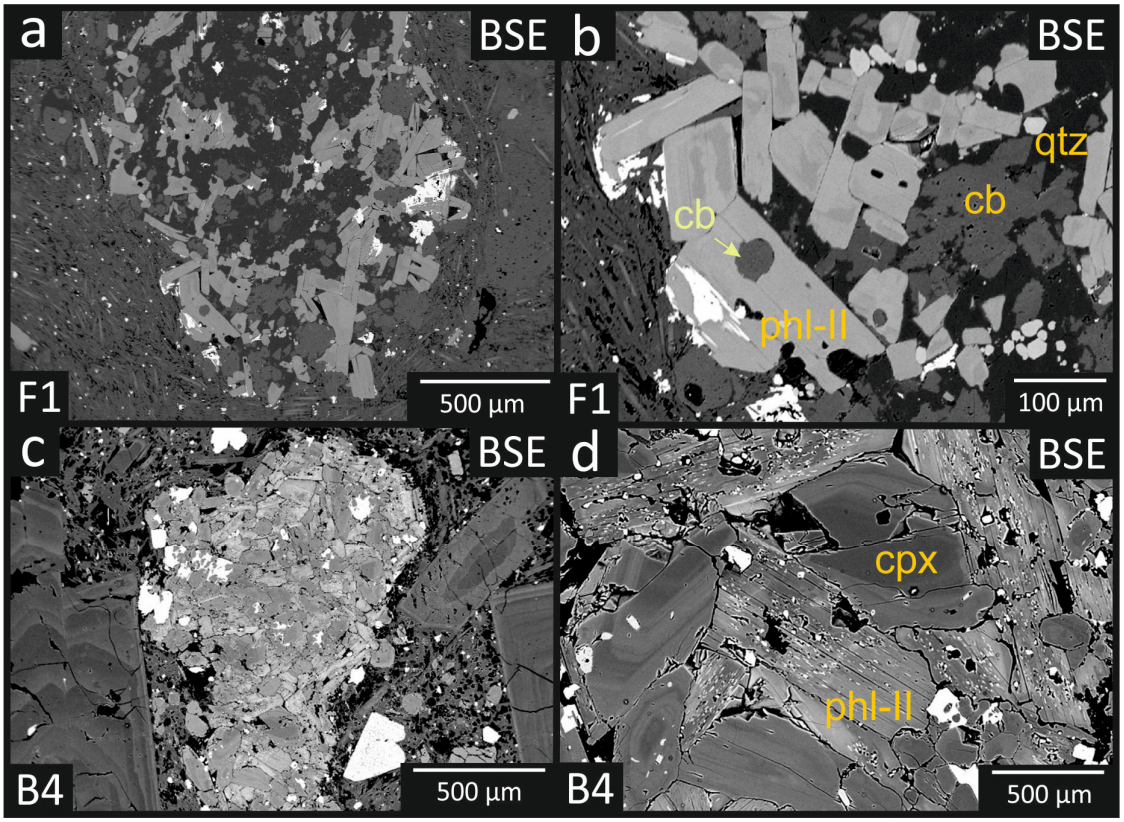

Figure 26: BSE images of glimmerite xenoliths a-b) found in a felsic minette with all diopside crystals being replaced by carbonate and quartz, c-d) in trachyte with corroded phlogopite crystals showing hematite exsolution lamellae

Pyroxenite xenolith (Figure 27): The xenoliths contain large pyroxene crystals (Figure 27a). Main mineral phase in these xenoliths are euhedral pyroxene phenocrysts with abundant euhedral apatite inclusions (Figure 27b). Their groundmass is fine-grained and consists mainly of glass and sanidine crystals. Notable are strongly resorbed leucite crystals, showing typical crosshatched crystal twinning in cross-polarized light (Figure 27c).

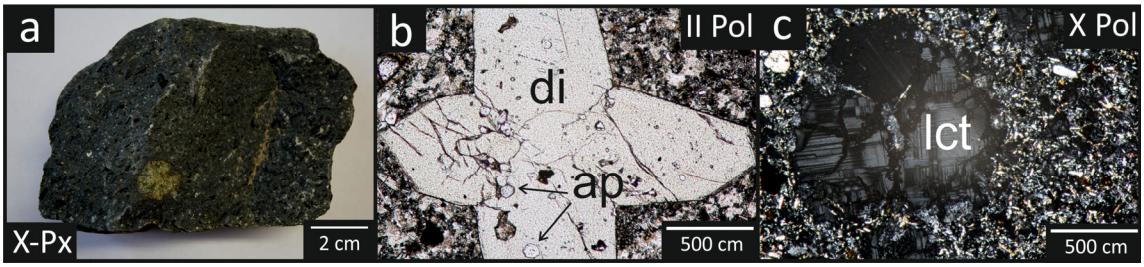

Figure 27: a) Photo of a pyroxenite xenolith with a peridotite inclusion, b) diopside crystal with apatite inclusions c) leucite in a sanidine-rich groundmass

Table 2: Mineral paragenesis observed in the investigated rocks of Saray Volcano. Abbreviations are taken from IUGS Mineral abbreviation list (Siivola and Schmid 2007); di repl. = diopside replaced by carbonates + quartz

sample	sa	ab	hy	lct	glass	cb	di	ae	di repl	phl-I	phl-II	ol	tlc	qtz	ap	mag	hem	ttn	zrc	brt
L1	x					x	x	x		x	x				x	x	x	x	x	
L2	x					x	x			x					x	x		x		
L3	x						x			x	x	x			x	x	x	x		
B1					x		x								x	x				
B2	x				x		x	x		x					x	x		x		
B3					x	x	x		x		x			x	x	x	x		x	
B4	x				x	x	x			x	x				x	x	x			
B5	x				x	x	x			x					x	x				
B6	x				x	x	x			x					x	x				
B7	x				x	x	x			x					x	x				
F1	x					x	x		x		x	x		x	x	x				
F2	x					x	x		x		x	x			x	x				
F3	x					x	x		x		x			x	x	x				x
F4	x					x	x		x		x				x	x				
M1					x		x			x	x				x	x				
M2	x				x		x			x	x			x	x	x				
M3					x		x			x	x			x	x	x				
X-Gl		x			x		x				x				x	x				
X-Ol	x	x	x		x	x	x				x	x	x		x	x				
X-Px	x			x			x								x	x				

3.3.3 WHOLE-ROCK COMPOSITION

The whole-rock compositions of the investigated samples are listed in Table A1-A2 in appendix A-1a. After the criteria of Foley et al. (1987), most of the samples can be classified as ultrapotassic (MgO > 3 wt%; $K_2O/Na_2O > 2$; $K_2O > 3$). As shown in the TAS-diagram (Figure 28a) the samples from the lava dome (L1) and the bombs from the L-PCL have the highest SiO_2-concentrations; they plot in the field of "trachyte". The lava samples L2 and L3, and the bombs from the U-PCL show slightly lower SiO_2 concentrations; they plot in the field of "trachyte" and "trachyandesite" (see Figure 28a). Their SiO_2 content is comparable with those of the felsic minettes (F1-F4). The Harker diagram in Figure 28b shows, however, that the felsic minettes have slightly lower K_2O and higher N_2O contents. The mafic minettes are characterized by lower SiO_2 and alkali contents, thus plotting in the field of "basaltic trachyandesite" and "phonotephrite" (see Figure 28a). The xenoliths have the lowest alkali and SiO_2 concentrations. In general, rocks are clearly enriched in K_2O, with 5-7 wt% for minette and 8-11 wt% for trachyte (Figure 28b).

Major elements (Figure 29) and trace elements (Figure 30) plotted against SiO_2 to show the chemical variability of the eruption products of Saray Volcano. Al_2O_3 and K_2O shows a positive correlation with SiO_2. The end members represent trachytic lavas with the highest SiO_2 contents as well as highest Al_2O_3 and K_2O concentrations, while the mafic minette and xenoliths show the lowest concentrations for these oxides. In comparison to the trachytic eruption products, the mafic minettes exhibit a negative correlation of following elements with SiO_2: Fe_2O_3T (mafic minette: 8-9 wt%, trachyte: 4-7 wt%), MgO (mafic minette: 8-9 wt%, trachyte: 1-4 wt%), CaO (mafic minette: ~ 9 wt%, trachyte: 3.6 wt%), TiO_2 (mafic minette: ~ 1 wt%, trachyte: <1 wt%) and P_2O_5 (mafic minette: ~2 wt%, trachyte: < 1 wt%).

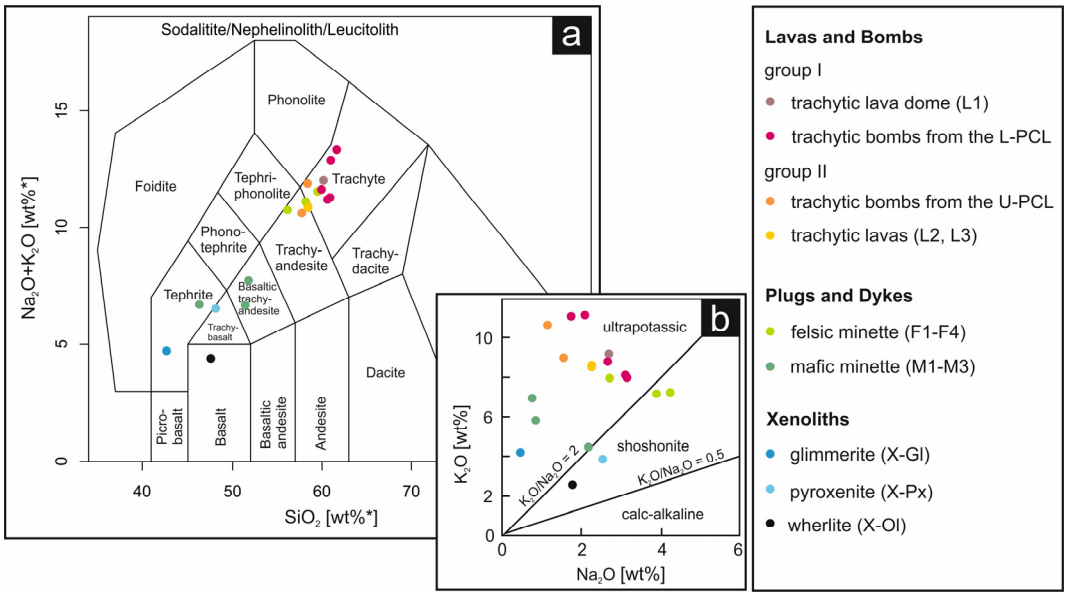

Figure 28: Whole-rock composition of the trachytic lavas and bombs, mafic and felsic minette and glimmerite, pyroxenite and wherlite xenoliths plotted in: a) TAS diagram after Middlemost (1994) on a volatile free basis [wt*]. b) Na_2O-K_2O diagram shows that the majority of the investigated samples can be assigned as ultrapotassic rocks

Felsic minette has the highest LOI and CO_2 concentrations. This fact corresponds to the high proportion of carbonates observed in thin sections. F concentrations of the samples vary widely between ~1000 ppm in trachyte, moderate values (F = 1700 ppm) in mafic minette, and highest values for glimmerite (F = 2900 ppm). All investigated eruption products show high Ba concentrations ranging between 2300 and 4500 ppm. Notably, glimmerite and trachyte lava L1 show the highest Ba values > 5000 ppm. Glimmerite, however, exposes the lowest Sr values (700 ppm), whereas Sr concentrations in trachyte range up to 2100 ppm. Cu, Ni and Cr concentrations are highest in wherlite and mafic minette, while concentrations in Zr, Hf and Th are highest in trachyte.

As shown in the Harker diagram (Figures 29 and 30), these trends can also be observed on a smaller scale within trachyte, with lava L1 and L-PCL bombs representing group I, and lava L2 and L3 as well as U-PCL bombs group II. They show increasing concentrations in MgO, CaO, TiO_2, P_2O_5 and FeOt as well as F, Cr, Cu and Ni with SiO_2, whereas concentrations in Al_2O_3 and K_2O decrease; no significant correlation exists between SiO_2 and Na, LOI, Cl, Ba, Sr, Hf, Zr, Th.

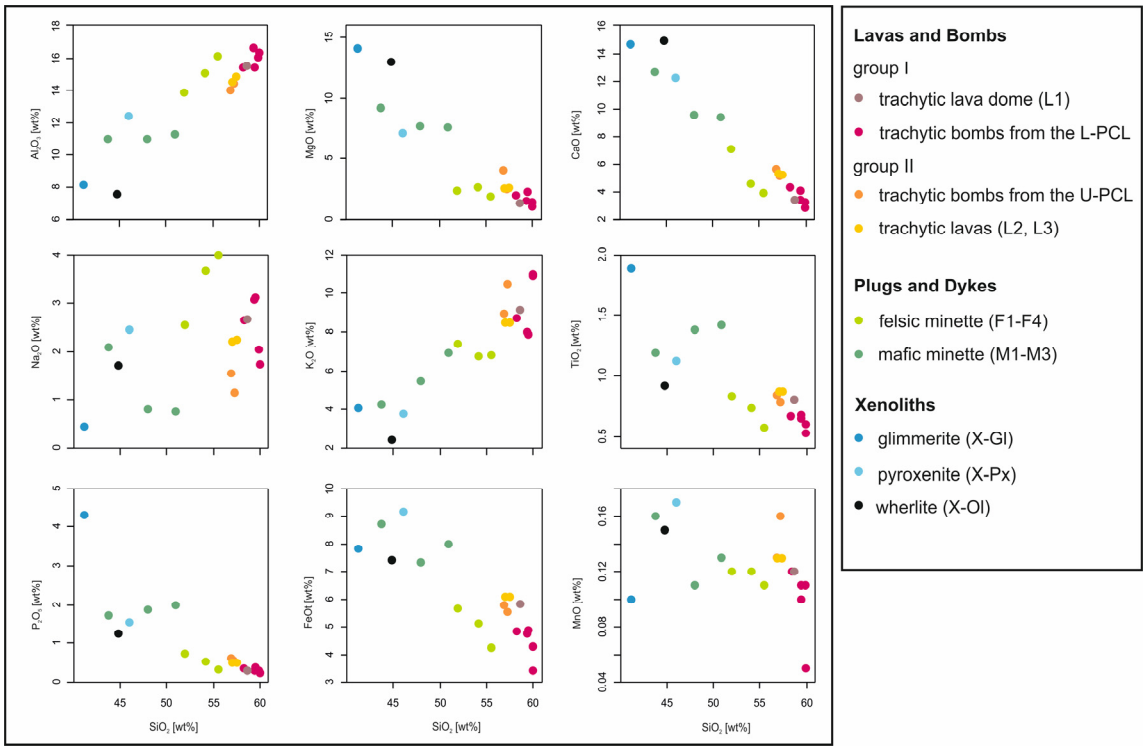

Figure 29: Whole-rock composition of the trachytic lavas and bombs, mafic and felsic minette and glimmerite-, pyroxenite- and wherlite-xenoliths plotted in Harker diagram of the major and minor elements vs. SiO_2

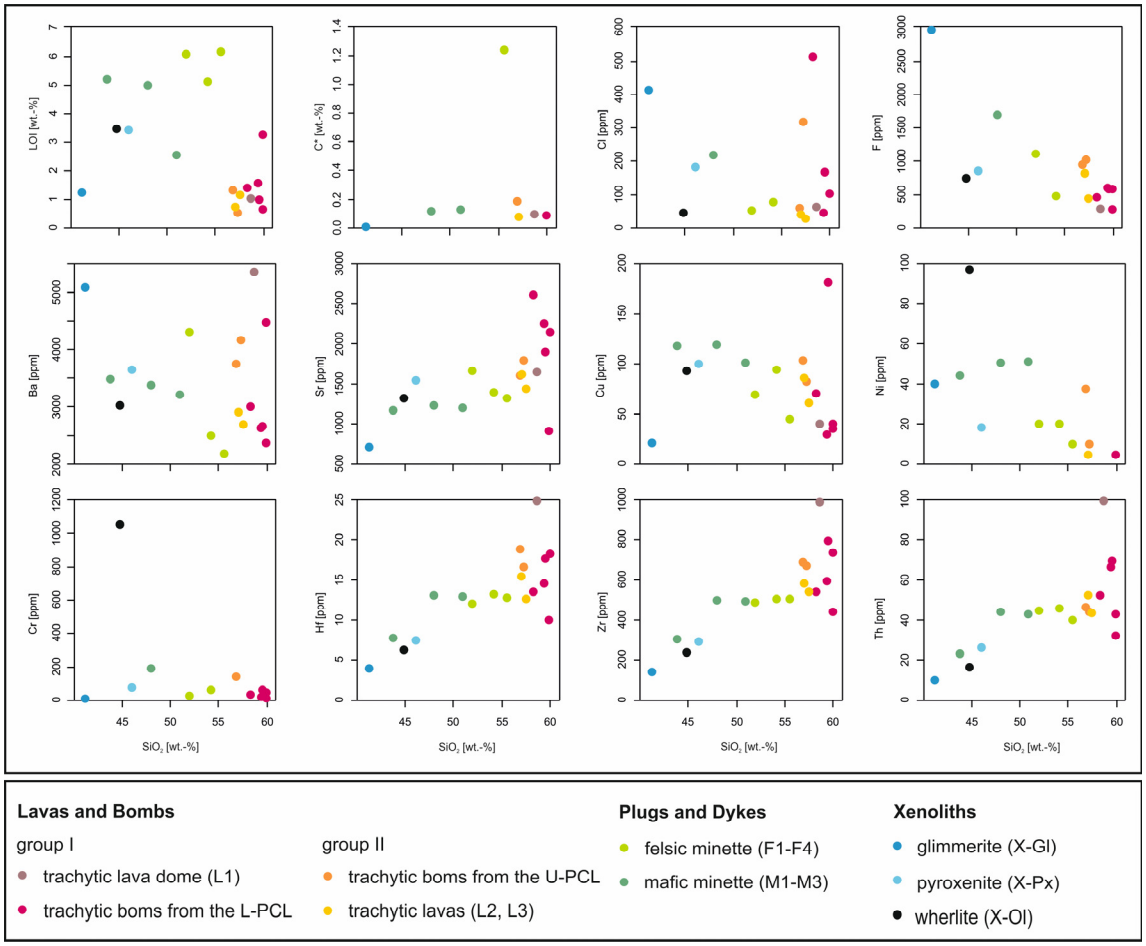

Figure 30: Whole-rock composition of the trachytic lavas and bombs, mafic and felsic minette and glimmerite-, pyroxenite- and wherlite-xenoliths plotted in Harker diagrams of the major and minor elements vs. SiO_2; C* = total carbon

3.3.4 MINERAL CHEMISTRY

After thorough polarized light microscopy and scanning electron microscope (SEM) analyses, electron microprobe analyses (EMPA) were performed for the minerals of 14 carefully selected samples. It included back scattered electron (BSE) images, element distribution maps, transsects and point analyses. Representative analyses can be found in Table A6-A19 in appendix A-2a. Following, the microchemical variation of the main mineral phases are presented:

3.3.4.1 SANIDINE

Sanidine phenocrysts occur only in the trachytic eruption products (lavas and bombs). Sanidine is also major phase in the holocrystalline to hypidiocrystalline (partly glassy) groundmass of the trachytes. In felsic minette, sanidine is restricted to the groundmass, where it is the main phase, with exception of one sample (F2) with individual sanidine xenocrysts. As the composition of the groundmass crystals in felsic minette is similar to those in trachyte, we will focus here on the features of sanidine in trachyte.

In trachyte, EMPA analyses were performed on 49 sanidine macro- and megacrysts including 32 detailed transects in selected crystals. Sanidine reflects a large compositional variation ($Or_{49-76}An_{0-4}Ab_{17-47}Cn_{0-12}$). As shown in Figure 31, K-feldspar (Or) component varies between 49 and 76 mol% and albite component (Ab) between 17 and 47 mol%. The low Ca-content is reflected in a low anorthite (An) component (< 4 mol%). Sanidine is characterized by high Ba concentrations up to 6.6 wt% BaO, which translates into 12 mol% celsian component (Cn). Furthermore, concentrations up to 1.0 wt% Fe_2O_3 and 1.1 wt% SrO were measured. Figure 31b shows the positive correlation between BaO and Fe_2O_3 of some sanidine crystals in trachyte. In one wherlite-xenolith (X-Ol), one feldspar (hyalophane) with extremely high concentrations of approximately 30 wt% BaO was observed.

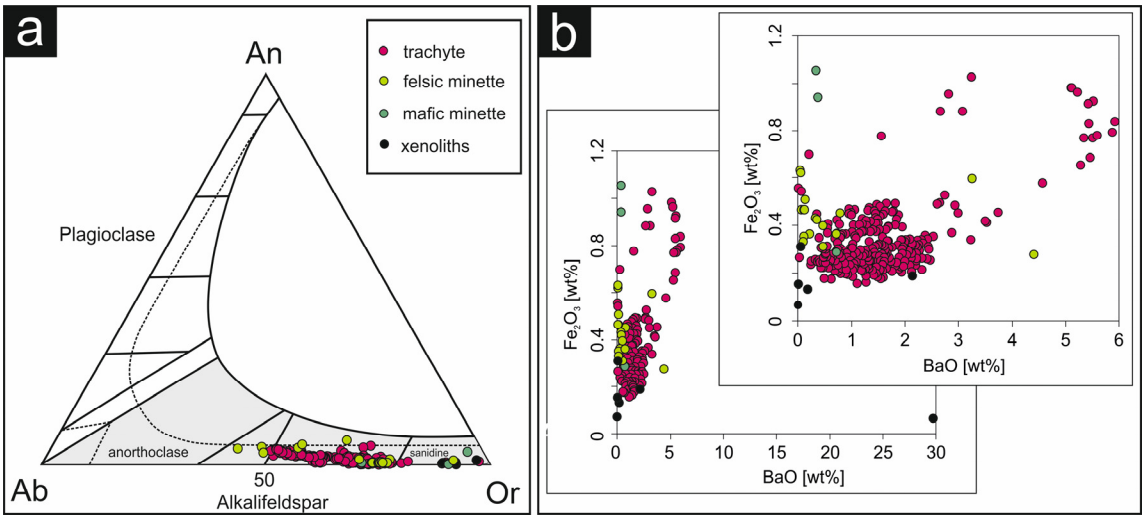

Figure 31: a) Ternary plot showing the chemical variation of feldspar in trachyte, minette and wherlite-xenolith, b) variation diagram showing the concentrations of BaO and Fe_2O_3 in sanidine

All sanidine megacrysts exhibit a systematic zoning pattern. In general, Na concentrations decrease from core to rim. The substitution of Na by K occurs regardless of the Ba-zoning. The characteristic zoning pattern, visible in BSE image, reflects predominantly the variations in Ba. The comparison of all sanidine macro- and megacrysts and groundmass crystals from the different eruption products of Saray Volcano revealed a systematic in the changes in Ba: a chemical stratigraphy with four clearly distinguishable crystallization zones. Figure 32 presents this stratigraphy schematically.

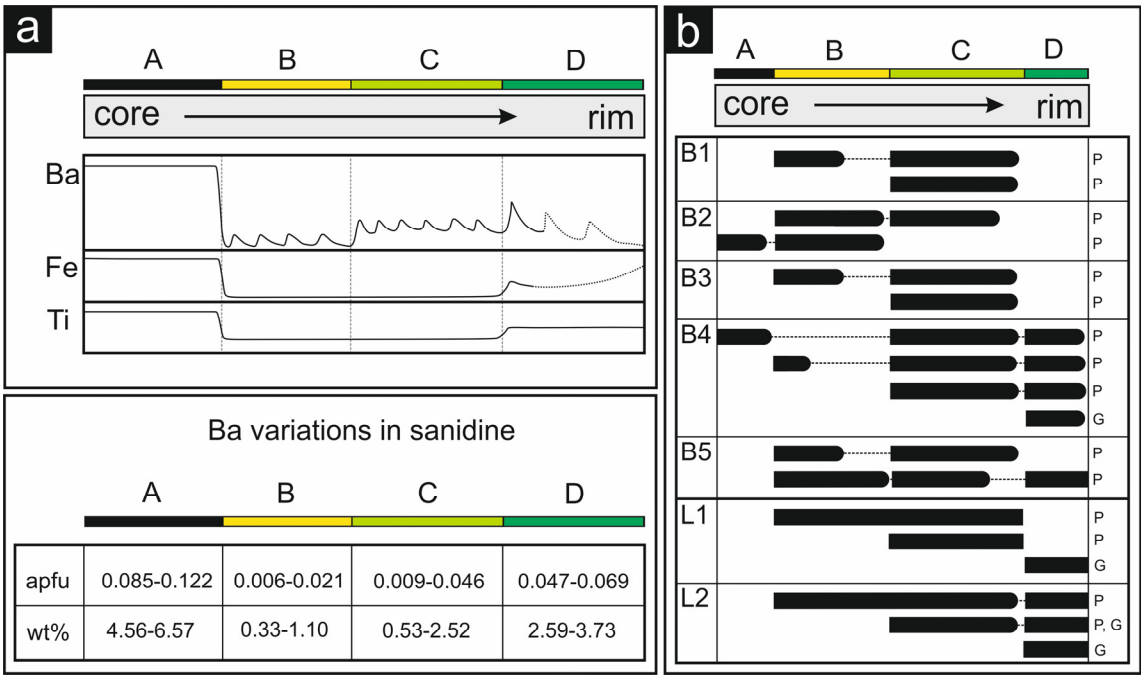

Figure 32: Schematic sketches showing a) the characteristic variations of Ba, Fe and Ti in the sanidine megacrysts of the trachytic eruption products and a table showing the variability of Ba [wt%] and calculated per formula unit [apfu] for each crystallization zone A-D, b) overview of the crystallization stages observed in sanidine crystals of the different trachytic eruption products

Each of the four identified zones is characterized by a typical range of Ba concentration and superimposed specific features, such as oscillatory zoning. Figure 32a shows an overview of Ba, Fe and Ti along transects and the characteristic zoning and compositional trends within each zone.

Zone A sanidine (**SAN-A**) domains with the highest Ba concentrations were only found in the bomb samples B2, B3 and B4, which represent the oldest magmatic event in the investigated eruption products. These crystals are characterized by normal zoning, with Ba-rich plateaus (up to 6.6 wt% BaO) in the cores and decreasing Ba contents towards the rims (down to < 4.6 wt%). Two larger sanidine crystals (> 1 cm) in sample B4 exhibit additional oscillatory zoning in the outermost part of zone A. High concentrations of Fe^{3+}, up to 1.0 wt% Fe_2O_3 (0.036 apfu), and Sr, up to 1.1 wt% SrO (0.03 apfu) is typical for SAN-A. SAN-A cores may also exist in sanidine crystals of other samples but are not visible due to cutting effects. “High-grade resorption” surfaces, indicated by deep dissolution embayments, mark the transition from zone A to zone B. It is accompanied by a sudden drop in Ba concentration from > 5 wt% in zone A to < 1 wt% in zone B (see Figures 33a and 34a).

Zone B (Figures 10, 33 and 34) occurs in sanidine crystals of all investigated samples. Nonetheless, it is not displayed in every crystal most likely due to intense resorption or cutting-effects. It is characterized by the lowest measured Ba concentrations, ranging from 0.3-1.1 wt% BaO (0.01-0.02 apfu). Oscillatory zoning is prevalent in SAN-B. The distance of the oscillation peaks is between 50 µm and 200 µm with an amplitude in concentration of 0.8 wt% within each sequence. A characteristic feature is the "high grade resorption" of the pattern at the transition to zone C observed in all investigated bomb samples (e.g. Figure 10c).

Zone C can be distinguished from zone B by higher Ba concentrations up to 2.5 wt% BaO (0.046 apfu; e.g., Figures 33 and 34) and shows a saw-tooth oscillatory zoning with up to 40 cycles per crystals. Each of the cycles consists of an abrupt increase in Ba concentration, which then decreases continuously resulting in a characteristic saw-tooth pattern. The distance between the oscillation peaks varies between 50 µm and 150 µm with BaO concentration oscillating between 0.5 and 2.5 wt%. In addition, SAN-C shows several types of resorption: each oscillation cycle is terminated by a resorption surface (weak resorption, e.g. see Figure 10a). In addition, this oscillatory zoning pattern is often cut by resorption surfaces (strong resorption, see Figure 10b). At the transition to of zone C to zone D, high-grade resorption occurs, typically marked by a jump in Ba concentration (see Figure 10c).

Zone D represents the final growth stage of sanidine. It is characterized by an abrupt increase of Ba up to 3.7 wt% BaO (0.07 apfu), accompanied by an increase of Fe. In addition, SAN-D shows saw-tooth oscillatory zoning with decreasing Ba-maxima in each oscillatory cycle towards the rims (Figures 33 and 34).

In lava L1, the typical features of zone D can only be found in the microcrystals of the groundmass (Figure 33e): most of them exhibit (oscillatory) zoning of Ba with concentrations up to 3.2 wt% BaO (0.06 apfu) and elevated Fe concentrations of approximately 1.0 wt% Fe_2O_3 (0.04 apfu; see Figure 34e). Lava L2 shows smaller sanidine (micro-) phenocrysts without any oscillatory zoning. In this sample, "Ba-rings" produced by an abrupt increase in Ba and Fe represent zone D (Figure 33f). The shape of the inner and outer boundary of these Ba-rings is irregular with occasional dissolution embayments. High-grade resorption not only of the cores of the sanidines, but also of the following Ba-rich zone apparently produced these "Ba-rich rings".

Notable, each zone of the sanidine megacrysts has a specific chemical composition (SAN-A, SAN-B and SAN-C) and terminates with high-grade resorption. Due to the composition of the phenocrysts, it is possible to conclude potential changes in the Ba-, Fe- and Ti- content of the melt during the respective crystallization sequence. Major distinguishing feature of the four crystallization stages in sanidine is the different trace element composition (Figure 35). Most obvious is the characteristic Ba concentration in each zone: It changes from high Ba contents in SAN-A, to the lowest concentrations in SAN-B, then intermediate concentrations in SAN-C. The again high Ba concentrations in SAN-D are remarkable. In addition, SAN-A and SAN-D have the highest Fe and lowest Ca concentrations, whereas SAN-B has the highest Ca and lowest Fe concentrations.

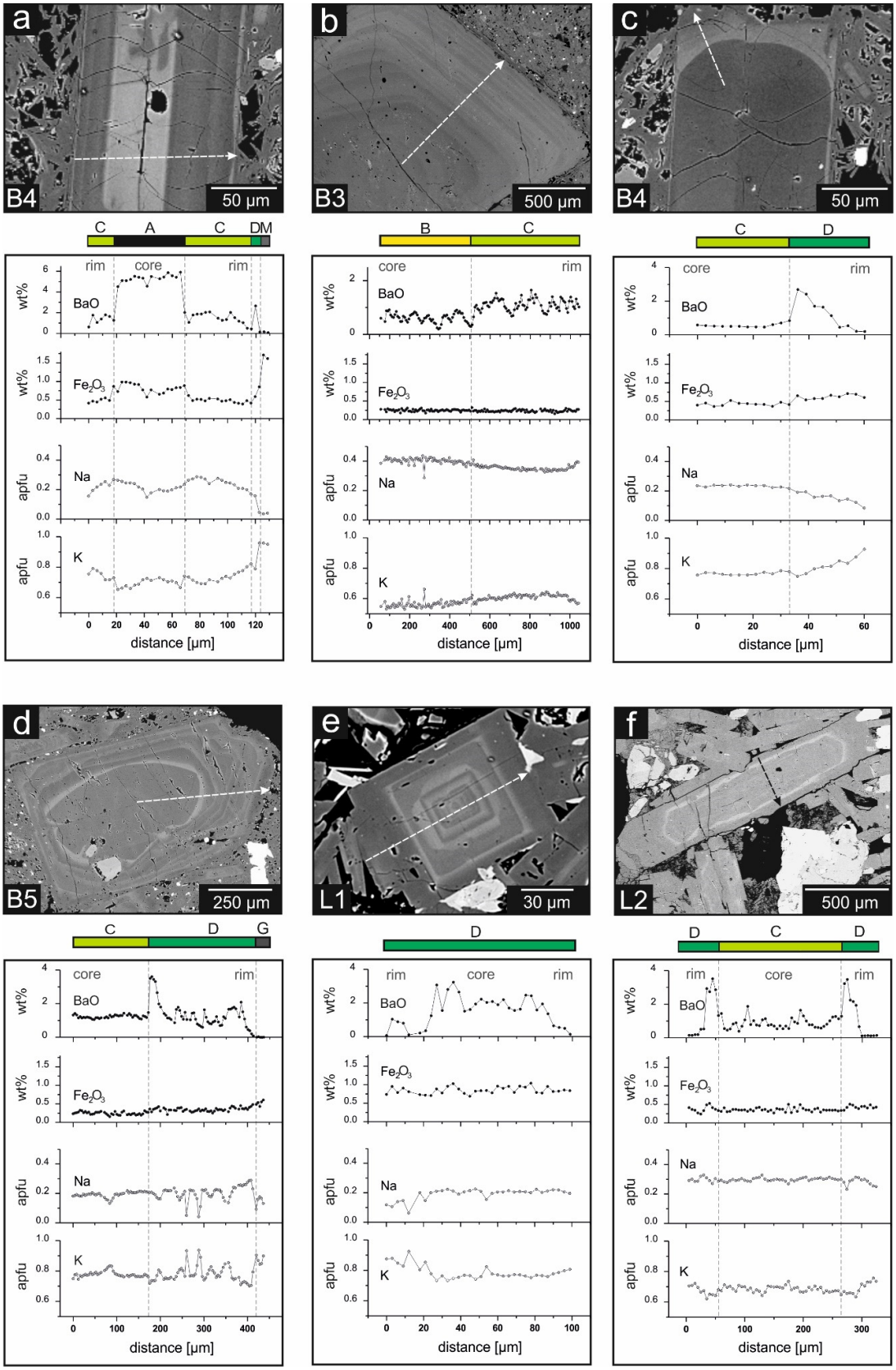

Figure 33: BSE images and selected EMP analyses of sanidine crystals from bombs (B3-B5) and lava samples (L1-L2) showing the variation of the sanidine composition along a profile

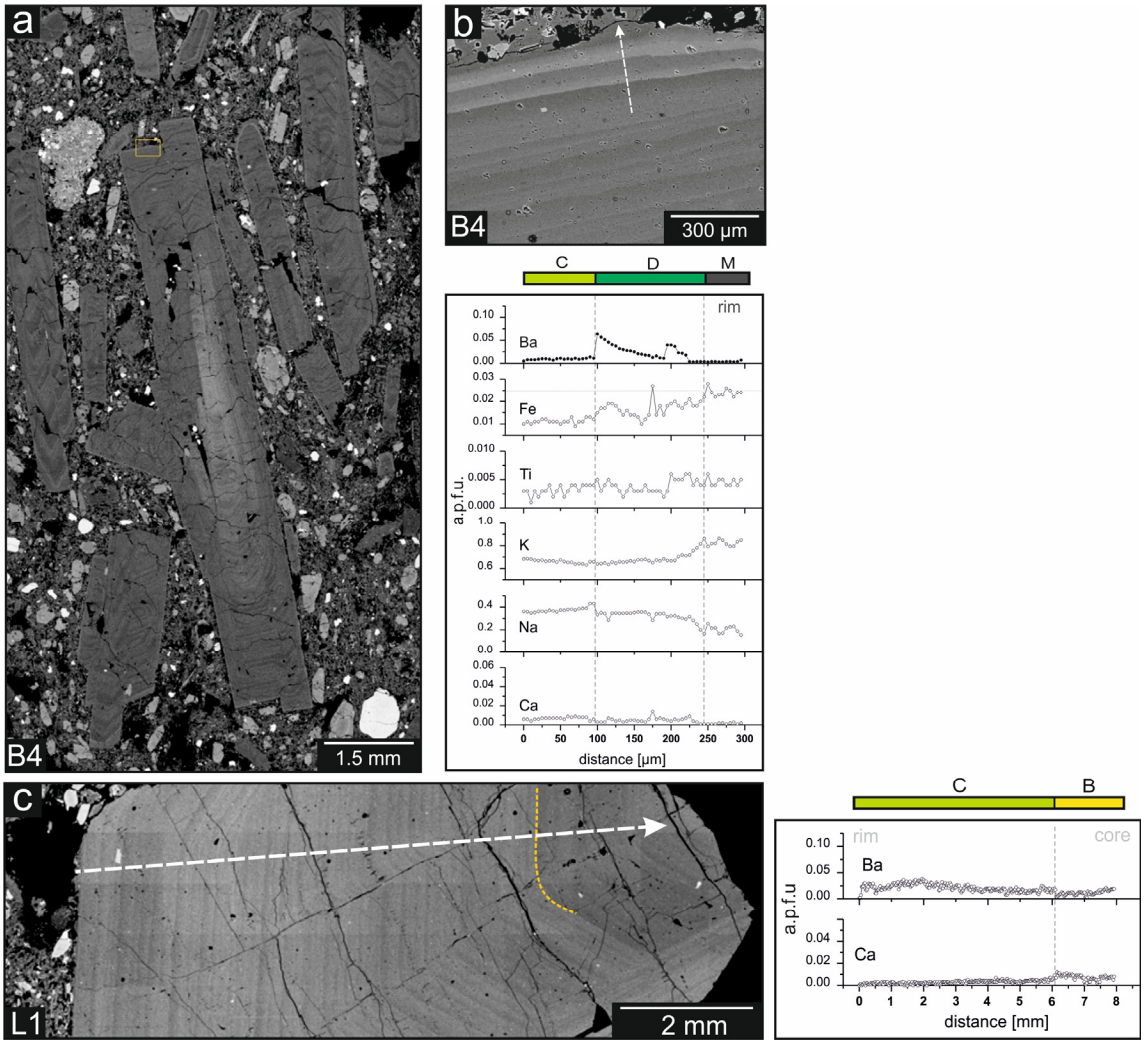

Figure 34: a-c) BSE images and selected EMP analyses of sanidine crystals from bombs (B3-B5) and lava samples (L1-L2) showing the variations of the sanidine composition along a profile

.

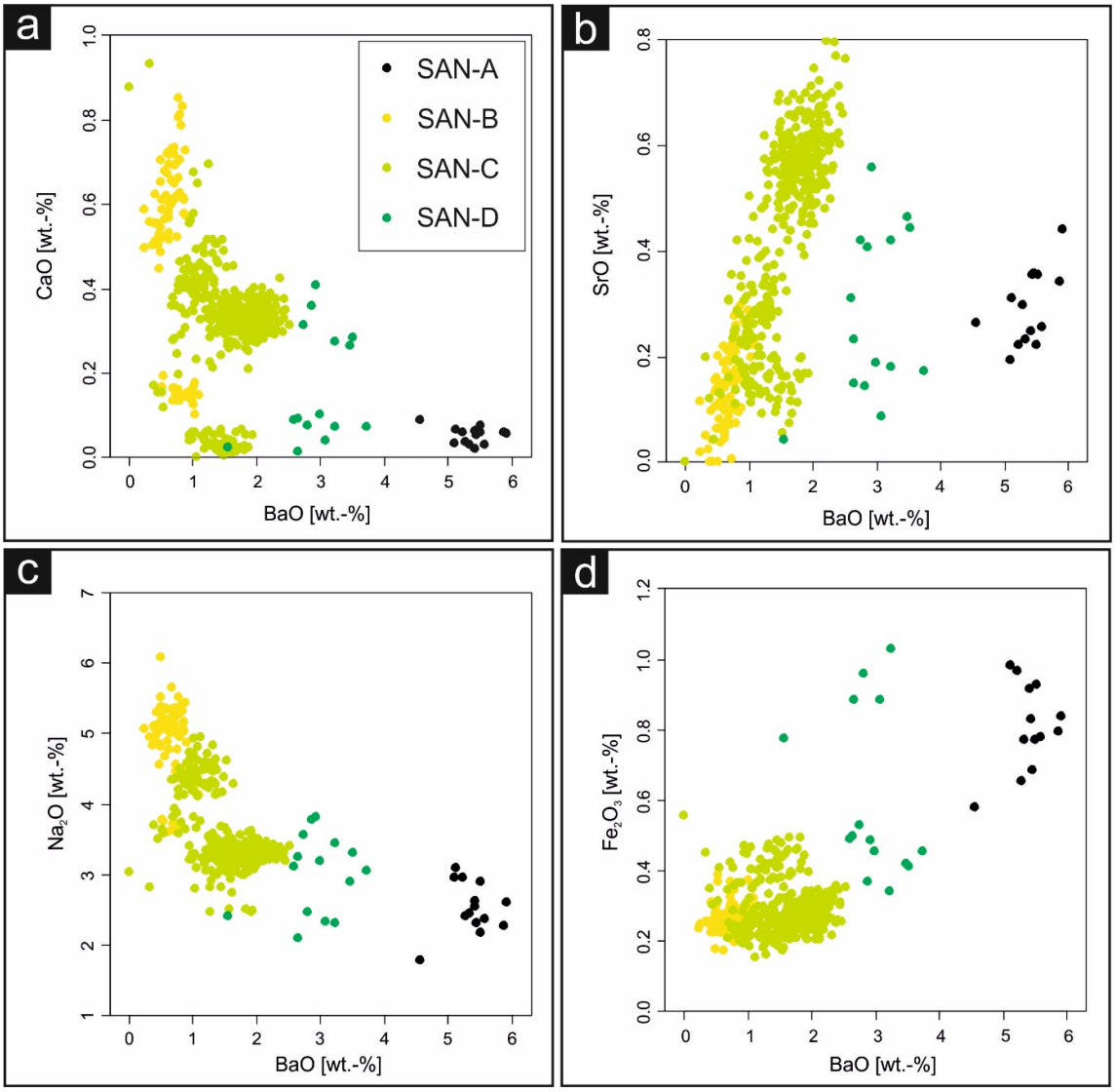

Figure 35: Variation diagrams with EMP analyses of sanidine of all trachyte samples with BaO plotted against a) CaO, b) SrO and c) Na_2O and d) Fe_2O_3. The different diagrams show the chemical characteristic of each crystallization stage A-D in sanidine

3.3.4.2 CLINOPYROXENE

All clinopyroxene phenocrysts show zoning, which is often already visible in the polarizing microscope with crossed polarizers. In trachyte, they show multiple zoning patterns which can sometimes turn into oscillatory zoning (Figure 36). In mafic and felsic minette (in case that clinopyroxene is not replaced by carbonates and quartz) zoning is less pronounced. EMP analyses of all samples show that the majority of the clinopyroxene phenocrysts have diopside composition. In trachyte, aegirine-augite occurs only as rims of some diopside crystals, especially in L1 and B5 samples, where it also occurs as single xenomorphic crystals within the groundmass. In sample B5, one pyroxene crystal contains also a core with aegirine-augite composition (Figure 36b).

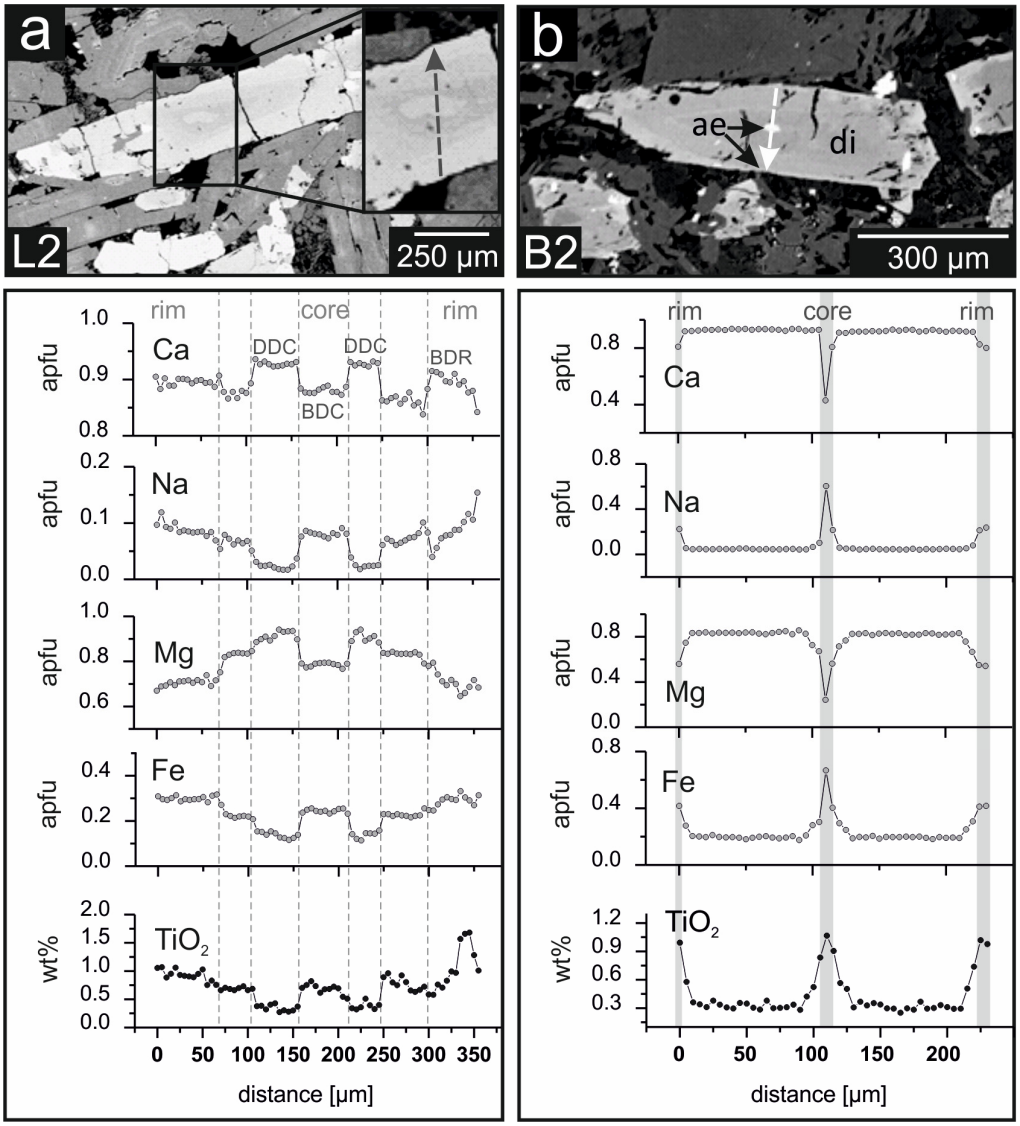

Figure 36: BSE images and EMP analyses show the chemical variations along the profile of selected clinopyroxene crystals with a) multiple zoning pattern and b) diopside with aegirine-augite in the core and as overgrowth

Zoning of the clinopyroxene in the trachyte has been studied in detail and will be presented in the following section. Figure 37a shows a Mg- and Ca-rich core of clinopyroxene appearing dark in BSE-image, and hence called **d**ark **d**iopsidic **c**ore [DDC], surrounded by a Fe- (and Na-, Ti-) rich rim, appearing bright in BSE, and hence called **B**right **d**iopsidic **r**im [BDR]. High concentrations in Fe, Na and Ti in cores can also cause a **b**right **d**iopsidic **c**ore [BDC], as shown in Figure 36a. The strongly resorbed boundaries between these zones results in a crystallization sequence of first BDC, then DDC, and finally BDR (Figure 37d). The microchemical variations are presented in Figures 36 and 37d. Diopside crystals in samples B2 and L1 have rims with aegirine-augite composition (**a**egirine-augite **r**im [AR] in Figures 36b and 37b). Single, xenomorphic aegirine-augite crystals occur also as individual crystals within the groundmass of L1.

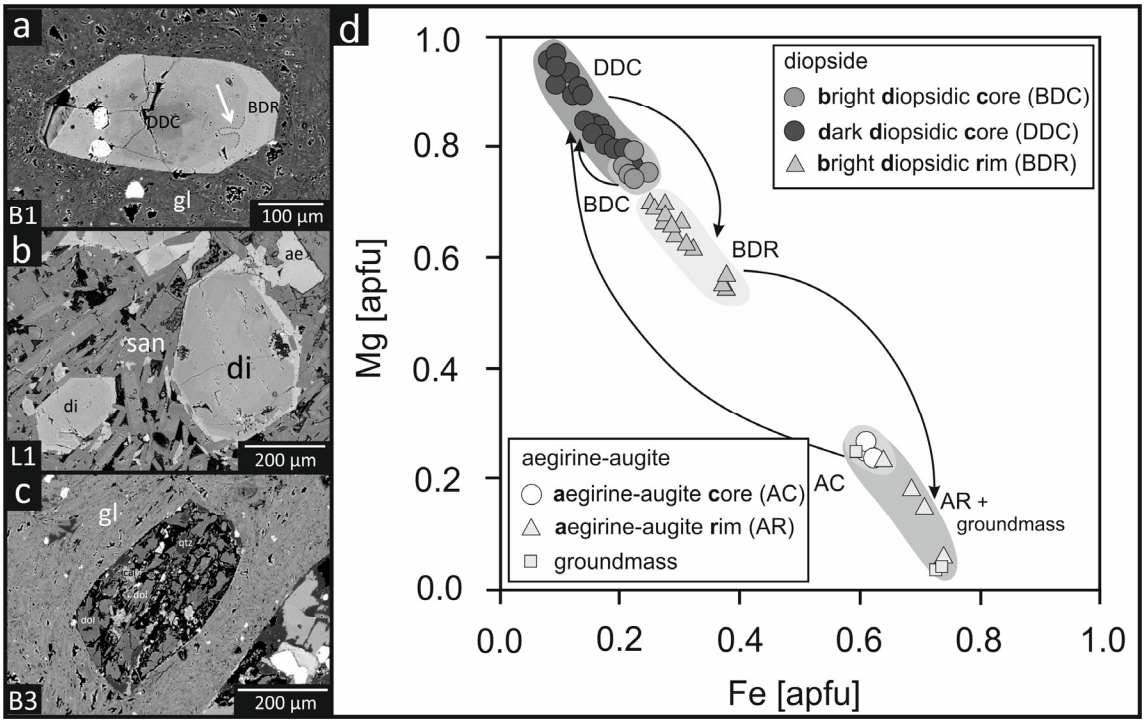

Figure 37: a-c) BSE images of a) zoned diopside with dissolution embayments, b) diopside with aegirine-augite rim from lava L1 and c) pseudomorph of carbonates + quartz after diopside. d) EMP analyses showing the chemical variation of Fe and Mg of clinopyroxene in trachyte

3.3.4.3 PHLOGOPITE

Mica occurs in trachyte as well as in lamprophyre. In both rock types, mica can be classified as phlogopite or Mg-rich biotite. Microchemical investigations show that two different populations, phl-I and phl-II, can be distinguished, with phl-II having a higher Mg number.

PHLOGOPITE TYPE I (PHL-I)

Phl-I in trachyte (red in Figure 38) is characterized by high MgO (> 24 wt%, Mg > 6 apfu), low TiO_2 (1.1-1.5 wt%) and low BaO (< 0.3 wt%) concentrations (Figure 38). Cr_2O_3 concentrations vary between 1.1 wt% in their cores and below detection towards the outermost rims (Figure 38a). In trachyte, the concentrations of FeO and TiO_2 (~ 1.4 wt%) increase slightly from the core (~ 4 wt% FeOt, ~ 1 wt% TiO_2) to the rim (~ 10 wt% FeOt, ~ 2.5 wt% TiO_2) substituting Mg (see Figures 38a, b, and 39a). In addition, phl-I in trachyte shows clear increase in F up to 5.7 wt% in their rims (Figures 38c and 39a).

Raman spectroscopy of phl-I revealed that Mg-rich cores contain OH^- as the main anion and no F. Towards the outermost rim, the content of F increases significantly up to 5.7 wt%, while no OH could be detected (see Figure 39). The transition of the Mg- and OH-rich core to the Fe- and F-rich rim is also marked by hematite exsolution lamellae (see Figures 39a and b).

Phl-I in minette (green in Figure 38) are also characterized by high Mg concentrations up to 21-24 wt% (5-6 apfu). Towards the rims, the chemical variation changes compared to trachyte (Figure 38): here the concentrations in Ti, Ba and Fe increases while F increases only slightly.

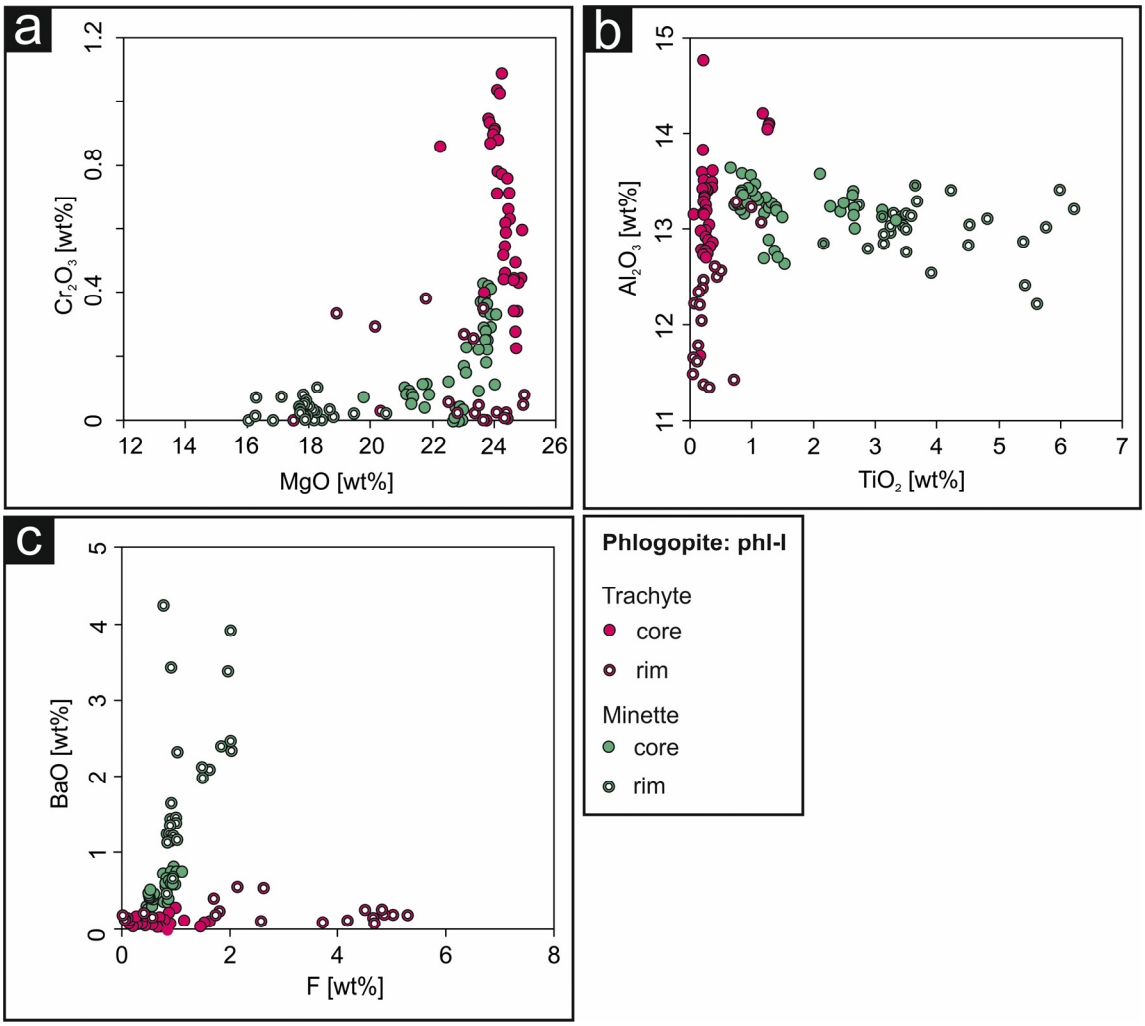

Figure 38: Binary diagrams showing the chemical variation of phlogopite phl-I crystals in trachyte (red) and minette (green)

In minette, phl-I has usually has no inclusions and shows often signs of mechanical stress. It is noteworthy that in both, trachyte and lamprophyre, the phl-I cores have the same composition, but show different trends towards the rims: In contrast to phl-I in trachyte, phl-I cores in the lamprophyres are strongly resorbed and replaced by a newly grown rim which has phl-II composition (lower Mg, higher Ba, Fe, Ti).

PHLOGOPITE TYPE II (PHL-II)

Phl-II is an F-rich phlogopite with concentrations ranging from 1.0 to 4.5 wt% F. Raman spectra show that most phl-II are free of OH (Figures 39c and d). Most of the phl-II crystals show no distinct zoning, whereas others have patchy areas with varying compositions. As shown in Table A16 in the appendix, phl-II shows a compositional spread with a lower Mg concentration (~ 1.8 apfu) compensated by higher concentrations of Fe (0.5-1.2 apfu),

Ti (4.4-5.2 wt%, 0.2-0.3 apfu) and Ba (up to 1.8 wt%). In felsic minette and in the glimmerite, some larger phl-II crystals show Mg- and Cr-rich cores (up to 2.0 wt% Cr_2O_3). In contrast, Phl-II phenocrysts and groundmass crystals in mafic minette have the highest concentrations in Ba (up to 6.0 wt%) and Ti (up to 8.0 wt%).

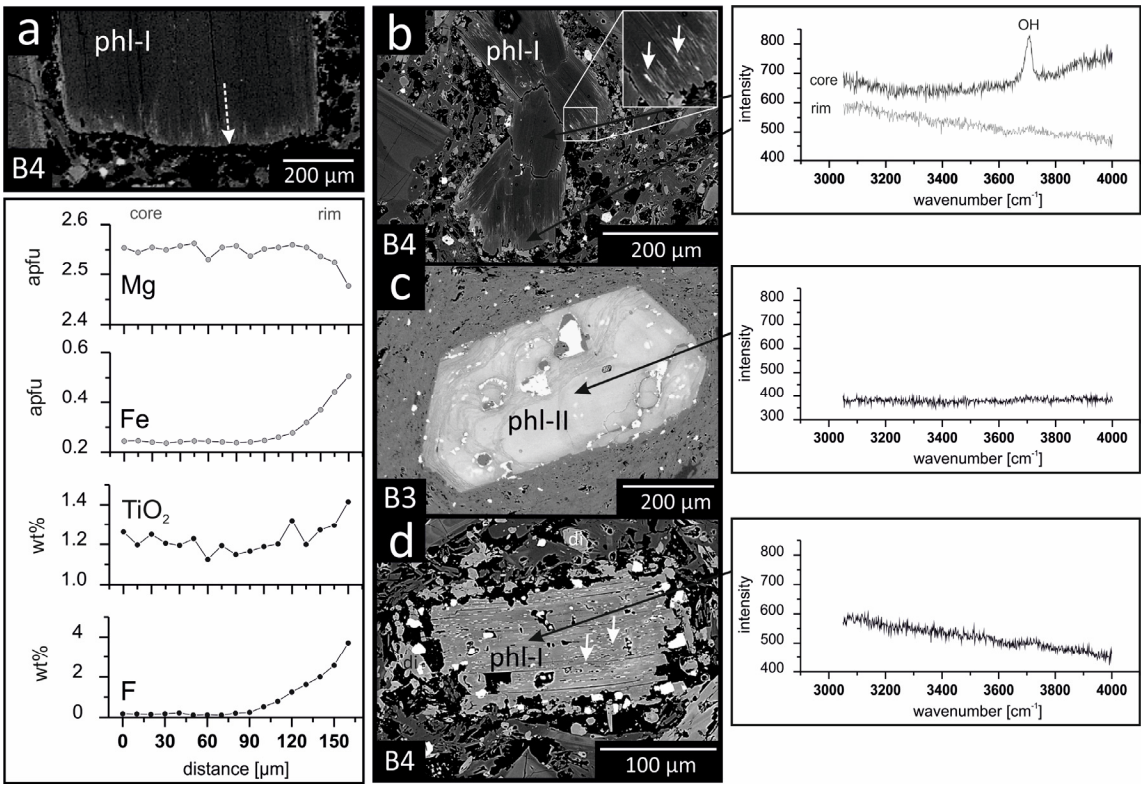

Figure 39: a) Transsect showing the chemical change in phl-I crystal in trachyte. Raman spectra of b) core and rim of phl-I, c) of phl-II of earlier erupted bomb from the L-PCL and d) of phl-II of later erupted bomb from the U-PCL

3.3.4.4 CARBONATES

Carbonate occurs in form of a "melt cloud", in-between the sanidine crystals or as melt inclusions in phl-II. It has mostly dolomitic composition (Magnesio-carbonatite, Figure 40) with relatively high Fe-concentrations up to 14.36 wt% FeO. With up to 1.19 wt% MnO they are also enriched in MnO. Locally, exsolution of calcite (Calcio-carbonatite, Figure 40), with higher concentrations in Fe (up to 5.51 wt% FeO) and Mn (up to 1.71 wt% MnO) occurs. Generally, in all carbonates the concentrations of Na and Ba are low (< 0.14 wt% Na_2O, 0.1 wt% BaO). SrO content is always below the detection limit.

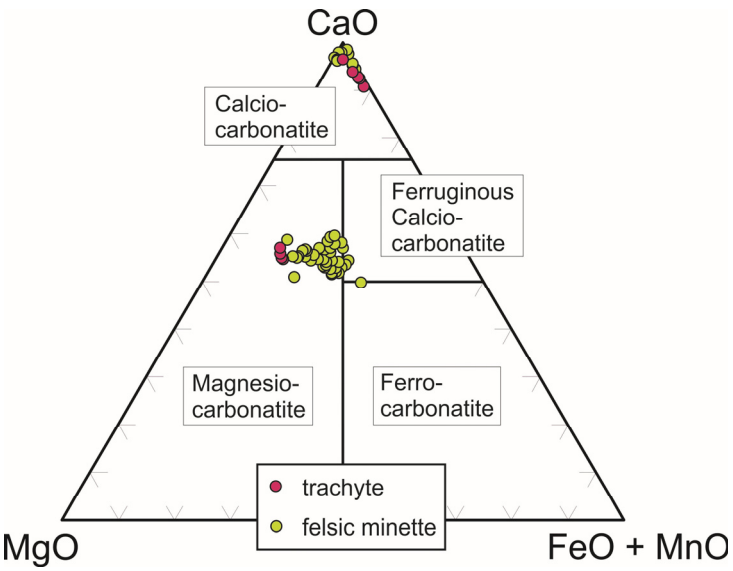

Figure 40: Triangle plot showing the chemical variation of carbonatite in trachyte and minette; two groups are present: calciocarbonatite and magnesiocarbonatite

3.3.4.5 GLASS

Silicate melt/glass is only present in some trachytic bombs and in the groundmass of mafic minette. In both rock types, silicate melt has approximately trachytic composition (see Table A 19 in appendix A-2a). Glass in mafic minette has higher Na concentrations in comparison to the more K-rich glasses in trachyte.

3.3.5 CRYSTALLIZATION SEQUENCE IN TRACHYTE

Based on repeated events of high-grade resorption in sanidine phenocrysts, four chemically distinct crystallization stages (A-D) were distinguished. In combination with the respective mineral inclusions, it was possible to deduce the following crystallization sequences, with the older minerals being always overgrown by the next step: [SAN-A + aegirine-augite] → [SAN-B + diopside] → [SAN-C + diopside + phl-I] → [SAN-D + diopside + phl-I + apatite + Fe-oxide + aegirine-augite]. SAN-A, SAN-B and SAN-C were observed in all trachytic eruption products. SAN-D however, was only observed in bombs from the U-PCL and the lavas L2 and L3. This, combined with field observations, yielded two major groups.

- **Early erupted group I** comprises the bombs from the L-PCL and lava dome L1. They are characterized by a glassy (bombs) to microlitic (bombs and lava) groundmass and the lack of stage D characteristics.
- **Later erupted group II** comprises bombs from the U-PCL and lavas L2 and L3. Group II samples are characterized by glassy to microlitic groundmass (bombs) or millimeter sized groundmass crystals (L2 and L3). In addition, group II samples show stage D characteristic including SAN-D.

3.4 DISCUSSION OF THE RESULTS OF SARAY VOLCANO

3.4.1 CRYSTALLIZATION DEPTH OF TRACHYTE

The petrographic investigations together with field observation showed that the erupted materials can be divided in two groups: early erupted group I trachyte representing the upper part and later erupted group II trachyte most likely the lower part of the magma chamber.

The geological setting of the trachytic magma chamber can be constrained by thermobarometric calculations. However, most thermobarometers cannot be used as the required mineral assemblages are missing in the volcanic rocks of Saray volcano. For olivine-plagioclase-clinopyroxene geothermometer by Yang et al. (1996) or the plagioclase-melt thermobarometer by Putirka (2008) the presence of plagioclase is required. The Ti in zircon and Ti in magnetite geothermometer are not applicable due to the absence of rutile and ilmenite, respectively. The clinopyroxene-melt or pyroxene geothermobarometers of, e.g. Nimis (1999) or Putirka et al. (1996) and Putirka (2008), are also not suitable for the eruption products of Saray volcano because they are not calibrated for alkaline systems. One exception exposes the thermobarometric calculation of diopside in equilibrium with melt after Putirka et al. (2003). It is widely used in recent petrological studies and is confirmed by various other methods (e.g. Longpré et al. 2008; Barker et al. 2012; Dahren et al. 2012; Chadwick et al. 2013).

The calculation of 27 clinopyroxene crystals yielded pressures ranging from approximately 16 kbar to 2 kbar (Figure 41). Standard error of estimate (SEE) of this method is ± 33 °C and ± 1.7 kbar. The microchemical composition of clinopyroxene rims was calculated in equilibrium with their respective whole-rock composition. The result of the calculations and the compositions of the selected crystals are shown in Table A35 in appendix A-3. The calculated pressures translate into a continuous crystallization of diopside beginning in a maximal depth of ~ 45 km (Figure 42). In Northwest of Iran, the Moho is assumed to be in a depth of 46-50 km (Mokhtari et al. 2004). Accordingly, based on the thermobarometry, the location of the trachytic magma chamber was most likely in the lower crust next to the upper mantle.

As shown in Figure 42, only diopside of the early erupted samples (group I) recorded high pressures of approximately 12-16 kbar and temperatures of 980-990 °C (Figure 41). These values indicate that the high-pressure conditions were quenched as further crystallization was suppressed because of rapid ascent. Accordingly, SAN-D rims are absent in the L-PCL bombs of group I and the groundmass is glassy. As shown in Figure 41, the results revealed two different temperature ranges at ~ 12 kbar. For clinopyroxene of the later erupted samples (group II) significantly higher temperatures > 1136 °C were calculated. This means that the lower part of the magma chamber was ~ 100 °C hotter than the upper part.

This trend corresponds to the petrographic observations. In the lava sample L2, the composition of clinopyroxene changes towards the rim and the calculated values correspond to the lower PT-conditions. This has two implications: 1) The crystals in the later erupted U-PCL samples continued to grow during the ascent of the magma and therefore reflect lower pressures and temperatures, 2) the diopside rims and coexisting melt reflect

the adaptation to the new conditions. Correspondingly, the minerals of the later erupted samples (group II) exhibit the stage D characteristics.

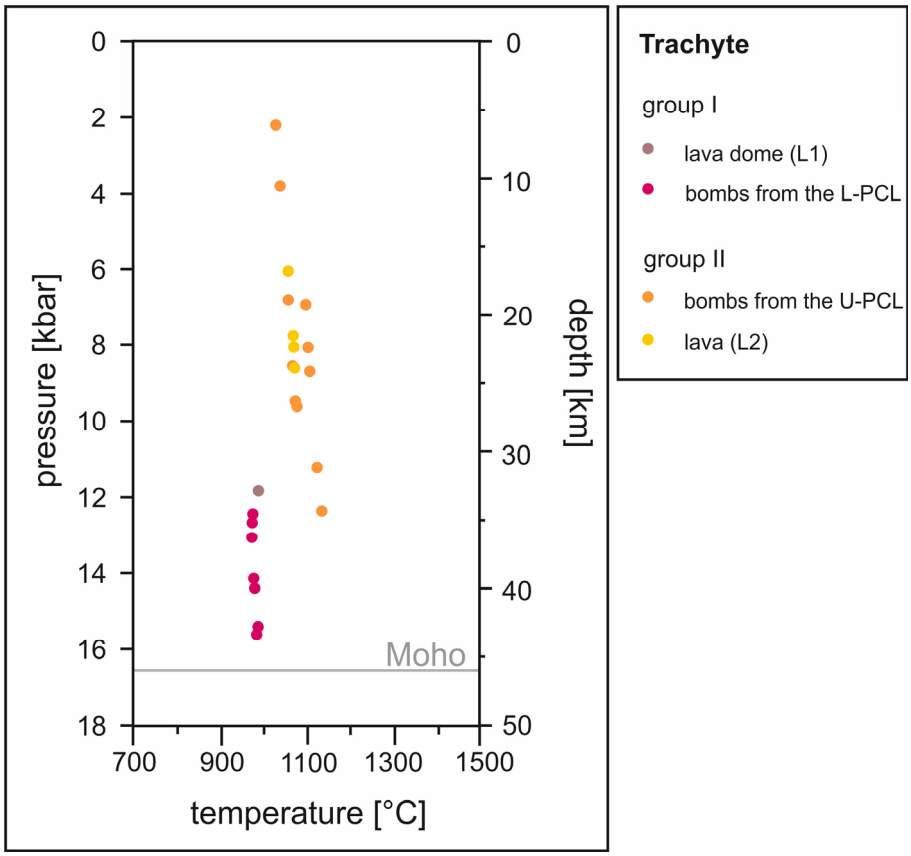

Figure 41: P-T diagram showing the calculated conditions for diopside in trachyte calculated after Putirka et al. (2003) and the corresponding crystallization depths. Moho is in Northwest Iran in 46-50 km depth (Mokhtari et al. 2004)

3.4.2 SOURCE OF LAMPROPHYRE

Lamprophyres are reported in various parts of northwestern Iran including the Arasbaran region and the Mishu ranges, but only minette of Saray volcano can be classified as ultrapotassic (Aghazadeh et al. 2015a). High Mg and Ni values indicate their origin in the subcontinental lithospheric mantle (Moayyed et al. 2008; Pang et al. 2013; Moghadam et al. 2014; Aghazadeh et al. 2015). However, their formation conditions are still under discussion. Figure 42 shows a spider diagram of the minette whole-rock analyses together with additional data determined by (Aghazadeh et al. 2015). It shows negative Nb and Ti, and positive Pb anomalies, which are typical for subduction zone related magmatism, and positive Ba, Th, U and K anomalies, which are typical signs of crustal contamination. The pronounced positive Pb anomaly is indicative of fluid enrichment.

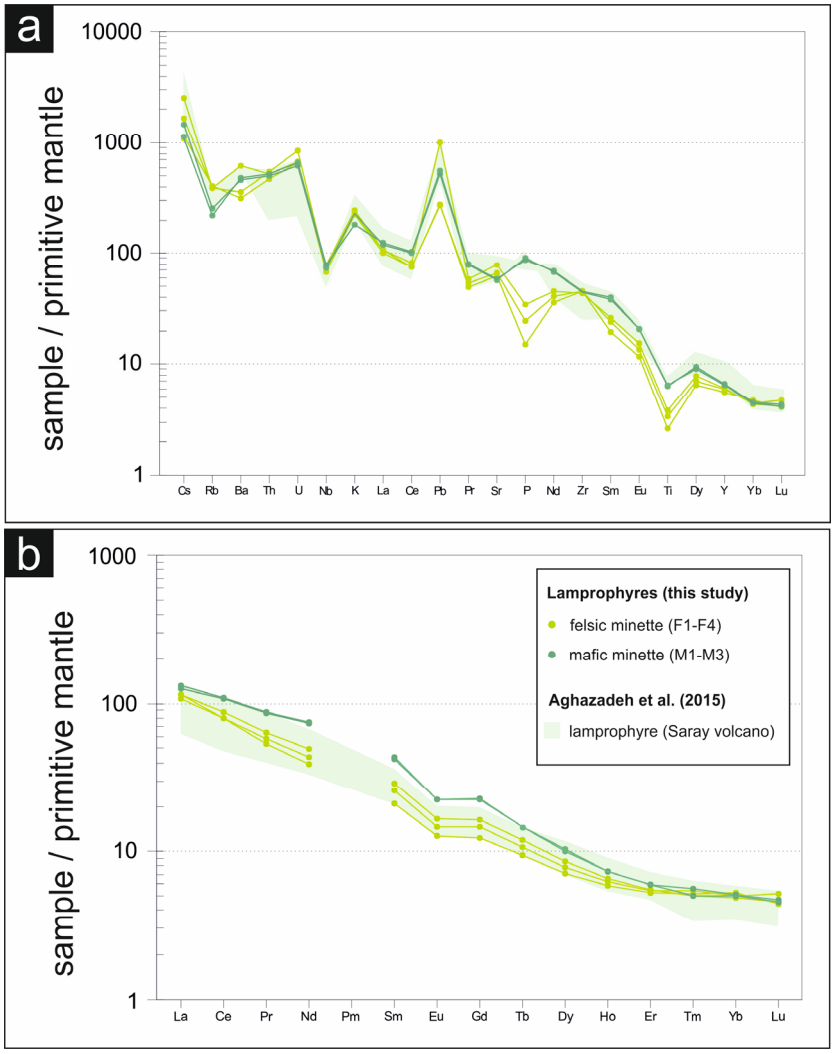

Figure 42: Spider diagram of studied mafic and felsic minette, normalized to primitive mantle a) after Sun and McDonough (1989) and b) after McDonough and Sun (1995). Additional data from Aghazadeh et al. (2015) are included

Minette carried glimmerite, pyroxenite, and peridotite xenolith, which suggests that a phlogopite-rich peridotite in a metasomatic mantle is the source of the lamprophyric melt. These results are consistent with the recent studies from northwestern Iran (Lechmann et al. 2018). The authors concluded that there are local heterogeneities in the lithospheric mantle caused by sublithospheric convection. Mica with similar compositions as phl-II are described from glimmerite veins in peridotites from the Bohemian massif (Becker et al. 1999). These glimmerites are suggested to be generated by the supply of fluids released from the subducted crust and penetrated into the mantle peridotite (Becker et al. 1999), or more generally, to be the result of the interaction of K-rich fluids with peridotite (e.g. Wass 1979; Jones et al. 1982; O'Reilly and Griffin 2000). Various studies indicate that phlogopite-rich vein networks within the mantle wedge can be formed by the metasomatic reaction of peridotite with fluids (e.g. Foley and Peccerillo 1992; Beccaluva et al. 2004). Conticelli and Peccerillo (1989) studied glimmerites from Torre Alfina, Italy, and concluded that the phlogopitic xenolites are remnants of pervasive metasomatic events in the upper mantle.

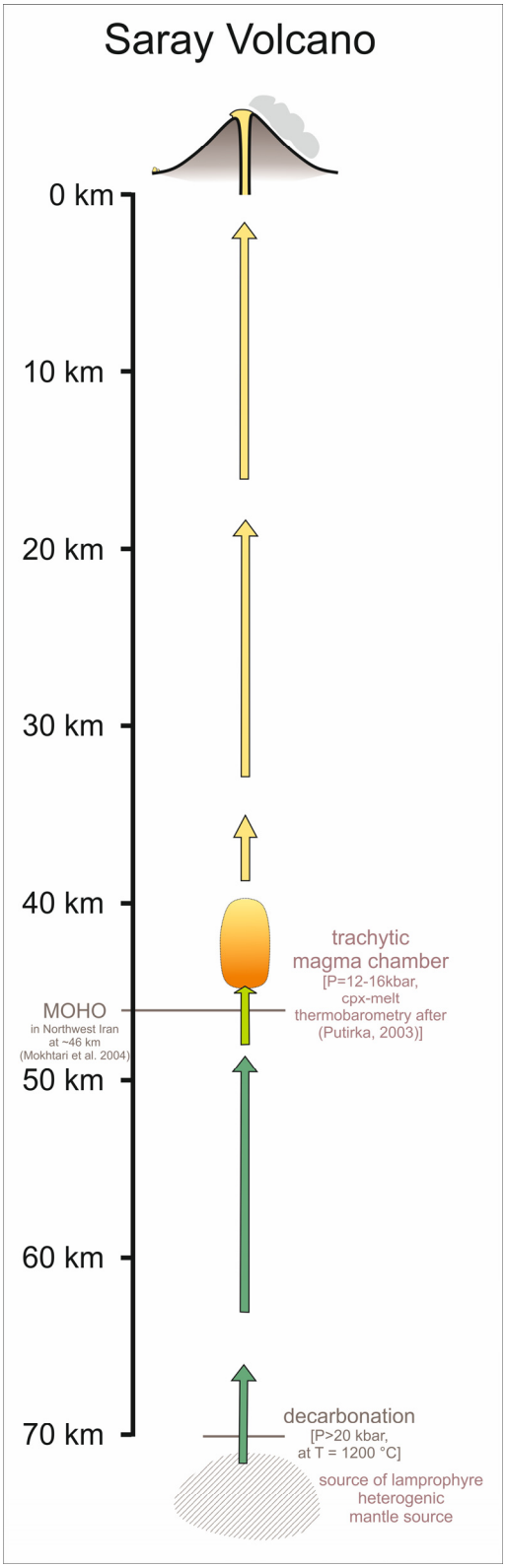

Figure 43: Sketch showing the calculated depth of the Saray magma chamber, the depth of the MOHO in Northwest Iran after Mokhtari et al. (2004) and the estimated minimum source depth of minette from Saray Volcano

Due to the similarity of the isotopic signature of these xenolites and those of the ultrapotassic host rocks, Conticelli and Peccerillo (1989) concluded that the same ultrapotassic magma was the source.

The source region of minette of Saray Volcano cannot be further determined, because no geothermobarometer is suitable for calculating the crystallization depth. The assumption that Moho is 45 km deep in northwestern Iran (Mokhtari et al. 2004) suggests that this value represents the minimum depth for the melt source of minette.

The stability field of carbonatite offers further possibilities to limit the source of the minette. Carbonatite and silicate melt inclusions in phl-II crystals observed in felsic minette demonstrate the growth of phl-II in the presence of both types of melt. Melt experiments with H_2O-saturated felsic minette melts showed the mineral assemblage diopside, titanoferrous phlogopite, and forsterite-rich olivine at 1000-1200 °C and 10 kbar (Esperança and Holloway 1987). Accordingly, the temperature for the comparably water poor, CO_2-rich minette of Saray Volcano must have been even higher than 1000-1200 °C. The presence of carbonatite shifts the possible source region of minette further down to depths > 70 km (20 kbar, Figure 43). Experiments showed that carbonatite and carbonate-rich melts are stable at 1200°C and pressures > 20 kbar (2 GPa) and at lower pressures, they begin to decompose and release CO_2-rich fluid (Canil 1990; Yaxley et al. 1998). According to Esperança and Holloway (1987), minette melts, which originate from the mantle, rise quickly without significant heat loss. Mobilization of the melt can be caused either by raising the temperature of the surrounding rocks or by introducing fluids into the source containing mica and pyroxene.

3.4.3 RELATIONSHIP BETWEEN TRACHYTE AND MAFIC AND FELSIC MINETTE

The similar age of the trachytic eruption products (10.3 ± 0.1 Ma; Moghadam et al. 2014)) and the lamprophyric intrusions (10.35 ± 0.02 Ma; Aghazadeh et al. 2015) along with the field observations that show the intrusion of mafic and felsic minette (lamprophyres) after the eruption of the trachytes, raise the question of whether trachyte and minette interacted. Several studies point to the association of lamprophyres with alkaline magmas, such as trachytes or syenite (Rock 1991; Plá Cid et al. 2006; Yanev et al. 2010; Nardi et al. 2012; Soder et al. 2016), however, the nature of the relationship is still controversial.

3.4.3.1 GEOCHEMICAL APPROACH

Prelevic et al. (2004) investigated lamproites, leuco-minettes and dacites from Veliki Majdan (Serbia) and assumed that leuco-minette was formed by mixing of lamproite melt with felsic dacite melt. The phenocrysts of these rocks are similar to those in minette of Saray Volcano. Mixing of trachyte and minette melts of Saray Volcano could explain the coexistence of these minerals in both rocks and the observed microchemical changes in the rims of the minerals. Generally, such microchemical changes are attributed to the recharge of a chemically different (usually less developed, more mafic) magma. According to their geochemistry, the early-erupted (group I) trachyte and the mafic minette including xenoliths represent the end-members of compositional variability. The approximately linear trend for most elements shown in the Harker diagram (see Figures 29 and 30), suggests hybridization of the two types of melt. Al_2O_3, K_2O and Zr expose a positive correlation with SiO_2, while MgO, CaO, TiO_2, P_2O_5, FeOt and F represent a negative correlation. However, in detail, the values for the latter elements in trachyte and felsic minette group II are almost the same. The small variation between group I and group II trachytes in comparison to the significantly higher chemical variance of mafic and felsic minette indicates that only limited contamination of the trachytic magma with the lamprophyric melt has occurred.

Magma mixing is difficult to detect by microscopic techniques. However, both magmas contain xenocrysts that that after a long time required for complete mixing would have been dissolved. Therefore, magma mixing can be ruled out. Since enclaves or schlieren of mafic or lamprophyric melt were not observed in trachyte, neither in the outcrops nor on a macroscopic or microscopic scale, mingling of the magmas can also be excluded. What other process could explain the shift in the whole-rock composition of trachyte and lamprophyre, and in particular the different composition of mineral rims in the trachyte?

3.4.3.2 PETROLOGICAL APPROACH

Remarkable is that in addition to carbonatite, sanidine, two types of phlogopite and glimmerite occur in both magma types. What kind of interaction occurred between the chemically different melts?

EVIDENCE FOR A STRATIFIED TRACHYTIC AND LAMPROPHYRIC MAGMA CHAMBER

The coexistence of mafic and felsic minette is a special feature of Saray Volcano. Based on the Harker diagram, felsic minette appears to represent hybrid melts contaminated by trachytic melt. The co-occurrence of mafic and felsic minette is reported from Buell Park, Arizona. Roden and Smith (1971) explained the different composition of the mafic and felsic minettes by crystal fractionation or different degrees of partial melting of the same source. According to the experimental investigation of Esperança and Holloway (1987), the crystallization of 20-30 % of a (mafic) minette-like melt is enough to yield a felsic minette. They concluded that the felsic minette represents daughter melts formed from a mafic minette-like parental melt. However, a closer look at the trace elements shows that felsic minette of Saray volcano has much higher concentrations of Na and CO_2, and in general a higher loss on ignition (LOI) than the mafic minette and trachyte. Furthermore, mafic minette contains abundant apatite and clinopyroxene crystals embedded in a groundmass of glass and small flakes of both types of phlogopite (phl-I and phl-II). Accordingly, another mechanism must have contributed to the formation of felsic minette from Saray volcano.

Compared to mafic minette, the whole-rock composition of felsic minette shows higher concentrations in SiO_2 and Al_2O_3 as well as less MgO, CaO, TiO_2, P_2O_5, FeOt and MnO. A higher proportion of clinopyroxene, olivine and magnetite in the mafic minette than in the felsic minette might explain the chemical shift of the lamprophyres to a more mafic composition. In addition, they contain large strongly resorbed Mg-rich phl-I crystals. Furthermore, felsic minette shows the following main differences compared to mafic minette: the presence of carbonates, the abundance of large phl-II crystals with carbonate melt inclusions, and the replacement of clinopyroxene by carbonate and quartz, indicating a high $X(CO_2) > 0.9$. The accumulation of carbonate melt together with the phl-II in the felsic minettes can be the result of their low density. Both, phlogopite (average density of 2.8 g/cm³) and carbonate (2.7-2.8 g/cm³) float up in the lamprophyric melt (2.95 g/cm³). Consequently, they contribute to the different composition of the entire rock. CO_2 resulting from the decomposition of carbonatite in the lamprophyric melt may actively contribute to the formation of felsic minette.

A similar trend is evident in the different erupted trachytes. The chemical change observed between the early-erupted bombs (L-PCL) and lava (L1) and the late erupted bombs (U-PCL) and lavas (L2, L3) – lower SiO_2 and Al_2O_3 and higher MgO, CaO, TiO_2, P_2O_5, FeOt and MnO contents. This points to a stratified magma chamber, with more felsic (group I) trachyte in the upper part and slightly more mafic (group II) trachyte in the lower part of the magma chamber. This phenomenon can also be explained by mechanisms similar to the lamprophyric dykes. Trachyte has an average density of 2.77 g/cm³. Therefore, clinopyroxene (diopside; 3.25-3.55 g/cm³) and phlogopite (2.7-2.9 g/cm³) are suggested to sink to the lower part of the magma chamber whereas sanidine (2.52 g/cm³) is suggested to float up.

EVIDENCE FOR CRYSTAL TRANSFER

Sanidine megacrysts as well as both types of phlogopite, phl-I and phl-II, occur in both, trachyte and minette. Glimmerite and carbonatite are more abundant in the minette, but were also identified in trachyte. The combination of petrological and mineral chemical investigations enabled to determine which of the minerals in the respective melt are phenocrysts or xenocrysts and from which source carbonatite and glimmerite originated.

SANIDINE

The dominance of sanidine megacrysts in trachyte clearly indicates that they are phenocrysts of this magma. Further evidence is the abundance of sanidine as microlites in lava dome L1, in group II bombs as well as larger crystals in group II lavas (L2 and L3). In felsic minette, sanidine is also the main phase of the groundmass. However, the occasional observed megacrysts are always broken and show strong dissolution phenomena, indicating a disequilibrium with the environment. It is therefore clear that these megacrysts originate from the trachyte and were entrained as xenocrysts in the felsic minette. This is consistent with the general statement by (Chapman and Powell 1976) that anorthoclase megacrysts are xenocrysts in alkali lamprophyres, most likely derived from associated syenites or nepheline-syenites (Rock 1991). The dissolution of the sanidine xenocrysts explains the shift of felsic minette to a more felsic composition.

PHLOGOPITE

Lamprophyres contain typically different types of chemically variable phlogopite (Rock 1991). Thus, the observation of two chemically distinct types of phlogopite (phl-I and phl-II) in minette is not surprising. In case of Saray Volcano, however, both types of phlogopite are also found in trachyte.

Inclusions of phl-I in the cores of sanidine megacrysts and clinopyroxene are clear indicators for their co-genetic formation in the trachytic melt. In contrast, phl-I in lamprophyres are often mechanically deformed or broken and their rims are clearly resorbed. In addition, they exhibit newly grown rims with a phl-II composition indicating that the original phl-I composition was not stable in the mafic melt. It is expected that the dissolution of phl-I crystals in minette melt shifts the whole-rock chemistry to a more mafic composition.

Based on the microtexture, phl-II is the stable type in the minette environment (Figure 17). Euhedral to subhedral phl-II crystals were observed in both, mafic and felsic minette. Correspondingly, the composition of the Ti- and Cr-rich phlogopite is typical for minette (Esperança and Holloway 1987; Krüger et al. 2013). Phl-II is main mineral phase in glimmerite and occurs in peridotite (wherlites) xenoliths. Notably, euhedral phl-II phenocrysts preferentially coexist with carbonatite and they often contain carbonate melt inclusions. Additional silicate melt inclusions in phl-II indicate the coexistence of carbonatite and lamprophyric melt during the crystallization of the mica.

The texture of phl-II is strongly dependent of the rock type: they are intact in minette as well as in glimmerite xenoliths found in minette. In trachyte, however, the intense resorption of phl-II single crystals indicates that

these crystals are xenocrysts in this environment. Phl-II of the glimmerite xenoliths in trachyte also shows moderate to strong resorption. In particular, the rims of phl-II in the xenoliths exposed to the trachytic melt exhibit intense resorption and hematite exsolution lamellae.

In sum, the microtexture of the two phlogopites, phl-I and phl-II, points to clearly different sources: phl-I crystallized in trachyte, whereas phl-II was formed in the lamprophyric melt and the mantle derived xenoliths. The complementary trends of phl-I and phl-II show that they were not in equilibrium in the respective melt and accordingly started to dissolve. The subsequent growth of rims with complementary composition demonstrates that they have adapted their chemistry to the respective environment.

GLIMMERITE

Glimmerites are the only xenoliths, which occur in both, minette and trachyte. The textures differ considerably in different environments. In minette, glimmerite xenoliths with up to 30 cm in diameter and single phlogopite crystals up to 1 cm show no signs of alteration (see Figure 25). However, in felsic minette diopside crystals show cracks and are replaced by carbonate and quartz (see Figures 26a and b). In trachyte, glimmerite xenoliths are rare, always < 5 mm in diameter and were only observed in group II trachytes. Signs of dissolution and alteration occur preferentially at the contact to trachytic melt. Corrosion of the mica can be moderate (limited to the rims, see Figures 26c and d) or very strong (in this case only traces of the glimmerites are preserved). As these glimmerites show similar textures and dissolution characteristics as phl-II in the trachyte, it can be concluded that glimmerite xenoliths have also been transferred from minette into trachyte.

Phlogopite in glimmerite has always phl-II composition. It is therefore likely that glimmerite originates from the same source as minette. They always exhibit hematite exsolution lamellae. The decomposition of diopside to carbonate and quartz in glimmerite contained in felsic minette is evidence for an extreme enrichment of CO_2 in this environment. This is consistent with the observation of decomposed diopside phenocryst in felsic minette.

CARBONATITE

This study documents for the first time the occurrence of primary **carbonatite** in minette and trachyte of Saray Volcano. Aghazadeh et al. (2015) already reported the occurrence of carbonates in the minettes of Saray Volcano, but they discussed them as a secondary product. However, the following features support the assumption that the observed carbonatite is a primary phase:

- Occurrence of carbonatite in form of “clouds” or schlieren in both, trachyte and minette.
- Carbonatite inclusions observed in many phl-II crystals
- Coexistence of carbonatite with phl-II xenocrysts in the trachyte

The occurrence of carbonatite or schlieren within a glassy, silicic melt groundmass of sample (B3) and fine-grained groundmass of trachyte sample (L1) is evidence for the coexistence of the two melts (see Figure 15). Felsic minette often contains fine-grained calcite particles distributed throughout the sample, but also as

schlieren-like or “cloud”-like areas between the sanidine groundmass crystals (see Figure 17). Since carbonatite is always present in trachyte together with phl-II xenocrysts, it is obvious that this carbonatite also represents a xenolithic melt transferred from minette into trachyte.

Lamprophyres are often associated with aplite, pegmatite or carbonatite (Ayres and Higgins 1939; Rock 1991). Carbonatite bearing lamprophyres are also reported in southern Tuscany (Italy). Vichi et al. (2005) suggested that they are the result of the immiscibility of carbonate-lamprophyre melts. Based on whole-rock analyses and Sr, Pb and Nd isotope characteristics, they proposed a mantle origin.

3.4.3.3 IMPACT OF THE CRYSTAL TRANSFER ON THE MELT COMPOSITION

The closer view on the mineral assemblages and textures of trachyte and minette indicates crystal transfer between these melts and in consequence an interaction between these xenocrysts with the respective melt, which has an impact on the whole-rock chemistry.

INTERACTION OF PHENORYSTS AND XENOCRYSTS WITH TRACHYTIC AND LAMPROPHYRIC (MINETTE) MELT

The texture of **phl-I** shows clearly that it is the stable phase in the trachytic melt. It exposes special features:

- enrichment of **Fe, Ti and F** in the rims, observed in trachyte and minette (see Figure 38a),
- formation of a relatively thin rim with phl-II composition around phl-I in mafic minette, indicating a short residence time of the mica as xenocryst in the minette,
- substitution of Mg by (Fe + Ti) observed in trachyte, even though the whole-rock compositions of the trachytic samples have relatively low concentrations of Fe, Ti and F.

The complexity of the interaction between phlogopite and melt is most evident in bomb sample B4, since both types of phlogopite, phl-I and phl-II, were observed adjacent to sanidine (see Figure 12).

Phl-II xenocrysts in trachyte show strong signs of corrosion. The dissolution of Ti-phlogopite (phl-II) releases Ba, Ti, Fe and F into the surrounding melt and therefore induces a local shift in the chemistry of the trachytic melt. This can explain the growth of a rim enriched in Fe and Ti around phl-I. The absence of F in the cores of phl-I, and its increase towards the rims (replacing OH) underlines a significant change in the chemical environment. The first crystallization stages of trachyte occurred at F-free conditions. During the last crystallization stage D, the conditions changed to an F-pronounced environment. Crystallization experiments with F-rich melts showed that F preferentially partitions into solids (Schilling et al. 1980; Candela 1986), and that it is highly compatible in phlogopite and apatite (Vukadinovic and Edgar, 1993; Edgar and Pizzolato, 1995; Edgar et al., 1996). Accordingly, a small increase in F in the melt immediately results in the incorporation of F into the crystal structure of these minerals.

The formation of **Ba zoning** in mica and sanidine is also ambiguous. In general, a preferential partitioning of Ba in phlogopite is expected (Zhang et al. 1993). Accordingly, the Ba-rich composition of the mafic minette causes

Ba-rich (phl-II) rims around the strongly resorbed phl-I xenocrysts. In trachyte, however, Ba increased abruptly in sanidine but not in the coexisting phl-I. A complementary phenomenon was also observed in another minette sample with Ba-rich phl-II: In this case, the rims of phl-II are Ba-poor, while the coexisting cores of the sanidine microlites in the groundmass are Ba-rich. These trends show that Ba partitions into phlogopite only when sanidine is absent or its crystallization suppressed. When both, sanidine and phlogopite coexist in the melt, Ba preferentially partitions in sanidine. However, experiments are required to confirm this relationship.

IMPLICATION FOR GEOCHEMICAL RESULTS

The observed material transfer between the two types of magma has consequences for the whole-rock composition of the samples. Great care has been taken in the preparation of the samples for the analysis of whole-rock composition in order to avoid contamination of the materials by xenoliths. However, the study of the microtextures in the different samples revealed that they also contain smaller xenoliths (< 5 mm) in addition to the xenocrysts. In consequence, the composition of all xenolith and xenocryst containing rocks can be shifted to both, more mafic and felsic compositions, respectively. The input of phl-II xenocrysts and glimmerite xenoliths into trachyte causes an increase of Fe, Ti, Ba and F content in the whole-rock composition. At the same time, the contribution of carbonatitic xenoliths increases the amount of Ca and CO_2 in trachyte. In case of felsic minette, the entrainment of sanidine xenocrysts observed in the early erupted samples results in a more felsic composition, whereas the entrainment of phl-I xenocrysts from the bottom of the magma chamber into the mafic minettes let them appear more mafic than they actually are.

In summary, this study shows that two mechanisms were crucial for the geochemical properties, in particular the characteristics of the trace elements, of the investigated rocks: stratification of the trachytic and minette by gravity and crystal transfer from trachyte into minette and vice versa.

3.4.4 INDICATIONS FOR CO_2 IN THE AREA OF SARAY VOLCANO AND ITS BEHAVIOUR IN DEEP SETTINGS

All observations point to low OH activity in the trachytes and lamprophyres of Saray Volcano. Phlogopite (phl-I) is the only OH-bearing phase in trachyte. Remarkable, is also the absence of plagioclase in trachyte and in lamprophyre. In particular the absence of anorthite-rich plagioclase is a critical indicator for low H_2O and high CO_2 conditions (Giuffrida 2017), as high CO_2 activities suppress the formation of plagioclase (Rock 1977). Evidence for a massive shift in the fluid composition of the trachytic magma are phl-I phenocrysts showing a change from OH-cores to F-rims. Rather low OH activity in the minette source are indicated by Raman spectra showing only a few phl-II cores with small OH-bands. The decomposition of diopside and its replacement by carbonate and quartz observed in the trachytic sample (B3) requires, at least locally, an extremely high $X(CO_2) > 0.9$ (Lüttge and Metz, 1993). The decomposition of olivine to carbonate and talc, observed in felsic minette and included peridotite xenoliths, also requires the presence of a CO_2-rich fluid. Further indications for CO_2-rich conditions provide batches of carbonatite observed in trachyte and minette. Centimeter-sized bubbles and channels in the

groundmass of the trachytic lava dome samples (L1) and the felsic minette are evidence for a separated fluid phase.

The combination of the macroscopic and microscopic observations, such as primary gas cavities and channels or CO_2 induced decomposition of diopside, points to a massive percolation or flushing of the trachytic magma chamber by CO_2. Continuous or episodical CO_2 bubbling through the magmatic systems (and the host rock) is a common feature (Blundy et al. 2010; Burton et al. 2013; Edmonds and Wallace 2017). It is known that specific magmas such as kimberlites can transport huge amounts of CO_2 (up to 10-17 wt%) in form of bubbles (Price et al. 2000). CO_2 flushing is also reported from other volcanos, such as Etna (Giuffrida 2017) and Stromboli (Aiuppa et al. 2010; Burton et al. 2013).

Carbonatite observed in trachyte indicates that at least during a short period both phases, carbonate and CO_2 were stable within the trachytic magma. Carbonatite and carbonate-rich melts are stable at pressures > 20 kbar and they start to decompose at lower pressures (Canil 1990; Yaxley et al. 1998). The stability field of dolomite extends towards lower pressures of ~ 15 kbar. The stability field of CO_2 (Dalton and Wood 1993) matches also with the calculated P-T-conditions of 12-16 kbar and 970-1150 °C calculated for trachyte (after the method of Putirka et al. 2003). These findings suggest that at the level (pressure) of the trachytic magma chamber and given temperature, carbonatite breaks down. By passing the carbonate stability field (corresponding to lithospheric depths ≤ 70 km), massive CO_2 fluxes are expected by outgassing of the carbonate melts (Frezzotti et al. 2010; Frezzotti and Touret 2014) and transported with the rising magma. Pressure release due to open cracks leads to decreasing solubility of CO_2 in the silica melt (Ni and Keppler 2013) and in consequence enhances the CO_2 production due to a CO_2 gradient within the melt. Accordingly, the deep degassing of the mantle, the lamprophyric melt and decomposition of carbonatite are most likely the source of CO_2 percolation upwards through the trachytic magma chamber and it can explain the continuous flushing of the magma chamber with CO_2. In case of a higher CO_2 influx into the magma chamber than outflow, an enormous accumulation of CO_2 in the magma chamber roof is most probable, which explains high $X(CO_2) > 0.9$, which is required to decompose diopside in group I trachyte.

In general, the degassing behavior of CO_2 and H_2O is completely different. CO_2 degasses already at a lithospheric depth of ~70 km, whereas H_2O – if present – is still dissolved in the silicate melt (Dixon and Stolper 1995). In calc-alkaline rocks, the solubility of CO_2 is assumed to be very low (~1000 ppm), and with increasing melt alkalinity the solubility of CO_2 increases (Ni and Keppler 2013). Concentrations up to 8 wt% CO_2 were measured at 1500°C and 20 kbar for synthetic Na-rich (SNAC) silica melt (Morizet et al. 2002). Under corresponding conditions, the concentration of dissolved CO_2 in basaltic melt is 80 times lower. Mass balance calculations of Frezzotti and Touret (2014) predicted that potentially ~ 1.35 Mt/km³ of CO_2 is released by outgassing of only 0.1 wt% of carbonatite present in a metasomatized upper mantle. On regional scale, Frezzotti et al. (2010) proposed a CO_2-flux of ~ 70 Mt/a due to outgassing of carbonate-rich melt. Furthermore, they state that in the lithosphere-asthenosphere beneath the western Mediterranean region the CO_2 emissions of the Italian volcanoes per year exceeds largely this value.

Subduction zone settings provide the right conditions for continuous outflow of CO_2, due to carbonate metasomatism of the upper mantle by the retreating slab (Poli and Schmidt 2002). The closer look shows that in Northwest Iran, magmatic CO_2 production is still ongoing. One impressive sign is the formation of travertine deposits exposed all over along the Urumieh-Dokhtar magmatic arc (Iran). One of the largest still active travertine deposits in the world with a height of up to 150 m is located in the direct neighborhood of Saray Volcano, proving a long lasting and extensive history of CO_2 degassing with magmatic source in this region. Zarasvandi et al. (2019) describe several features of thermogene travertine formation such as mound and cascade morphology and positive values of $\delta^{13}C$ (PDB) combined with negative values of $\delta^{18}O$ (PDB) (Chafetz and Lawrence 1994).

3.4.5 ROLE OF CO_2

The results indicate extremely high CO_2 conditions in the top of the trachytic magma chamber as well as in felsic minette. A clear indication for CO_2-rich fluid in early-erupted trachytic bombs and in felsic minettes is the complete replacement of clinopyroxene (diopside) by carbonate and quartz. According to experiments of Lüttge and Metz (1993) an $X(CO_2) > 0.9$ is required to enable this reaction. This raises the question of the impact of CO_2 on the reaction mechanism, and in particular, whether CO_2 flushing enabled or supported the transfer of the crystals from one melt into the other.

3.4.5.1 CRYSTAL TRANSFER VIA CO_2 PERCOLATION

Field observations show that the minette plugs and dykes intruded after the eruption of the trachytes. The crystal transfer from one melt into the other and vice versa indicates at least for a short period a direct contact between trachyte and minette. The missing signs for magma mixing or mingling imply another mechanism for the vertical transfer of carbonate and phl-II from minette into trachyte.

Microtextures provide indications for CO_2 upwards-migration facilitating crystal and material transfer. The elongated or schlieren-like shape of carbonatite in trachyte occurs often in the pressure shadow of the CO_2 gas bubbles and channels. Accordingly, CO_2 percolation in trachytic melt facilitated the migration of carbonatite blubs. Together they enable the transfer of phl-II crystals and of smaller glimmerite xenoliths from minette into trachyte indicated by the occurrence of phl-II close to or within carbonatite. It is reasonable, that a part of the trachytic magma erupted. Remaining phl-I and sanidine phenocrysts from trachyte were then entrained in the intruding minette, where they first started to dissolve before adapting to the new conditions in minette and recrystallize.

3.4.5.2 HEATING OF THE MAGMA CHAMBER

Thermobarometric calculations yielded a temperature difference of approximately 150°C between the group I trachyte (980-990°C) and group II trachyte (1135°C) at pressures of 11-16 kbar (see Figure 41). This corresponds or even exceed the liquidus temperature of sanidine in trachyte (980-1000°C) at comparable pressures (Kunzmann 2010). This fact implies a massive reheating at least of the lower part of the magma chamber. Moreover, it suggests that the lower part of the magma chamber was more affected by the reheating compared to the upper part of the magma chamber (see Figure 44). Resorption of the minerals in trachyte confirm this assumption. As shown in chapter 3.4.3., magma mixing of trachyte with minette can be ruled out as a reason for the reheating of the trachyte magma.

Striking is that only the anhydrous minerals are affected by resorption, whereas the only hydrous mineral phase phlogopite (phl-I) grew continuously. Such phenomenon was also observed by Bachmann and Bergantz (2006) in samples from the Fish Canyon Tuff. They attributed the partial remelting of anhydrous minerals and growth of hydrous minerals to a reheating event. They assumed that heat conduction is most likely too slow to explain the rejuvenation as a heating of a magma chamber by 50.8°C needs a few millions of years. Therefore, they proposed the new concept of "gas sparging": According to their calculations, upward migration of a hot volatile phase heats a magma rapidly by a few tens of degrees. Based on numerical simulations they quantified the thermal effects of a two-phase (H_2O-CO_2) fluid influx into a silicic melt and came up for required minimum gas fluxes > 0.1 m^3/m^2 yr, which is significantly faster than for heat conduction or heat transfer via magma mixing. Considering the spontaneous release of volatiles from the underplating mafic magma, these high fluxes can be promptly reached. Bachmann and Bergantz (2006) estimated that sill-like batches of mushes with volumes similar to the 1995-present eruption of the Soufrière Hills (Montserrat, W.I.) can be reheated by a few tens of degrees and remobilized within days to weeks. Such high fluxes need a considerable volume of volatiles, approximately similar to the volume of mush to be reheated. Therefore, they concluded multi-episodical percolation of a silicic mush by fluids, generated from an underplated mafic melt, could provide enough heat to melt anhydrous mineral phases. Due to the low specific heat capacity and thermal conductivity of CO_2 (cp = 1.40 J/gK for fluid and 1.65-1.90 J/gK for melt) compared to H_2O (cp= 3.88 J/gK), they assumed that the volatile phase consists predominately of H_2O. Applying this concept to Saray Volcano means that CO_2 needs at least twice the volume to compensate for the expected effect of H_2O. An alternative would be a much higher temperature of the CO_2 source.

At Saray Volcano, the carbonate-bearing minette is obviously the main carrier of the CO_2 fluid. Based on the experimental results of Esperança and Holloway (1987), the temperature for the comparably water poor, CO_2-rich minettes of Saray Volcano must have been even higher than 1200°C (at 10 kbar) obtained for H_2O-saturated felsic minette melts. Such a heat source provides enough heat for CO_2 to heat up the trachytic magma. In comparison, Bachmann and Bergantz (2006) assumed an input temperature of ~900-1000°C (from a hydrous basalt) to heat an andesite from ~825 to 855°C within 30 days at shallow crustal levels (5-6 km).

3.4.6 IMPLICATIONS OF CO_2 FOR SANIDINE ZONING, OSCILLATORY ZONING AND MEGACRYST FORMATION

Particularly in volcanic rocks, sanidine megacrysts are unusual. At Saray Volcano, sanidine is extraordinary due to two distinct phenomena: 1) Formation of four clearly distinguishable stages, characterized by a significant change in Ba after high grade-resorption events, 2) partly extremely fine-sized oscillatory cycles (< 1 µm) during the individual stages. In alkali-feldspar, zoning of K and Na is mostly absent due to fast K-Na diffusion (Smith and Brown 1988), whereas in plagioclase, zoning is preserved over a long period due to the slow Al-Si diffusion (Brown and Parsons 1994). Accordingly, trace element zoning caused by substitution of K with divalent elements, such as Ba, Sr and Ca is preserved over a long time.

In general, chemical zoning of major, minor and trace elements are widespread in minerals of magmatic origin. They can be a consequence of changes in the parameters temperature T, pressure P, melt composition X, oxygen fugacity $f_{(O2)}$ and water fugacity $f_{(H2O)}$.

3.4.6.1 OSCILLATORY ZONING AND FORMATION OF MEGACRYSTS

Oscillatory zoning is present in each stage of sanidine crystallization. In particular, SAN-B and SAN-C show uniform and monotonous oscillations, with Ba fluctuating around an almost constant level.

Many factors have been proposed to cause the oscillatory zoning in phenocrysts: Shore and Fowler (1996) proposed that it is related to rapid growth of the crystals. In case of plagioclase, it is assumed to be effected by changes in external reaction conditions, e.g. pressure and temperature (Brown and Parsons 1994) or the combination of surface reaction kinetics and melt diffusion (Ghiorso 1987). Another attempt to explain this phenomenon are growth mechanisms at disequilibrium conditions (Smith and Brown 1988) or multiple magma recharge (Perugini et al. 2005; Słaby et al. 2011).

In detail, the oscillatory zoning of Ba resembles not a sine curve and hence, it is not an oscillatory zoning sensu stricto. The cycles typically show a saw tooth pattern: each cycle starts with resorption of the sanidine crystal followed by an abrupt increase in Ba concentration and smoothly decreasing Ba concentrations towards the rims (see Figure 32). L'heureux and Fowler (1994) simulated the formation of oscillatory Ca-zoning in plagioclase by undercooling the melt and observed that the grade of undercooling influenced the degree of asymmetry of peaks and thus the saw-tooth shape. The authors considered both, diffusion and growth kinetics of the minerals in the melt and explained the smooth rise in Ca content followed by a rather sharp drop by fast growth of plagioclase and sluggish diffusion of Ca. The complementary asymmetric shape of sanidine in this study suggests that heating of the melt controls the process. The element variations of the oscillations, however, are restricted to Ba and subordinate Sr. Changes in other elements, such as Fe, which is indicative for changes in magma composition by e.g. mafic recharge, are not evident. Therefore, another mechanism than recharge has to be taken into account to explain the required fluctuations in temperature without changes in melt composition. Similar pseudo-oscillatory zoning patterns of repeated resorption and crystallization were observed in plagioclase from

Parinacota volcano (north Chile, Ginibre et al. 2002) and in sanidine from Laacher See Volcano (Ginibre et al. 2004). The required temperature variations were explained by convection of the crystals through the magma chamber.

Thermobarometric calculations (see Chapter 3.4.1) yielded temperatures of 980-990 °C in early erupted samples, corresponding to the liquidus temperature of sanidine in trachyte of 980-1000°C (Kunzmann 2010) at corresponding pressures. Cooling below liquidus is the normal behavior of a magma with time. The sanidine megacrysts, however, recorded manifold (> 40 oscillatory cycles) of slight reheating, resulting in temperatures fluctuating around the liquidus. It seems not very likely, that magma recharges heated the magma chamber repeatedly without modifying the composition of the magma. Reheating of the trachytic magma by long-lasting, episodical CO_2-flushing provides an alternative concept to explain the pseudo-oscillatory zoning. This way, the trachytic magma system can be hold within a small temperature interval around the liquidus temperature. Each pulse of CO_2 providing heat supply above the liquidus temperature leads to the resorption of the sanidine phenocrysts and groundmass crystals. During subsequent cooling, sanidine starts again to grow. As a result, series of fine monotonic low-amplitude Ba layers form.

This concept provides perfect conditions for the formation of crystals > 1 cm, like sanidine and phl-I, which are characteristic for the trachyte from Saray Volcano. The occurrence of macro- and megacrysts isolated within the melt or microlites in the groundmass, respectively, indicates high melt/crystal ratio > 50 % which argues for a formation in a magma chamber rather than in the mush zone (Bachmann and Bergantz 2008). This mechanism corresponds to the concept of megacrysts growth during an early, magmatic stage (Vernon 1986, 2018; Higgins 2000; Moore and Sisson 2008; Vernon and Paterson 2008; Słaby et al. 2011). The formation of K-feldspar megacrysts requires the suppression of K-feldspar nucleation in granitic melts (Vernon 1986). Only in one example, the sanidine megacrysts of lava L3 entrapped manifold groundmass crystals in the outermost rims, which may indicate porphyroblastic growth under subsolidus conditions (Glazner and Johnson 2013). The formation of megacrysts at low melt/solids ratios, however, may explain the formation of megacrysts in plutons, but would inhibit the extrusion of the magma. Therefore, the porphyroclastic growth of the sanidine rims in lava L3 are suggested to take place during or after the extrusion of the lava.

The results of this case study, however, showed that sanidine megacryst formation took place at conditions, where the trachytic magma was held at a rather small temperature window around the liquidus. The massive travertine deposits in the direct neighbourhood of Saray Volcano prove a long lasting, continuous CO_2 percolation, which provides not only the required conditions for the formation of oscillatory zoning, but also for the growth of sanidine to megacryst size. The peculiarity of this concept is that heat supply via CO_2 can heat the trachytic magma body without significantly changing the melt composition.

Notably, the largest phenocrysts were observed in the early-erupted samples (group I), specifically in the lava dome L1, which represents the upper part of the magma chamber. In comparison, sanidine phenocrysts of the later erupted samples lava L2 and L3 and bombs B4 and B5 (group II) which represent the lower part of the magma chamber, are much smaller. Thermobarometric calculations showed, that the temperature is significantly

higher in the lower part of the magma chamber (1136 °C) compared to approximately 980 °C in the upper part of the magma chamber, which exceeds the liquidus temperature of sanidine by ~100°C. Consequently, all sanidine crystals of group II are strongly resorbed. If CO_2 percolates through the magma chamber, the originally "hot" CO_2 will transfer part of its heat from the hotter source into the lower part of the trachytic magma body and successively "loose heat" during upwards migration through the magma chamber. In consequence, heating is more effective in the lower part of the magma chamber. The significantly higher temperatures in the lower part of the magma chamber evoke higher resorption rates of the crystals in this environment, which hinders the growth of sanidine megacrysts. In contrast, heating by CO_2-percolation in the upper part of the magma chamber is effective enough to suppress groundmass crystallization, but weak enough that in this environment "growth" and not "resorption" is the dominant factor. These conditions enable the growth of sanidine megacrysts up to 10 cm in length. This is also reflected in the resorption patterns of sanidine megacrysts from the upper and the lower part of the magma chamber. Sanidine from the top part of the magma chamber, which grew to megacryst size > 4 cm show only weak resorption at the end of each oscillatory cycle. The smaller sanidine megacryst and macrocrysts from the lower part of the magma chamber show multiple, repeated cases of strong and high-grade resorption, often resorbing the major parts of the crystals (see Figure 10).

In contrast to anhydrous minerals, hydrous minerals get not resorbed when heated, but grow continuously in case of reheating without changes in chemistry (Bachmann and Bergantz 2006). Therefore, reheating via CO_2-percolation can also explain the growth of phl-I to megacrysts of several centimeters.

3.4.6.2 CONTROL OF CO_2 ON THE FORMATION OF THE DIFFERENT CRYSTALLIZATION STAGES OF SANIDINE

Intense resorption is characteristic for each stage transition SAN-A→SAN-B, SAN-B→SAN-C and SAN-C→SAN-D. Noteworthy is the abrupt change in Ba, which is characteristic for each crystallization stage, following high-grade resorption at the end of each crystallization stage: While the transition from SAN-A to SAN-B is accompanied by a significant decrease in Ba, the transition from SAN-B to SAN-C shows a slight increase in Ba, and SAN-C to SAN-D a strong Ba increase. How can this be integrated into the CO_2 flushing concept?

STAGE A TO B

In contrast to the other stages in the sanidine megacrysts, the transition from **stage A to stage B** is characterized by a sudden drop in Ba-content combined with an increase in Ca content. Such a trend requires a change in the melt, either by removal or dilution, e.g. by injection of a mafic, low-Ba melt. However, microtexture and microchemistry provide no evidence for such an event. At the same time, sanidine in zone B shows only weak resorption surfaces at the end of each oscillation cycle, and there is no indication of strong resorption. Massive nucleation and growth of a new generation of sanidine in the groundmass during stage B can explain the low Ba concentrations in B-SAN, thereby creating a crystal mush, as consequence of cooling of the melt. As a result, the available Ba in the melt is distributed to a bigger number of crystals, which in sum causes the low Ba

concentration in each SAN-B. A comparatively reduced CO_2 flux can explain the temperature decrease, which facilitated massive crystallization in the groundmass.

STAGE B TO C

Characteristic at the transition from **stage B to stage C** is the growth of a SAN-C rims with higher Ba and lower Ca contents after strong resorption of SAN-B. The different behavior of Ba and Ca is unexpected. An effect caused by the contribution of other materials such as xenocrysts or mafic melt is unlikely, as the concentration of e.g. Fe or Ti has not changed significantly. An explanation for the higher Ba concentration in SAN-C could be the result of strong re-heating of the crystal mush, which caused resorption of SAN-B phenocrysts and dissolution of the groundmass crystals. The observed simultaneous nucleation and growth of clinopyroxene with sanidine in stage C can be an explanation for the decrease of Ca in SAN-C.

STAGE D

All trachytes show the features of stages A, B and C, suggesting the growth of all the sanidine megacrysts in the same environment. **Stage D**, however, is restricted to later erupted (group II) trachytes. It shows reaction rims with different major or trace element concentrations: SAN-D with high Ba and Fe contents, clinopyroxene with higher Fe and Ti contents, and phl-I with higher F, Fe and Ti concentrations. The limitation of stage D crystallization to the later erupted group II products implies that this stage took not place in the magma chamber but during the ascent and eruption of the magma. The absence of stage D characteristics in consequence indicates that group I trachyte was not affected or that the contained crystals did not have enough time to adapt to the new conditions.

With the evolution of the magma, the Ba concentration in the melt decreases, resulting in decreasing Ba concentrations in sanidine (normal zoning). A sharp increase in Ba as observed in SAN-D was also observed in sanidine from Bishop Tuff (Anderson et al. 2000; Morgan and London 2003; Evans and Bachmann 2013; Chamberlain et al. 2014). The formation of the Ba-rims was explained by remelting of Ba-rich sanidine causing a local Ba-enrichment in the melt (Bachmann and Bergantz 2006). As Ba is highly compatible in sanidine, a preferred incorporation of Ba into the next growing sanidine will occur. According to calculations by Bachmann and Bergantz (2006) for the Fish Canyon Tuff, the resorption of a relatively small amount of Ba-containing sanidine is sufficient to increase the Ba content in the melt, which subsequently results in the strong increase of Ba during regrowth of sanidine.

In the case of Saray Volcano, reheating due to massive CO_2 percolation caused not only local Ba enrichment of the melt. Together with the influx of CO_2 and carbonatite from the uprising minette, also phl-II xenocrysts and glimmerites were transferred into the trachytic magma. In the chemical distinct trachyte, phl-II and glimmerite start to dissolve and release Fe, Ti, Ba and F into the melt. The preferential incorporation of elements in the minerals of group II trachyte caused rims with an increase in Fe and Ti in sanidine, clinopyroxene, and phl-I, and additionally the increase of Ba in sanidine and F in phl-I phenocrysts (Figure 46).

3.4.7 TIMESCALES

In general, the preservation of xenocrysts transferred from the complementary magma type indicates a fast ascent from the trachytic magma chamber to the surface. A longer residence time of the xenocrysts causes a complete dissolution of the xenocrysts and at slow ascent rates, the heavy mantle xenoliths would sink and thus not reach the surface. Therefore, the large mantle xenoliths, such as peridotite (wherlite), pyroxenite and glimmerite, which were carried with the mafic and felsic minette to the surface, can be used as markers for the ascent rate. The transport of such dense xenoliths with densities of 3.1-3.6 g/cm³ (pyroxenite) or 2.8-3.4 g/cm³ (peridotite) with the minette melt (ρ = 2.6-2.7 g/cm³) requires an ascent velocity faster than the settling velocity (V_x). The settling velocity for spherical particles in a laminar flow can be calculated using basic stokes velocity (e.g. Spera 1984):

(1) $V_x = (2*g*\Delta\rho*r^2) / (9*\eta)$

V_x settling velocity

η melt viscosity

$\Delta\rho$ density difference between the xenolith and melt

r xenolith radius

The parameters used to calculate the minimum settling velocity shows Table 3. The largest xenoliths (peridotite and pyroxenite) have a diameter of up to 30 cm. Therefore, calculations yielded a minimum ascent velocity of 3 m/s (~ 11 km/h) for the transfer of these xenoliths to the surface. Based on that, the magma ascent needed less than 6 h from the proposed minette source (> 70 km) and less than 4 h from the depth of the trachytic magma chamber to the surface. In an overview, Rutherford (2008) compared the magma ascent rates of different volcanos. Similar or even higher ascent rates are known from kimberlites, ranging between 3 and 17 m/s (Sparks et al., 2006), occasionally reaching ascent rates of even 10-30 m/s on the last kilometers. In comparison, extrusive ascent rates of Mt. St. Helens were with ~ 0.01 m/s (Rutherford 2008) one order of magnitude slower than the magma of Saray Volcano. The glassy groundmass and the lack of SAN-D in bombs from L-PCL are also indicative of a rapid magma ascent trachyte.

Table 3: Parameters used to calculate the minimum settling velocity

Parameter	unit	estimated range	used value
melt viscosity minette	Pa s	50-500	100
density minette	g/cm³	2.6-2.7	2.65
density pyroxenite	g/cm³	3.1-3.6	3.3
density peridotite	g/cm³	2.78-3.37	3.15
particle radius	cm		15

The transfer of mafic and felsic minette directly from depths > 20 kbar to the surface without re-equilibration under crustal levels was proposed by Esperança and Holloway (1987) for Colorado plateau. At Saray Volcano, however, the interaction between trachyte and minette implies that the emplacement of trachyte must have

been as fast as the emplacement of the lamprophyres, which could explain the preservation of manifold disequilibrium textures observed in both, trachyte and minette. Carbonatite is expected to decompose outside its P-T-stability field (carbonatite is stable at pressures > 20 kbar which corresponds to depths > 70 km). Therefore, only in case of a fast and violent eruption carbonatite can reach the surface, e.g. via kimberlites (Bodinier et al. 2004). Thus, the occurrence of phl-II xenocrysts and primary **carbonates** in trachyte samples proves a rapid ascent not only of minette but also of trachyte.

A rapid ascent not only of lamprophyre but also of trachyte is manifested in several petrological observations. Based on the assumption that trachyte had to ascent as rapid as the lamprophyre (3 m/s), the trachytic magma needed about 4 hours to ascent from about ~40 km depth in the lower crust to the surface. In general, the breakdown of hydrous minerals such as amphibole and phlogopite occurs when the water activity in the melt is too low. Therefore, high level of CO_2 activity can force phlogopite breakdown. The kelyphytic diopside rims observed around phl-I and phl-II from the later-erupted group II trachyte, point to a degradation of phlogopite by dehydration. These rims are a strong indicator that group I trachyte reached the surface of the earth directly without any stop, whereas group II trachyte had some residence time near the surface before eruption, e.g. due to the plugging of the dome. Similar features were observed for amphiboles from Mt. St. Helens. Rutherford (2008) showed experimentally that the thickness of these rims can be used to estimate the ascent rates. He observed first rims around amphibole after 4 days, while rims up to 2 µm needed 7 days, and 32 µm thick rims 20 days. Accordingly, those less than 5 µm thin diopside rims around phl-I and phl-II point to a short residence time of group II samples in the conduit (less than several days) before the explosion. However, comparable experiments for phlogopite are required to be more precise. Stage D characteristics were obviously formed during the ascent of the magma and during residence time at shallow levels due to plugging of the vent. Therefore, for the SAN-D rims, which are about 250 µm thick, a crystallization time between ~ 4 h (ascent time) and several days (residence time at shallow levels) can be assumed.

Residence times of minerals in the magma chamber can be estimated by diffusion modeling of zoned minerals. The wavelength of one oscillation cycle in sanidine megacrysts of Saray Volcano, determined as the distance between the respective maximum amplitude of the Ba, varies between 50 and 200 µm. However, these are only minimal values, since the resorbed sections are not known. Diffusion of Ba is slow (Cherniak 2002), which explains the sharp boundaries in Ba concentrations.

In general, diffusion of the elements is temperature dependent. Therefore, the diffusion rates are calculated for a given temperature. For Saray Volcano, however, high temperature differences must be taken into account, which can vary between 980°C in the upper part of the magma chamber and 1135°C in the lower part of the magma chamber. According to Cherniak (2002), a 100 µm Ba zonation gets lost after 10,000 years at 900 °C and after only 100 years at 1000°C. Sr diffusion can also be used to estimate the residence time of the crystals. Diffusion of Sr is about one order of magnitude faster than Ba due to the smaller ionic radius (Shannon 1976). The preservation of Sr zonation in the sanidine megacrysts of Saray Volcano is therefore indicative of a short residence of the sanidine crystals in the melt. In the case of Saray Volcano, the preservation of Sr zonation suggests a maximum residence time of the crystal in the trachyte melt of 100 years at 900 °C and less than 10

years at 1000°C. These rough estimates support the assumption of Zellmer and Clavero (2006) that megacrysts grow relatively fast.

3.4.8 ERUPTION MECHANISM

Two different types of magma are involved in the last (trachytic-lamprophyric) eruption of the Saray Volcano. The intermediate viscosity of trachyte magma ranging between rhyolite and phonolite (Giordano et al. 2004), favors the formation of lava domes or explosive eruptions. This property explains also the short distance of the lava flow from the vent of Saray Volcano, the numerous large-scale broken lava blocks observed in *Agh Gonbad* valley, and the massive block-and-ash flow deposits. The question therefore arises of what enabled mobilization and the rapid ascent of the sanidine megacrysts-containing trachytic magma?

Wilson and Head (2007) assumed two different mechanisms as the cause of the rapid ascent of the kimberlites: 1) the accumulation of CO_2 in the top part of the magma mass and 2) buoyancy caused by the formation of CO_2 bubbles. This is consistent with the decomposition of diopside, occurring in early-erupted bombs from Saray Volcano, which indicate an enormous accumulation of CO_2 in the magma chamber roof. Decomposed diopside in felsic minettes show that CO_2 accumulated also there. Breakdown of carbonatites in minette under crustal conditions provides also a large volume of CO_2. This suggests that a CO_2-gas pocket acted as avant-garde of the ascending felsic minette magma and flushed through the trachytic magma chamber. The CO_2 influx caused a critical overpressure in the magmatic system. In consequence, not the lamprophyric magma recharge itself, but the overpressure due to the addition of its CO_2 cargo to the already pressurized trachytic magma triggered the eruption. If a critical overpressure is reached, the wall rock above the magma chamber fails. The resulting fissures and cracks provide channels to enable the ascent of magma to the surface. The CO_2 pressure built up is enhanced by expansion of the CO_2 molecules during ascent. Each fragmentation of the country-rock evokes a pressure release, which consequences further expansion of CO_2 and thus again fragmentation. The expansion of CO_2 is most pronounced at ~ 800 m below the surface, which could explain the outburst of the volcano and specifically, the explosive eruption of the trachytic magma.

The sudden pressure release accelerates the degassing of CO_2 and other volatiles, leading to a foaming of the melt. The high CO_2 bubble ratio in the magma effects a reduction of the melt density caused by the formation of a foam like texture. The buoyancy coupled with this process enables a rapid ascent of the melt together with the megacrysts. Flushing of the trachytic magma by hot CO_2 transfers heat into the magma, which consequences a lowering of the melt viscosity. Carbonatite infiltrating the trachytic magma chamber acts as a lubricant supporting the rise of the megacrysts-containing trachytic magma.

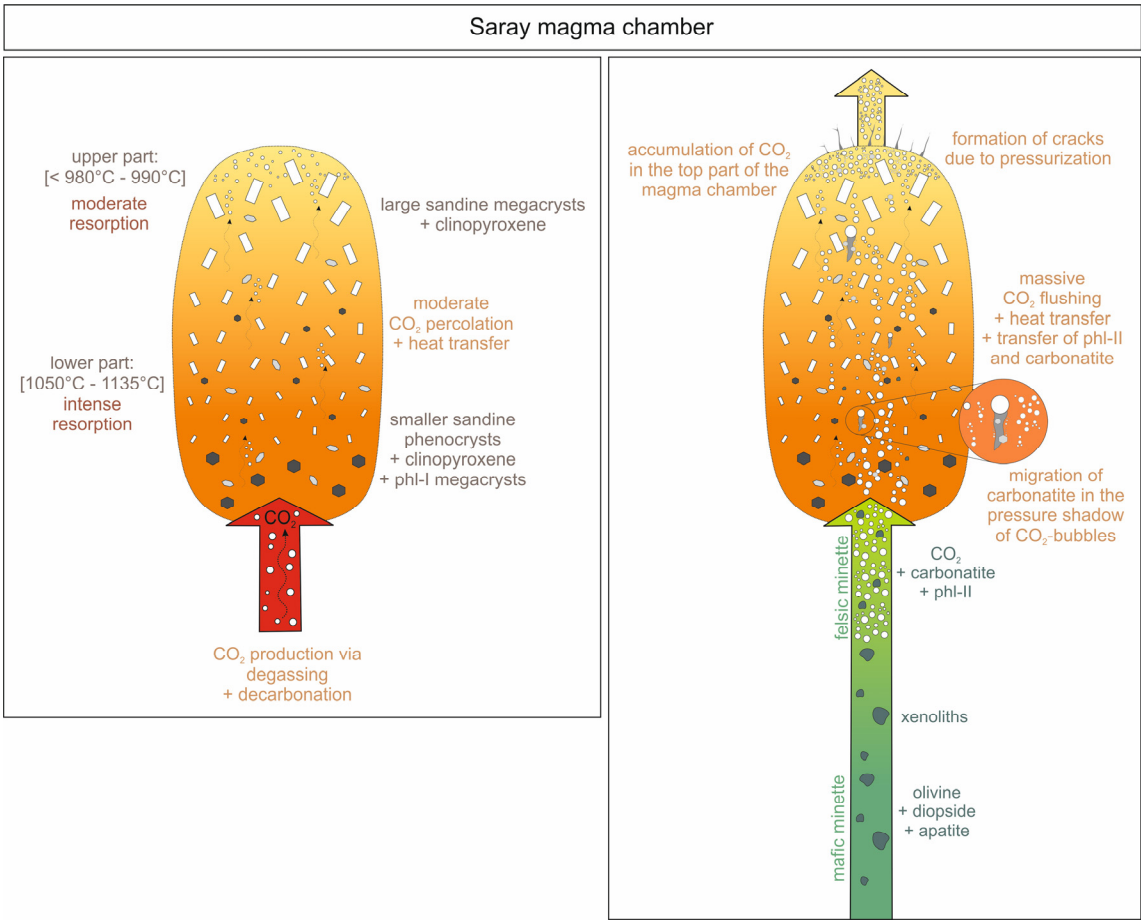

Figure 44: Schematic sketch showing a model of the Saray magma chamber. Left: Mantle derived, hot, CO_2 percolates through the magma chamber and accumulates in the magma chamber roof. Right: Arrival of CO_2-loaden lamprophyre leads to a critical overpressure

3.4.9 CHRONOLOGY

All features observed in the different samples were combined to develop a model for the eruptive events (Figure 45). Based on the results four distinct eruption phases can be distinguished (Figure 46):

Preeruption phase: the repeated heating of the magma via CO_2 percolation enabled the preferential growth of sanidine megacrysts with pseudo-oscillatory zoning and phl-I megacrysts (Figure 44 left). The occurrence of sanidine megacrysts in the products of the first eruption phase and smaller sized crystals in products of later eruption stage is in accordance with the concept of heating of the magma. The heating of the lower part of the magma chamber causes a dissolution of the small anhydrous crystals, while the continuous growth of the fluid-containing phases such as phlogopite is supported. As a result, the size of newly formed sanidine crystals remained low and phlogopite could grow to megacrysts. The sequential CO_2 percolation in the "cooler" upper part of the magma chamber leads to partly strong resorption of the larger sanidine crystals without dissolving them completely. These crystals subsequently grow to megacrysts as heating is sufficient to suppress groundmass crystallization. Gravimetric processes in combination with CO_2 upwards-percolation favors the

formation of a slightly stratified magma chamber with sanidine crystals floating up and phl-I settling down Figure 44).

CO_2, carried with the ascending minette is injected into the already pressurized trachytic magma chamber, causing a critical overpressure. Failure of the country-rock above the magma chamber and formation of cracks is the consequence. During ascend volume expansion of CO_2 with decreasing pressure clears the way to the surface. CO_2 bubbles in trachyte create a buoyancy supporting the uplift of the trachytic magma.

Eruption phase I is marked by the explosion of group I trachytes including sanidine-rich ejecta with blocks and bombs (C1 in Figure 46, deposited in L-PCL in Figure 45) and the extrusion of the main lava dome (L1) in the central part of Saray Volcano (C2 in Figures 46 and 45). It is obviously triggered by an overpressure caused by addition of CO_2 from the uprising felsic minette to an already pressurized magma chamber with accumulated CO_2 in the top part of the magma chamber (C1 in Figures 46 and 44 right).

The absence of stage D crystals in the ejecta indicates that the mineral assemblage was quenched before they could adapt to the new conditions. The transfer rate was around 3 m/sec. The porous groundmass, SAN-D microlites in lava dome L1 and the frequency of centimeter-sized gas bubbles in the samples indicate ongoing crystallization in the residual melt parallel to the degassing process. The microlitic groundmass indicates a rapid cooling of the melt, which resulted in plugging of the vent (Figure 45) and prevented an outgassing of volatiles (Sparks 1997).

Eruption phase II is marked by an explosion resulting in a second block-and-ash flow deposit (U-PCL in Figure 45) which contains numerous sanidine-rich blocks and bombs (D1 in Figure 46). The following observations show that various reactions occurred after the mobilization of the magma and before the second eruption phase:

- Formation of new reaction rims are marked by the sudden increase in Ba in sanidine, Fe and Ti in diopside, as well as F, Fe and Ti in phl-I. This process points to an ongoing adjustment of the melt to changing reaction conditions caused by the dissolution of phl-II in these rocks (see stage D in Figure 46).
- Phlogopites show thin kelifitic rims of diopside, which were absent in samples from the first eruption phase. Therefore, the dehydration reaction must have occurred within a short time after the first eruption phase (most likely hours to days).
- Abundant bubbles in the B4 groundmass are clear signs of fluid supersaturation and thus a large fluid overpressure, which prevailed at shallow depths in the uppermost part of the conduit. It is possibly caused by a second boiling of the residual fluid including H_2O in the melt, which was enriched in the residual melt after microlite formation (Sparks 1997), triggering the second violent explosive activity (Figure 45).

Eruption phase III comprises the extrusion of trachytic lavas (L2 and L3 in Figure 45, see D2 in Figure 46) at the flanks of the Saray Volcano. The eruption of the lavas at the flanks of Saray Volcano was most enabled by the generation of a fracture systems during the first eruption phases, as the main path was plugged by lava L1. In contrast to L1, sanidine crystals in the matrix of lava samples L2 and L3 have a larger particle size (D2 in Figure 46)

which indicates a slower cooling rate of the melt. The porphyroblastic growth of sanidine rims (sample L3) point to supercooling of this melt, e.g. after extrusion. Rare sanidine megacrysts and comparatively small phenocrysts (≤ 1cm) in sample L2 indicate a more intense resorption of the sanidine crystals in the hotter, lower part of the magma chamber before the eruption.

The intrusion of minette plugs and dykes marks the **last phase IV** (see E in Figure 46), which terminated the volcanic activity of Saray Volcano. The still high temperature of the lamprophyric magma during intrusion and subsequent rapid cooling is indicated by the glassy groundmass of the mafic minettes (E2 in Figure 46) and the microlitic groundmass of the felsic minettes (E1 in Figure 46). The significantly higher temperature of the felsic minette compared to trachyte in combination with an extremely high CO_2-input and an elevated carbonatite content probably enabled the felsic minette to penetrate the crater area (Figure 45) leading again, to a plugging of the vent. CO_2-rich conditions are indicated by abundant gas bubbles in mafic minette and frequent carbonatite melt in the matrix and decomposed diopside of the felsic minette. Mafic minette intruded all over Saray Volcano, most likely along cracks and weakness zones (Figure 45) resulting in radial and vertical sills and dykes.

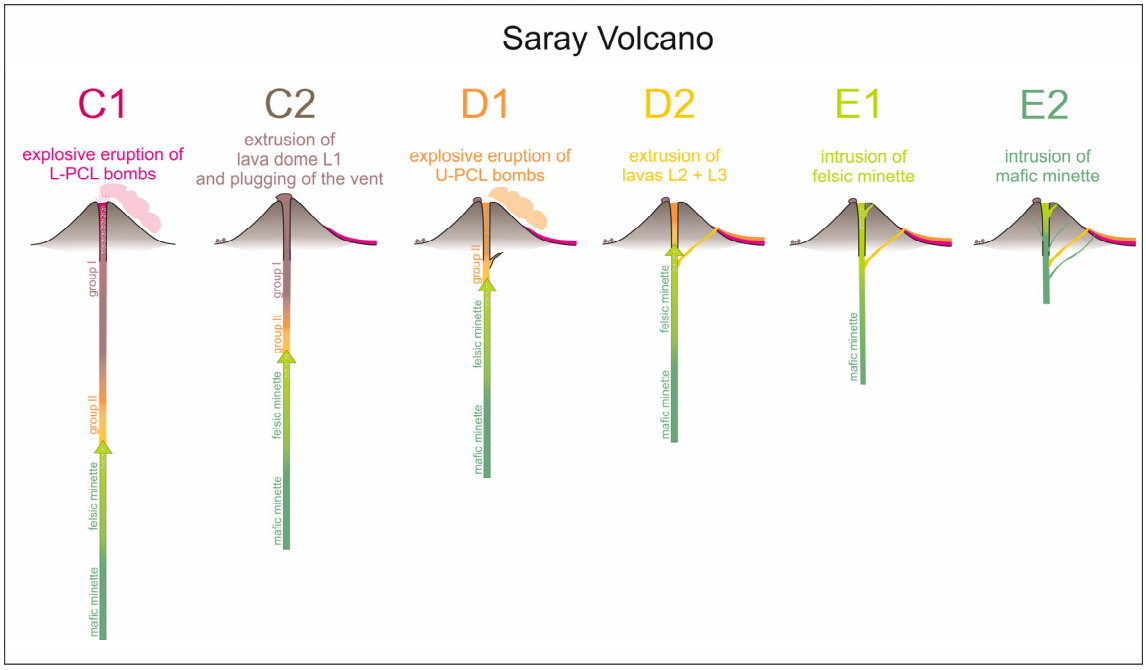

Figure 45: Schematic sketch showing the eruption chronology of the trachytic-lamprophyric eruption period of Saray Volcano starting with the explosive eruption of the trachytes of the lower pyroclastic layer (L-PCL) and the extrusion of the lava dome (L1) and ending with the intrusion of felsic and mafic minette. The numbers, C1, C2, D1, D2, E1 and E2 refer to the eruption phases in Figure 46. Detailed descriptions are given in the text

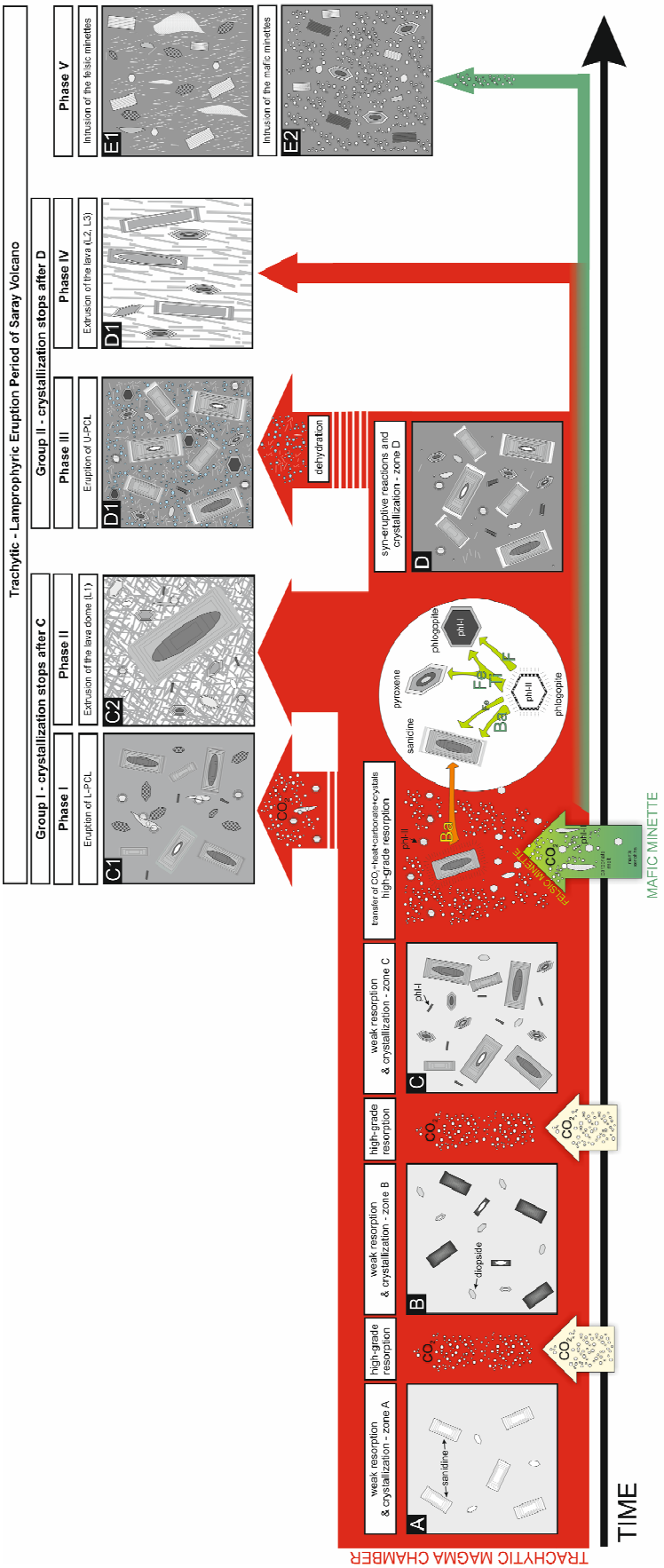

Figure 46: Schematic Sketch showing the evolution in the magma chamber and eruption chronology of four distinct eruption phases. The pre-eruption phase includes four crystallization stages A-D within the magma chamber. The decomposition of phl-II crystals in stage D leads to the release of F, Ba, Fe and Ti into the melt. This causes the increase of [Ba, Fe] in the rims of sanidine, [F, Fe, Ti] in phl-I and [Fe, Ti] in clinopyroxene. The sequence of eruption phases I-V are based on detailed petrological and microchemical investigations and field observations. The detailed process is described in the text

In den Dellen, Eifel

4 PETROLOGICAL INVESTIGATION OF SANIDINITES FROM LAACHER SEE VOLCANO

4.1 INTRODUCTION TO LAACHER SEE VOLCANO

The phreatomagmatic and vulcanian eruption of Laacher See Volcano (Eifel, Germany) 12.900 BP (Bogaard 1995), was the most violent eruption in the younger history of Central Europe. Within a few days, a volume of 6.3 km^3 of an alkali-rich, chemically zoned, phonolitic magma chamber was erupted explosively. Recent CO_2-emission (mofettes) in the lake "Laacher See", the former crater, indicate that volcanic activities at Laacher See has not subsided (Giggenbach et al. 1991; Aeschbach-Hertig et al. 1996).

Laacher See Volcano was subject of numerous studies since at least the 1860s. Schürmann (1960) summarized the history of scientific research. Special interest arose early on the sanidinites, which are felsic nodules embedded in the Laacher See tephra. In the mid of the 19th century, Pater Theodor Wolf from the nearby Monastery Maria Laach recognized, that the characteristic minerals – nosean and haüyne – occur never within the same rock fragment. Consequently, they were classified as nosean-sanidinites and haüyne-sanidinites. For about 100 years, there has been a controversial debate on the formation conditions of these sanidinites. They were interpreted either as magmatic cumulates, co-genetic with the Laacher See phonolite (Laspeyres 1866), or as pegmatitic dykes (Wolf 1867/68, Dressel 1971) or as rocks overprinted by a hot gas phase (Brauns 1907-1934). In the 1930s, further confusion ensued, followed by debates between Brauns and Kalb after recognizing that country rock fragments, which also occur as xenoliths in the Laacher See tephra, show similar modifications as the sanidinites. Brauns insisted to call the overprinted country rock "sanidine-rock" and the overprinted magmatic cumulates "sanidinite". Kalb, however, recognized the similarities of the overprinted country rock pieces at Laacher See with fenitized country rock at Fen (Brögger 1921) and termed this type consequently "fenite".

Several studies dealt with the contribution of the volatile species in the melt of Laacher See (Tait 1988; Harms and Schmincke 2000). However, the contribution of the gas phase, specifically CO_2 on processes within the magma chamber and on the eruption mechanism was not yet investigated (Schmincke 2008).

Tait (1988) showed that the haüyne-sanidinites are part of a series of mafic, intermediate and felsic cumulates which cumulated at the magma chamber margin. Since the 1980s, major attention was set on the Laacher See tephra with focus on geology (Bogaard and Schmincke 1984, 1985), petrology (Wörner and Schmincke 1984a; Wörner and Wright 1984; Tait 1988; Tait et al. 1989; Ginibre et al. 2004), geochemistry (Wörner et al. 1983; Wörner and Schmincke 1984b; Wörner et al. 1985, 1987; Harms and Schmincke 2000) and geochronology (Bourdon et al. 1994; Bogaard 1995). The Laacher See tephra deposit is interpreted as a reverse deposited, chemically zoned magma body (Wörner and Schmincke 1984b). Since the 1990s, nosean-sanidinites were interpreted as carbonatite-bearing syenite intruding the magma chamber carapace, but with a close relationship to the phonolitic magma chamber (Liebsch 1996; Schmitt et al. 2010).

There are only few studies about volatiles such as CO_2 in the eruption products of Laacher See. XRF measurements of matrix glasses of the Laacher See Tephra yielded 100-500 ppm CO_2 (Wörner and Schmincke 1984b). Therefore, Harms and Schmincke (2000) did not consider the contribution of CO_2 to the whole Laacher See volatile budget. Nonetheless, there is clear evidence for the presence of CO_2 in the Laacher See Volcano: 1) the occurrence of carbonates in felsic cumulates from the magma chamber roof and 2) current CO_2 mofettes in the lake "Laacher See" with mantle signature. In shallow levels in the crust, such as the magma chamber of Laacher See Volcano at 5-8 km depth (~1 kbar), most of the CO_2 is "degassed" and present as a "free phase".

Aim of this case study is therefore to investigate the crystallization conditions in the upper part of the magma chamber of Laacher See and the impact of volatiles on the crystallization process. Special focus will be set on the role of CO_2 and its contribution to the eruption mechanism. For this purpose, I sampled a large number of different types of sanidinites and analyzed them by geochemical, petrographic and mineral chemical methods. Subsequently, I integrated the results into the existing model of the Laacher See magmatic system.

4.2 GEOLOGICAL SETTING OF LAACHER SEE VOLCANO

The Laacher See Volcano and about 100 other volcanic centers with scoria cones and a few maar volcanos, belong to the East Eifel volcanic field (EEVF, 400 km² in areal extent) of the intraplate Tertiary-Quaternary central (Figure 47) and western European volcanic province (Schmincke 2007), which also includes significant volcanic activities in the Massif Central (France). The East Eifel volcanic field is characterized by alkaline volcanism (basanites, tephrites, phonolites, leucitites and nephelinites; Schmincke 2007). It is located in close spatial proximity to the Rhine Graben system including the volcanoes Kaiserstuhl and Vogelsberg and the Egergraben. These regions are all characterized by complex spatio-temporal patterns of regional uplift (doming), alkaline volcanism, and rifting. The terraces of the Rhine river document an increased uplift during the last 600.000 years (Meyer and Stets 2007).

The East Eifel volcanic field was formed on top of the recently uplifted (ca. 300 m) and eroded Rhenish Shield (Fuchs 1983). The Rhenish shield is part of the last major crustal consolidation during the Hercynian-/Variscian orogeny, a major late Paleozoic continent-continent collision that resulted in mantle turnover, thereby affecting the geochemical signature of the lithosphere. Volcanic activity in this region follows and accompanies the uplift of the Rhenish Shield and the Eocene to Miocene rifting of the Rhine Graben (Wilson and Downes 1991; Lustrino and Wilson 2007).

The Tertiary activity period was dominated by alkaline to transitional basaltic lavas including the 15-16 Ma Vogelsberg shield volcano, which covered a large area of approximately 600 m² (Bogaard and Wörner 2003). The Quaternary activity period in the East Eifel volcanic field started approximately ~ 600 ka ago and produced highly alkaline, potassic and silica-undersaturated magmas (Mertes and Schmincke 1983, 1985; Schmincke 2007). The three major eruptive centers are the Rieden-Complex, Wehr Volcano and Laacher See Volcano. Four eruptive periods with gaps of a few thousand to ten thousands of years can be distinguished. The oldest (pre-Rieden)

Quaternary volcanic activity took place at ~ 600 ka. The Rieden-Complex erupted in several phases between ~ 450-400 ka (van den Bogaard et al. 1989), followed by the eruptive activity of the Wehr Volcano to the East between 350 and 215 ka. The last and the most voluminous eruption was that of the Laacher See Volcano 12.900 BP (Bogaard 1995).

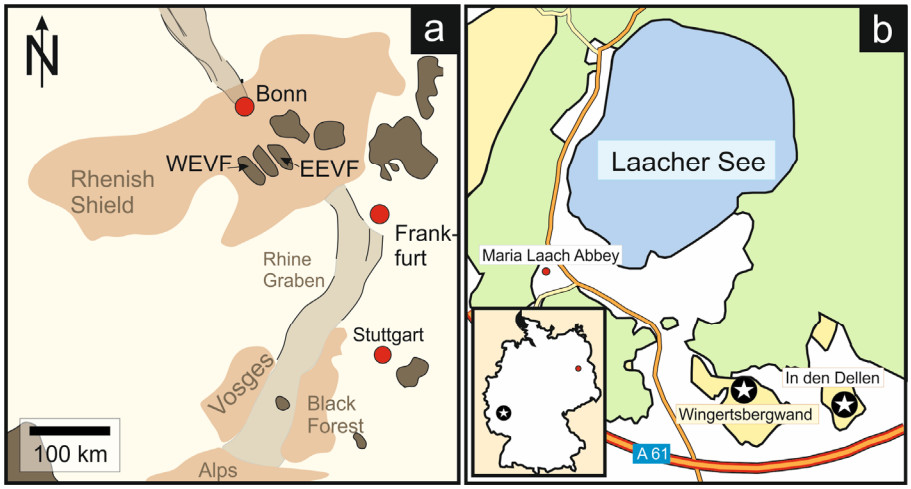

Figure 47: a) Simplified map of Tertiary and Quaternary volcanism of Germany after Schmincke (2007), b) Map of the Laacher See area with the outcrops Wingertsbergwand and Pint Zieglowski with sanidinites

At Laacher See, approximately 6.3 km³ of phonolitic magma was erupted within a few days (Harms and Schmincke 2000) resulting in the deposition of the compositionally zoned Laacher See Tephra (Wörner and Schmincke 1984b, a), the most voluminous pyroclastic deposit in the East Eifel volcanic field. Outcrops near to the vent show a complex sequence of phreato-plinian fall and surge deposits, as well as air-fall deposits and pyroclastic flows in the lower part and again phreato-magmatic fall and pyroclastic flow deposits on the top. Ash layers of the Laacher See eruption are dispersed over Central and Eastern Europe (Bogaard and Schmincke 1984, 1985; van den Bogaard et al. 1989). According to the volatile-saturation barometric calculations, the top of the magma chamber is assumed to be at 5-6 km (Wörner and Schmincke 1984a). A total height of 1.2 km was calculated for the magma body, based on geographic evidence, geometry and the volcanic depression and estimates about the erupted volumes (Wörner and Schmincke 1984a).

4.2.1 LAACHER SEE TEPHRA

Bogaard and Schmincke (1984, 1985) investigated the Laacher See Tephra (LST) from the bottom of the deposition to the top. Based on lithology, chemical composition, eruption and deposition type, the Laacher See tephra can be divided into three units (Bogaard and Schmincke 1984; Wörner and Schmincke 1984b, a, Figure 48):

- Lower Laacher See Tephra (LLST), highly evolved white phonolites with < 2% phenocrysts
- Middle Laacher See Tephra (MLST), crystal-poor, differentiated phonolite
- Upper Laacher See Tephra (ULST), mafic, gray phonolites with up to 55% crystals.

The tephra are interpreted as inversely deposited material of a stratified phonolitic magma body (Wörner et al. 1983; Wörner and Schmincke 1984b). The bottom of the magma chamber was hotter (at least 840-860°C), more mafic and crystal-rich but less volatile-rich, whereas the top part was cooler (~ 700 °C), more evolved and volatile-rich (see Figure 49; Wörner and Schmincke 1984b, a; Harms and Schmincke 2000; Harms et al. 2004). The detailed study of the Laacher See tephra revealed a systematic change from upper Laacher See tephra to the lower Laacher See tephra in petrographic characteristics and in whole-rock chemistry (Wörner et al. 1983; Wörner and Schmincke 1984b). The Laacher See tephra show only small variations in SiO_2-content (Figure 49), but a chemical gradient in alkali content increasing from upper Laacher See tephra to the lower Laacher See tephra (Figure 49). In detail, there is a shift from Ca-, K-, Al-, Ti-rich conditions in upper Laacher See tephra towards Na- and Mn-rich conditions in lower Laacher See tephra (Wörner and Schmincke 1984b). Remnants of hybrid lavas with a more mafic composition compared to the phonolite of the upper Laacher See tephra occur within the uppermost layer of the deposit and are suggested to be formed by spatial limited mingling and mixing of the phonolite with a basanitic magma recharge (Wörner and Wright 1984).

Ginibre et al. (2004) showed that sanidine as well as plagioclase has a gradient in anorthite component with the highest Ca concentrations in the bottom and the lowest in the upper part of the magma chamber (Figure 48). Based on the textures, they grouped the sanidine crystals in the tephra of the Laacher See Volcano into three distinct types representing the growth of sanidine within different sectors of the magma chamber:

- **R-type**: are **resorbed** and patchy-zoned sanidine crystals reflecting an early growth in a differentiated boundary layer, followed by resorption and overgrowth in the main magma body.
- **C-type**: are lamellar **composite alkali feldspars** with low trace element concentrations. They crystallized at temperatures of ~ 650°C in a highly differentiated and volatile-rich boundary layer at the magma chamber roof or wall.
- **PO-type**: are **pseudo-oscillatory** zoned sanidine crystals with repeated resorption accompanied by variations in An-component (1–4 mol %) and water content. The calculated temperature varies within a range of 100 - 300 °C. Combined with variations in Ba, Sr and Ti, which are decoupled from the pseudo-oscillations of the major elements, these zonings are interpreted as the progressive influence of a more mafic, hotter melt.

Based on the results, Ginibre et al. (2004) assumed local convection cells promoting the resorption and growth of the sanidine crystals.

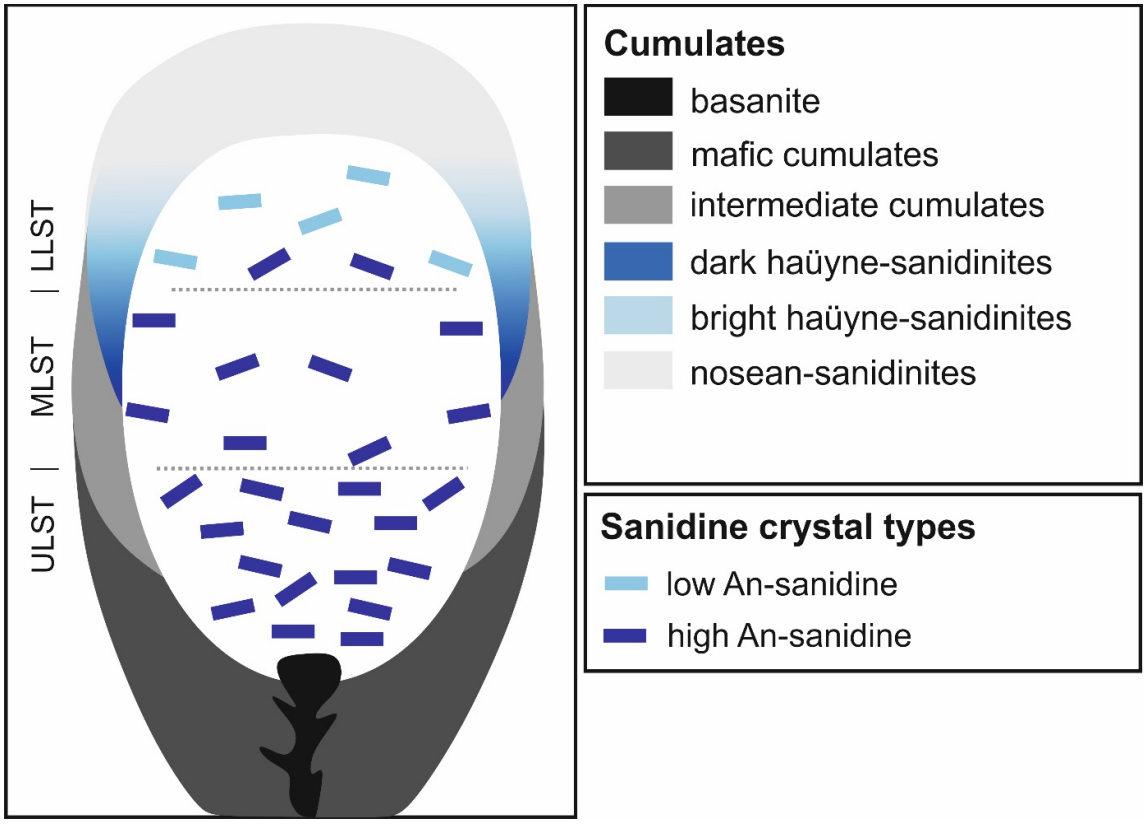

Figure 48: Schematic model of the Laacher See magma chamber prior to eruption (after Wörner and Schmincke 1984b, Tait et al, 1989, Ginibre et al. 2004, Schmitt et al. 2010)

4.2.2 LAACHER SEE CUMULATES

The Laacher See tephra contain abundant fragments of contact metamorphic xenoliths of the Devonian country rock and mafic to felsic magmatic cumulates. Country rock xenoliths predominate in the lower and middle Laacher See tephra deposit whereas magmatic cumulates occur mainly in the middle and upper Laacher See tephra. The cumulates are crystal-rich (< 25 %) and cover geochemically the whole spectrum of mafic (basanitic), intermediate and felsic (syenitic) composition (Figure 49) and were classified by Tait (1988). The mafic cumulates consist of clinopyroxene, amphibole, magnetite and apatite. The intermediate contain plagioclase, clinopyroxene, amphibole, magnetite and titanite and rarely sanidine. The felsic cumulates, the so-called sanidinites, consist predominantly of sanidine and contain always sodalite-group minerals, either haüyne or nosean, but never both of them within the same cumulate. Accordingly, they can be subdivided into haüyne-sanidinites and nosean-sanidinites. Haüyne-sanidinites consist predominantly of sanidine and minor amounts of haüyne, plagioclase, clinopyroxene, magnetite, apatite, and titanite. Nosean-sanidinites consist of sanidine, nosean and calcite, magnetite, zircon and pyrochlore. Haüyne-sanidinites from Laacher See, gained particular fame due to their clear blue haüyne phenocrysts whereas the carbonate bearing sanidine-rich ejecta are generally less noticeable in the field.

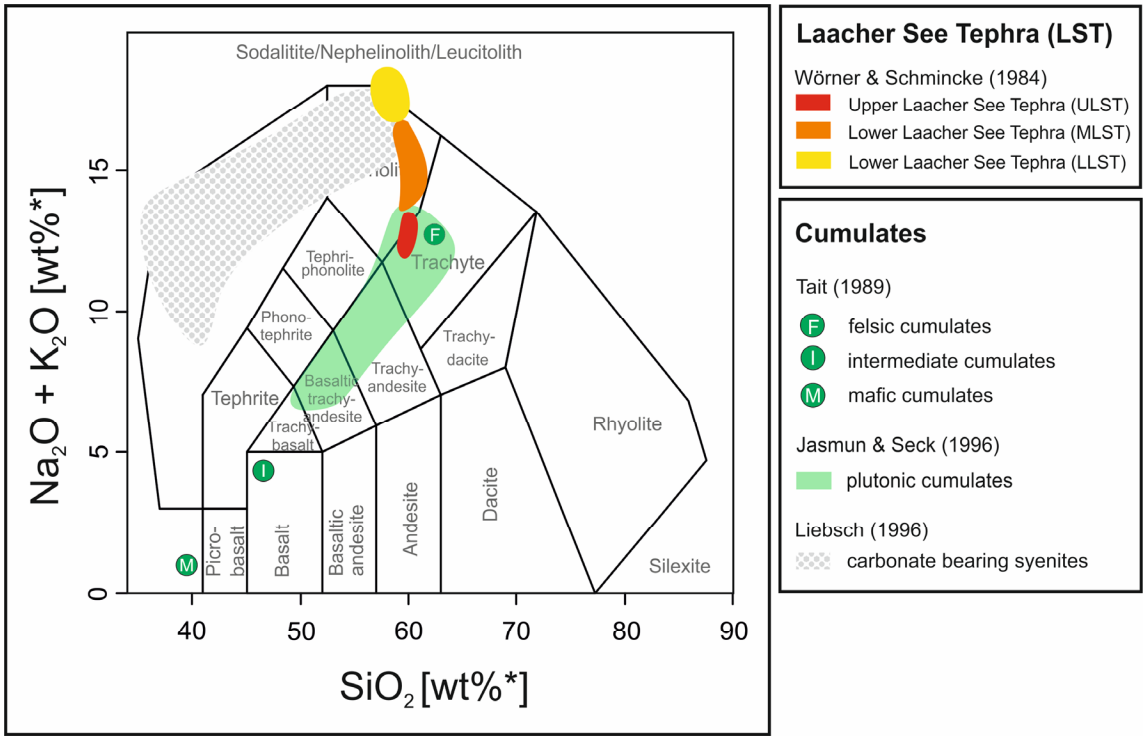

Figure 49: TAS diagram showing the chemical composition of the eruption products of Laacher See Volcano, including the different cumulates (Jasmund and Seck 1964; Tait et al. 1989), carbonate bearing syenites (Liebsch 1996) and different types of Laacher See tephra (Wörner and Schmincke 1984a)

According to Tait (1988), these nodules crystallized at the interface between the crystal-mush and the wall of the magma chamber. He suggested the mafic nodules to represent the bottom of the magma chamber, whereas the intermediate and felsic nodules crystallized at the walls and the roof of the magma chamber. The nosean-sanidinites, however, are only poorly studied. Carbonate-rich varieties were studied by Liebsch (1996) and Schmitt et al. (2010) and are interpreted as carbonatite-bearing syenite intruded in the carapace of the Laacher See magma chamber. Liebsch (1996) distinguished three different types, calcite bearing nosean-syenites containing sovite domains (LSC-1), sovite-syenites (LSC-2) and calcite bearing nosean-syenites (LSC-3). The majority of nosean-sanidinites, however, have lower calcite contents, with some of the being carbonate free.

4.3 RESULTS

4.3.1 SAMPLES

For this study, more than 200 sanidinites (felsic, ejected nodules) were collected from two outcrops of the Laacher See Tephra around the village Mendig from the Grube Zieglowski (In den Dellen) and the Wingertsbergwand (see Figure 47b). It was taken care to collect a broad variety of sanidinite cumulates ranging from dense white samples over greenish glass-rich pieces to holocrystalline rocks with macroscopically visible cavities between the sanidine crystals. Most eye-catching, but rather rare, are cumulates containing clear blue haüyne crystals. Most abundant are holocrystalline white to grey-white cumulates with nosean, which are often covered by beige-brown tephra.

In total, 30 samples were selected for detailed petrological and microchemical study. They consist mainly of sanidine laths with varying mineral assemblage in the cavities. According to their macroscopic appearance, three major groups of sanidinites can be distinguished:

- **Dark haüyne-sanidinite:** porous nodules with sanidine and dark glass containing **clear blue haüyne** crystals (Figure 50),
- **Bright haüyne-sanidinite:** macroscopically visible remolten sanidine laths and **pale blue haüyne** crystals (Figure 51),
- **Nosean-sanidinite:** white sanidine laths creating macroscopically visible cavities and grey nosean crystals (Figure 52). Nosean-sanidinite is famous for the HFSE minerals it contains.

The mechanical strength increases significantly from dark haüyne-sanidinite over bright haüyne-sanidinite to nosean-sanidinite. Some of the dark haüyne-sanidinite samples can be easily crumbeled between the fingers. Correspondingly, the proportion of glass in the rock decreases from haüyne-sanidinite to nosean-sanidinite. Due to the high proportion of glass, haüyne-sanidinite appears dark greenish to grey. In glassy areas, bright haüyne-sanidinite appears greenish or even pinkish.

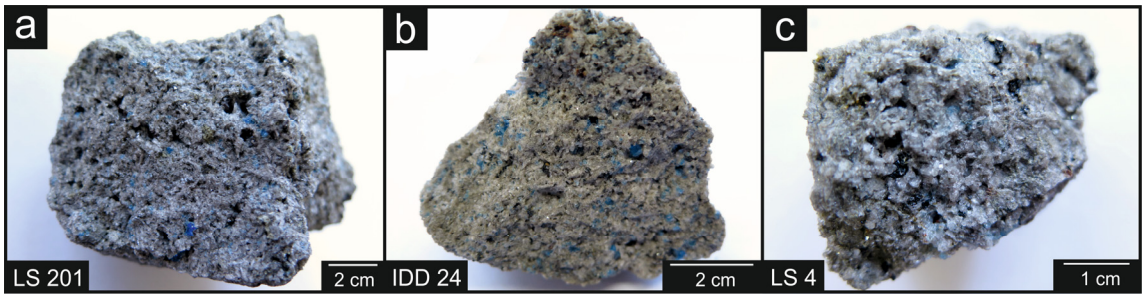

Figure 50: Photos of dark haüyne-sanidinites from Laacher See; grey = sanidine crystals with interstitial melt, blue = haüyne

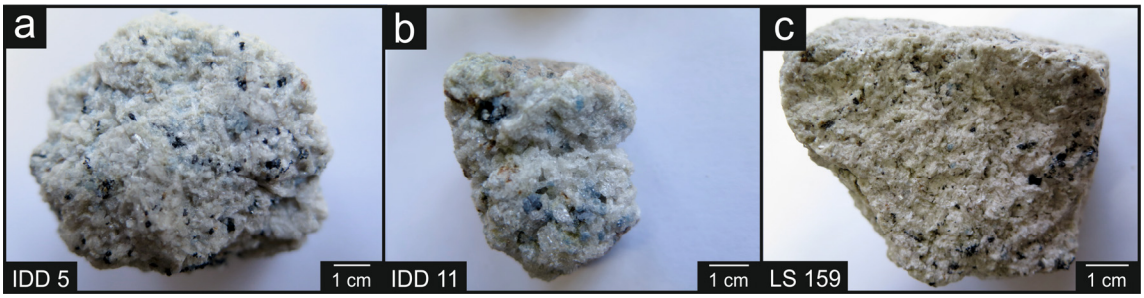

Figure 51: Photos of bright haüyne-sanidinites from Laacher See; white = sanidine, blue = haüyne

Figure 52: Photos of nosean-sanidinite from Laacher See; white = sanidine, grey = nosean and carbonate

4.3.2 PETROGRAPHY

The main component of sanidinite is always alkali-feldspar as the name suggests. In addition, minerals of the sodalite-group are always present. The color of the sodalite-group minerals subdivides them into two major groups: **Haüyne-sanidinite** containing clear blue haüyne and **nosean-sanidinite** with grey to colorless nosean. The two types of haüyne-sanidinite – **bright** and the **dark haüyne-sanidinite** – were distinguished by the color of the groundmass. Notably, both types of haüyne-sanidinite are carbonatite-free. In contrast, nosean-sanidinite contains a variable amount of carbonate ranging from carbonate free nosean-sanidinites to carbonate bearing nosean-sanidinite with 1-20 vol% carbonate. Another criterion is the degree of crystallinity in sanidinite. The glass proportion decreases from dark haüyne-sanidinite over bright haüyne-sanidinite to holocrystalline nosean-sanidinite. In haüyne-sanidinite, sanidine laths form a lose framework as they are not directly conjoined but connected via vesicles-rich glass showing the same or a brighter shade of grey as sanidine in BSE image. In contrast, nosean-sanidinite is mostly holocrystalline. Some samples contain glass in form of thin interstitial films, always rich in vesicles.

On closer examination, the different types of sanidinite show similar mineral assemblages consisting of sanidine, sodalite-group minerals, clinopyroxene and biotite. However, the proportions of these minerals differ greatly in haüyne-sanidinite and nosean-sanidinite. Approximately 80-90 vol% of dark haüyne-sanidinite consists of sanidine, with minor amount of the phases haüyne (< 10 vol%), plagioclase (< 5 vol.%) and glass (< 5 vol %). The present mafic minerals (< 5 vol%) are clinopyroxene, biotite, and amphibole. In comparison, the proportion of

sanidine in bright haüyne-sanidinite is slightly lower in favor of sodalite-group minerals. In nosean-sanidinite, the difference gets more pronounced, with up to 15-30 vol% nosean in expense of sanidine. The amount of mafic minerals reach a maximal proportion < 5 vol% and plagioclase mostly absent. Noteworthy is that carbonate occurs only in nosean-sanidinite, with a proportion between zero and 20 vol%.

4.3.2.1 HAÜYNE-SANIDINITE

Haüyne-sanidinites are hypidiocrystalline rocks with a porous texture. **Sanidine** is the main mineral phase with 80-90 vol%. The lath-shaped crystals with sizes up to 5 mm form a loose framework (Figure 53). Straight grain boundaries only occur adjacent to the "empty" miarolithic cavities (Figure 53a). In most cases, however, the grain boundaries of the sanidine crystals are not well-defined showing clear signs of resorption. They are typically surrounded by a bubble-rich glass (melt) film (Figure 53f). The resulting loose and partially interrupted connection between the sanidine crystals is obviously the cause for a reduced mechanical strength of these sanidinites. As shown in Figures 53f and g, in one sample two different types of glass can be distinguished: the one glass appears light grey in BSE-image, the other glass appears dark grey comparable to sanidine (Figures 53f and g). Needle shaped clinopyroxene crystals occur frequently within the light grey glass. Occasionally these needles form even rims between the sanidine crystal and glass (Figures 53f and g).

Haüyne reaches sizes up to 5 mm and occurs always in the pore spaces in between the sanidine crystals (Figures 53b and d). These crystals often show rounded crystal shapes (Figure 53d) surrounded by a thin film of vesicle rich glass (melt). **Plagioclase** is less abundant and occurs mainly next to haüyne or intergrown with it. In these rocks, the proportion of plagioclase + haüyne is normally less than 15 vol%. Subordinate clinopyroxene, biotite and amphibole occur. The accessory phases apatite, magnetite and titanite (Figure 53e) expose both, euhedral and rounded crystal shapes and are often surrounded by glass (see e.g. apatite in Figures 53f and g). In dark haüyne-sanidinite, euhedral **apatite** crystals with sizes up to several hundred microns occur.

In general, the mineral phases of haüyne-sanidinites are mostly free of mineral inclusions. The rare mineral inclusions in sanidine are apatite, magnetite or titanite. Few melt-inclusions occur in sanidine, biotite, clinopyroxene, magnetite and titanite (e.g. Figure 53e). In bright haüyne-sanidinite mineral phases such as sanidine, haüyne, biotite, titanite, and to a lesser extent plagioclase, occasionally contain ellipsoidal holes. In addition, some haüyne crystals of bright haüyne-sanidinite contain fluid-inclusions (FI). Raman Spectroscopy revealed that these FI contain pure CO_2 vapor.

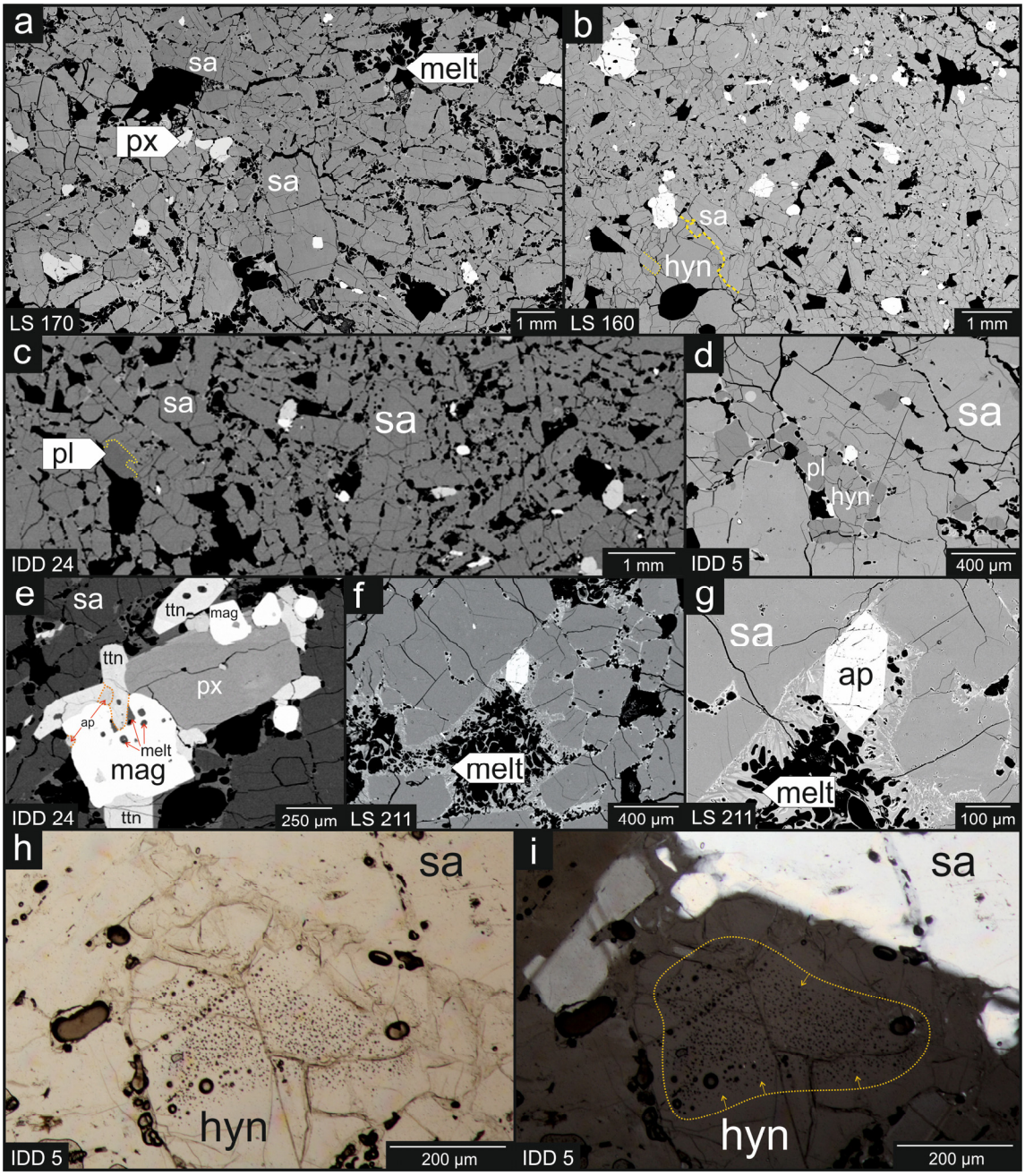

Figure 53: Microscopic pictures of haüyne-sanidinite: a-b) lose framework of sanidine laths with vesicle-rich interstitial glass, d) resorbed haüyne-crystal adjacent to plagioclase between sanidine crystals, e) mineral assemblage of pyroxene, magnetite, titanite and apatite; magnetite and titanite with melt inclusions, f-g) apatite crystal in a cavity between resorbed sanidine crystals; interstitial glass with two gray scales; it is rich in vesicles and contains small clinopyroxene needles, h-i) haüyne crystals with abundant CO_2-inclusions marked by the dashed line

4.3.2.2 NOSEAN-SANIDINITE

The majority of the nosean-sanidinite samples is holocrystalline and exhibits abundant cavities created by an interlocked framework of sanidine and nosean crystals (Figure 54). Sanidine is the main constituent of these nodules, even though the proportion of 50-70 vol% is lower than in haüyne-sanidinite. The proportion of the sodalite-group minerals (**nosean**) varies greatly and is with 20-40 vol% much higher compared to haüyne-sanidinite. Within the cavities, crystals such as nosean, calcite and high-field strength element containing minerals are present (Figure 54). Calcite occurs in between the sanidine crystals of the nosean-sanidinites. Its proportion varies from zero to 20 vol%, with calcite occasionally being the third abundant mineral after sanidine and nosean (Figure 54c).

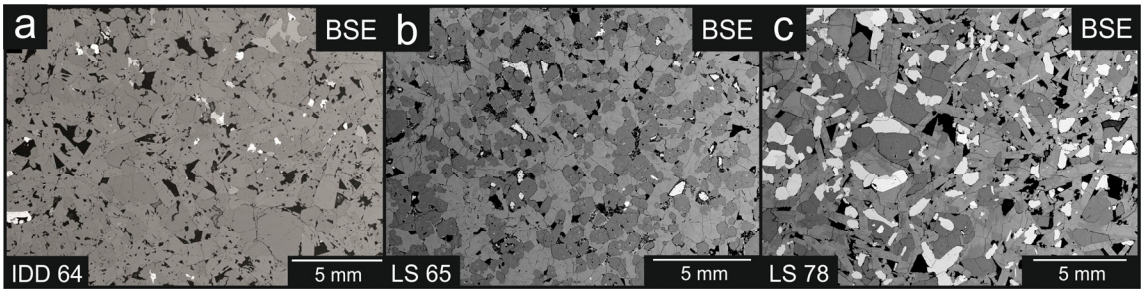

Figure 54: Overview BSE images showing the structure of nosean-sanidinite; light grey = carbonate, middle grey = sanidine, dark grey = nosean; a) interlocking framework of sanidine laths and nosean, in between abundant cavities with only a view carbonate crystals, b) nosean-rich variety of nosean-sanidinite with minor carbonate and c) nosean-sanidinite with higher proportion of carbonates but still abundant cavities

In detail, nosean-sanidinite contains two types of sanidine. **SAN-1** laths have a size of up to 5 mm with either straight (euhedral), jagged or lobed grain boundaries (Figure 55). Remarkable is the orientation of the jagged grain boundaries since they often appear only on one side of the sanidine laths, while on the other side, the grain boundary remains unchanged. In total, it gives the impression of a windward/leeward effect (Figure 55b). SAN-1 is often associated with the second type of sanidine (SAN-2) but has a distinct composition. In BSE image, SAN-2 shows different shade of grey and a higher porosity (Figure 55b). The pores occur preferentially at the interface of these two types of sanidine. In SAN-1, holes are abundant (Figures 55c-d). The smaller holes are mostly angular, sometimes elongated and occur preferentially along the cleavage planes or as tiny round holes in the outermost rims of the SAN-1 crystals. Bigger holes (several tens of microns in size) are anhedral with round or lobate boundaries and occur often along cracks and veins (Figures 55c and d). All holes are either empty or filled with calcite and partly with zircon (Figures 55c and d). SAN-1 shows often deep dissolution embayments, which are mostly filled with calcite (Figure 55e). **SAN-2** occurs also radially arranged or as bundles of skeletal crystals in between the nosean crystals giving the shape of a frond and filling the cavities (Figure 55f). This type of sanidine shows no holes or dissolution textures. **Glass** (melt) is rare and if present, always rich in vesicles. In one sample (LS113), some of the vesicles contain calcite crystals.

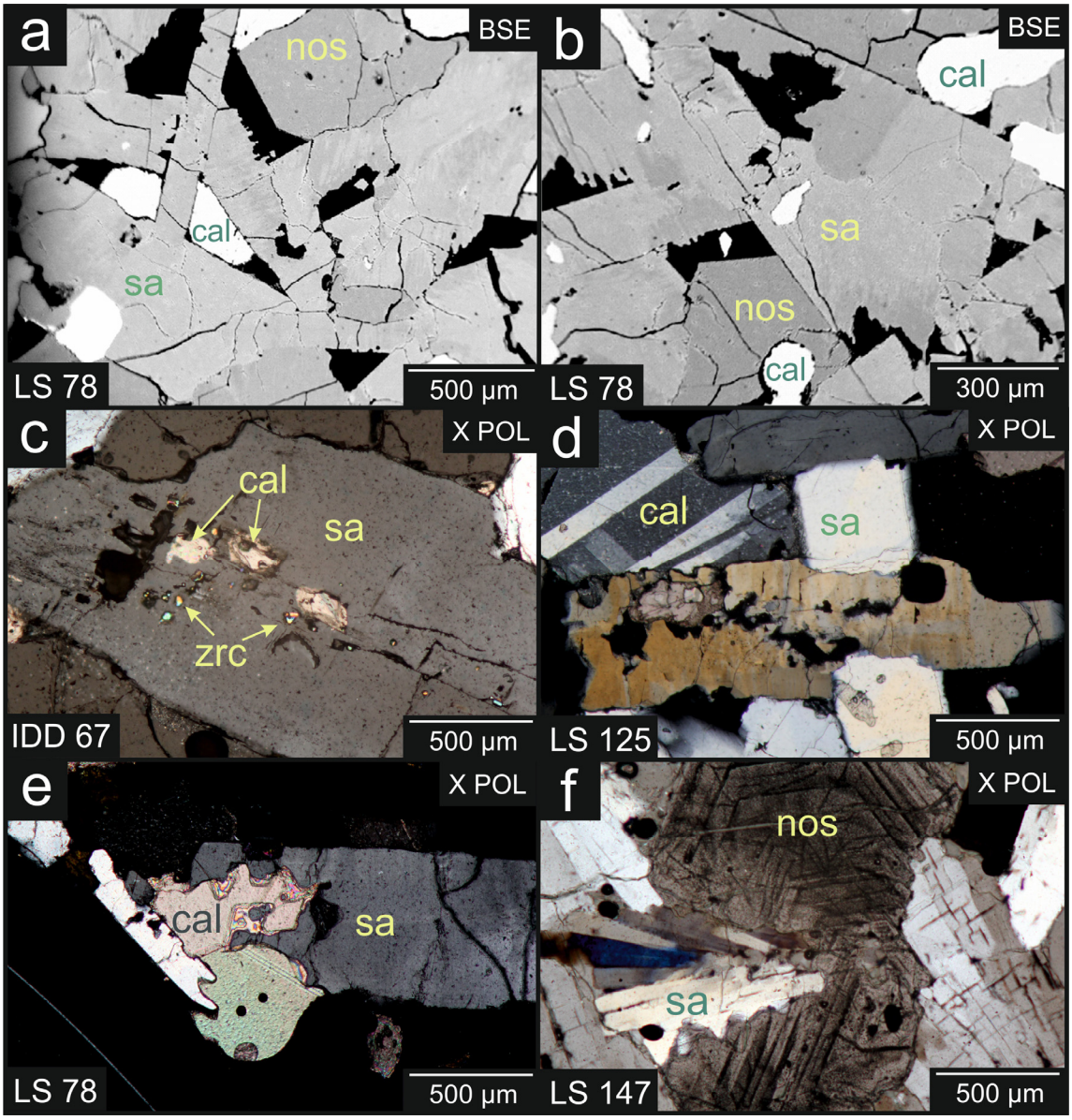

Figure 55: Microscopic pictures showing the different textures of sanidine (sa) in nosean-sanidinite, a) interlocked SAN-1 laths with straight grain boundaries on one side and jagged grain boundaries on the other side, and calcite (cal) growing in the cavities formed by the sanidine laths, b) SAN-1 crystals with jagged grain boundaries and differently composed sanidine (SAN-2) only at one side of the crystal (windward/leeward effect), c) SAN-1 with irregular shaped holes partly filled with calcite and zircon (zrc), d) strongly corroded sanidine crystal with jagged surfaces partly filled with calcite, e) SAN-1 crystal with deep dissolution embayments filled with calcite and f) bunch of SAN-2 crystals adjacent to a nosean crystal with dissolved surfaces

There are also two different types of nosean: **NOS-1** crystals are typically intergrown with sanidine. The size of the euhedral to anhedral crystals ranges up to several millimeters. Characteristic for the nosean crystals are the enormous number of CO_2-inclusions. Raman spectroscopy revealed that the fluid inclusions are pure CO_2 vapor inclusions (see “sodalite group” in the chapter 5.4.3). These inclusions are often concentrically arranged (Figure 56a) or occur evenly distributed throughout the whole crystal (Figure 56b). These inclusions are mostly two-phase-inclusions with a silica melt surrounding one or more CO_2-vapor bubbles (Figure 56b). Towards the rims, abundant fine sized pure CO_2 vapor bubbles dominate. These CO_2-inclusions are most likely responsible for the grey color of the nosean crystals. Some of the crystals contain such a high amount of CO_2-inclusions that they

appear almost black in thin section even with parallel polarizers (Figure 56a). Fe-sulfide inclusions are also very common in nosean (Figures 56c and d). They are either restricted to the core area of the crystals or are concentrated along the rim area of the nosean crystals (Figure 56d) or both (Figure 56c). Holes with sizes up to 300 µm occur often in nosean (Figure 56b). They have always a rounded and often oval shape, connected by veins or cracks (Figure 56b). These holes and veins are either empty or filled by calcite (see Figure 57b) or occasionally by zircon. In contrast, **NOS-2** is mostly free of CO_2-inclusions and occurs as euhedral crystals within the miarolithic cavities or fills them completely (Figure 56f).

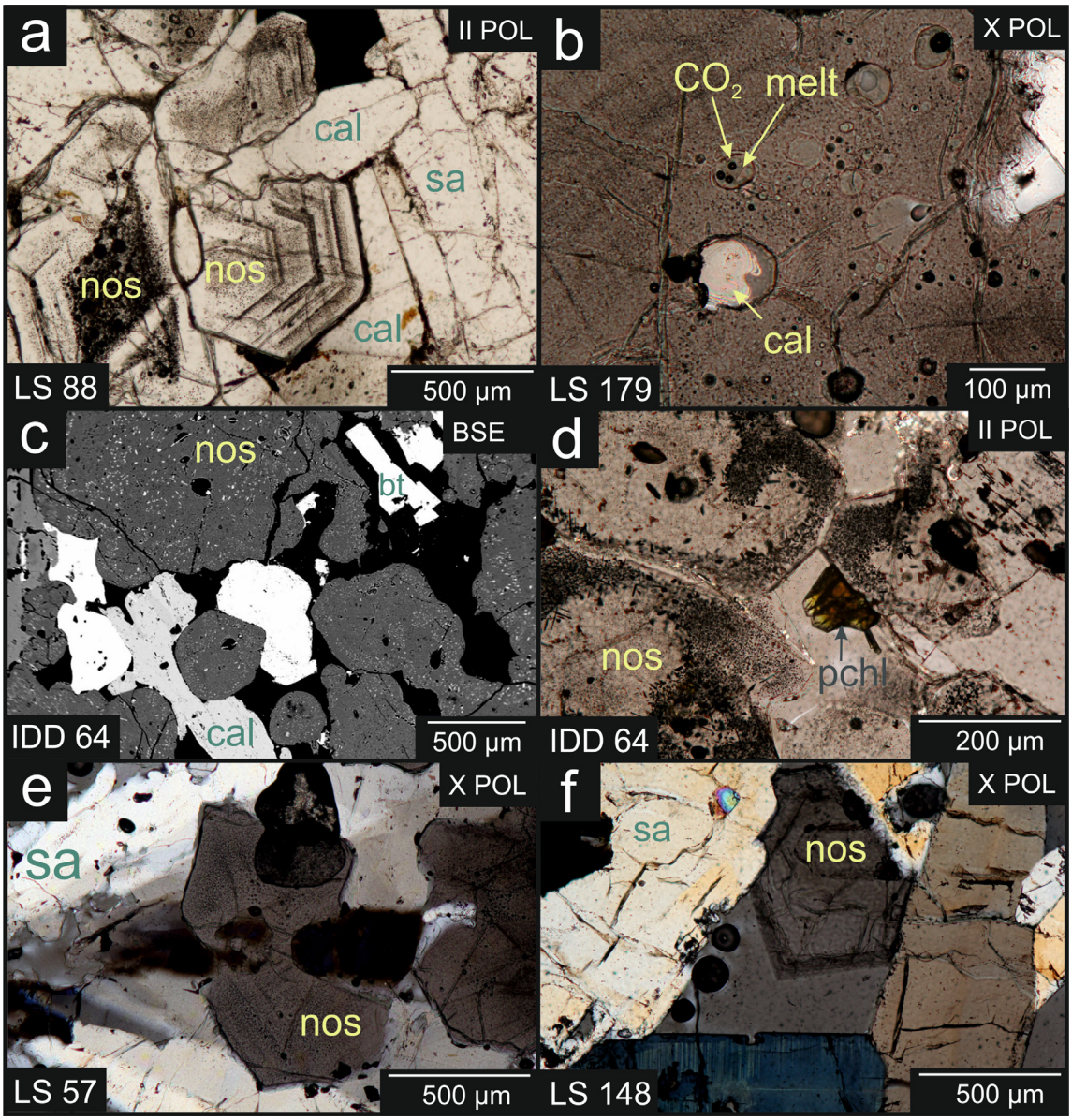

Figure 56: Microscopic pictures showing the different textures of nosean (nos) in nosean-sanidinite a) NOS-1 with abundant concentrically arranged CO_2 ± melt inclusions, b) NOS-1 with abundant tiny CO_2-inclusions, and bigger CO_2 + melt inclusions, bigger inclusions are connected via fluid veins and sometimes filled with calcite (cal), c) NOS-1 with Fe-sulfide inclusions in the core and Fe-sulfide rims mimicking the shape of the roundly dissolved crystal surfaces, calcite (cal) and biotite (bt) growing in the cavities between the nosean crystals, d) NOS-1 with Fe-sulfide rims mimicking the shape of the roundly dissolved crystal surfaces and a pyrochlore crystal (pchl) projecting into the empty pore space between the nosean crystals, e) NOS-1 with dissolution surfaces surrounded by feathery SAN-2 crystals (sa), f) euhedral NOS-2 crystals in a cavity between SAN-1 laths

Calcite is widespread in most of the nosean-sanidinite samples, but is not present in all of them. In some samples, calcite has a fine rim of Mn-rich carbonate (rhodocrosite). Calcite occurs mainly within the cavities (see Figures 55a, 57a and b), partly filling them completely (Figure 57b). These calcite crystals have often serrated grain boundaries (Figure 57a), but they can also occur as euhedral or ball like crystals. They are often observed next to lobate or jagged grain boundaries of silicates, specifically SAN-1 (see Figures 55e, 57c and e), NOS-1 or ZRC-1 (see Figure 58a). Therefore, it often seems as if calcite is replacing dissolved areas of these minerals. Correspondingly, calcite occurs often as fillings of the holes of SAN-1 (Figures 55c and d), NOS-1 (Figure 56b), or pores or dissolved areas of ZRC-2.

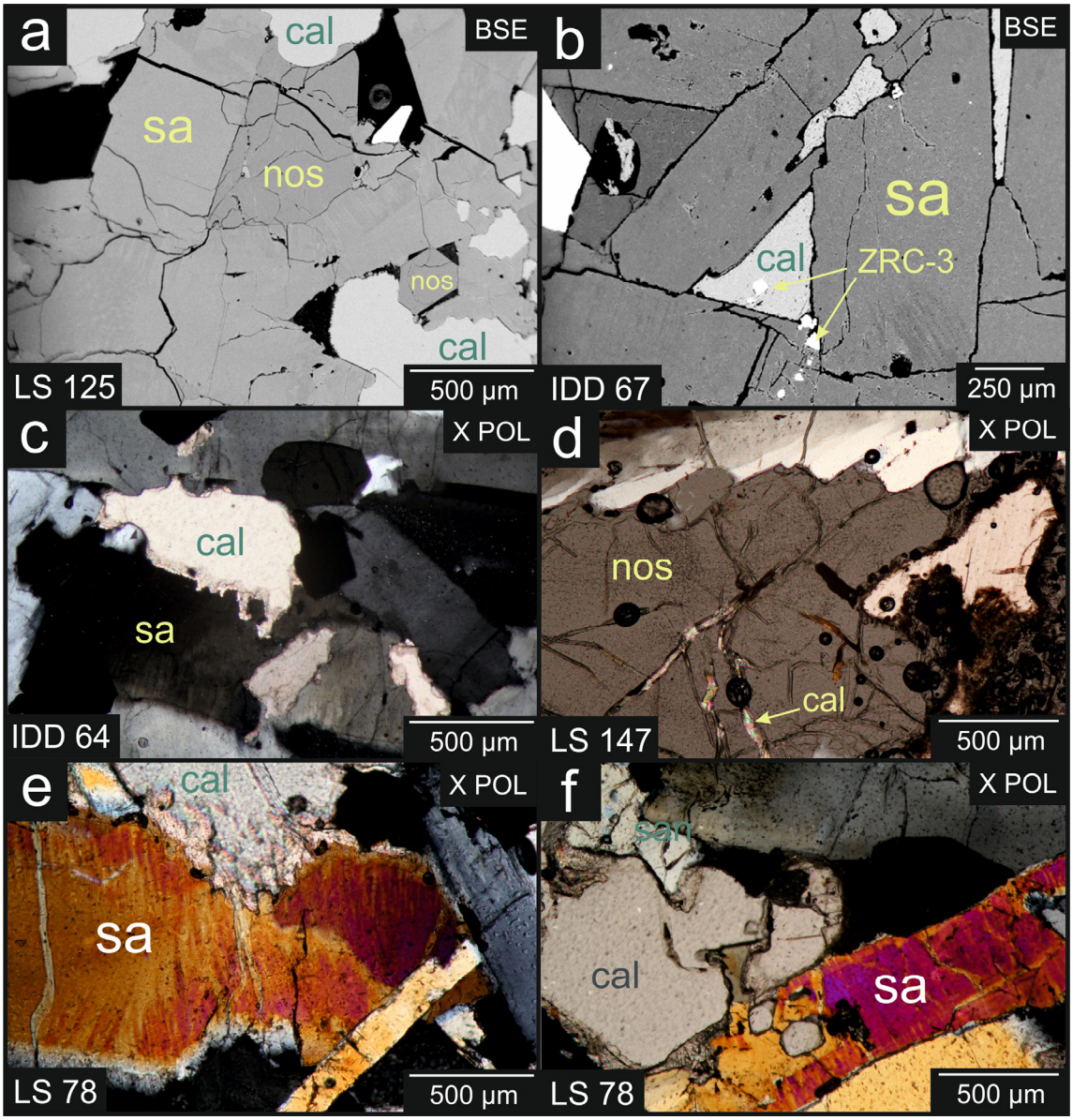

Figure 57: Microscopic pictures showing the different textures of calcite (cal) together with sanidine (sa) and nosean (nos) in nosean-sanidinite, a) SAN-1 laths forming cavities filled with NOS-2 and calcite with serrated grain boundaries, b) cavity formed by SAN-1 laths completely filled with calcite, c) SAN-1 with jagged grain boundary adjacent to calcite, d) NOS-1 with tiny CO_2-inclusions penetrated by fluid veins, partially filled with calcite; note: bigger black bubbles are artificial bubbles in the epoxy-raisin from thin section preparation, e) SAN-1 with dissolution features and (pseudo) perthitic lamellae and jagged grain boundary adjacent to calcite, f) SAN-1 with dissolution holes along a crack filled with calcite

Mafic phases such as clinopyroxene and biotite are rare in nosean-sanidinite. Clinopyroxene occurs as euhedral crystals within the miarolithic cavities or as anhedral filling of the space between sanidine and nosean. Biotite occurs within the cavities and adjacent or intergrown with sanidine or calcite.

Zircon occurs in all investigated nosean-sanidinites. Three major types of zircon occur (Figure 58). **ZRC-1** is a mostly oscillatory or sometimes patchy zoned zircon (Figure 58b) and contains occasionally silicate melt inclusions. It shows strong signs of resorption preferentially along cracks and fissures (Figures 58a and b) or preferentially along bright zones in BSE-image (see Figure 58b), which often results in deep dissolution embayments (Figures 58a and b). **ZRC-2** appears in the dissolved areas of ZRC-1, partly completely replacing it (Figure 58). Characteristic for ZRC-2 is its high porosity, the lack of zoning and the occurrence of thorite inclusions. The pores host sometimes pyrochlore and occasionally calcite. ZRC-2 also forms individual crystals, preferentially in cavities and along grain boundaries (Figure 58c). **ZRC-3** represents euhedral bipyramidal crystals growing along cracks and fluid veins or in pores in SAN-1 or NOS-1 (Figures 58d and e). These crystals occur often together with calcite and or pyrochlore (Figure 58) as well as at the interface between calcite and silicates.

Characteristic for nosean-sanidinite is the crystallization of manifold **high field strength element (HFSE) minerals**, including zircon ($ZrSiO_4$), baddeleyite (ZrO_2), pyrochlore ($Ca_2Nb_2O_7$), REE-apatite, thorite ($(Th,U)[SiO_4]$), allanite ($(CaREE)(Al_2Fe^{II})(Si_3O_{11})O(OH)$), monazite ($(Ce,La,Nd,Th)(PO_4,SiO_4)$) among others. **Pyrochlore** often occurs next to zircon and or calcite (Figure 58d), but it was also observed as individual euhedral crystals within the cavities. Baddeleyite occurs often together with zircon (ZRC-2). It was also observed as micro-crystals in a bubble enclosed in nosean. Occasionally, euhedral baddeleyite crystals were found, projecting into empty cavities between SAN-1 laths (Figure 58f).

In nosean-sanidinite two chemically distinct types of **apatite** occur. Apatite sensu strictu, comparable to apatite in haüyne-sanidinite, and REE-apatite (britholite-group). Apatit has always rounded, resorbed surfaces and occurs as relicts between the SAN-1 crystals. Britholite, however, occurs always as euhedral crystal within the cavities formed by the SAN-1 laths.

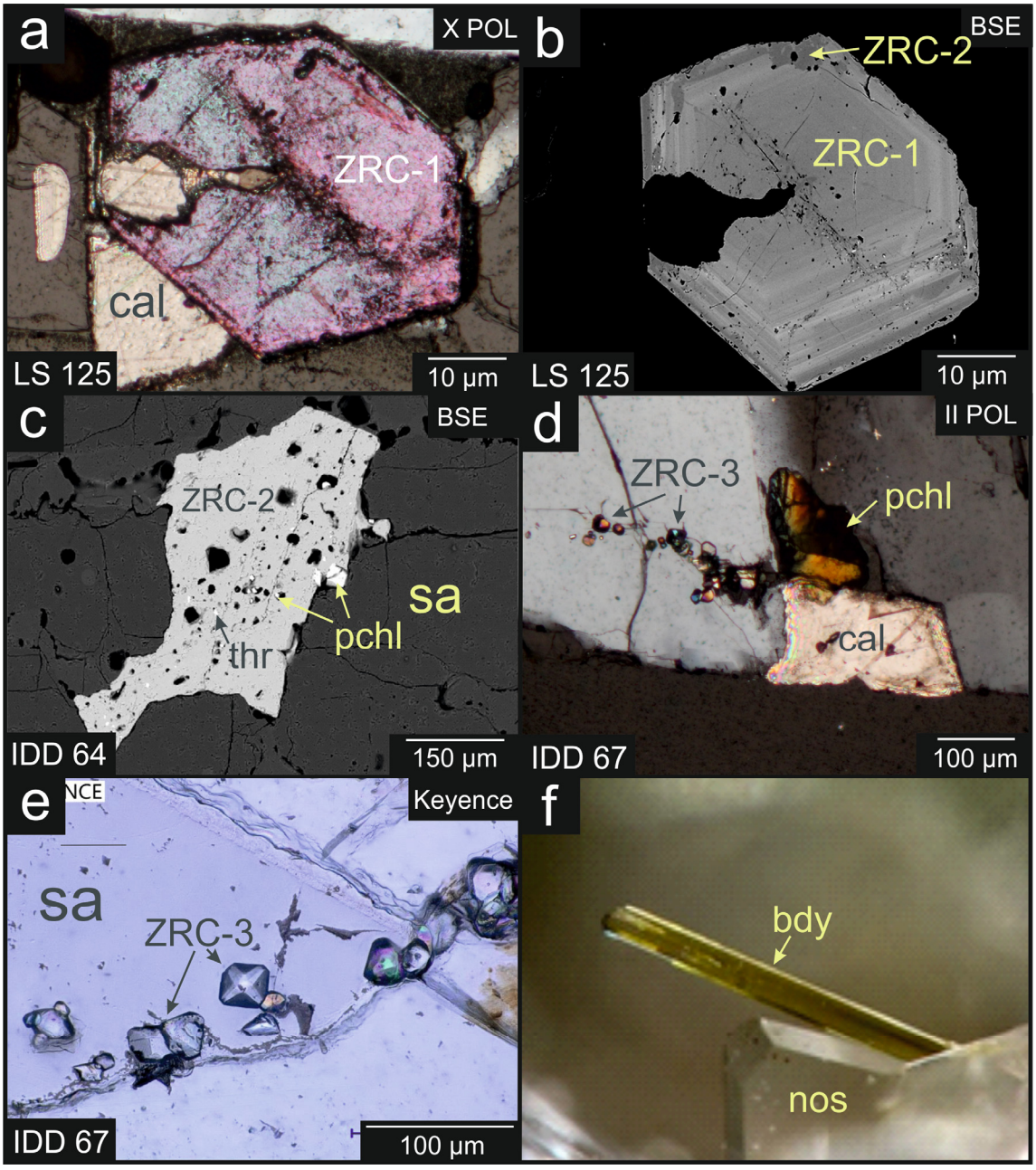

Figure 58: Microscopic pictures showing the different textures of zircon (zrc), pyrochlore (pchl) and baddeleyite (bdy) in nosean-sanidinite; a and b) euhedral ZRC-1 crystals showing preferential dissolution along cracks. It shows deep dissolution embayments partly replaced by calcite and porous ZRC-2, c) Individual porous ZRC-2 crystal in between dissolved sanidine crystals with pyrochlore and thorite inclusions, d) mineral assemblage of calcite and pyrochlore filling up the cavities in SAN-1 together with euhedral bipyramids of ZRC-3 crystals growing along cracks in SAN-1, e) euhedral bipyramids of ZRC-3 crystals along a crack in SAN-1 f) euhedral baddeleyite and nosean crystal growing in an otherwise empty cavity between SAN-1 laths (Photo: Christian Rewitzer)

4.3.3 MINERAL CHEMISTRY

Sanidine, sodalite-group minerals, biotite, clinopyroxene, amphibole and magnetite occur in all investigated rock types. Electron microprobe analyses (EMPA) yielded a systematic chemical change in the mineral chemistry from dark haüyne-sanidinite over bright haüyne-sanidinite to nosean-sanidinite. Representative microchemical analysis are provided in Table A20-34 in appendix A-2b.

4.3.3.1 FELDSPAR

Two types of **feldspar** occur in the investigated rocks: sanidine, which is the main constituent in all rocks, and plagioclase, which is restricted to haüyne-sanidinite. The analysis of feldspar shows a characteristic change in chemical composition. The Ca content decreases systematically from dark haüyne-sanidinite (An_{3-15} in sanidine, An_{22-24} in plagioclase), over bright haüyne-sanidinite (An_{1-6} in sanidine, An_{12-15} in plagioclase) to nosean-sanidinite (An_{0-2} in sanidine). The ternary diagram in Figure 59a shows that the analyses plot on three different isopleths depending on type of rock. Sanidine of the different rock types differs also in its texture: sanidine in dark haüyne-sanidinite shows no zoning, whereas sanidine in bright haüyne-sanidinite is zoned with Or-rich cores and Ab-rich rims. Sanidine in nosean-sanidinite has the lowest Ca content. In nosean-sanidinite, the sanidine crystals expose often textures similar to perthitic exsolutions or a patchy zoning with Na- and Ca-rich sections and K-rich zones. The transsect in Figure 59b shows that the core of SAN-1 has higher Na- and Ca-concentrations, while SAN-2 is Ca-poor and K-rich. In the BSE image, the gray shade reflects directly the differences in the Ab and Or components due to the low An component in sanidine.

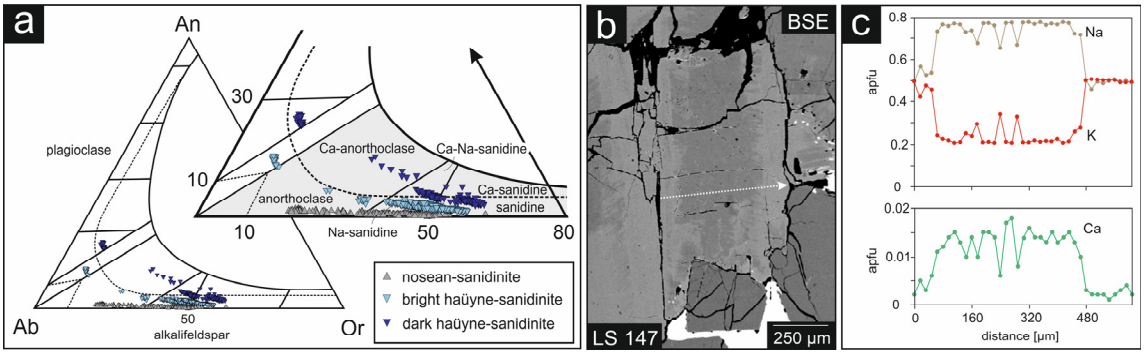

Figure 59: a) Feldspar diagram showing the chemical composition of sanidine and plagioclase of the three different types of Laacher See sanidinites b) BSE image showing a zoned sanidine crystal from a nosean-sanidinite. The white arrow marks the position of the transsect, c) chemical variation along a transsect through a feldspar in a nosean-sanidinite with An and Ab rich SAN-1 in the core and Or rich SAN-2 in the rims

4.3.3.2 SODALITE GROUP

The **sodalite group** comprises the end-members sodalite ($Na_8[Al_6Si_6O_{24}]Cl_2$), nosean ($Na_8[Al_6Si_6O_{24}]SO_4 \cdot H_2O$), haüyne ($Na_6Ca_2$ $[Al_6Si_6O_{24}](SO_4)_2$) and lazurite (Na_6Ca_2 $[Al_6Si_6O_{24}]S_2$). The composition of the sodalite-group minerals differs clearly in the different investigated rock types (Figure 60a): Haüyne in dark haüyne-sanidinite has the highest Ca contents: they plot clearly in the field of haüyne. In comparison, the sodalite-group minerals of bright haüyne-sanidinite have higher Na-contents. The analyses plot clearly in the field of nosean. To be consistent with literature about Laacher See eruption products and their blue appearance we keep the name "haüyne" for the sodalite group minerals in bright haüyne-sanidinite. In nosean-sanidinite the composition of the sodalite-group minerals are clearly Na-rich, classifying them as nosean.

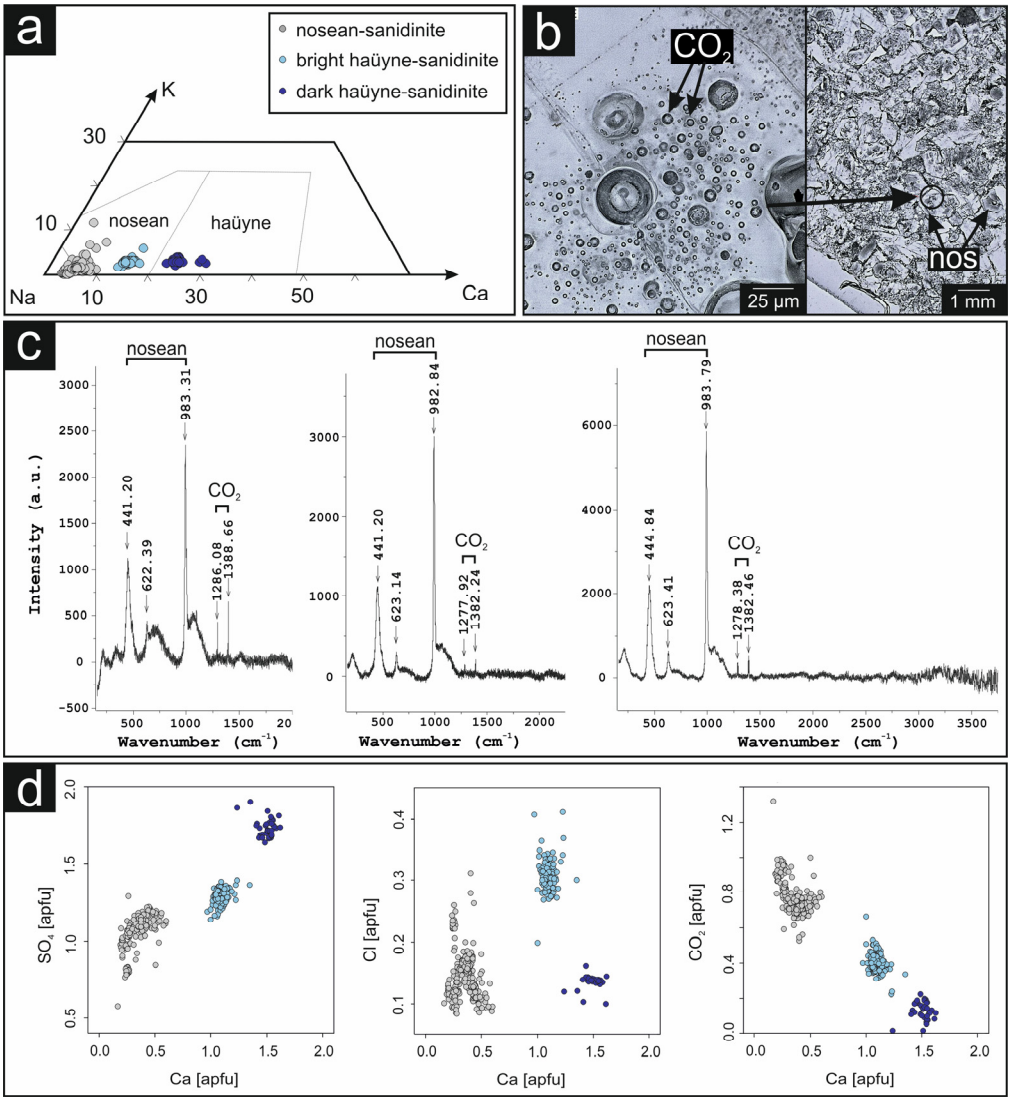

Figure 60: a) Sodalite mineral classification diagram after Lessing and Grout (1971) showing that only haüyne from dark haüyne-sanidinite can be classified as "haüyne" sensu stricto; the sodalite group minerals in bright haüyne-sanidinite and nosean-sanidinite have "nosean" composition. b) CO_2 ± melt inclusions in nosean crystals c) Raman spectra from three measuring points showing the composition of the entrapped bubble (CO_2) and the host (nosean); the raman spectrum on the right shows that nosean contains no structurally bound water. d) Variation diagrams showing the structurally bound volatile concentrations of SO_4, Cl and CO_2* against Ca-concentration in the sodalite group minerals; *CO_2 is calculated by the difference to the full position of 2 apfu

A remarkable feature of most nosean crystals in nosean-sanidinite and some haüyne crystals in bright haüyne-sanidinite are entrapped CO_2-inclusions (Figure 60b). Investigations by Raman Spectroscopy showed that the entrapped fluid inclusions consist of pure (low density) CO_2-vapor (Figure 60c). The Raman spectra of nosean from nosean-sanidinite in (Figure 60c) also confirmed that nosean is H_2O-free (Figure 60c, right), even though sodalite-group minerals are known to be able to incorporate H_2O in their cage-structure. Accordingly, the CO_2-content in the sodalite-group minerals could be estimated by calculating the difference of analyzed and calculated Cl and SO_3 in apfu from the maximum possible of 2 apfu. The volatile composition of the sodalite minerals differs also clearly (Figures 60c and d): The highest Cl-concentrations were measured in haüyne from bright haüyne-sanidinite. Haüyne in dark haüyne-sanidinite contains up to 1.6-1.9 apfu SO_4 compared to the lower values in bright haüyne-sanidinite (1.4-1.6 apfu) and in nosean of nosean-sanidinite (0.7-1.3 apfu). In consequence, nosean in nosean-sanidinite has the highest CO_2 content, intermediate concentrations in the bright haüyne-sanidinite and the lowest in dark haüyne-sanidinite.

4.3.3.3 CARBONATES

The majority of **carbonates** of Laacher See have calcite composition, with minor contents of FeO (up to 0.7 wt%) and MgO (< 0.5 wt%), but up to 3.6 wt% MnO (Figure 61). In addition, rhodochrosite occurs as thin rims around calcite or small grains along the grain boundaries of calcite. These grains, however, were too small for EMP analysis, but qualitative EDX-measurement proved their Mn-rich composition.

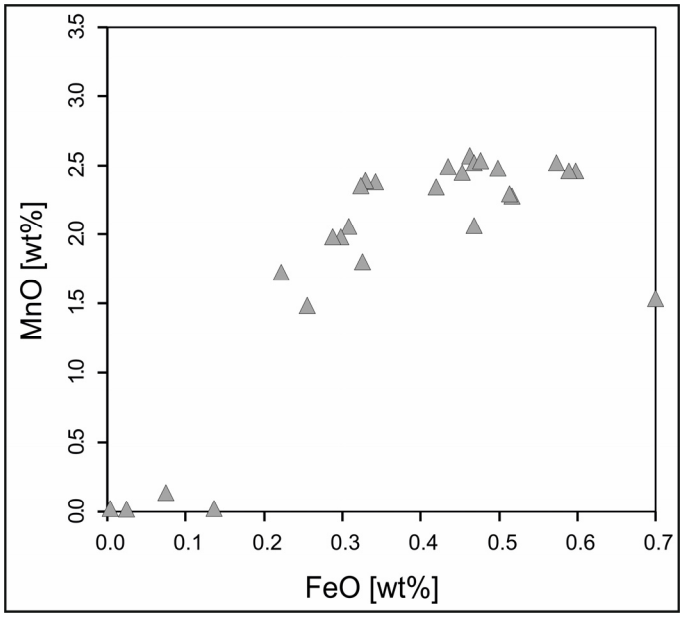

Figure 61: FeO-MnO diagram showing the chemical variation of the carbonates

4.3.3.4 CLINOPYROXENE AND BIOTITE

In sanidinites from Laacher See clinopyroxene is the only present pyroxene. In **haüyne-sanidinite**, clinopyroxene shows no zoning and has hedenbergite composition (Figure 62a). In detail, the chemical composition of hedenbergite in dark haüyne-sanidinite and bright haüyne-sanidinite differs significantly (Figure 62): in dark haüyne-sanidinite, the concentration of Ca, Mg and Ti is higher, whereas in bright haüyne-sanidinite clinopyroxene has a higher concentration of Fe and Mg. The composition of clinopyroxene in **nosean-sanidinite** differs completely from haüyne-sanidinite (Figures 62a and b): They were only plotted in the clinopyroxene triangle to show the deviation from clinopyroxene in haüyne-sanidinite. The closer look showed that clinopyroxene in nosean-sanidinite has unusual high MnO concentration up to 15.8 wt% (Figure 62b), which corresponds to up to 17 % of johannsenite component ($CaMnSi_2O_6$, see also Table A-27 in appendix A-2b).The crystals show an irregular zoning with widely varying concentrations of Mn, Ca, Ti and Na.

The composition of the rare **biotite** differs considerably in haüyne-sanidinite and nosean-sanidinite: in haüyne-sanidinite biotite is rich in Ti and Mg, while in nosean-sanidinite the concentrations of Fe and Mn are higher.

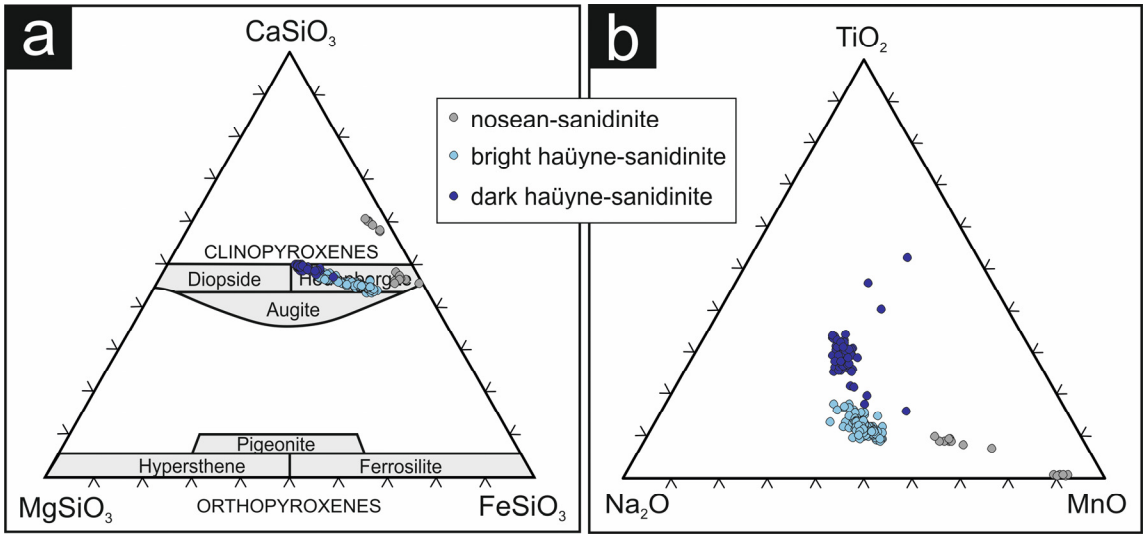

Figure 62: a) Ternary classification diagram after Morimoto et al. (1988) showing the chemical variation of clinopyroxene from the Laacher See sanidinites and b) Na_2O-TiO_2-MnO diagram showing the systematic trend in clinopyroxene composition from Ti-Na-rich compositions in dark haüyne-sanidinite towards Mn-rich composition in nosean-sanidinite

4.3.3.5 MAGNETITE

Magnetite occurs in all sanidinites and shows either no or irregular to patchy zoning. The composition of magnetite differs clearly in dark and bright haüyne-sanidinite and nosean-sanidinite. Al and Mn show a systematic trend from dark haüyne-sanidinite over bright haüyne-sanidinite to nosean-sanidinite (Figure 63a) with the highest Al_2O_3 concentrations in dark haüyne-sanidinite (1.60-1.86 wt%) and the lowest concentrations in nosean-sanidinite (< 0.5 wt%). The highest MnO concentrations shows magnetite in nosean-sanidinite (5.83-7.63 wt% MnO) and the lowest in dark haüyne-sanidinite (< 1 wt%). In dark haüyne-sanidinite, magnetite shows the highest concentrations of TiO_2 (11.01-11.79 wt%) whereas the contents in bright haüyne-sanidinite and nosean-sanidinite are generally < 7 wt%. In contrast, the ZnO concentrations of dark haüyne-sanidinite and bright haüyne-sanidinite are in a comparable range, with a maximal value of 0.50 wt% in bright haüyne-sanidinite. In comparison, the ZnO concentration in nosean-sanidinite is generally higher ranging from 0.39 to 0.79 wt% (Figure 63b).

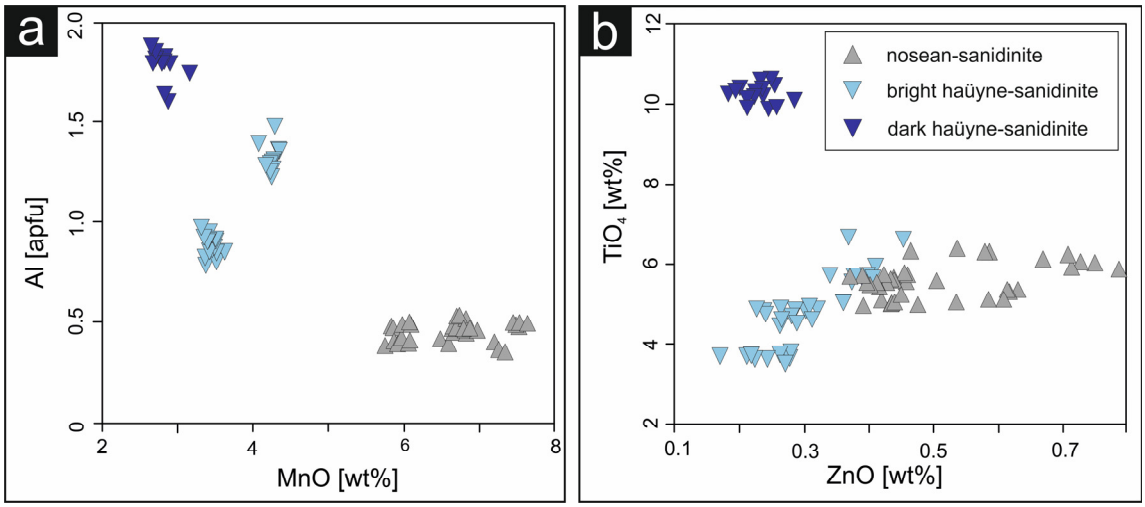

Figure 63: Diagrams showing the variation of a) Al_2O_3 and MnO and b) TiO_2 and ZnO of magnetite

4.3.3.6 TITANITE

Titanite occurs also in all types of sanidinites. It contains variable amounts of Nb_2O_3, ranging between 1.2 and 3.8 wt% (Figure 64). Titanite in nosean-sanidinite and haüyne-sanidinite shows systematic differences in MnO, FeO, ZrO_2 and LREE. In detail, the MnO and FeO contents of the titanite in nosean-sanidinite are slightly higher, compared to haüyne-sanidinite. Titanite in nosean-sanidinite has low ZrO_2 concentrations < 0.4 wt% as well as low concentrations in LREE (< 0.02 wt% La_2O_3). In haüyne-sanidinite, both Zr (0.4-1.5 wt%) and LREE (0.03-0.08 wt% La_2O_3) are clearly higher (Figure 64).

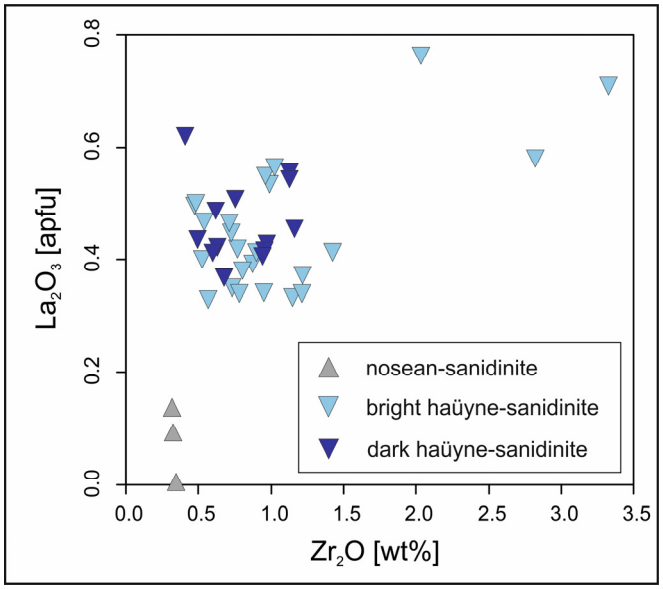

Figure 64: Diagram showing the variation of ZrO_2 and La_2O_3 of titanite

4.3.3.7 APATITE

Apatite occurs predominantly in haüyne-sanidinite but occurs also occasionally in nosean-sanidinite. The microchemical profile from an apatite crystal from dark haüyne-sanidinite (Figure 65a) shows a rather constant F-content varying around 2 wt% (Figure 65b). SO_3, Cl and Na_2O concentrations show a zoning with high concentrations in the core and decreasing concentrations towards the rims. The comparison of the apatite compositions showed that the concentration of SO_3 (and Cl) in apatite decreases from dark haüyne-sanidinite over bright haüyne-sanidinite to nosean-sanidinite (Figure 65b). The Na_2O concentration decrease also from dark haüyne-sanidinite to bright haüyne-sanidinite, but shows slightly elevated values in nosean-sanidinite.

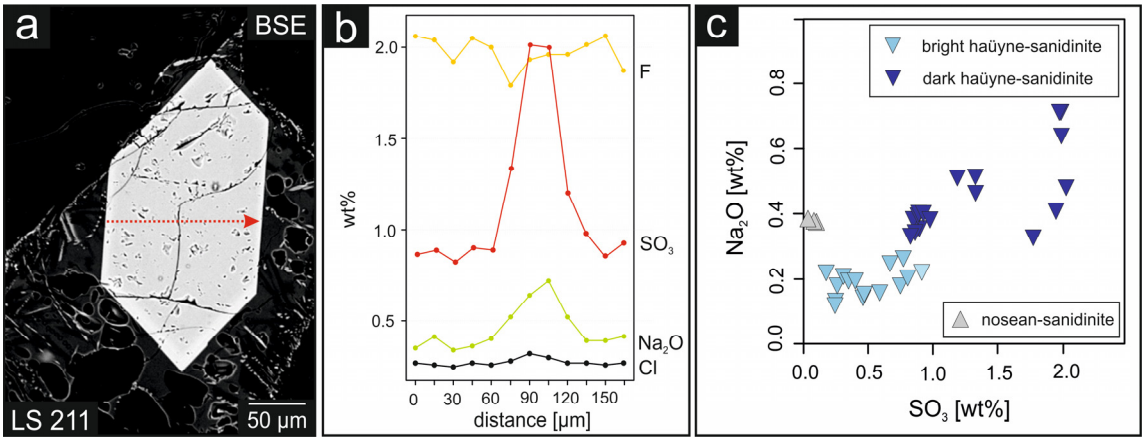

Figure 65: a) Euhedral apatite crystal in dark haüyne-sanidinite; the red arrow marks the position and direction of the transsect, b) transsect showing the chemical variation from along the profile, c) diagram showing the chemical variation of Na_2O and SO_3 in apatite

4.3.3.8 ZIRCON, BADDELEYITE AND PYROCHLORE

Zircon, **baddeleyite** and **pyrochlore** occur only in nosean-sanidinite. Compared to BSE-image, photoluminescence (PL) maps of Sm and Dy applied to different zircon crystals of nosean-sanidinite show a significant difference in REE concentration in coexisting ZRC-1 and ZRC-2. **ZRC-1** exhibits mostly oscillatory zoning and is characterized by higher REE (e.g. up to 1.4 wt% Y_2O_3), ThO_2 (up to 3.0 wt%) and UO_2 (up to 0.22 wt%) compared to both, ZRC-2 and ZRC-3 (Figure 66). **ZRC-2** and **ZRC-3** are characterized by rather "pure" zircon composition with low concentrations in ThO_2, UO_2 and REE (Figure 66). PL-images show also the deep irregular dissolution of ZRC-1 replaced by ZRC-2 (Figure 66).

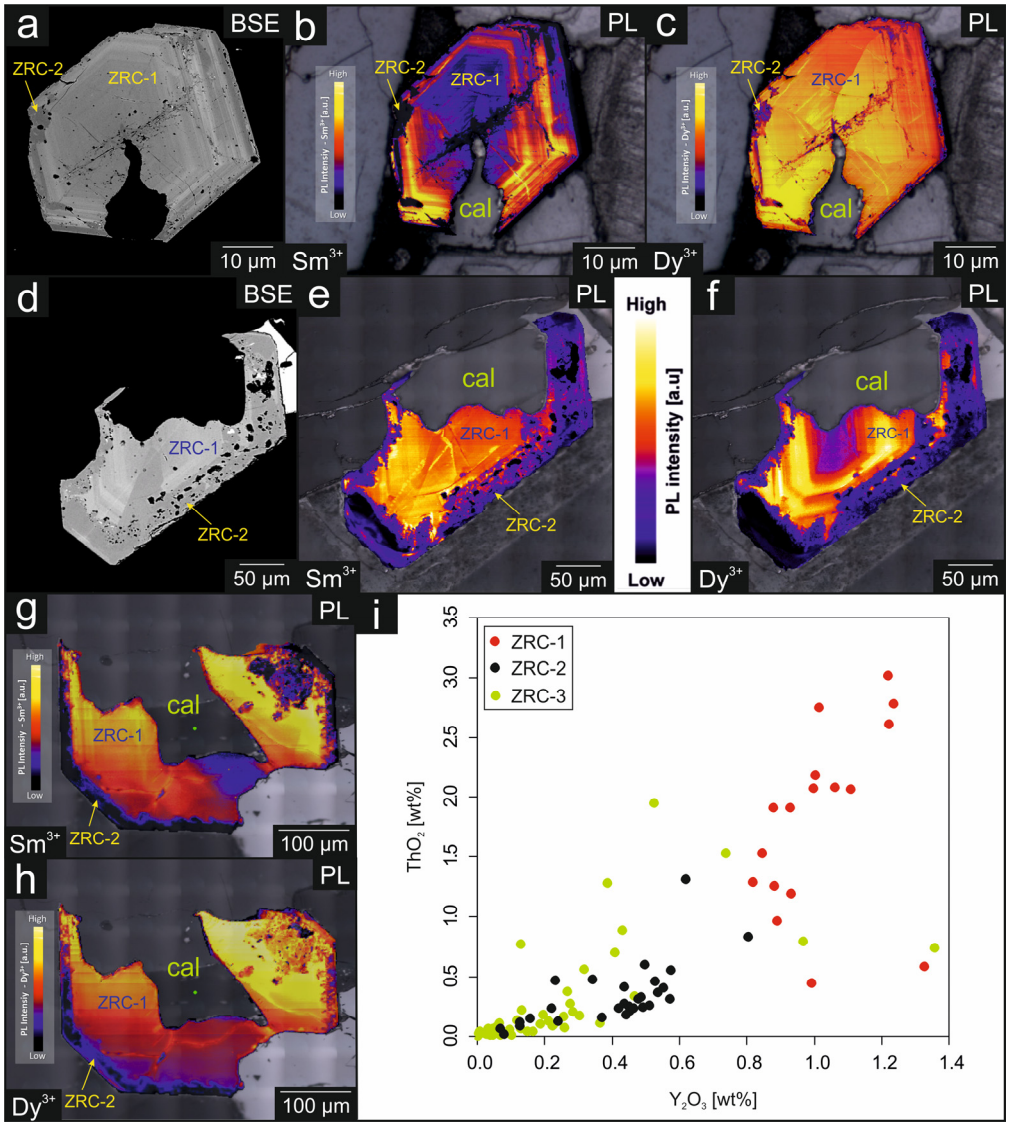

Figure 66: a and d) BSE-images and b, c, e-h) photoluminescence maps showing the chemical difference of ZRC-1 and ZRC-2. Yellow to red colors of ZRC-1 refer to high concentrations in Sm and Dy; ZRC-2 shows purple-blue color, which testifies low Sm and Dy concentrations. i) Diagram showing the variation of ThO_2 and Y_2O_3 of ZRC-1, ZRC-2 and ZRC-3

Baddeleyite (ZrO_2) is characterized by the absence of REE and Th (below the detection limit of EMPA) but notable high levels of Nb (up to 5.3 wt% Nb_2O_5), Ti , Fe and Mn. **Pyrochlore** shows often concentrically or oscillatory zoning and is characterized by unusually high concentrations of ZrO_2 (6.8 wt%) and REE_2O_3 (2.12 wt%). As shown in Figure 67, compared to HREE, the content of LREE is relatively enriched, with values ranging between 0-0.2 wt% $HREE_2O_3$ and 0.5-2.2 wt% $LREE_2O_3$, respectively.

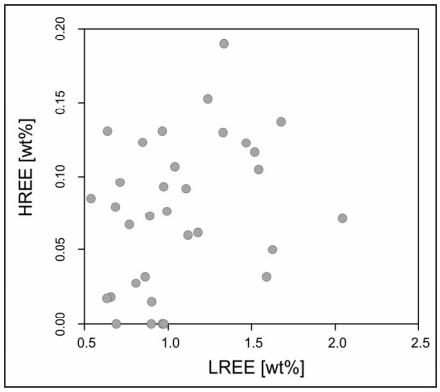

Figure 67: Diagram showing the chemical variation of HREE and LREE in pyrochlore

4.3.3.9 GLASS

In all types of sanidinite, mostly in haüyne-sanidinite and only occasionally also in nosean-sanidinite, vesicle-rich glass occurs adjacent to resorbed sanidine or haüyne, respectively. This type of glass has approximately feldspar composition (Figure 68a). Consistently to higher Ca-contents in sanidine and haüyne in haüyne-sanidinite, the Ca-contents in glass are also elevated. In nosean-sanidinite, glass adjacent to a resorbed Fe-oxide crystal shows elevated Fe-concentrations (Figure 68b). In haüyne-sanidinite, also glass with another composition occurs. This glass is generally comparable to sanidine, but with a higher content of Ti, Mg, Mn and Fe (Figure 68b).

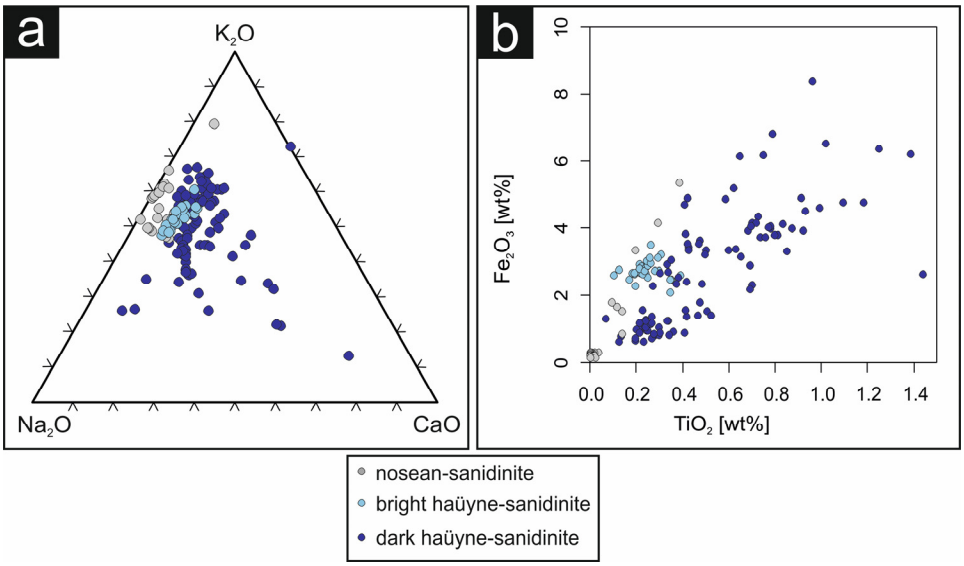

Figure 68: a) Ternary Na_2O-K_2O-CaO diagram and b) TiO_2-Fe_2O_3 diagram showing the chemical variation of interstitial glass in sanidinite

4.3.4 WHOLE-ROCK COMPOSITION

The whole-rock compositions of the investigated samples are listed in Table A3-A5 in appendix A-1b.The whole-rock composition of all investigated sanidinite samples varies between trachytic to phonolitic composition: The TAS diagram (Figures 69a and b) shows that dark and bright haüyne-sanidinite plot mainly in the field of trachyte, whereas nosean-sanidinite plot in the field of phonolite. The closer look at the Na_2O-K_2O-variation diagram shows that haüyne-sanidinite is characterized by higher K_2O-contents, whereas nosean-sanidinite shows higher Na_2O-concentrations (Figure 69c). The variation diagram in Figure 69d shows that in addition to the shift from K_2O-dominant composition in the haüyne-sanidinite to Na_2O in the nosean-sanidinite, the contents in nosean-sanidinite also increase towards higher CaO values. Notably, haüyne-sanidinite shows higher TiO_2 concentrations whereas the concentration in MnO is higher in nosean-sanidinite.

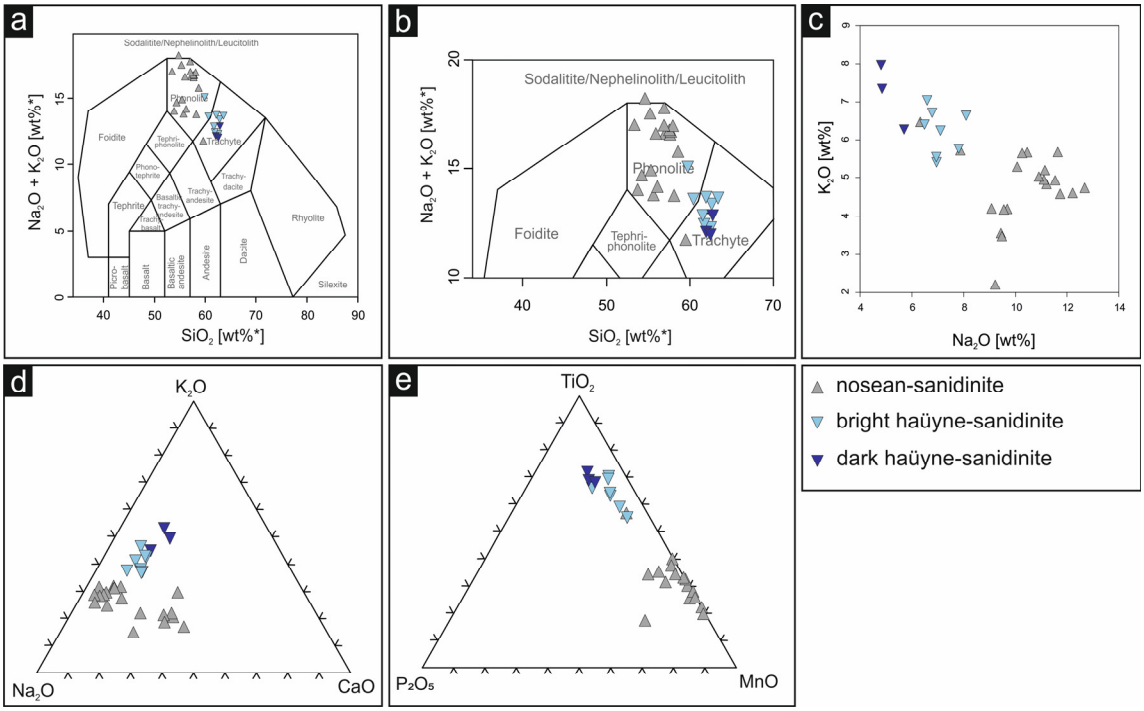

Figure 69: Whole-rock composition of the sanidinite samples of this study plotted in a-b) the TAS diagram after Middlemost (1994) on a volatile free basis [wt%*], c) a Na_2O-K_2O variation diagram d) Na_2O-K_2O-CaO diagram and e) a P_2O_5-TiO_2-MnO diagram

Figure 70 shows Harker diagrams of major, minor and trace elements. K_2O/Na_2O was chosen as x-axis as it shows the greatest variability (Figure 69c). SiO_2 and K_2O show a positive correlation with K_2O/Na_2O. Na_2O, SO_3, CO_2 and Cl as well as the trace elements Zr, Th, Hf and U show a negative correlation. The divalent elements Ca, Mn, Ce, La and Y, however, show a special trend. They show decreasing concentration from dark haüyne-sanidinite over bright haüyne-sanidinite towards carbonate-free nosean-sanidinite, but a strong enrichment in carbonate-bearing nosean-sanidinites (Figure 70).

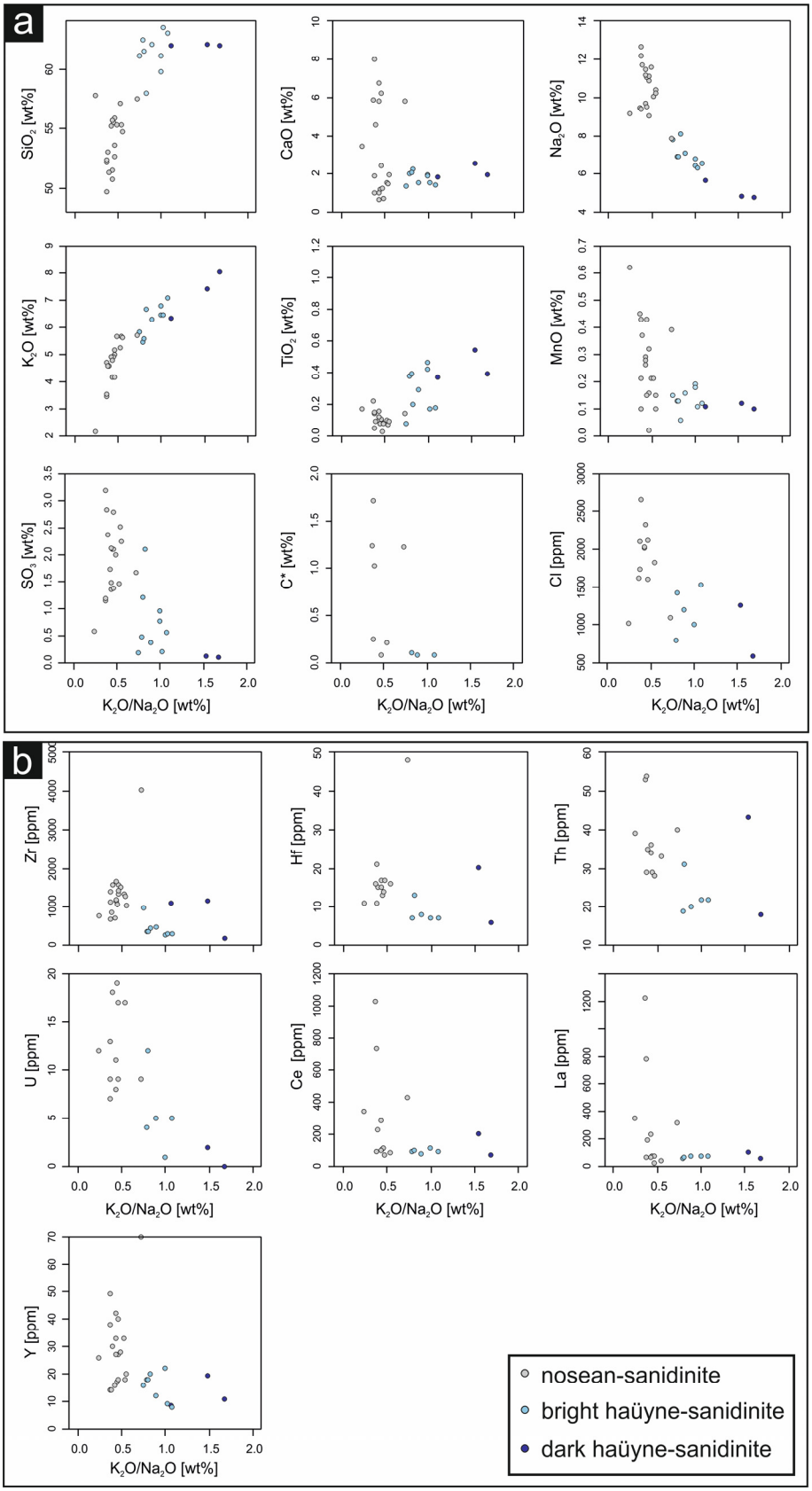

Figure 70: Harker diagrams of a) major and minor elements including the volatiles SO_4, Cl, and CO_2 (expressed as total carbon C*) and b) trace elements versus K_2O/Na_2O

4.3.5 SANIDINITES – SAME SAME, BUT DIFFERENT?

The typical feature of sanidinite is the magmatic cumulate texture of sanidine together with occurrence of two different types of sodalite-group minerals, either haüyne or nosean. On the first view, **nosean-sanidinite** seems to be just a holocrystalline variant of **haüyne-sanidinite**. The degree of crystallinity in sanidinite changes systematically. The glass proportion decreases from dark haüyne-sanidinite over bright haüyne-sanidinite to the holocrystalline nosean-sanidinite. The glass in haüyne-sanidinite has higher concentrations of Ti, Fe and Mg, which is indicative of a residual melt. If glass is present in nosean-sanidinite, it occurs as thin interstitial films, always rich in vesicles. The identical chemistry of this glass with that of sanidine suggests that they are caused by decompression melting.

The closer look reveals clear differences in whole-rock composition, mineral assemblage and mineral chemistry of haüyne-sanidinite and nosean-sanidinite. Their whole-rock composition differs clearly in major, minor and trace elements. The calculation of the enrichment and depletion factor according to Hildreth (1979) highlights the difference between haüyne-sanidinite and nosean-sanidinite. As shown in Figure 71, haüyne-sanidinite is more mafic, dominated by Mg, Ti, P, K, F, as well as Ba, Sr and V. In contrast, nosean-sanidinite is more felsic (Ca, Na dominated) and is enriched in elements with volatile property like Cl, SO_3 and CO_2 or in general LOI, in addition to the refractory elements including Zr, Th, Hf, REE, Mn.

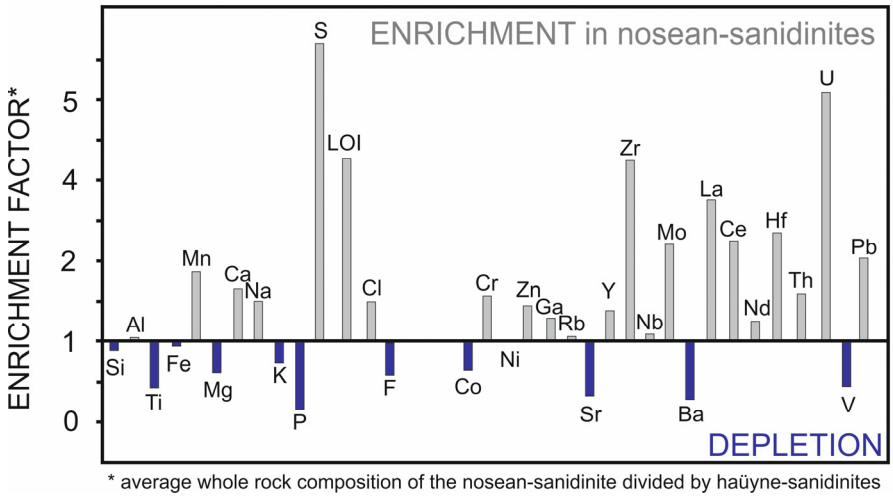

Figure 71: Enrichment and depletion factors for major, minor and trace elements of the Laacher See sanidinites, calculated after Hildreth (1979), by dividing the average composition of nosean-sanidinite by that of haüyne-sanidinite

The differences in whole-rock composition reflect the distinct mineral assemblages. In haüyne-sanidinite, silicates dominate and the only non-silicate mineral phases are the accessories magnetite and apatite. Remarkably, nosean-sanidinite has a higher proportion of non-silicate minerals. These are mainly carbonates (calcite and rhodochrosite), oxides (magnetite, pyrochlore, baddeleyite) and subordinate phosphates (REE apatite).

The look at the whole range of samples shows that there is a gradual change in whole-rock composition and mineral assemblage from haüyne-sanidinite to nosean-sanidinite. As shown in Figure 72, dark haüyne-sanidinite and carbonate bearing nosean-sanidinite represent “endmembers” of the sanidinites including the intermediate varieties bright haüyne-sanidinite and carbonate free nosean-sanidinite hybrids.

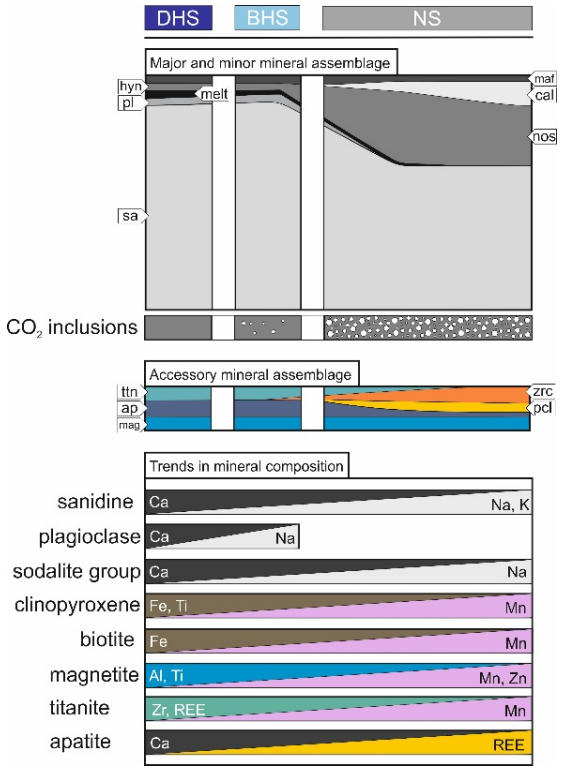

Figure 72: Major and minor mineral assemblage of sanidinites and trends of selected elements in the minerals compositions of sanidine, plagioclase, sodalite group, clinopyroxene and biotite

The **chemistry of the minerals** also shows a systematic change from dark haüyne-sanidinite over bright haüyne-sanidinite and carbonate-free nosean-sanidinite to carbonate bearing nosean-sanidinite (Figure 72):

The CaO concentration in the whole-rock composition decreases slightly from dark haüyne-sanidinite over bright haüyne-sanidinite to carbonate free nosean-sanidinite (see Figure 70). This corresponds also with the trend in glass (melt) content in the samples. Remarkable is that the whole-rock compositions of the nosean-sanidinite samples show an opposite trend, where the CaO-concentration increases from < 1 wt% in carbonate free nosean-sanidinite up to ~ 8 wt% in carbonate-bearing nosean-sanidinite (Figure 70). This correlates with increasing amount of calcite in the nosean-sanidinite samples. In silicates, decreasing Ca-content is compensated by increase in Na_2O, as shown by the minerals of the sodalite group, sanidine and plagioclase (Figure 72). In general, decreasing Ca-content in feldspar argues for decreasing temperature in the magma chamber.

The amount of **MnO** in the whole-rock composition decreases slightly from dark haüyne-sanidinite to bright haüyne-sanidinite, but is clearly elevated in nosean-sanidinite (see Figure 70). Calcite contains MnO up to 2-3 wt% and occasionally rhodochrosite was observed. Correspondingly, all **mafic minerals** (pyroxene, biotite and magnetite) show a systematic increase in MnO from dark haüyne-sanidinite to nosean-sanidinite. Following the general trend, in nosean sanidinite, the MnO content of magnetite and titanite and **ZnO** in magnetite are higher.

A remarkable trend show the **high-field strength elements (HFSE)**. In haüyne-sanidinite as well as in LS-tephra zircons are rare and titanite contains a higher amount of Zr. In nosean-sanidinite, however, the high number of HFSE-minerals such as zircon and pyrochlore correlates with their high concentrations in REE and Nb, which are also major components of pyrochlore. Apatite also has higher REE contents, indicated by the occurrence of the REE-apatite britholite. Titanite, however, shows a controversial trend for Zr, Nb and REE, as their content in titanite of nosean-sanidinite is much lower than in haüyne-sanidinite. This seems amazing, as the presence of

zircon and pyrochlore indicates an enrichment of these elements in nosean-sanidinite. This trend suggests a preferential incorporation of Zr, REE and Nb in zircon and pyrochlore in comparison to the syngenetic titanite. This means also an enrichment of the elements in nosean-sanidinite, since the concentration of Zr in LS-tephra and the haüyne-sanidinite was not saturated to allow the growth of zircons and therefore favored the incorporation of Zr in titanite.

Another aspect of volatile-bearing minerals in nosean-sanidinite compared to haüyne-sanidinite: the amount of nosean in nosean-sanidinites varies between 20 and 30 vol%, and of calcite up to 15 vol%. The increase in volatiles is also reflected in the increasing amount of CO_2-vapor inclusions from haüyne to nosean: In dark haüyne-sanidinite, they are completely absent, whereas in bright haüyne-sanidinite, CO_2-inclusions were entrapped frequently. In nosean-sanidinite, the nosean crystals contain huge amount of CO_2-inclusions. In sum, they clearly indicate a volatile saturated crystallization environment in nosean-sanidinite.

4.4 DISCUSSION OF THE RESULTS OF SANIDINITES FROM LAACHER SEE VOLCANO

4.4.1 SANIDINITES IN THE CONTEXT OF LAACHER SEE VOLCANO

The different types of sanidinite and carbonatite-bearing syenite are part of a wide spectrum of magmatic cumulates covering mafic (ultrabasic), intermediate and felsic (trachytic-phonolitic) compositions (Tait 1988). Nosean-sanidinite, however, was interpreted as carbonate-bearing syenite, representing a cognate magma body that intruded in the carapace of the magma chamber of Laacher See Volcano (Liebsch 1996; Schmitt et al. 2010). The contained carbonatite is explained by segregation from the highly evolved syenite/phonolite in the upper part of the magma chamber (Liebsch 1996). The mechanism of carbonatite formation, however, is still not understood (Schmitt et al. 2010). The similarity of the O- and C-isotopes of the carbonatites and the phonolite indicate a close relationship between the carbonate-bearing syenite and the phonolitic magma body (Liebsch 1996), although it remains puzzling how they are related.

In order to integrate the sanidinites into the context of the other erupted rocks of Laacher See Volcano and to identify their relationship, principle component analysis was applied to whole-rock compositions. In general, variation diagrams are used to visualize the chemical variation of mineral- and whole-rock compositions using either 2 or 3 axis dimensions, where each element or element group represents one dimension. More than three variables are, however, difficult to display in a multi-dimensional hyperspace. The Principal Component Analysis (PCA) is a method to summarize and to visualize all information of a multivariate data set. Based on linear combination of the original data, all important information are extracted and reduced to a new set of variables, represented by the principle components (PC). The major advantage of the PCA is the identification of the principle components (directions) of maximal data variation. This provides a graphical output a multivariate system in two or three dimensions without major loss of information. The number of principle components is always less or equal to the number of variables in the data set. Herein, the first five principle components (PC1-

PC5) cover approximately 87 % of the information of the data set. In general, PC1 axis (= the first principal direction) shows the largest variations of the samples, and PC2 the second most important variations.

The application of the principal component analysis to all whole-rock composition data of various eruption products from Laacher See shows Figure 73. Four clusters of major and minor elements can be identified which turned out to be characteristic for specific types of igneous rocks. Accordingly, four distinct clusters (I-IV) were distinguished:

- **Cluster I** comprises Fe_2O_3t, MgO, TiO_2 and P_2O_5. These elements represent the major chemistry of the group of mafic and intermediate cumulates.
- **Cluster II** covers SiO_2, Al_2O_3 and K_2O. Correspondingly, it represents the sanidine rich felsic cumulates (haüyne-sanidinite) and the LS-tephra.
- **Cluster III** covers the elements Na_2O, SO_4 in addition to LOI, as the sum of all volatiles. It coincides with the nosean-sanidinite, reflecting the high proportion of nosean.
- **Cluster IV** includes CaO, MnO and CO_2. It represents extremely carbonate-rich variants of the nosean-sanidinites (LS-carbonatites).

The clusters shown in Figure 73 describe a systematic change in chemistry. With PC2 (y-axis), the eruption products can be divided in two different groups. Tephra and cumulates, including haüyne-sanidinite, are dominated by the elements contained in Cluster I and II (SiO_2, Al_2O_3, K_2O and Fe_2O_3, MgO, TiO_2 and P_2O_5). Nosean-sanidinite including the LS-carbonatites show higher concentrations in the elements represented in Cluster III and IV (Na_2O, CaO and MnO in addition to LOI, including the volatiles CO_2 and SO_3).

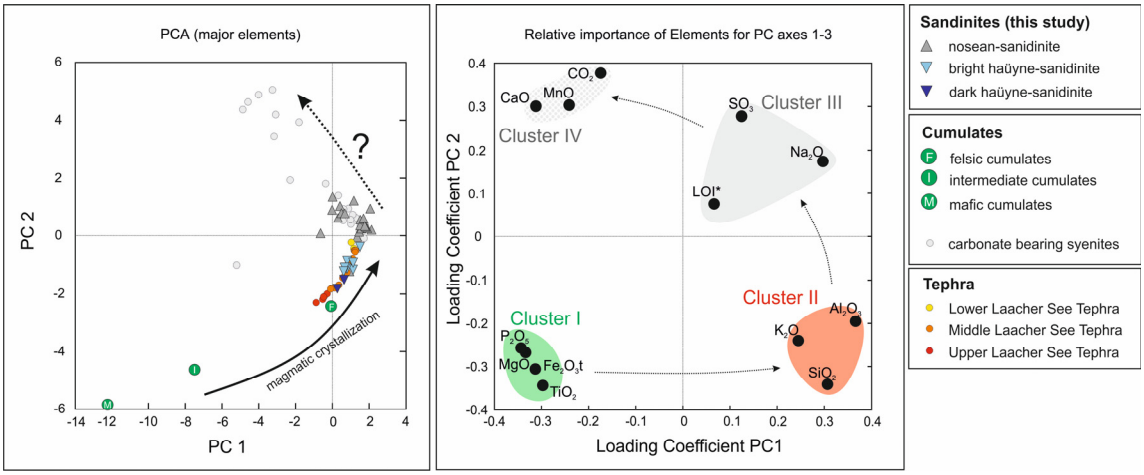

Figure 73: Principal component analyses of the whole-rock composition of the Laacher See eruption products. Data include the different cumulates (Tait et al. 1989), carbonatite bearing syenites (Liebsch 1996) and different types of LS-tephra (Wörner and Schmincke 1984a)

The trend from cluster I to cluster II corresponds with the evolution of a primitive, mafic melt to an evolved phonolitic melt via fractionated crystallization. Haüyne-sanidinites have a similar whole-rock composition as the LS-tephra, and the composition of the minerals contained in haüyne-sanidinite coincide with the composition of the minerals in LS-tephra, specifically with those in middle LS-tephra. Therefore, dark haüyne-sanidinite is

suggested to represent the cumulates at the magma chamber margin around the level of the middle LS-tephra (Figure 74). The whole-rock composition of the carbonate-poor to carbonate-free nosean-sanidinites coincide with the composition of the lower LS-tephra (Figure 73). Therefore they are suggested to represent the cumulates in the magma chamber roof (Figure 74). The bright haüyne-sanidinites are hybrids between the dark haüyne-sanidinites and the nosean-sanidinites. They are therefore suggested to represent the cumulates at the magma chamber margins between dark haüyne-sanidinite and nosean-sanidinite (Figure 74).

The transition from cluster III to cluster IV corresponds with a systematic enrichment enriched in Ca, Mn and LOI, including CO_2 in LS-carbonatite. The age of the rocks derived from zircons correlates also with the temperature: the carbonate bearing syenites with the youngest zircon ages reflect higher temperatures whereas the oldest zircons were found in rocks reflecting lower temperatures (Schmitt et al. 2010). Therefore Schmitt et al. (2010) interpreted the samples of younger age to originate from areas closer to the magma chamber, while samples with older zircons stem from areas that are more distant. The similarity of the nosean-sanidinite composition with that of lower Laacher See tephra and its correlation with carbonate-bearing syenite including Laacher See carbonatite (Liebsch 1996; Schmitt et al. 2010) indicates that they represent several varieties of one rock type. Thus, the sanidinites represent the link between the phonolitic magma (LS-tephra) in the magma chamber and the carbonate bearing syenite (nosean-sanidinite) in the outermost part of the magma chamber (Figure 74). The temperature gradient, recorded in feldspar composition and degree of crystallinity suggests, that dark haüyne-sanidinite represent the cumulates closest to the phonolitic magma body, followed by the bright haüyne-sanidinite in the direction to the top of the magma chamber (Figure 74). The magma chamber roof, however, is built up by nosean-sanidinite including the carbonate-rich varieties known as LS-carbonatites.

The significant change in the trends of the PC2 value from cluster I and II on the one hand and cluster III and IV on the other hand indicates different crystallization conditions of these rocks, which cannot be explained only by differentiation of the melt.

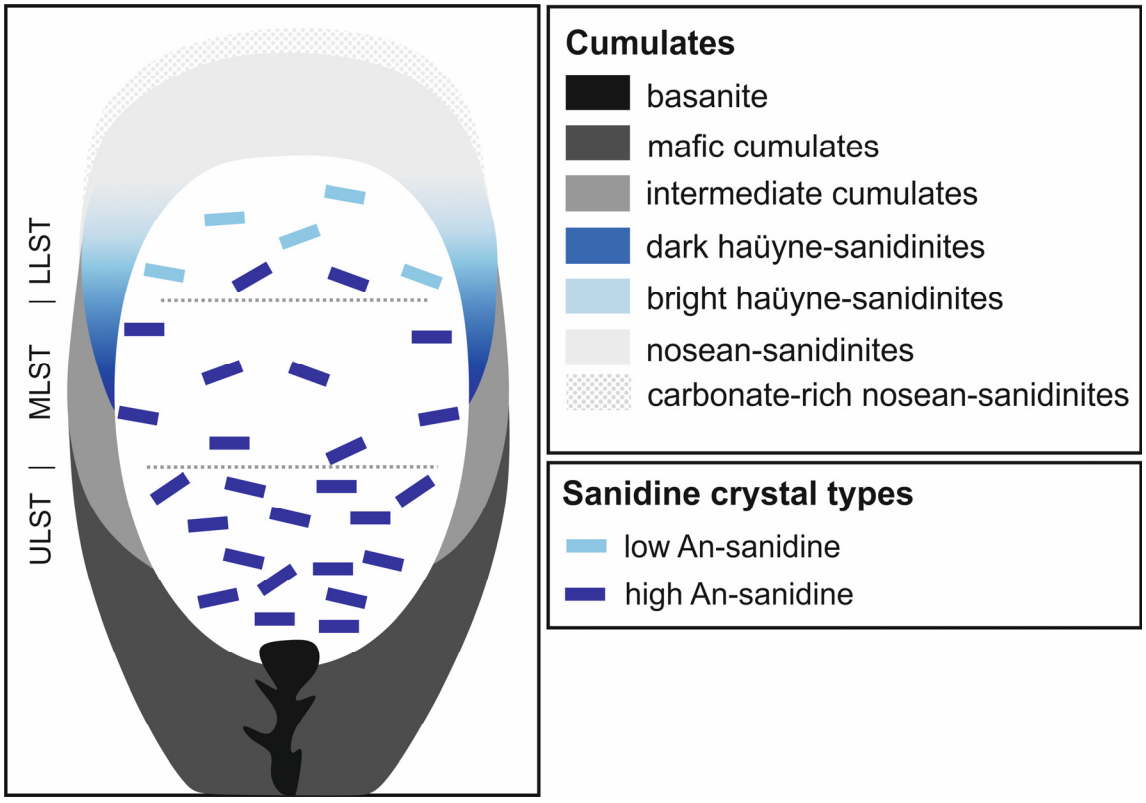

Figure 74: Modified model of the Laacher See magma chamber (after Wörner and Schmincke 1984b, Tait et al, 1989, Ginibre et al. 2004, Schmitt et al. 2010)

4.4.2 LS-CARBONATITE – AN EXTREME VARIETY OF NOSEAN-SANIDINITE

The carbonate contents in the LS-carbonatites can reach up to 76 vol% and are described Laacher See carbonatite as enclaves within the carbonatite-bearing syenites, which are part of an intrusive carbonatite-bearing syenite surrounding the upper part of the magma chamber (Liebsch 1996). The carbonatites are suggested to be formed by dissociation as a carbonatite melt from the highly differentiated phonolite in the upper part of the magma chamber (Liebsch 1996). He interpreted the observed rounded and lobate contacts between calcite and silicate minerals in the LS-carbonatites as textures representing the phonolite melt in equilibrium with the exsolved carbonatite. In particular, the jagged or lobed grain boundaries of sanidine adjacent to calcite were regarded as the result of equilibrium growth.

Several facts argue strongly against the coexistence of a carbonatite melt with a silicate melt in the Laacher See magma chamber: At Laacher See, field observations showed that carbonate-rich syenites are extremely rare. The carbonate-rich syenites (Liebsch 1996), however, are equivalent to the nosean-sanidinites. The vast majority of the nodules within the LS-tephra are represented by nosean-sanidinite with carbonate content varying between 0-20 vol%. Both contain Mn-enriched minerals and calcite with typically ~ 2-3 wt% MnO. Based on this study, the main difference between nosean-sanidinite and LS-carbonatite is the carbonate ratio. The texture of sanidine and calcite in nosean-sanidinite does also not support this assumption. Silicates without any direct contact to calcite show irregular grain boundaries, while the grain boundaries next to cavities are straight and the newly

formed minerals like sanidine are typically euhedral. The preferential occurrence of carbonate in the pore space between the sanidine and nosean crystals implies that calcite crystallized at a later stage, after the crystallization of sanidine and nosean.

It is unrealistic that a Ca-carbonatite melt was in equilibrium with the relatively "cold" phonolitic melt. Temperatures of approximately 840-860°C were estimated for the lower part and about 720°C in the upper part of the Laacher See magma chamber (Wörner and Schmincke 1984a, b; Harms and Schmincke 2000; Berndt et al. 2001; Harms et al. 2004). Ti-in-zircon temperature estimation by Schmitt et al. (2010) yielded even lower average temperatures of 665 ± 58 °C for the carbonate bearing syenite (nosean-sanidinite). Calcite has a liquidus temperature of > 1200 °C. The contribution of alkalis would decrease the liquidus temperature at the presence of the phonolite magma (Cooper and Reid 1998; Weidendorfer et al. 2016). Experiments show that a proportion of at least 40 wt% N_2O is required to lower the liquidus of calcite to 800 °C with nyerite ($Na_2Ca(CO_3)_2$) crystallizing first (Weidendorfer et al. 2016). However, the amount of alkalis in calcite from Laacher See is very low ($Na_2O + K_2O < 0.5$ wt%). Therefore, alteration of Na-rich carbonatites by magmatic fluids or meteoric water are supposed to remove the alkalis leaving behind Na-poor carbonatites (Keller and Zaitsev 2006). In this case, inclusions of carbonate in feldspar, nosean or zircon should preserve the higher alkali content of the melt before entrapment. This phenomenon was observed e.g. in carbonatites from Oka complex in Canada, where Na-rich carbonates were detected in inclusions of magnetite while calcite was analyzed in the groundmass (Chen et al. 2013). However, microchemical analyses of all Laacher See carbonates occurring in the matrix and in inclusions exhibited the same alkali-free composition.

The decrease of F in the silica melt would be another indication of coexistence with a carbonatite. Experiments with carbonate and silicate performed at temperatures between 965-1200°C and pressures of 0.8-10 kbar demonstrated a preferential partition of F in carbonatite melt (e.g. Hamilton et al. 1989; Jones et al. 1995; Veksler et al. 1998). However, in case of Laacher See, the concentration of F in the carbonate-poor cumulates, specifically in haüyne-sanidinite, is much higher than in the carbonate-bearing rocks (nosean-sanidinite and LS-carbonatite) (see Tab. A3- A5 in Appendix). Microchemical transsects from core to rim of apatite in haüyne-sanidinite showed constant F concentrations throughout the whole crystal, while SO_3 and Cl concentrations decreased.

The stability field of carbonatite should also be considered. Carbonatite melt is stable under mantle or lower crust conditions, whereas under upper crustal PT-conditions it is instable and degasses (Frezzotti and Touret 2014; see also chapter 3.5.4). All these aspects indicate that it is not very likely that carbonatite was generated due to the immiscibility of carbonate/silicate melts at Laacher See. Moreover, the similarity of mineral chemistry and textures in nosean-sanidinite and LS-carbonatite indicates similar crystallization conditions. This suggests that the LS-carbonatites are merely an extreme, carbonate rich variety of nosean-sanidinite. Therefore, the question is which process enabled the formation of carbonates in nosean-sanidinite and in carbonate-rich enclaves, respectively.

4.4.3 TWO MINERAL GENERATIONS IN NOSEAN-SANIDINITE - INDICATOR FOR CHANGED GROWTH CONDITIONS

In nosean-sanidinite, both major mineral phases – nosean and sanidine – contain little to no Ca, although the Ca-content of the whole-rock composition is high. Microscopic study revealed that in these samples two distinct generations of sanidine, nosean and zircon are present. The analysis of the microtexture, taking into account mineral chemistry, has clearly shown that two completely different environments dominated during the growth of generation-1 and generation-2 minerals – a result that cannot be deduced from geochemical studies alone.

Generation-1 minerals SAN-1, NOS-1 and ZRC-1 show the characteristics of a crystallization from the melt, like cumulate texture. Most of the ZRC-I crystals show oscillatory and/or vector zoning (see Figure 58) and their high concentrations in REE and Th is typical for zircons growing from a highly evolved melt (Belousova et al. 2002). In addition, the presence of silicate melt inclusions in some ZRC-I crystals verifies its crystallization from a phonolitic melt. Features like abundant CO_2 ± melt inclusions in NOS-1 indicate its formation from a melt enriched in CO_2 bubbles (see Figure 56). Noteworthy are the interlocked SAN-1 laths forming cavities, which are always free of melt. A special feature of these generation-1 minerals are signs of intense dissolution, etching or leaching (see Figures 55, 58 and 66). In particular, SAN-1 and NOS-1 show etching-holes, which are typically rounded or have lobate boundaries, arranged along the cleavage planes and connected by fissures or cracks (SAN-1) or by fluid veins (NOS-1). In general, these etching holes, fluid veins and cracks are either empty or filled with calcite. Some of them also contain further phases such as baddeleyite, zircon or pyrochlore.

Generation-2 minerals represent, beside SAN-2 and NOS-2, a broad variety of minerals such as calcite (and rhodochrosite), biotite and clinopyroxene typically with high Mn contents, as well as various HFSE minerals including ZRC-2 and pyrochlore. Rims of generation-2 minerals around the dissolved generation-1 crystals, replacing generation-1 crystals, are evident. A specific feature is the euhedral growth of generation-2 crystals projecting into empty cavities between the SAN-1 laths, e.g. the growth of fluid-free NOS-2 with euhedral crystal shape or euhedral HFSE minerals like zircon and pyrochlore and less abundant baddeleyite, thorite or REE-apatite (britholite). Outstanding examples of these crystals can be found on collector websites, e.g. www.mineralienatlas.de.

SAN-2 and ZRC-2 replacing SAN-1 and ZRC-1, respectively, show high porosity. The pores in SAN-2, which are preferentially distributed at the interface to SAN-1, are often filled with calcite, while those in ZRC-2 contain thorite ± pyrochlore ± calcite. The “pure” zircon-composition of ZRC-2 distinguishes it chemically clearly from ZRC-1. The small bipyramid shape of ZRC-3 is typical for growth from a hydrothermal fluid (Yang et al. 2014). Their occurrence in sanidine and nosean shows that a Zr-saturated fluid migrated not only along the grain boundaries but also along solution holes, cracks, or veins within the crystals. Little tension cracks in SAN-1 crystals indicate pressurization caused by volume increase during the growth of the zircons. The identical composition of ZRC-2 and ZRC-3 points to their common origin and their crystallization from the same fluid phase.

A “secondary” accumulation of the cavity mineral assemblage in the environment is also supported by the trends in whole-rock composition (see Figure 70). Although Ca, Mn and REE show a decrease from dark haüyne-

sanidinite over bright haüyne-sanidinite to carbonate free nosean-sanidinite (with decreasing K_2O/Na_2O), exactly these elements are enriched in carbonate-bearing nosean-sanidinite at an approximately constant K_2O/Na_2O value (see Figure 70).

4.4.4 CARBOTHERMAL PROCESSES

All observations point to a significant change in the environment of the later crystallized minerals of the 2nd generation compared to the minerals of the 1st generation.

- Dissolution textures of generation-1 crystals
- Abundant cavities between generation-1 crystals
- Generation-2 crystals with different shape, mineral chemistry and texture

The dissolution of generation-1 and crystallization of generation-2 minerals indicates a shift from melt-based matrix to melt-free conditions. In magmatic systems, melt-free dissolution-crystallization processes are normally explained by hydrothermal processes. The term "**hydrothermal"** implicates water ("hydro") as the main solvent. Species such as Cl, S, F, PO_4 and CO_2, which are considered to be additives in "hydrothermal" systems, are gaining more attention because of their contribution to a higher solubility of solids and transportability of the fluid. Demazeau (2008) introduced the term **"solvothermal**" in applied chemistry to describe processes of dissolution, transport and recrystallization induced by **any solvent** ("solvo") at a certain temperature ("thermal"). Correspondingly, **"carbothermal**" implies CO_2 as the main solvent.

4.4.4.1 REACTION CONDITIONS

Harms and Schmincke (2000) showed that the H_2O contents in glass inclusions increase slightly with differentiation of the magma up to 2.5-5.7 wt%. They explained it by relative enrichment of H_2O in the more evolved melt at a later stage. Abundant vesicles in the erupted tephra and low H_2O concentration in matrix glasses (0.2-2.8 wt%) argue for a late degassing during the eruption (Harms et al 2000). XRF measurements of matrix glasses of the LS-tephra yielded 100-500 ppm CO_2 (Wörner and Schmincke 1984b).

Groundmass glass (melt), however, does not reflect the entire budget of the volatiles present in the magma chamber as the components have different degassing properties. Under the same conditions, the solubility of CO_2 in melt is 50-100 times lower, compared to H_2O. Therefore, CO_2 and SO_2 are already "degassed" before the melt reaches the surface. As a result, free CO_2 dominates volcanic activity at early stages, whereas just before eruption mainly water degasses. Accordingly, only volatiles, which are highly soluble in a silicate melt, such as water, fluorine and to a lesser extend chlorine and sulfur, can be measured in glass. Consequently, only melt inclusions trapped in a way that loss of the primary volatiles is inhibited may capture the composition of volatiles in the magma chamber.

The Laacher See magma chamber was located in a depth of 5–6 km (Harms et al. 2004). At this shallow crustal level, most mantle derived carbonate and CO_2 is already degassed and partitioned into a separate free fluid

phase. This, however, does not mean that CO_2 is removed from the system. CO_2 exsolves continuously already under upper mantle conditions or from more primitive magmas in a lower level of the magma plumbing system and migrates upwards through feeder dykes, where it migrates through e.g. magma bodies at shallower crustal level. The $\delta^{13}C$ values of current CO_2 emissions in the Laacher See region show a mantle signature similar to the studies of $^3He/^4He$ ratios (Giggenbach et al. 1991; Aeschbach-Hertig et al. 1996). CO_2 flushing of magma chambers is a common feature in mafic and felsic magmas (Caricchi et al. 2018). Papale (2005) simulated numerically the dynamics of CO_2 influx from a deep shoshonitic magma into a shallow phonolitic magma. They showed that at pressures comparable to the Laacher See magma chamber, > 90 wt% of the exsolved vapor accumulated in the top part of the magma chamber consists of CO_2. This corresponds to the widespread CO_2-inclusion observed in nosean from nosean-sanidinites, where CO_2 has been identified as the major component of the fluid phase.

What about the other volatile species? Apatite and minerals of the sodalite-group and are excellent indicators for the prevailing reaction conditions and the composition of the fluid phase. The investigated larger zoned **apatite** crystals from haüyne-sanidinite show decreasing SO_3 and Cl content from the core towards the rim, whereas F content remains constant along the whole transect (see Figure 65b). This trend implies a depletion of these elements in the melt during the growth of apatite either caused by a preferential crystallization of SO_3- and Cl-bearing phases consuming these species, or the loss of these elements by degassing. Experimental studies showed that F partitions preferentially into the liquid (Schilling et al. 1980; Candela 1986) whereas SO_4 tends to degas (Scaillet et al. 1998; Keppler 1999).

Sodalite-group minerals are very sensitive for the prevailing reaction conditions and in particular, existence of a free fluid phase. They are indicator for the Si-activity during their formation: Under volatile-undersaturated and Si-saturated conditions, they react to albite, and under Si-undersaturated conditions to nepheline (Parat and Baudouin 2015). Correspondingly, in the more silica-rich haüyne-sanidinite, plagioclase occurs preferentially together with haüyne whereas no plagioclase was observed in nosean-sanidinite. The mostly round haüyne grains are often surrounded by plagioclase and melt, indicating the formation of plagioclase after haüyne according to the reaction (1), releasing SO_3.

(1) $Na_3CaAl_3Si_3O_{12}(SO_4) + 8\ SiO_2 + Al_2O_3 = 4\ Na_{0,75}Ca_{0,25}Al_{1,25}Si_{2,75}O_8 + SO_3$

haüyne melt albite

Due to their cage-structure, **sodalite group minerals** are able to incorporate volatiles, such as SO_4, Cl and H_2O in their structure (e.g. Gesing and Buhl 1998). Additionally, nosean and haüyne are one of the few magmatic minerals, besides e.g. apatite and carbonate, which are able to incorporate CO_2. Therefore, sodalite-group minerals are also suitable indicators for the prevailing volatile composition during their growth. The absence of H_2O in sodalite group minerals is a clear indicator for low H_2O activity in the system. The ratio of the three volatile phases SO_4, Cl and CO_2 trapped in the sodalite group minerals changes in dependence of the rock type (Figure 75): the CO_2 concentration increased from dark haüyne-sanidinite over bright haüyne-sanidinite to nosean-sanidinite, which has the highest CO_2 concentrations. In dark haüyne-sanidinite, SO_4 is the dominant anion, while in bright haüyne-sanidinite the Cl content in haüyne is the highest.

Increasing CO_2-activity in the environment of dark haüyne-sanidinite to bright haüyne-sanidinite and nosean-sanidinite is also reflected in the increasing amount of bubbles entrapped in nosean (Figure 75). CO_2-inlusions are completely absent in haüyne of the dark haüyne-sanidinite and occur occasionally in haüyne of bright haüyne-sanidinite. The analysis of pure CO_2-vapor inclusions in nosean are clear indications for high CO_2-activity in nosean-sanidinite. CO_2 inclusions with low density detected by Raman spectroscopy indicates that CO_2 was present as a gas phase.

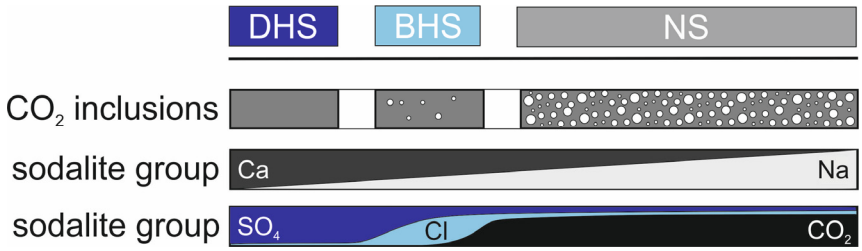

Figure 75: Schematic figure showing the chemical gradient of the cations Ca, Na, and the anions SO_4, Cl and CO_2 in haüyne and nosean

The composition of nosean and haüyne in the different types of sanidinite suggests the presence of SO_4 and Cl in addition to CO_2. Lowenstern (2000) reviewed the behavior of Cl and CO_2 in silicic melts under crustal conditions. At the presence of CO_2, the limited solubility of Cl promotes a separation of the fluid into two phases, a CO_2-rich vapor with low amount of ideally mixed H_2O and SO_3, and a brine with less volatile Cl complexes, alkalis or Fe species (Lowenstern 2000).

In sum, a two-phase **carbothermal** fluid consisting of a CO_2-rich gas with minor amounts of SO_3 and H_2O and a Cl-rich brine is proposed to dominate in the top part of the magma chamber. Due to the nature of gases, it is expected to be distributed evenly in all cavities between the silicates in the crystallized top part of the Laacher See magma chamber. A smaller amount of dissolved brine preferentially wets the surface of the minerals locally or fills in smaller cavities.

4.4.4.2 DISSOLUTION, ETCHING AND LEACHING OF GENERATION-1 CRYSTALS

Consequence of the presence of the carbothermal fluid are dissolution and/or etching phenomena of generation-1 crystals (SAN-1, NOS-1 and ZRC-1) such as lobed or jagged grain boundaries, deep dissolution embayments and etching holes.

ZIRCON

ZRC-1 in nosean-sanidinite is clearly affected by leaching or coupled dissolution-crystallization processes. The moderate to strong dissolution occurred preferentially along weakness zones such as the mineral surfaces, cracks or fissures (see Figures 58a and 66). As shown in Figure 66, these areas are also enriched in REE, Th and U. That means preferential attack of the zones with strongly deformed crystal lattice, and replacement by highly porous "pure" ZRC-2 with low concentrations in REE and Th.

Porous zircons similar to ZRC-2 with thorite inclusions are a common phenomenon in metamorphic rocks. They are interpreted as results of dissolution and recrystallization under subsolidus conditions (Hoskin and Black 2000; Geisler et al. 2003; Tomaschek et al. 2003; Spandler et al. 2004). Similar porous textures have been reported also for fluorapatite and monazite and was referred to coupled dissolution-crystallization processes (Putnis 2002; Harlov et al. 2005; Putnis et al. 2005). Zircon textures, similar to those observed in nosean-sanidinites were also discussed to be the result of vapor-phase crystallization (Rubin et al. 1989).

In contact with fluid, the solubility of zircon, rich in trace elements such as ZRC-1, is higher than pure zircon (Geisler et al. 2007). The generally low solubility of Zr in a fluid, in particular at the presence of silica is assumed to promote the crystallization of a "pure" and therefore simple zircon like ZRC-2. Expelled "impurities" such as Th are concentrated in newly formed minerals like thorite ($ThSiO_4$) growing in small enclaves within ZRC-2. The occasional growth of baddeleyite (ZrO_2) on the surface of ZRC-2 or within open pores indicates locally low Si activity, thus promoting the growth of ZrO_2. Experiments showed that baddeleyite is the stable phase in low-silica carbonatite melts, as a significant concentration of SiO_2 is required to stabilize zircon (Gervasoni et al. 2017).

NOSEAN

NOS-1 often shows rounded surfaces or less intense dissolution embayments in comparison to SAN-1 and ZRC-1. Some NOS-1 crystals have rims with tiny Fe-sulfide crystals pointing to a change in the environment with low redox conditions. Notably, the rims of Fe-sulfide mimic the overprinted rounded shape of these crystals with deep dissolution embayments. The typically round to oval holes connected by fluid veins crosscut the NOS-1 crystals along cracks and weakness zones and are therefore interpreted as etching holes. These holes are either empty or partially or completely filled with calcite with occasional tiny calcite crystals along the fluid veins. These empty holes, large CO_2 ± melt inclusions and holes filled with calcite – all connected via fluid veins – show all the same round to oval shape. Calcite occasionally filling up these fluid veins or dissolution holes indicate that CO_2 penetrated the crystals and migrated along weakness zones, such as the CO_2-vapor inclusions

One special feature provides dissolved NOS-1 where individual SAN-2 crystals appear aligned in parallel bundles, radial or feathery, filling up the space between generation-1 crystals. These unusual features of feldspars occur always adjacent to nosean specifically in nosean-rich samples. Spherulitic to feathery growth indicates a rapid growth of few numbers of nuclei into a fluid rich space (Petersen and Lofgren 1986). With the dissolution of nosean, volatiles including Cl are released into the fluid, leading to the formation of new brine. This interaction enhances the release of Cl and the dissolution of the mineral phases in a form of "autometasomatism".

SANIDINE

Remarkable is the similarity of SAN-1 microstructure with perthitic exsolution showing a patchy zoning with either Na-rich or K-rich zones. Some of them might be indeed perthitic exsolution indicating a long sub-solidus residence time of these samples (Schmitt et al. 2010). The closer look however shows that many of these "perthites" are the result of coupled dissolution crystallization processes in the presence of the carbothermal fluid. The deep saw-tooth like dissolution embayments of SAN-1 replaced by porous SAN-2 (Figure 76a) correspond exactly with a phenomenon described by Norberg et al. (2011). They studied the albitization of K-feldspar at 500°C and 200 MPa using aqueous NaCl solutions and observed a highly anisotropic attack of K-feldspar leading to a sawtooth-shaped reaction front as shown in Figures 76b and c. The pseudomorphic replacement of K-feldspar by parallel albite "blades" along preferred crystal orientation resembles to perthitic intergrowths. The authors explained the accompanying porosity in the host feldspar with a two-step formation of albite. Their microstructural investigations exhibited nano-scaled pores in early polycrystalline albite subgrains. With time, they are replaced by larger well-ordered albite patches with only few pores (Figure 76c). The recrystallization of albite achieved a higher degree of permeability by coarsening of the pores and development of an interconnected porosity. The calculated volume reduction by the dissolution of K-feldspar and the crystallization of albite is about 7.5 %.

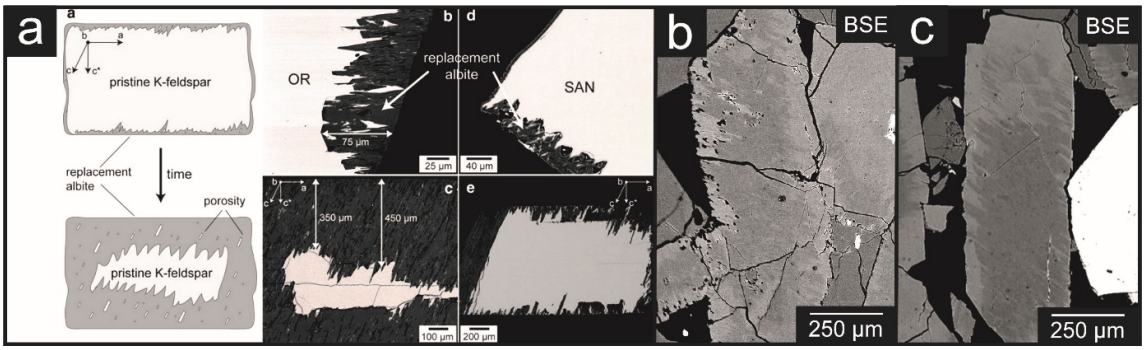

Figure 76: a) Results of the experiments by Norberg et al. 2011 showing the replacement of K-feldspar by albite by metasomatic processes, b) SAN-1 replaced by highly porous SAN-2 and c) densified SAN-2 around dissolved SAN-1 crystals reminding of perthitic exsolutions

The porosity in SAN-1 occurs particularly along the reaction front, with some of the pores filled with calcite (Figure 76b). The shift in the microchemical composition of SAN-1, which is characterized by Na-rich and Ca-poor compositions, to lower Na and lack of Ca contents of the recrystallized SAN-2 indicates a continuous leaching of Ca ± Na out of the structure and replacement by pure K-rich feldspar.

4.4.4.3 EXTRACTION AND TRANSPORT OF DIVALENT ELEMENTS

The presence of a two-phase carbothermal fluid provides ideal conditions, not only for dissolution but also for leaching of relevant elements from exposed minerals, in particular bivalent elements. Various technical applications show that supercritical CO_2 can act as a solvent in order to remove Fe, Ca, Mg and Sr from clay minerals (Pearce et al. 2016) or together with extractants to remove Zn, Cu, Pb, Cd and Cr from sands and fly ashes (Kersch et al. 2004). During natural rock weathering, carbonic acid leaches Ca (and Mg) from silicates in order to form carbonates. Similar experiments are performed in the context of CO_2 sequestration and carbonation processes. The concept of carbonation is to precipitate carbonate after leaching Ca from silicates by CO_2. Therefore, the effect of CO_2 on the solubility of feldspars is studied intensively. In both cases, experiments showed that the anorthite component of plagioclase is preferentially dissolved (e.g. Tutolo et al., 2015, Fischer et al. 2010), and the Ca-content in K-feldspar is affected by CO_2 (Fischer et al. 2010). An indirect prove of the effectiveness of element extraction by CO_2 is the geologic carbon sequestration.

Dissolution embayment and etching pits – similar to those in nosean-sanidinite – were observed in feldspars exposed to CO_2 (Tutolo et al. 2015). These experiments describe best the observed association of corroded generation-1 minerals in nosean-sanidinite with subsequent formation of calcite. The preferential extraction of divalent elements Such as Ca^{2+} and Mn^{2+} by CO_2 can also explain its unusual high concentration in generation-2 minerals such as calcite (2-3 wt% MnO), rhodochrosite and other silicates such as biotite and clinopyroxene (johannsenite) occurring in nosean-sanidinite.

This reaction mechanism can also enable the cleaning or purification of REE- and Th-bearing zircons exposed to CO_2-gas, which leads to “pure” zircon, “pure” thorite and REE-containing oxides, such as pyrochlore. Studies on the partitioning behavior of CO_2 between silicate melt, carbonatite melt and CO_2 vapor at crustal conditions pointed to a preferentially partition of REE in CO_2 vapor (Wendlandt and Harrison 1979).

The major mineral assemblage SAN-1, SAN-2 and NOS-2 observed in nosean-sanidinite points to following reaction:

(2) $50\ [Ca_{0.02}Na_{0.5}K_{0.48}AlSi_3O_8] + [3\ Cl + 3\ SO_3 + 4\ CO_2] \rightarrow 3\ [Na_8Al_6Si_6O_{24}\ [Cl\ SO_4\ CO_2]] + 24[KAlSi_3O_8] + 60[SiO_2] + 4[Al_2O_3] + 1\ CaCO_3$

SAN-1 volatiles NOS-2 SAN-2 silica corundum calcite

Based on the composition of SAN-1, 50 mol sanidine are required to form 1 mol calcite. Furthermore, the ratio of SAN-1 : SAN-2 is 50:24. This means that the newly formed SAN-2 occupies less than half of the space required by SAN-1. This may explain the higher porosity of SAN-2. However, the high proportion of calcite in these rocks cannot be explained by this reaction alone.

Ca extraction by CO_2 is not restricted to the rigid upper part of the magma chamber, where nosean-sanidinite crystallized. Experiments for solid-gas interaction at 600-800°C showed that degassing of SO_2 can promote the Ca extraction from a melt leaving behind a residual melt enriched in Na and Mg (Renggli et al. 2019). The oxidation of SO_2 during degassing is accompanied by reduction of sulfur, which promotes the formation of sulfides (Renggli et al. 2019). This phenomenon correlates very well with the systematics observed for the

sanidinites from Laacher See as it can explain the presence of Fe-sulfides in the cores of NOS-1, although nosean contains structurally bound SO_3.

One further aspect of CO_2 interaction with its environment is obviously the extraction of Ca from the melt. The number and size of the CO_2-bubbles entrapped in nosean and haüyne increases from dark haüyne-sanidinite over bright haüyne-sanidinite to nosean-sanidinite (see Figure 75) reflecting an accumulation of CO_2 towards the magma chamber roof. At the same time, the Ca content in sanidine and haüyne/nosean and in whole-rock composition decreases from haüyne-sanidinite to carbonate-free nosean-sanidinite (see Figure 75). The extraction of Ca from the melt via CO_2 is most effective in that part of the phonolite melt where CO_2-vapor bubbles are accumulated. This trend could explain the lower Ca concentrations in sanidine from the lower LS-tephra (top of the magma chamber) compared to sanidine from the middle and upper LS-tephra (bottom of the magma chamber), observed by Ginibre et al. (2002). Application of this concept raises the question of whether the generally low Ca content of trachytic to phonolitic melts is the result of a successive extraction of elements such as Ca, Mn or REE by CO_2.

4.4.4.4 TRANSPORT AND RECRYSTALLIZATION OF ZIRCONIUM

Minerals without divalent elements like zircon also belong to the generation-2 phase: porous ZRC-2, ZRC-3 bipyramids and baddeleyite. ZRC-2 occurs not only as replacement product of ZRC-1 but forms also individual crystals, preferentially along grain boundaries. ZRC-3 occurs in fissures and crack or etching holes in SAN-1. Small cracks around the euhedral crystals point to the pressurization of sanidine during the solvothermal growth of ZRC-2 within a SAN-1 host crystal. Co-crystallization with carbothermal calcite and calcite fillings of the pores in ZRC-2 suggest a transport of zirconium with and a crystallization of these minerals from a carbothermal fluid.

Hynes (1980) investigated metabasalts and showed that at high CO_2 activity elements, which are thought to be immobile like Zr and Ti can be mobilized. Various studies describe the formation of zircon in a postmagmatic stage. Zozulya et al. (2012), for example, observed multistage crystallization of zircons in nepheline syenite. In addition to bipyramidal zircons, they observed porous crystals with the lowest ZrO_2/HfO_2 ratio formed during the postmagmatic hydrothermal stage. Formation of secondary zircon replacing magmatic crystals by dissolution-crystallization process were observed by Rubatto et al. (2008). The authors found also individual newly grown, euhedral zircon crystals. They suggested that the dissolution process was more persuasive leading occasionally to complete dissolution of the magmatic zircons and fluid-induced transport of Zr before the “secondary” crystallization started. The formation of zircon requires a sufficiently high Si activity in its environment (Gervasoni et al. 2017). This corresponds with our observation, that zircon crystallized only adjacent or in holes and fractures within sanidine (Al:Si ratio = 8:24), whereas in nosean (Al:Si ratio = 24:24), Zr crystallized mainly as ZrO_2 (baddeleyite) or Zr-bearing pyrochlore. This association indicates that under certain circumstances the carbothermal fluids can mobilize Zr in addition to REE.

4.4.4.5 LIMITING FACTOR FOR THE CRYSTALLIZATION OF CARBOTHERMAL CARBONATES

This study shows that the nosean-sanidinites are affected by CO_2-induced leaching and coupled dissolution crystallization processes. Ca and REE, extracted from the melt and leached from generation-1 crystals, partition into the CO_2-vapor and precipitate as chemical vapor-deposits (CVD) when conditions for precipitation are given. However, not all types of nosean-sanidinites contain carbonates. What is therefore the limiting factor for the precipitation of calcite?

Microtextural analysis showed that only one part of the extracted elements like Ca, Mn and REE precipitated onsite. REEs are known to react strongly with CO_2 under formation of carbonates. However, REE-carbonates were not observed in the nosean-sanidinites. Depending on pressure, carbonates are stable below the decarbonation temperatures (620-800°C) and therefore chemical vapor-deposition of carbonates from CO_2-vapor is only expected in the outer boundary of the magma chamber or in the country rock. At higher temperatures, REE-bearing oxides such as pyrochlore dominate.

4.4.5 FORMATION OF A CO_2-GAS CAP

Nosean-sanidinite represents the uppermost, rigid part of the magma chamber (see Figure 74). Characteristic are cavities between interlocked sanidine laths and miarolithic cavities. The observation of enormous amount the CO_2 ± melt-inclusions in NOS-1 indicates 1) massive percolation and accumulation of CO_2 in the phonolitic melt during the formation of the nosean crystals, and 2) rapid growth of the nosean crystals to entrap CO_2 together with melt as inclusions. Following questions arise in this context:

- How is it possible to have two different environments in one system – a Ca-containing melt promoting the growth of haüyne, and a Ca-depleted melt enabling the crystallization of nosean?
- Which mechanism enabled the formation of a melt free space in the magmatic system in which carbothermal processes dominate?

In general, syenite is dense and therefore, the formation of miarolithic cavities and the cavities between the generation-1 crystals requires the absence of melt and the presence of a fluid and/or gas. The existence of a fluid pocket was proposed by Lake (2013) for silicic magma chambers. He used numerical simulations to model saturation fronts along magma chamber walls based on the theory of a solidification front of Marsh (2015). Marsh (2015) postulated that a completely solidified, rigid crust formed at the outermost part of the magma chamber, which encloses a zone of crystal mush and a zone of suspension on the melt-facing side of the magma chamber. Lake (2013) used a dacitic melt for his modeling and assumed pure H_2O as volatile phase. His calculations showed that the addition of CO_2 to the melt shifts the saturation front further into the magma chamber. He showed that the fluid cap has maximum expansion when the volatile phase consists mainly of CO_2. Accordingly, the fluid pocket expands with progressive accumulation of CO_2 in the top part of the magma chamber.

At Laacher See, there is evidence of a continuous directional fluid flow of the degassing CO_2 through the rigid zone. Oriented jagged and recrystallized grain boundaries occurring only on one side of the sanidine laths indicate a Lee effect of the fluid flow (see Figure 55), which has presumably developed along preferred venting channels. This phenomenon implies a continuous release of CO_2 from the melt in deeper levels of the plumbing system. Without obstruction, this fluid flow would pass the boundary of the magma chamber and penetrate the country rock. That means, in an open system, pressure buildup to form a fluid cap is hardly possible.

4.4.5.1 SEALING OF CARAPACE BY CARBOTHERMAL DENSIFICATION

The retention of volatiles requires the formation of a gas-tight carapace. Skarns, fenites and hydrothermal ore deposits prove that the exsolved fluid escapes into the country rock if the carapace is not sealed. What mechanism can therefore promote the sealing the top margin of the magma chamber?

This study showed that the cavities of many nosean-sanidinites are partially or completely filled with calcite. It is known from petroleum science that carbonates, because of their low porosity and permeability, can function as gas-tight cap rocks for preservation of hydrocarbons (Wu et al. 2017). Therefore, carbothermal densification of the nosean-sanidinite has the potential to seal the magma chamber carapace.

CO_2 SEQUESTRATION OR WHAT WE CAN LEARN FROM TECHNICAL APPLICATIONS

Carbonation processes are intensively studied in experiments in the technical context of CO_2 sequestration. For this purpose, two different techniques are used, in-situ and ex-situ processes. The in-situ process involves sequestration in geologic systems where CO_2 is pumped into a Ca- and/or Mg-silicate bearing target formation. In an ex-situ process, carbonation takes place in a separate reactor at the surface. The principals of natural weathering processes are used to form carbonates by reaction of CO_2 gas and/or aqueous CO_2 with Ca- or Mg-silicates. By pumping CO_2 into Ca-silicate containing sediment layers, Ca is leached from feldspars in order to form carbonates according to following simplified carbonation reaction (3):

(3) “$(Ca,Mg)SiO_3$” (s) + CO_2 (g) → $(Ca,Mg)CO_3$ (s) + SiO_2 (s)

silicate carbonate quartz

The potential for carbonate formation depends on temperature, pH and composition of the injected solutions. Porosity and permeability of the target formation are among the most critical factors for estimating the potential of CO_2-injection. In general, carbonates are gas-tight and remain it over a long time (Gerlach et al. 2019). Calcite, which is increasingly filling the pores and cavities between the leached generation-1 minerals in nosean-sanidinite, agrees well with the carbonation in the **“dry” (direct) in-situ CO_2-sequestration**. Experiments in the context of CO_2-sequestration showed self-sealing abilities of the cap rock by carbonation in the presence of CO_2-flux (Fischer et al. 2010; Pearce et al. 2018).

FENITIZATION AND CARBOTHERMAL DENSIFICATION

Migration of CO_2 and other volatiles to the top of the magma chamber has several implications. In general, alkaline magmatism is accompanied by fenitization, the metasomatic overprint of the country rock by exsolved fluids from the magma chamber (Elliott et al. 2018). It is often the main source for REE and Nb, which precipitate in a complex vein network in a strongly brecciated country rock. The different stages of fenitization described by Brögger (1921) based on the mineral assemblages at Fen, Norway, correlates with the observations from Laacher See Volcano: the less intense fenitized sections contain feldspars with perthitic textures, and in the most intense fenitization section next to the intrusion carbonate precipitates.

Isotope measurements of the carbonates at Laacher See Volcano showed that the C^{13}/C^{12} and O^{18}/O^{16} ratios correspond to mantle values (Taylor et al. 1967). Therefore, they assumed that the carbonate from Laacher See Volcano were formed by segregation from the evolving magma under mantle conditions. Later investigation however revealed that the magma chamber of Laacher See Volcano was located in the upper crust at shallow levels of 5-6 km depth (Harms et al. 2004). As shown in chapter 4.4.2, several arguments rule out a segregation of a carbonatitic melt from the phonolite under the low temperatures and pressures. If calcite forms as chemical vapor-deposits from mantle derived CO_2, calcite will preserve the mantle signature of CO_2.

During the evolution of the magmatic system, the magma chamber margin cools down resulting in a temperature gradient from the wall-rock towards the core of the magma chamber. At the same time, the co-magmatic Ca-bearing carbothermal fluid migrates to the top of the magma chamber and into the country rock. Precipitation of carbonates from CO_2-vapor requires temperatures below the decarbonation temperature. In an early stage of the phonolitic magma evolution, this condition prevails in the country-rock. With ongoing crystallization and cooling of the phonolite and crystallization of sanidine along the magma chamber margins, the first framework for the development of a rigid part in the upper part of the magma chamber is set. The temperature gradient within the rigid part enables carbonate precipitation in the outermost rigid part. Only after a carbothermal densification of the country rock and/or rigid part of the crystal mush and the generation of a gas-tight carapace, gas pockets can develop in niches within this section, which are fed from the upwardly percolating CO_2. In general, CO_2 emissions at the surface, e.g. in mofettes at recent Laacher See, prove that the country rock alone does not act as a gas-tight seal.

The rigid framework of generation-1 crystal in the magma chamber roof represents the first barrier for CO_2. CO_2 migrates through fissures and cracks or along grain boundaries, which explains the preferential precipitation of generation-2 minerals along these paths. Fluid veins and dissolution textures prove that with time and presumably increasing gas pressure, the carbothermal fluid also penetrates generation-1 crystals, preferentially along weakness zones, indicated by fluid veins, occasionally filled with calcite. Depending on the temperature gradient, the leached and dissolved elements are transported to the cooler magma chamber margin and precipitate when the saturation conditions are achieved. The exposure time of nosean-sanidinite to the aggressive environment of the CO_2-gas cap defines the degree of carbothermal overprint. In this context, the textures of the carbonate-rich variety “LS-carbonatite” described by Liebsch (1996) are the result of intense

silicate dissolution and carbonate precipitation. The large carbonate enclaves represent miarolitic cavities and vugs, which are now completely filled with calcite precipitated from the CO_2-fluid phase.

4.4.5.2 CO_2-FOAM LAYER

The extraordinary high amount of CO_2 ± melt inclusions in NOS-1 demonstrates the accumulation of CO_2-bubbles in the phonolitic melt in the form of a "foam layer". Gas monitoring at Stromboli volcano show at first a decrease in CO_2 emissions, followed by increase of CO_2 just before the eruptions (Aiuppa et al. 2011). They explained this phenomenon by retention of CO_2 in the foam layer and release of CO_2, when the foam collapses. However, it does not explain the mechanism promoting the foaming of an upwards percolating CO_2, in particular if CO_2 can escape through the wall rock to the surface.

Under normal circumstances, the internal fluid pressure is higher than the external fluid pressure forcing the fluids or gases to escape into the country rock (Taylor 1987). This mechanism is used in glassmaking where the external pressure is lowered by applying vacuum to remove gas bubbles from the melt. The formation of a gas cap in the top of a magma chamber corresponds to a closed system in which now the fluid internal pressure can rise and thus counteracts the escape of further gas bubbles. The example of sparkling water shows that gas remains in the liquid as long as the bottle is sealed and the volume of free gas above the liquid is small. After opening a bottle, CO_2-gas cannot be easily retained in the liquid. In a partially filled closed or open bottle, the CO_2 content in the liquid will decrease over time to equilibrate with the air in the bottle. The same effect is expected in magmatic systems. Accordingly, a tightly sealed carapace, e.g. via carbothermal densification, is necessary to develop a pressurized CO_2-fluid cap in the top of the magma chamber. Under these conditions, CO_2 bubbles remain in the melt and upwards sparkling bubbles accumulate in a foam layer at the liquid-gas interface. The enormous amount of fine CO_2 bubbles in nosean, which causes many nosean crystals to appear dark gray or almost black, suggests a high gas pressure that prevents the expansion of gas bubbles. Larger bubbles could have formed due to bubble coalescence or temporal pressure drop, e.g. if local overpressure leads to minor brecciation of the country rock.

4.4.5.3 DYNAMIC CO_2-VAPOR FRONT AND CONSEQUENCE FOR THE HAÜYNE – NOSEAN PARADOXON

The occurrence of nosean and haüyne in the same magmatic system is curious and not self-evident. Parat and Baudouin (2015) compared the haüyne-plagioclase-bearing Si-K-rich phonolites from Laacher See and nosean-nepheline-bearing Si-poor phonolites from Saghros (Marocco). They concluded that the crystallization of haüyne in Laacher See was enabled by a silicate melt with low sodium content at fluid-undersaturated oxidized conditions, whereas nosean in the phonolite from Saghros (Marocco) crystallized from a Si-poor and peralkaline melt under more reducing conditions. In consequence, the authors assumed that differences in the initial magma caused the crystallization of haüyne in case of Laacher See phonolite and nosean in case of Saghros phonolite. This assumption contradicts the observation that haüyne and nosean coexist in the Laacher See eruption

products. Therefore, another mechanism must be considered to explain the formation of these two different sodalite group minerals from the same magma.

Textural investigations indicate that sanidinites are “active” magmatic cumulates. The generation-1 mineral assemblage of the nosean-sanidinites represents the CO_2-foam zone. It is located in the uppermost part of the phonolitic magma body beneath the CO_2 gas cap while the “older” nosean-sanidinites represent the rigid crystal mush part of the magma chamber exposed to the CO_2-gas cap. In consequence, these samples show an overprint by the carbothermal fluid. A continuous flushing of CO_2 from lower levels leads over time to an accumulation of CO_2 in the magma chamber roof as long as the densified nosean-sanidinite layer prevents the escape of gas. The expansion of a gas cap forces the movement of the dynamic CO_2-vapor-front from the top region inwards to the magma chamber, which is accompanied by increasing degree of crystallization and densification of the section. In some oil reservoirs, the gas cap created by the extraction of oil is used to pressurize the fluid and in consequence to increase the oil production rate.

The concept of a dynamic CO_2-vapor-front shows that nosean and haüyne can grow from the same melt, but at different position of the stratified CO_2-vapor-front. To illustrate the dynamics of these zones, they are termed “**active nosean-sanidinite-zone**”, “**active bright haüyne-sanidinite zone**” and “**active dark haüyne-sanidinite zone**”. The term “**carbothermal nosean-sanidinites**” describes those nosean-sanidinites, which are exposed to the CO_2-gas cap. With time, the extending CO_2-gas cap within the zone of **carbothermal nosean-sanidinites** shifts the front of the **active nosean-sanidinite**, and with the propagation of the CO_2-vapor-front, the zone of the metastable dark haüyne-sanidinite further inward into the magma chamber. As a result, the former dark haüyne-sanidinite section gets transformed to active **bright haüyne-sanidinite,** and the former bright haüyne-sanidinite section is converted to nosean-sanidinite. Nosean can be taken as an indicator of the spreading of the foam layer because it can only grow in the Ca-depleted foam layer. It also explains the prevalence of nosean-sanidinites compared to rare haüyne-sanidinites at Laacher See Volcano.

Accordingly, the different “active” zones represent a steady state where each of the respective assemblages is in equilibration with its specific environment. In consequence, depending to the reaction rate, some of the sanidine crystal cores can survive, which could explain the occurrence of some sanidine crystals with slightly higher An-component than the average in their cores. However, most of the sanidine and haüyne crystals (generation-1) are etched or dissolved due to their instability in the new environment. They are replaced by crystals with compositions typical for the respective growth zone. A propagating CO_2-vapor-front implies that – depending on the reaction conditions – the thickness of the carbothermal nosean-sanidinite zone can increase which has a direct impact on the buildup of the internal overpressure of the magma chamber.

The oldest zircons in nosean-sanidinite have ages of 32.6 ± 4.1 ka, which is ~20 ka before eruption (12.900 BP), whereas the youngest zircons have near eruption age (Schmitt et al. 2010). Accordingly, the first nosean-sanidinite cumulates were formed already 20 ka prior to eruption. This “old” crystal age implies the existence of highly evolved phonolite for ~10-20 ka (Schmitt et al. 2010). Since the formation of nosean requires an extremely Ca-depleted environment, it is assumed that also the CO_2-gas cap began to form around this time. This long

exposure time explains also the strong carbothermal overprint of generation-1 crystals in some samples. In particular, the carbonate-rich samples investigated by Liebsch (1996) show severe dissolution characteristics which are filled with carbonate and HFSE-minerals formed by carbothermal vapor deposition.

4.4.6 CONTRIBUTION OF CO_2 TO THE ERUPTION MECHANISM

There is evidence for a mafic magma recharge short time prior to eruption, but it was ruled out as eruption trigger (Wörner and Wright 1984). Foaming of the lava was also excluded as trigger of the eruption of Laacher See Volcano because the lowermost layer of eruption products consists of a centimeter thick fine-grained ash layer, which contains fragments of quartz pebbles, clay stone and wood pieces (Schmincke 2007). There are only a few sharply edged pieces of magmatic glass poor in vesicles. Therefore, the authors suggested heating of the groundwater, either by magmatic gas percolation or by ascent of the magma body initiated a sudden vaporization of the groundwater causing a fragmentation of the country rock, specifically of the clay units overlying the aquifers.

Phreatomagmatic activity is evident; the question, however, is if the interaction with external water was the trigger of the eruption. Two arguments speak against this assumption: 1) with certainty, interaction with external water is responsible for thermal anomalies of the groundwater in regions with magmatic activity. It is a common feature that gases escape from the magma chamber and diffuse to the surface. Eruption of magmas, however, is not the rule, and most of the plutons remain in the crust and die a thermal death. 2) There is evidence that the magma chamber was surrounded by thick carapace of crystallized igneous rocks, including mafic, intermediate and felsic cumulates (Tait 1988), which would hinder the magma body from rising. In addition, it should be noted that the LS-phonolite was a relatively cool melt (720 - 860°C).

The results of this study point to an active role of CO_2 during the magmatic process of one of the most violent eruptions in recent geological time in Europe. The contribution of CO_2 to the eruption process is still not understood (Schmincke 2008). Furthermore, the results of this study indicate the formation of a gas cap in the upper part of the magma chamber below the gastight layer, which allows to develop a high fluid pressure due to the accumulation of fluid and especially CO_2. Fenites typically show fracturing of the country rock, with carbonates filling up these fractures and veins (Elliott et al. 2018). In general, these carbonates are interpreted as carbonatite melt, which intruded into the fractures of the country rock. In the context of Laacher See Volcano, however, it seems more likely that brecciation was caused by CO_2 overpressure and healing of the fractures by carbonization.

Therefore, the question is still what might have triggered the eruption and how can a contribution of CO_2 be reconciled with the obvious phreatomagmatic processes? The combination of the results of this study with data for the model of the Laacher See magma chamber yielded the following six steps, leading to the eruption:

1. **Gas-tight sealing of the carapace and formation of a CO_2-gas cap:**
   CO_2 derived from the mantle or deeper levels of the plumbing system flushes through the phonolitic magma chamber and percolates towards the magma chamber roof. Carbothermal densification leads

to a sealing of the rigid crystal mush in the uppermost part of the magma chamber. Since CO_2 is prevented to escape into the country rock, it accumulates in the magma chamber roof and with time forms a pressurized CO_2-gas cap.

2. **Critical overpressure**

   Ongoing CO_2 flushing and accumulation in the CO_2-gas cap leads with time to a critical overpressure. The expansion of the CO_2 volume during ascent from deeper crustal levels to the phonolitic magma chamber enhances the pressure buildup in the CO_2-gas cap. Injection of high amounts of CO_2 with the magma recharge, leads to a sudden volume increase within the magma chamber and therefore accelerates the achievement of a critical overpressure (Caricchi et al. 2018).

3. **Failure of the cap rock and explosive expansion of the CO_2-gas cap**

   Failure of the cap rock occurs, when the internal pressure or fluid pressure exceeds the tensile strength of the cap rock. The critical pressure and thus failure of the carbothermally densified cap rock causes massive brecciation of the rigid upper part of the magma chamber. The induced pressure release causes an explosive expansion of pressurized CO_2 and fragments the rigid part of the magma chamber and country rock.

   This fragmentation process is most likely a multi-step, expansion driven CO_2 explosion starting in the magma chamber and spreading to the surface. Each fragmentation step lowers the pressure in the CO_2-gas-cap. The coupled CO_2 expansion causes further pressure buildup, which leads to further fragmentation of the rocks. With each step, CO_2 will continue to expand and, step by step, clear the way to the surface.

4. **Phreatomagmatic activity**

   The sudden release of “hot” CO_2 from the fluid cap moving to the surface vaporizes the groundwater and in consequence triggers further fragmentations blowing out the material to the surface.

5. **Magma eruption**

   The sudden pressure release has also consequences for the magma body as decompression lowers the liquidus temperature. Melting of the crystals along the grain boundaries mobilizes the crystal mush. Decompression boiling of the melt evokes degassing of volatiles such as H_2O dissolved in the magma and, this way, initiates the main phase of magma eruption. At shallower levels, the ascending magma gets in contact with the different levels of aquifers, resulting in the Phreatomagmatic Plinian eruption of the Laacher See Tephra.

This process is not in contradiction with the phreatomagmatic eruption, but represents the missing link to the driving force, which triggered a chain reaction of eruption mechanisms including phreatomagmatic activity. Accordingly, carbothermal densification was a prerequisite for initiating the eruption of Laacher See Volcano. The two-step CO_2 gas explosion was triggered by 1) failure and thus massive brecciation of the cap rock due to overpressure and 2) explosive expansion of the CO_2-fluid cap. As long as the cap rock of the magma chamber is not gas-tightly sealed, CO_2 will penetrate into the country rock and rises further to the surface. The current CO_2 emanations in the Lake Laacher See (mofettes) show that the Laacher See magma chamber carapace is, at the present time, not sealed. Based on the zircon ages (Schmitt et al. 2010), at least 20 000 years are required to

produce a gas-tight seal and accumulate a CO_2-gas cap for a magma chamber with the size of the Laacher See Volcano. The gas emission pattern at the surface produced by the above described scenario is consistent with gas emission pattern, measured from recent explosive volcanos. In general, CO_2 emanations dominate between and prior eruptions, whereas more melt soluble volatiles, such as water (> 85%) and lesser CO_2 and SO_2 (2-10%) and halogen gases (HF, HCL, CO) prevail when the magma reaches the surface (Edmonds et al. 2018).

5 SARAY VOLCANO AND LAACHER SEE VOLCANO IN THE CONTEXT OF CO_2

Both, Laacher See Volcano (LSV) and Saray Volcano (SV), differ clearly in their geological and tectonic setting as well as the size of the magma chamber. An overview of the geological setting of the volcanos shows Table 4. In particular, sanidine-rich ejected bombs from Saray Volcano and Laacher See Volcano show several differences summarized in Table 4. One of the most remarkable difference is the occurrence of sanidine megacrysts at Saray Volcano compared to equigranular sanidine-rich hypidiomorphic to holocrystalline cumulates, the so called "sanidinites" at Laacher See.

They have also many aspects in common: Both are explosive volcanos and erupted (ultra-)potassic trachytic to phonolitic melts accompanied with carbonate-rich rocks, and both contain ejected sanidine-rich cumulates. Common feature of both volcanoes is also the occurrence of pseudo-oscillatory zoned sanidine phenocrysts in the trachytic/phonolitic melt (Chapter 3 in this study; Ginibre et al. 2004), and in both areas are manifold indications of high CO_2 activity. Current CO_2 emissions, such as mofettes in case of Laacher See Volcano and the formation of massive travertine deposits in the neighborhood of Saray Volcano, demonstrate ongoing high CO_2 activity in these regions. In addition, eruption products of both volcanos show an enormous accumulation of CO_2 in the magma chamber roof.

Table 4: Overview of the main differences of the alkaline/potassic explosive volcanos Saray Volcano (Northwest Iran) and Laacher See Volcano (Eifel, Germany) and the characteristics of the ejected bombs

Parameter	Saray Volcano	Laacher See Volcano
Geological Setting	Subduction-related	Intraplate
Depth of the magma chamber	**Deep crust (~ 30 km)**	**Shallow crust (~ 5-6 km)**
Temperature of the magma	> 980°C	740-860°C
Eruption style	Dome eruption	Phreatomagmatic Plinian eruption
Type of felsic cumulate	- High melt/crystal ratio - located in interior of the magma chamber	- Holocrystalline to hypidiocrystalline - located in the magma chamber roof
Special feature	Sanidine megacrysts up to 10 cm	Cavity crystals in the felsic cumulates, specifically HFSE-minerals
Bombs		
Proportion of melt	High	Low to no melt
Texture	Porphyric	Equigranular
Size of sanidine phenocrysts	1-10 cm	< 5mm
Sodalite group minerals	-	haüyne and nosean
Carbonatite	Calcite + dolomite	Mn-bearing calcite

The following part discusses the extent to which the results of the two case studies are applicable to other alkaline volcanos in general. The focus is on the influence of CO_2 on the alkaline explosive volcanism, including how the boundary conditions such as the depth of the magma chamber influence the process.

5.1 CONTRIBUTION OF CO_2 TO RESORPTION, MINERAL ZONING AND MEGACRYST FORMATION

At Saray Volcano, repeated heating evidently caused the growth of pseudo-oscillatory zoned sanidine megacrysts. CO_2 flushing through the magma chamber transferred heat from the mantle or deeper parts of the plumbing system to the reaction site (see chapter 3.8.3). Based on the interpretation of microtextures, the growth of the megacrysts is the result of two different processes, both caused by heat transfer via CO_2:

1) The formation of pseudo-oscillatory zoning of Ba-rich sanidine can be explained by the periodic percolation of CO_2. The evoked repeated heating of the melt leads to cyclic resorption and recrystallization of the minerals. Depending on the temperature deviation from the liquidus temperature, the growth of smaller crystals in the groundmass is suppressed and the growth of larger ones is promoted.
2) Strong resorption of crystals such as sanidine requires a significant increase in the temperature of the melt. This requires a huge influx of CO_2, which can be caused by magma charging.

A similar sawtooth-like zoning pattern of sanidine (pseudo-oscillatory PO-type sanidine) has been reported by Ginibre et al. (2004) for the Laacher See tephra (LS-tephra). The authors calculated a temperature difference of ~100°C between growth and resorption cycle. They attributed the main resorption to reheating of the melt due to magma recharge, while explaining a minor resorption by convection of the crystals between the differently tempered layers in the magma chamber (see Figure 48 in Chapter 4.2.1). The strong resorption observed in the Upper LS-tephra (bottom of the magma chamber) and the predominantly pseudo-oscillatory zoning in the Middle LS-tephra were explained by a hot magma recharge, and the temperature contrast between the two different melts initiated convection of the melts in the magma chamber. This concept was justified by the occurrence of hybrid rocks at the top of the deposit (bottom of the magma chamber). According to Wörner and Wright (1984), mingling of hot (~1080°C) basanite melt with the phonolitic magma occurred shortly prior to the eruption. However, Bachmann and Bergantz (2006) stated that the conduction is most likely too slow to explain the reheating of the melt. They estimated that it take several millions of years to increase the temperature in the magma chamber by about 50°C.

There are several indications for high CO_2 flux through the magma chamber of Laacher See Volcano and its accumulation in the top of the magma chamber, such as CO_2-inclusions in nosean (see Chapter 4.3.3). Still persisting CO_2 emissions in the lake Laacher See has mantle signature (Taylor et al. 1967; Giggenbach et al. 1991). It is therefore likely that not only the injection of the mafic melt, but in particular the simultaneous supply of CO_2 caused both, the strong resorption of sanidine in the lower part of the magma chamber and pseudo-oscillatory zoning in the middle and upper part of the magma chamber.

5.2 FACTORS CONTROLLING THE GROWTH OF MEGACRYSTS

Why did sanidine grow to megacrysts at Saray Volcano, but not at Laacher See Volcano, even though they were both exposed to massive CO_2 percolation?

The main reason is obviously the temperature of the magma. Thermobarometric calculations for Saray Volcano yielded temperatures of 980-990°C for the early-erupted group I trachytes, where the biggest sanidine megacrysts were formed. This temperature corresponds to the liquidus temperature of sanidine (980-100°C) at comparable pressures (Kunzmann 2010). Fluctuation around these temperatures and repeated reheating of the melt prevents effective nucleation of a high number of (small) groundmass crystals, but promotes the formation of few larger crystals that can grow to megacrysts. The liquidus temperature of sanidine at more shallow levels in a depth of 5-8 km is at lower temperatures around 875-900°C (1-3 kbar; Kunzmann 2010). In case of Laacher See Volcano, however, the temperature of the phonolitic melt was even lower, ranging between ~840-860°C in the lower part and ca. 720°C in the upper part of the magma chamber (Wörner and Schmincke, 1984a, 1984b; Harms and Schmincke, 2000; Berndt et al., 2001; Harms et al., 2004). The temperatures below the liquidus of sanidine (875-900°C at 1-3 kbar) may promote groundmass crystals to grow effectively. Latter differences may explain the high crystallinity and the small grain size of sanidine crystals at Laacher See Volcano in comparison to megacryst formation in Saray Volcano.

Another aspect that needs to be considered, is the depth of the magma chamber: the magma chamber of Saray Volcano is located in the lower crust at ~40 km (see Chapter 3.4.1.), while the Laacher See magma chamber is estimated to depths of 5-8 km (Harms et al. 2004). In the lower crust, the temperature difference between the magma chamber and the host rock is small, allowing the magma chamber to maintain the higher temperature for a longer period. In contrast, in the upper crust, the large temperature gradient between the magma chamber and the cooler host rock promotes effective cooling and thus faster crystallization of the melt.

As a result, magma chambers with deeper geological settings promote the formation of sanidine megacrysts, since the temperatures can be more easily maintained in the range of the liquidus temperature. This explains also why sanidine megacrysts are typically observed in deeper located plutons. In addition, melt temperatures that fluctuate around the liquidus require a controlled supply of CO_2, which may be easily explained by repeated batches of CO_2 flushing the magma chamber. Thus, nucleation of fine-grained matrix can be avoided and the growth of large crystals is promoted.

5.3 CONTRIBUTION OF CO_2 TO ERUPTION MECHANISMS IN A DEEP VS. SHALLOW MAGMA CHAMBER

The results of this study show that regardless of the geological conditions of both volcanoes, CO_2 plays an important role in the eruption mechanism. In both cases, there is evidence of a magma recharge just before the eruption, but also of CO_2 accumulation in the top of the magma chamber. To trigger an eruption, a critical overpressure in the magma chamber has to be established first. Increase in the internal pressure can take place by increasing the volume of melt e.g. by magma recharge. However, Bachmann & Bergantz (2006) intervened that a magma recharge would take too long to heat up the whole magma chamber via conduction or mixing. Therefore, a large volume of magma must be injected in the magma chamber to increase the internal pressure.

Another trigger for the eruption is an excess of volatiles. The pressure dependence of fluid compressibility can be decisive for an overpressure. The results of this study showed that the fluid of these volcanoes consists predominantly of CO_2 and therefore is available as free fluid phase at greater depths. Plutons surrounded by carbothermal fenites and solvothermally formed ore deposits indicate the intensive reaction of the country rock with escaping CO_2. However, there are also manifold examples of magmatic systems with high CO_2 exhalation without explosive eruption.

In great depths, the hydrostatic pressure is the same as the lithospheric pressure, and therefore the external hydrostatic pressure prevents CO_2 to escape. In consequence, the rate of CO_2 influx is critical to the generation of an overpressure caused by the accumulation of CO_2 in the magma chamber. The case of Saray Volcano has shown that the injected lamprophyric magma was not only a source of heat but also carrier for a large amount of extra CO_2. Based on these results, it is suggested that not the ascent of the minette magma itself was the trigger of the eruption, but the sudden addition of a large volume of CO_2 caused the critical overpressure. At shallow depths in the upper crust, the hydrostatic pressure is lower than the lithospheric pressure. The generation of an internal fluid pressure in the magma chamber facilitates the migration of CO_2 and other fluids into the bedrock, from where it can diffuse to the surface or alter the bedrock to form, for example, fenites. Local brecciation of fenites around plumes prevents violent eruptions, as the formation of a network of open fractures compensates the formation of a fluid overpressure. Seismic tremor, which is often regarded as a precursor of an eruption, can be the result of such brecciation.

Therefore, an actively sealed margin of the magma chamber is required as a gas-tight cap-rock to allow the accumulation of fluid within the magma chamber and ultimately the generation of overpressure. The following factors were identified as critical to carbothermal densification. By combining these factors, the prerequisite for building up a critical overpressure in the upper magma chamber can be met, which then might trigger an eruption.

1. **High rates of CO_2 production** over a long period together with **sufficient Ca supply** in the system: The extraction of Ca from the melt and leaching from silicates on the one hand and the formation of carbonate on the other hand require a free CO_2 fluid phase. Carbonate formation is prevented if Ca is not

sufficiently available in the magmatic system or the ambient temperature is too high. In consequence, CO_2 escapes into the country rock.

2. **Temperature of the melt** and **size of the magma chamber:** Size and temperature of the magma chamber are also critical factors. Thermal death of a magma will occur if the size of the magma chamber is too small, and/or heat supply e.g. via magma recharge is too low to prevent a fast cooling of the magma body. Finally, the magma will end up as a fully crystallized pluton.
3. **Properties of the country rock:** The country rock has to be sufficiently dense. A weak country rock cannot withstand the fluid pressure from the magma chamber and brecciation will enable the gas to escape. The tensile strength of slates is 1,400 psi and that of sandstone 900 psi, while the tensile strength of granite is 19,000 psi and of trap rocks about 20,000 psi. The formation of fenites is an evidence for carbothermal overprint of the country rock.
4. **Properties of the margin of the magma chamber:** In particular, in the upper crustal level, in addition to the carbothermal densified country rock, the formation of a **crystallized, rigid section** in the magma chamber roof is critical for the formation of a CO_2-gas cap in the magma chamber. Only then, the accumulation of fluids within the open spaces is possible. The thickness of the required carbonated layer is the controlling parameter for the critical overpressure and depends on the size of the magma chamber. The more compact the carapace, the heavier the expected explosion.

The eruption products of both volcanos indicate a series of explosions during the ascent. The failure of the carapace is expected to trigger the different explosive processes. The sudden release of CO_2 implies an enormous volume expansion of CO_2, which heavily fragments all materials on the way to the surface. Consequently, massive CO_2 emissions are expected to be the harbinger of the explosive eruption. Correspondingly, gas-monitoring of active volcanoes shows that at first, before an eruption, the gas flux of both, CO_2 and SO_2, is significantly lower than normal, followed by massive CO_2 degassing before an during the highly explosive eruption (Allard et al. 1989; Aiuppa et al. 2011). The expected subaerial CO_2-explosion and thus the fragmentation of the country rock correspond to volcano-tectonic earthquakes observed prior to eruption (Zobin 2012).

With the sudden decompression of CO_2 after brecciation-induced depressurization, a sudden drop in temperature in the local environment is expected. Accordingly, the cumulates in the uppermost part of the magma chamber should be quenched. This explains brittle fragmented glass pieces observed in the lowermost layer of the Laacher See Volcano deposit, reported by (Schmincke 2008). This also explains the high level of melt quenched in the group 1 samples of the Saray Volcano compared to the later erupted group 2 samples.

5.4 INDICATIONS FOR CO_2 IN FELSIC MAGMAS

The detection of CO_2 in magmatic system is a challenge. A major problem is that only a limited number of igneous minerals can incorporate CO_2. Therefore, the following section summarizes various direct and indirect indications for CO_2.

5.4.1 DIRECT INDICATORS

Monitoring **CO_2 emission on the surface** is the most effective method. This can be performed directly at the vent, in fumaroles, as diffusive soil gas or in CO_2 enriched aquifers. There are attempts to measure geological CO_2 emission by satellite on a global scale. However, it is difficult to process the data due to the generally high levels of CO_2 concentrations in the atmosphere. Currently, CO_2 emission of about 20 volcanos are monitored. They show that CO_2 emissions have a characteristic pattern before, during and after eruptions (Allard et al. 1989; Aiuppa et al. 2011). Therefore, the CO_2 emission patterns should be combined with the petrological analysis of the eruption products. Together they are a powerful tool to understand the eruption mechanism.

For historic volcanoes, a direct measurement of CO_2 is of course not possible. However, travertine deposits can be witness for long lasting CO_2 emissions in the region, e.g. the formation of massive travertine deposits up to 150 m high in NW Iran. Isotope measurements of CO_2 emissions as well as of travertine deposits may show, if the emitting gas is mantle derived or has a crustal source.

A clear indicator for CO_2 is the detection of CO_2 containing fluid inclusions, CO_2 in matrix glass or melt inclusions. However, the absence of CO_2 in matrix glass, melt inclusions or fluid inclusion does not prove that CO_2 was not present in the melt. It has to be considered that the degassing behavior of CO_2 and H_2O is completely different. CO_2 degasses already at a lithospheric depth of ~ 70 km, whereas H_2O – if present – is still dissolved in the silicate melt (Dixon and Stolper 1995). At lower depth, CO_2 occurs as a free fluid phase together with the melt. This is the major reason why most matrix glass and also melt inclusions do not reflect the presence of CO_2. Another difficulty arises with regard to fluid inclusions, because several criteria must be met to trap fluid inclusions. Not only that the fluid has to exist as a separate phase, the crystal needs to grow in a specific way to trap the fluid, as often, the fluid inclusions are too small for a proper analysis.

Clear indicators are minerals, which are able to incorporate CO_2 like carbonates. In igneous systems, apatite and sodalite group minerals have this ability. Change in mineral assemblage, like the decomposition of clinopyroxene to dolomite and quartz indicates extreme CO_2 saturated conditions ($X(CO_2) \geq 0.9$). Raman or FTIR analytics are analytical tools, which enable the detection of even a small amount of CO_2 or H_2O in minerals, glass or fluid inclusions.

5.4.2 INDIRECT INDICATORS

Nonetheless, it is not always possible to find direct indications for CO_2. Especially with a permeable cap rock, CO_2 can easily escape without any trace. This study showed that there are several indirect methods indicating the presence of CO_2 in the magma.

- Miarolithic cavities and cavities between crystals in magmatic rocks indicate the presence of a fluid cap. The late degassing of H_2O in contrast to CO_2 has the consequence that CO_2 is in most cases the phase that accumulates preferentially in the gas cap.
- Vapor deposited carbonates. This requires careful textural analysis of a variety of eruption products to avoid misinterpretation.
- Microtextures showing etching/leaching of minerals combined with a new generation of minerals
- Oscillatory, saw-tooth resorption/crystallization pattern of sanidine.
- The depletion of divalent elements, in particular Ca, and the occurrence of Ca-poor phases together with carbonates are indicators of an interaction of CO_2 with the melt.

6 CONCLUSION

The study of ejected magmatic cumulates provided the major clues to decipher pre- and syn-eruptive processes of both volcanos because, in contrast to highly fragmented tephra, the original mineral assemblage and mineral relationships are preserved. Fast ascent and ejection of the cumulates and rapid cooling during the explosive eruption quenches the latest stage of mineral reactions and (relicts of) xenocrysts. In case of **Saray Volcano**, two different layers with sanidine-rich cumulates represent snapshots of temporally and spatially distinct conditions just before and during the eruption. Combined with the completely crystallized, fully reacted lava samples, they provide valuable insights into the magmatic system and help to identify changes in conditions over time. **Laacher See Volcano** erupted decimeter sized fragments of the crystallized margins from a shallow magma chamber including sanidinites representing cumulates from the upper part of the magma chamber. The different types of sanidinite provide unique insight into the gas dominated processes in this sector of the magma chamber. The detailed investigation of the microtexture helped to comprehend the carbothermal processes including the carbothermal densification of the cap rock, which was crucial to initiate the eruption. The main findings of the two case studies are summarized below.

6.1 SARAY VOLCANO

Saray Volcano as a "natural lab": Following features qualify Saray Volcano as a "natural lab" to study quasi in-situ pre- and syn-eruptive magmatic processes. **The relatively small size of Saray Volcano** (~360 km²) implies that the magma body cannot buffer changes compared to larger igneous systems and small changes can more easily trigger a system response. The **phenocryst assemblage** of the investigated samples (trachyte and minette) consists of sanidine, diopside and phlogopite – a rather simple system. In particular, the **macro- to mega-sized phenocrysts** record a long history of resorption and crystallization as well as syn-eruptive mineral reactions. The occurrence of this paragenesis in all eruption products enabled to compare the samples and to derive a qualitative assessment of the mineral reaction stages and growth conditions. The **high Ba-concentrations** in the magmatic system resulted in extraordinary Ba zoning patterns preserved in sanidine. Due to preferential partitioning of Ba into alkali feldspar even small changes in the boundary conditions were immediately recorded in the sanidine crystals.

Calculated boundary conditions: Thermobarometric calculations of diopside in contact with trachytic melt yielded **temperatures** up to 1135°C in the lower part of the magma chamber and 980°C in the upper part of the magma chamber. **Crystallization depth** of trachyte ranged between 12 and 16 kbar, corresponding to the lower crust. Calculations based on mantle xenolith cargo in minette yielded **rapid ascent rates of 3 m/s** from a mantle source in more than 70 km depth.

Relationship of trachyte and lamprophyre (minette): The interaction of the two melts in the magma chamber is additional to the heat limited to the transfer of CO_2 + carbonatite and phlogopite (phl-II) into the trachyte and

entrainment of sanidine and phlogopite megacrysts from trachyte into minette. The rapid ascent rate suggests only short contact time between trachyte and minette during ascent (< 4h) and residence time at shallow depths during plugging of the vent by the trachytic lava dome (hours-days). The **unique resorption and zoning relationships** observed in case of sanidine and two chemically different types of phlogopite (phl-I and phl-II) in trachyte and in mafic and felsic minette provide an inimitable opportunity to retrace partitioning behavior of Ba and F between sanidine, phlogopite and melt depending on the reaction conditions and the present mineral assemblage.

Impact of CO_2: The study provides clear **evidence of the presence of CO_2 and its impact on magmatic processes**. There are many textural indications for CO_2 as the main species in the fluid phase leading to high $X(CO_2) > 0.9$ conditions at least in the upper part of the magma chamber and in felsic minette. **The heat transfer via CO_2** flushing keeps the trachytic magma at temperatures fluctuating around the liquidus temperature of sanidine (980-1000°C at 10-15 kbar). This explains the multiple pseudo-oscillatory zoning of Ba in sanidine in conjunction with different degrees of resorption events without any chemical changes typical for magma recharge. Under these conditions, the crystallization of sanidine in the groundmass was suppressed and sanidine phenocrysts could grow to megacrysts up to 10 cm in size. Consequences of **CO_2 percolation** is the flotation of these megacrysts into the upper magma chamber. Further, flushing the magma chamber with CO_2 and the associated heat transfer in combination with the **decomposition of carbonatite** lowers the viscosity of the trachytic melt, which enables a megacrysts containing melt to erupt. Most importantly, the massive influx of primarily CO_2 rich fluid initiated the explosive eruption. Major chemical changes are not the result of magma mixing or mingling but by **transfer of phl-I crystals and carbonatite** from minette into trachyte in the pressure shadow of upwards percolating CO_2-bubbles. The accumulation of exsolved CO_2 in minette magma as well as later in the trachyte magma result in the formation of a foam which lowers the density of the melt and provides enough **buoyancy** for the magma to rise. Finally, the accumulation of CO_2 in the top of the trachytic magma chamber led to a **critical overpressure**, which in consequence initiated the explosive eruption.

6.2 LAACHER SEE VOLCANO

Laacher See Volcano is an extraordinary case study for carbothermal processes. A broad variety of felsic magmatic cumulates, the so called “sanidinites”, was investigated with focus on the role of CO_2 in order to unveil the processes in the top part of the magma chamber. Based on the results, the existing model of the Laacher See magma chamber can be refined. Petrological investigation revealed a systematic pattern in mineral paragenesis, whole-rock composition and mineral composition and abundance of CO_2-inclusions in sodalite minerals from dark haüyne-sanidinite to carbonate bearing nosean-sanidinite. These rocks record the transition from magmatic crystallization to fluid dominated carbothermal reaction. The change is recorded in nosean-sanidinites, which represent the rigid part of the magma chamber roof. It is characterized by two specific features: 1) crystallization of sanidine, nosean and REE-Th-U-rich zircon from a highly evolved phonolitic magma, 2) carbothermal overprint

and crystallization of calcite, trace-element poor zircon with thorite inclusions, pyrochlore and Ca-depleted sanidine and nosean.

Carbothermal processes include dissolution or leaching, transport and precipitation by a CO_2-rich gas phase. This way, Ca is extracted from the magma and is leached from Ca-bearing silicates and transported to the cooler country rock or outermost magma chamber margin, where it crystallized when temperatures get below the decarbonation temperature < 680°C. With time, a gas tight carbothermally densified layer develops preventing further uprising gas to escape. Now, CO_2 can accumulate and form a CO_2-gas-cap. This has several consequences:

- The CO_2 atmosphere in the gas cap induces strong dissolution and recrystallization processes
- Purification of minerals due to preferential extraction of divalent elements and REE, for example Ca-bearing feldspar reacts to Ca-depleted feldspar and carbonate, or REE-rich zircon reacts to pure zircon and pyrochlore. In this context, consequences for geochronology and thermometry have to be considered
- Sealing of the magma chamber roof and accumulation of CO_2 in a gas cap creates a subsystem with an overpressure, that can be higher than the hydrostatic pressure
- The overpressure of the gas cap hinders CO_2 bubbles to escape from the magma body. As a result, a foam layer will be formed at the interface of the magma and the gas cap.
- The gas cap represents a dynamic vapor front: With increasing pressure, CO_2 bubbles will enter the gas cap, consequently the gas cap expands
- Sodalite group minerals are excellent indicators of the prevailing fluid compositions. The systematic increase of CO_2-inclusions entrapped in haüyne/nosean and structural bound CO_2 in nosean from dark haüyne-sanidinite, bright haüyne-sanidinite to nosean-sanidinite indicates that bubble accumulation was strongest in the uppermost part of the magma chamber.
- In the foam layer, the preferential extraction of Ca promotes a Na-enriched environment. With distance to the foam layer, Ca extraction by CO_2 degassing is less effective. The results of this study show that haüyne and nosean cannot coexist at the sample place, but may grow in neighboring places within the same magma chamber depending on the reaction conditions.
- By accumulation of CO_2, the critical overpressure can be exceeded, causing failure of the cap-rock

Changed reaction conditions are documented in two generations of minerals: 1) Generation-1 minerals reflect the magmatic stage and 2) Generation-2 minerals are the result of a carbothermal overprint. The combination of the different microtextures and mineral reactions with the change in whole-rock and mineral compositions resulted into an overall concept, which allows insight into the critical phase at the very beginning of the most violent explosive eruptions in recent geological history of Central Europe.

Many phenomena can be easily explained by introducing carbothermal processes in the presence of a free CO_2-gas phase. Three new findings were derived.

- **LS Carbonatite in a new light:** the carbonate-bearing nosean sanidinites correspond exactly with the described carbonate-rich syenites. This study shows that the carbonates were formed by carbothermal vapor deposition. Therefore, the interpretation of the carbonate-rich syenite from Laacher See as carbonatite formed from a melt has be to be revised.
- **Impact of carbothermal interaction:** Extraction of divalent elements occurred in small scale by leaching in particular Ca, Mn and REE from generation-1 minerals in sanidinites and in large scale directly from the phonolitic melt leading to a depletion of Ca in the phonolitic melt. Result of this process is the formation of nosean and Ca-poor sanidine together with calcite in nosean-sanidinite. A further aspect is the "purification" of silicates and crystallization of extracted divalent elements and REE as oxides (pyrochlore) or carbonate (Mn-bearing calcite). In consequence, this process can explain the formation of REE deposits in the associated carbonate-rich rocks.
- **Carbothermal overprint** of the rigid top part of the magma chamber is comparable with the processes of geological CO_2 sequestration. Ca leached from minerals and the melt are transported with CO_2 to the outer margin of the magma chamber and crystallize as purified secondary minerals and carbonates in the cooler environment. Carbonation by chemical vapor deposition took place in both, the country rock and the outer margin of the LS magma chamber, leading to
  - a densification of the country rock and the rigid top part of the magma chamber,
  - the formation of a gas-tight impermeable carapace by sealing the top margin of the magma chamber, which impedes the escape of fluids and enables the formation of a fluid cap,
  - build-up a sufficient fluid overpressure. Due to the accumulation of CO_2 in the fluid cap, a foam layer forms in the melt. Over time, the foam layer migrates as a dynamic vapor front towards the center of the magma chamber.

Finally, **failure of the carapace** due to ongoing CO_2 accumulation acts as tipping point for the explosive eruption. High influx of CO_2 can generate a critical overpressure, which triggers a three-step explosion. 1) Brecciation of the country rock and the rigid part of the magma chamber due to CO_2 overpressure. 2) The following sudden pressure release causes an explosive expansion of CO_2 leading to further brecciation and fragmentation of the wall-rock and the rigid part of the magma chamber. 3) Additional phreatomagmatic explosion due to sudden vaporization of the aquifer groundwater with the ascending CO_2 accelerates the fragmentation of the solids and blows the way to the surface.

6.3 RESUMÉE

This study showed that CO_2 has a great impact not only on eruption dynamics, but also on crystallization conditions. CO_2 degasses early, in the upper mantle or lower crust. Therefore, CO_2 is present as a free CO_2 gas phase at crustal conditions. Heat from the deeper source is transferred when CO_2 ascents from mantle depths or deeper parts of the plumbing system and flushes through a magma chamber. This mechanism may be therefore considered to be a major driver for preventing magmas to cool or even reheating them. CO_2 percolation is expected to be continuous but may change in intensity. Therefore, it is a perfect medium to keep magma temperatures at constant levels. If temperature is buffered at liquidus of anhydrous minerals, this result e.g., sanidine to grow, gets resorbed and grows again. This produces a pseudo-oscillatory growth zoning. If heat transfer inhibits undercooling of the magma and therefore nucleation, perfect conditions are given for megacryst formation. This condition is most likely in the deeper crust compared to shallow magma chambers, as the cooler wall-rock promotes undercooling.

CO_2 is a carrier of divalent elements. The case study of Laacher See Volcano demonstrates the preferential leaching and extraction of these elements.

CO_2 has also a major role in eruption dynamics, e.g. due to gas accumulation in the upper part of the magma chamber. At deeper levels, the high hydrostatic pressure is sufficient to hinder CO_2 gas escape into the country rock. At shallow levels, the hydrostatic pressure is lower than the internal fluid pressure. Consequently, CO_2 escapes to the country rock. Prerequisite for CO_2 gas accumulation is a gas-tight barrier, e.g. via carbothermal densification of the crystallized magma chamber roof.

The mantle isotope signature of carbonates does not demonstrate crystallization of carbonatite from a melt since carbothermally-formed calcite generated by CO_2 derived from the mantle has the same signature. Carbonation occurred at both volcanos: at Saray Volcano, carbonatite was formed under mantle conditions and was transferred into trachyte; at Laacher See Volcano, carbonates are a par excellence example of a carbothermal vapor deposited carbonate.

Although the impact of CO_2 can be severe, signs of CO_2 in the rocks are often inconspicuous. The **rapid magma ascent and rapid cooling of the samples** enabled direct insights into the processes within the magma chamber because it preserved the respective condition before the whole system was able to equilibrate. However, careful petrographic and mineral chemical investigation focusing on mineral reactions and microstructures of a whole range of different samples are essential to understand the impact of CO_2 and to avoid misinterpretation of geochemical data.

7 REFERENCES

Aeschbach-Hertig W, Kipfer R, Hofer M, et al (1996) Quantification of gas fluxes from the subcontinental mantle: The example of Laacher See, a maar lake in Germany. Geochim Cosmochim Acta 60:31–41. doi: 10.1016/0016-7037(95)00370-3

Aghazadeh M, Prelević D, Badrzadeh Z, et al (2015) Geochemistry, Sr–Nd–Pb isotopes and geochronology of amphibole- and mica-bearing lamprophyres in northwestern Iran: Implications for mantle wedge heterogeneity in a palaeo-subduction zone. Lithos 216–217:352–369. doi: 10.1016/j.lithos.2015.01.001

Aiuppa A, Burton M, Allard P, et al (2011) First observational evidence for the CO_2-driven origin of Stromboli's major explosions. Solid Earth 2:135–142. doi: 10.5194/se-2-135-2011

Aiuppa A, Burton M, Caltabiano T, et al (2010) Unusually large magmatic CO_2 gas emissions prior to a basaltic paroxysm. Geophys Res Lett 37:1–5. doi: 10.1029/2010GL043837

Allard P, Dajlevic D, Delarue C (1989) Origin of carbon dioxide emanation from the 1979 Dieng eruption, Indonesia: Implications for the origin of the 1986 Nyos catastrophe. J Volcanol Geotherm Res 39:195–206. doi: 10.1016/0377-0273(89)90058-9

Anderson AT, Davis AM, Lu F (2000) Evolution of Bishop Tuff rhyolitic magma based on melt and magnetite inclusions and zoned phenocrysts. J Petrol 41:449–473. doi: 10.1093/petrology/41.3.449

Ayati F, Yavuz F, Asadi HH, et al (2013) Petrology and geochemistry of calc-alkaline volcanic and subvolcanic rocks, Dalli porphyry copper-gold deposit, Markazi Province, Iran. Int Geol Rev 55:158–184. doi: 10.1080/00206814.2012.689640

Ayres VL, Higgins WD (1939) Differentiation in Xenolithic Lamprophyre Dikes at Marquette, Michigan. J Geol 46:561–582. doi: 10.1086/624813

Azizi H, Asahara Y, Tsuboi M, et al (2014) The role of heterogenetic mantle in the genesis of adakites northeast of Sanandaj, northwestern Iran. Chemie der Erde 74:87–97. doi: 10.1016/j.chemer.2013.09.008

Azizi H, Moinevaziri H (2009) Review of the tectonic setting of Cretaceous to Quaternary volcanism in northwestern Iran. J Geodyn 47:167–179. doi: 10.1016/j.jog.2008.12.002

Azizi H, Nouri F, Stern RJ, et al (2018) New evidence for Jurassic continental rifting in the northern Sanandaj Sirjan Zone, western Iran: the Ghalaylan seamount, southwest Ghorveh. Int Geol Rev 62:1635–1657. doi: 10.1080/00206814.2018.1535913

Azizi H, Stern RJ (2019) Jurassic igneous rocks of the central Sanandaj–Sirjan zone (Iran) mark a propagating continental rift, not a magmatic arc. Terra Nov. doi: 10.1111/ter.12404

Bachmann O, Bergantz G (2008) The Magma Reservoirs That Feed Supereruptions. Elements 4:17–21. doi: 10.2113/GSELEMENTS.4.1.17

Bachmann O, Bergantz GW (2006) Gas percolation in upper-crustal silicic crystal mushes as a mechanism for upward heat advection and rejuvenation of near-solidus magma bodies. J Volcanol Geotherm Res 149:85–102. doi: 10.1016/j.jvolgeores.2005.06.002

Balducci S, Leoni L (1981) Sanidine megacrysts from M. Amiata trachytes and Roccastrada rhyolites. Neues Jahrb Miner Abh 143:15–36

Barker AK, Troll VR, Ellam RM, et al (2012) Magmatic evolution of the Cadamosto Seamount, Cape Verde: Beyond the spatial extent of EM1. Contrib to Mineral Petrol 163:949–965. doi: 10.1007/s00410-011-0708-2

Beccaluva L, Coltorti M, Giunta G, Siena F (2004) Tethyan vs. Cordilleran ophiolites: A reappraisal of distinctive tectono-magmatic features of supra-subduction complexes in relation to the subduction mode. Tectonophysics 393:163–174. doi: 10.1016/j.tecto.2004.07.034

Becker H, Wenzel T, Volker F (1999) Geochemistry of glimmerite veins in peridotites from lower Austria-implications for the origin of K-rich magmas in collision zones. J Petrol 40:315–338. doi: 10.1093/petroj/40.2.315

Belousova EA, Griffin WL, O'Reilly SY, Fisher NI (2002) Igneous zircon: Trace element composition as an indicator of source rock type. Contrib to Mineral Petrol 143:602–622. doi: 10.1007/s00410-002-0364-7

Berberian F, Berberian M (1981) Tectono-plutonic episodes in Iran. In: Geodynamics Series, Vol. 3. pp 5–32

Berberian M, King GCP (1981) Towards a paleography and tectonic evolution of Iran. Can J Earth Sci 18:210–265. doi: 10.1139/e81-019

Berger A, Roselle G (2001) Crystallization processes in migmatites. Am Mineral 86:215–224. doi: 10.2138/am-2001-2-302

Berndt J, Holtz F, Koepke J (2001) Experimental constraints on storage conditions in the chemically zoned phonolitic magma chamber of the Laacher See volcano. Contrib to Mineral Petrol 140:469–486. doi: 10.1007/PL00007674

Blundy J, Cashman K V., Rust A, Witham F (2010) A case for CO_2-rich arc magmas. Earth Planet Sci Lett 290:289–301. doi: 10.1016/j.epsl.2009.12.013

Bodinier J-L, Menzies MA, Nombumichi S, et al (2004) Silicate, Hydrous and Carbonate Metasomatism at Lherz, France: Contemporaneous Derivatives of Silicate Melt-Harzburgite Reaction. J Petrol 45:299–320. doi: 10.1093/petrology/egg107

Bogaard P, Schmincke H-U (1985) Laacher See Tephra : A widespread isochronous late Quaternary tephra layer in central and northern Europe. Geol Soc Am Bull 96:1554–1571. doi: 10.1130/0016-7606(1985)96<1554

Bogaard PJF, Wörner G (2003) Petrogenesis of Basanitic to Tholeiitic Volcanic Rocks from the Miocene Vogelsberg, Central Germany. J Petrol 44:569–602. doi: 10.1093/petrology/44.3.569

Bogaard P, Schmincke HU (1984) The eruptive center of the late quaternary Laacher see tephra. Geol Rundschau 73:933–980. doi: 10.1007/BF01820883

Bogaard P, Hall CM, Schmincke H-U, York D (1989) Precise single-grain $^{40}Ar/^{39}$ Ar dating of a cold to warm climate transition in Central Europe. Nature 342:523–525. doi: 10.1038/342523a0

Bogaard P (1995) $^{40}Ar/^{39}Ar$ ages of sanidine phenocrysts from Laacher See Tephra (12,900 yr BP): Chronostratigraphic and petrological significance. Earth Planet Sci Lett 133:163–174. doi: 10.1016/0012-821X(95)00066-L

Bourdon B, Zindler A, Wörner G (1994) Evolution of the Laacher See magma chamber: Evidence from SIMS and TIMS measurements of UTh disequilibria in minerals and glasses. Earth Planet Sci Lett 126:75–90. doi: 10.1016/0012-821X(94)90243-7

Bowes DR, Kinloch ED, Wright AE (1964) Rhythmic amphibole overgrowths in appinites associated with explosion-breccias in Argyll. Mineral Mag J Mineral Soc 33:963–973. doi: 10.1180/minmag.1964.033.266.04

Brögger WC (1921) Die Eruptivgesteine des Kristianiagebietes, IV. Das Fengebiet in Telemark, Norwegen. Vit Selsk Skr Mat Nat Klasse, 1:494 pp. Kristiania (Oslo)

Brown WL, Parsons I (1994) Feldspars in igneous rocks. Feldspars their React Series C:449–499

Burton MR, Sawyer GM, Granieri D (2013) Deep Carbon Emissions from Volcanoes. Rev Mineral Geochemistry 75:323–354. doi: 10.2138/rmg.2013.75.11

Candela PA (1986) Toward a thermodynamic model for the halogens in magmatic systems: An application to melt-vapor-apatite equilibria. Chem Geol 57:289–301. doi: 10.1016/0009-2541(86)90055-0

Canil D (1990) Experimental study bearing on the absence of carbonate in mantle-derived xenoliths. Geology 18:1011–1013. doi: 10.1130/0091-7613(1990)018<1011:ESBOTA>2.3.CO;2

Caricchi L, Sheldrake TE, Blundy J (2018) Modulation of magmatic processes by CO_2 flushing. Earth Planet Sci Lett 491:160–171. doi: 10.1016/j.epsl.2018.03.042

Chadwick JP, Troll VR, Waight TE, et al (2013) Petrology and geochemistry of igneous inclusions in recent Merapi deposits: a window into the sub-volcanic plumbing system. Contrib to Mineral Petrol 165:259–282. doi: 10.1007/s00410-012-0808-7

Chafetz HS, Lawrence JR (1994) Stable Isotopic Variability within Modern Travertines. Géographie Phys Quat 48:257–273. doi: 10.7202/033007ar

Chamberlain KJ, Morgan DJ, Wilson CJN (2014) Timescales of mixing and mobilisation in the Bishop Tuff magma body: Perspectives from diffusion chronometry. Contrib to Mineral Petrol 168:1–24. doi: 10.1007/s00410-014-1034-2

Chapman NA, Powell R (1876) Origin of anorthoclase megacrysts in alkali basalts. Contrib to Mineral Petrol 6:365–394. doi: 10.1007/BF00384742

Chen W, Kamenetsky VS, Simonetti A (2013) Evidence for the alkaline nature of parental carbonatite melts at Oka complex in Canada. Nat Commun 4:1–6. doi: 10.1038/ncomms3687

Cherniak DJ (2002) Ba diffusion in feldspar. Geochim Cosmochim Acta 66:1641–1650. doi: 10.1016/S0016-7037(01)00866-3

Conticelli S, Peccerillo A (1989) Petrological significance of high-pressure ultramafic xenoliths from ultrapotassic rocks of Central Italy. Lithos 24:305–322. doi: 10.1016/0024-4937(89)90050-9

Cooper AF, Reid DL (1998) Nepheline Sövites as Parental Magmas in Carbonatite Complexes: Evidence from Dicker Willem, Southwest Namibia. J Petrol 39:2123–2136. doi: 10.1093/petroj/39.11-12.2123

Dahren B, Troll VR, Andersson UB, et al (2012) Magma plumbing beneath Anak Krakatau volcano, Indonesia: evidence for multiple magma storage regions. Contrib to Mineral Petrol 163:631–651. doi: 10.1007/s00410-011-0690-8

Dalton JA, Wood BJ (1993) The partitioning of Fe and Mg between olivine and carbonate and the stability of carbonate under mantle conditions. Contrib to Mineral Petrol 114:501–509. doi: 10.1007/BF00321754

Deevsalar R, Shinjo R, Ghaderi M, et al (2017) Mesozoic–Cenozoic mafic magmatism in Sanandaj–Sirjan Zone, Zagros Orogen (Western Iran): Geochemical and isotopic inferences from Middle Jurassic and Late Eocene gabbros. Lithos 284:588–607. doi: 10.1016/j.lithos.2017.05.009

Demazeau G (2008) Solvothermal processes: New trends in materials chemistry. J Phys Conf Ser 121:. doi: 10.1088/1742-6596/121/8/082003

Dixon JE, Stolper EM (1995) An Experimental Study of Water and Carbon Dioxide Solubilities in Mid-Ocean Ridge Basaltic Liquids. Part II: Applications to Degassing. J Petrol 36:1633–1646. doi: 10.1093/oxfordjournals.petrology.a037268

Edgar AD, Pizzolato LA, Sheen J (1996) Fluorine in Igneous Rocks and Minerals with Emphasis on Ultrapotassic Mafic and Ultramafic Magmas and Their Mantle Source Regions. Mineral Mag 60:243–257. doi: 10.1180/minmag.1996.060.399.01

Edmonds M, Grattan J, Michnowicz S (2018) Volcanic Gases: Silent Killers. In: Fearnley CJ, Bird DK, Haynes K, et al. (eds) Observing the Volcano World: Volcano Crisis Communication. Springer International Publishing, Cham, pp 65–83. doi: 10.1007/978-3-319-44097-2

Edmonds M, Wallace PJ (2017) Volatiles in magmatic Volcanic systems. Elements 1:19–24. doi: 10.2113/gselements.1.1.19

Eichelberger JC, Carrigan CR, Westrich HR, Price RH (1986) Non-explosive silicic volcanism. Nature 323:598–602. doi: 10.1038/323598a0

Elliott HAL, Wall F, Chakhmouradian AR, et al (2018) Fenites associated with carbonatite complexes: A review. Ore Geol Rev 93:38–59. doi: 10.1016/j.oregeorev.2017.12.003

Esperança S, Holloway JR (1987) On the origin of some mica-lamprophyres: experimental evidence from a mafic minette. Contrib to Mineral Petrol 95:207–216. doi: 10.1007/BF00381270

Evans BW, Bachmann O (2013) Implications of equilibrium and disequilibrium among crystal phases in the Bishop Tuff. Am Mineral 98:271–274. doi: 10.2138/am.2013.4280

Fischer S, Liebscher A, Wandrey M (2010) CO_2-brine-rock interaction - First results of long-term exposure experiments at in situ P-T conditions of the Ketzin CO_2 reservoir. Chemie der Erde 70:155–164. doi: 10.1016/j.chemer.2010.06.001

Foley S, Peccerillo A (1992) Potassic and ultrapotassic magmas and their origin. Lithos 28:181–185. doi: 10.1016/0024-4937(92)90005-J

Freda C, Gaeta M, Giaccio B, et al (2011) CO_2-driven large mafic explosive eruptions: The Pozzolane Rosse case study from the Colli Albani Volcanic District (Italy). Bull Volcanol 73:241–256. doi: 10.1007/s00445-010-0406-3

Frezzotti ML, Peccerillo A, Panza G, et al (2010) Earth's CO_2 degassing in Italy. doi: 10.3809/jvirtex.2009.00227

Frezzotti ML, Touret JLR (2014) CO_2, carbonate-rich melts, and brines in the mantle. Geosci Front 5:697–710. doi: 10.1016/j.gsf.2014.03.014

Fuchs K (1983) Recently formed elastic anisotropy and petrological models for the continental subcrustal lithosphere in southern Germany. Phys Earth Planet Inter. doi: 10.1016/0031-9201(83)90103-6

Gaeta M (1998) Petrogenetic implications of Ba-sanidine in the Lionato Tuff (Colli Albani Volcanic District , Central Italy). Mineral Mag 62:697–701. doi: 10.1180/002646198547927

Gagnevin D, Daly JS, Poli G, Morgan D (2005) Microchemical and Sr isotopic investigation of zoned K-feldspar megacrysts: Insights into the petrogenesis of a granitic system and disequilibrium crystal growth. J Petrol 46:1689–1724. doi: 10.1093/petrology/egi031

Geisler T, Rashwan AA, Rahn MKW, et al (2003) Low-temperature hydrothermal alteration of natural metamict zircons from the Eastern Desert, Egypt. Mineral Mag 67:485–508. doi: 10.1180/0026461036730112

Geisler T, Schaltegger U, Tomaschek F (2007) Re-equilibration of zircon in aqueous fluids and melts. Elements 3:43–50. doi: 10.2113/gselements.3.1.43

Gervasoni F, Klemme S, Rohrbach A, et al (2017) Experimental constraints on the stability of baddeleyite and zircon in carbonate- and silicate-carbonate melts. Am Mineral 102:860–866. doi: 10.2138/am-2017-5870

Gesing TM, Buhl JC (1998) Crystal structure of a Carbonate-Nosean $Na_8[AlSiO_4]$ $6CO_3$. Eur J Mineral 10:71–78

Ghiorso MS (1987) Chemical mass transfer in magmatic processes - III. Crystal growth, chemical diffusion and thermal diffusion in multicomponent silicate melts. Contrib to Mineral Petrol 96:291–313. doi: 10.1007/BF00371250

Giggenbach WF, Sano Y, Schmincke HU (1991) CO_2-rich gases from Lakes Nyos and Monoun, Cameroon; Laacher See, Germany; Dieng, Indonesia, and Mt. Gambier, Australia—variations on a common theme. J Volcanol Geotherm Res 45:311–323. doi: 10.1016/0377-0273(91)90065-8

Ginibre C, Kronz A, Wörner G (2002) High-resolution quantitative imaging of plagioclase composition using accumulated backscattered electron images: New constraints on oscillatory zoning. Contrib to Mineral Petrol 142:436–448. doi: 10.1007/s004100100298

Ginibre C, Wörner G, Kronz A (2004) Structure and dynamics of the Laacher See magma chamber (Eifel, Germany) from major and trace element zoning in sanidine: A cathodoluminescence and electron microprobe study. J Petrol 45:2197–2223. doi: 10.1093/petrology/egh053

Giordano D, Romano C, Papale P, Dingwell DB (2004) The viscosity of trachytes, and comparison with basalts, phonolites, and rhyolites. Chem Geol 213:49–61. doi: 10.1016/j.chemgeo.2004.08.032

Giuffrida M (2017) Magma Storage, ascent and degassing histories traced by textures and chamical zoning in crystals: Application to the CO_2-rich basaltic system of Mt. Etna Volcano. Università Degli Studi di Catania

Glazner AF, Johnson BR (2013) Late crystallization of K-feldspar and the paradox of megacrystic granites. Contrib to Mineral Petrol 166:777–799. doi: 10.1007/s00410-013-0914-1

Guo J, Green TH (1990) Experimental study of barium partitioning between phlogopite and silicate liquid at upper-mantle pressure and temperature. Lithos 24:83–95. doi: 10.1016/0024-4937(90)90018-V

Hajalilou B, Moayyed M, Hosseinzadeh G (2009) Petrography, geochemistry and geodynamic environment of potassic alkaline rocks in Eslamy peninsula, northwest of Iran. J Earth Syst Sci 118:643–657. doi: 10.1007/s12040-009-0054-1

Hamilton DL, Bedson P, Esson J (1989) The behaviour of trace elements in the evolution of carbonatites. In: (ed) Bell K. Carbonatites. Genesis and Evolution. Unwin Hyman, London. pp. 405-427

Harlov DE, Wirth R, Förster HJ (2005) An experimental study of dissolution-reprecipitation in fluorapatite: Fluid infiltration and the formation of monazite. Contrib to Mineral Petrol 150:268–286. doi: 10.1007/s00410-005-0017-8

Harms E, Gardner JE, Schmincke HU (2004) Phase equilibria of the Lower Laacher See Tephra (East Eifel, Germany): Constraints on pre-eruptive storage conditions of a phonolitic magma reservoir. J Volcanol Geotherm Res 134:135–148. doi: 10.1016/j.jvolgeores.2004.01.009

Harms E, Schmincke HU (2000) Volatile composition of the phonolitic Laacher See magma (12,900 yr BP): Implications for syn-eruptive degassing of S, F, Cl and H_2O. Contrib to Mineral Petrol 138:84–98. doi: 10.1007/PL00007665

Higgins MD (2011) Quantitative petrological evidence for the origin of K-feldspar megacrysts in dacites from Taapaca volcano, Chile. Contrib to Mineral Petrol 162:709–723. doi: 10.1007/s00410-011-0620-9

Higgins MD (2000) Origin of megacrysts in granitoids by textural coarsening: A crystal size distribution (CSD) study of microcline in the Cathedral Peak Granodiorite, Sierra Nevada, California. Geol Soc Spec Publ 168:207–219. doi: 10.1144/GSL.SP.1999.168.01.14

Hildreth W (1979) The Bishop Tuff: Evidence for the origin of compositional yonation in silicic magma chambers. GSA Spec Pap 180:43–75

Hoskin PWO, Black LP (2000) Metamorphic zircon formation by solid-state recrystallization of protolith igneous zircon. J Metamorph Geol 18:423–439. doi: 10.1046/j.1525-1314.2000.00266.x

Hunziker D, Burg JP, Bouilhol P, Von Quadt A (2015) Jurassic rifting at the Eurasian Tethys margin: Geochemical and geochronological constraints from granitoids of North Makran, southeastern Iran. Tectonics 34:571–593. doi: 10.1002/2014TC003768

Hynes A (1980) Carbonatization and mobility of Ti, Y, and Zr in Ascot Formation metabasalts, SE Quebec. Contrib to Mineral Petrol 75:79–87. doi: 10.1007/BF00371891

Jasmund K, Seck HA (1964) Geochemische Untersuchungen an Auswürflingen (Gleesiten) des Laacher-See-Gebietes. Beiträge zur Mineral und Petrol 10:275–295

Jaupart C, Vergniolle S (1988) Laboratory models of Hawaiian and Strombolian eruptions . Nature 331:58–60. doi: 10.1038/331058a0

Johnson BR, Glazner AF (2010) Formation of K-feldspar megacrysts in granodioritic plutons by thermal cycling and late-stage textural coarsening. Contrib to Mineral Petrol 159:599–619. doi: 10.1007/s00410-009-0444-z

Jones AP, Dobson D, Genge M (1995) Comment on physical properties of carbonatite magmas inferred from molten salt data, and application to extraction patterns from carbonatite-silicate magma chambers. Geol Mag 132:121–121. doi: 10.1017/S0016756800011481

Jones AP, Smith J V, Dawson JB (1982) Mantle Metasomatism in 14 Veined Peridotites from Bultfontein Mine, South Africa. J Geol 90:435–453. doi: 10.1086/628695

Keller J, Zaitsev AN (2006) Calciocarbonatite dykes at Oldoinyo Lengai, Tanzania: The fate of natrocarbonatite. Can Mineral 44:857–876. doi: 10.2113/gscanmin.44.4.857

Keppler H (1999) Experimental evidence for the source of excess sulfur in explosive volcanic eruptions. Science 284:1652–1654. doi: 10.1126/science.284.5420.1652

Kersch C, Peretó Ortiz S, Woerlee GF, Witkamp GJ (2004) Leachability of metals from fly ash: Leaching tests before and after extraction with supercritical CO2 and extractants. Hydrometallurgy 72:119–127. doi: 10.1016/S0304-386X(03)00125-7

Khalaji AA, Esmaeily D, Valizadeh M V., Rahimpour-Bonab H (2007) Petrology and geochemistry of the granitoid complex of Boroujerd, Sanandaj-Sirjan Zone, Western Iran. J Asian Earth Sci 29:859–877. doi: 10.1016/j.jseaes.2006.06.005

Krüger JC, Romer RL, Kämpf H (2013) Late Cretaceous ultramafic lamprophyres and carbonatites from the Delitzsch Complex, Germany. Chem Geol 353:140–150. doi: 10.1016/j.chemgeo.2012.09.026

Kunzmann T (2010) The solidus–liquidus phase relations of the Held-burg (Thuringia, Germany) phonolite up to 2.5 GPa. http://www.nets-work.de/phon.pdf

L'heureux I, Fowler AD (1994) A nonlinear dynamical model of oscillatory zoning in plagioclase. Am Mineral 79:885–891

Lake ET (2013) Crystallization and saturation front propagation in silicic magma chambers. Earth Planet Sci Lett 383:182–193. doi: 10.1016/j.epsl.2013.09.039

Landi P, La Felice S, Petrelli M, et al (2019) Deciphering textural and chemical zoning of K-feldspar megacrysts from Mt. Amiata Volcano (Southern Tuscany, Italy): Insights into the petrogenesis and abnormal crystal growth. Lithos 324–325:569–583. doi: 10.1016/j.lithos.2018.11.032

Lechmann A, Burg JP, Ulmer P, et al (2018) Metasomatized mantle as the source of Mid-Miocene-Quaternary volcanism in NW-Iranian Azerbaijan: Geochronological and geochemical evidence. Lithos 304–307:311–328. doi: 10.1016/j.lithos.2018.01.030

Lessing P, Grout CM (1971) Haüynite from Edwards, New York. Am Mineral 56:1096–1100

Liebsch H (1996) Die Genese der Laacher See-Karbonatite. Universität Göttingen

London D (1997) Estimating abundances of volatile and other mobile components in evolved silicic melts through mineral-melt equilibria. J Petrol 38:1691–1706. doi: 10.1093/petroj/38.12.1691

Long PE, Luth WC (1986) Origin of K-feldspar megacrysts in granitic rocks: implications of a partitioning model for barium. Am Mineral 71:367–375

Longpré MA, Troll VR, Hansteen TH (2008) Upper mantle magma storage and transport under a Canarian shield-volcano, Teno, Tenerife (Spain). J Geophys Res Solid Earth 113:1–11. doi: 10.1029/2007JB005422

Lowenstern JB (2000) A review of the contrasting behavior of two magmatic volcatiles: chlorine and carbon dioxide. J Geochemical Explor 69–70:287–290

Lustrino M, Wilson M (2007) The circum-Mediterranean anorogenic Cenozoic igneous province. Earth-Science Rev 8:1–65. doi: 10.1016/j.earscirev.2006.09.002

Lüttge A, Metz P (1993) Mechanism and kinetics of the reaction: 1 dolomite + 2 quartz = 1 diopside + 2 CO_2: a comparison of rock-sample and of powder experiments. Contrib to Mineral Petrol 115:155–164. doi: 10.1007/BF00321217

Marsh BD (2015) Magma Chambers. In: The Encyclopedia of Volcanoes, Second Edi. Elsevier Inc., pp 185–201

McDonough WF, Sun S s. (1995) The composition of the Earth. Chem Geol 120:223–253. doi: 10.1016/0009-2541(94)00140-4

Menand T, Phillips JC (2007) A note on gas segregation in dykes and sills at high volumetric gas fractions. J Volcanol Geotherm Res 162:185–188. doi: 10.1016/j.jvolgeores.2007.03.002

Mertes H, Schmincke HU (1985) Mafic potassic lavas of the Quaternary West Eifel volcanic field - I. Major and trace elements. Contrib to Mineral Petrol 89:330–345. doi: 10.1007/BF00381555

Mertes H, Schmincke HU (1983) Age distribution of volcanoes in the West-Eifel. N Jb Geol Paläont Abh 166:260–283

Meyer W, Stets J (2007) Quaternary uplift in the Eifel area. In: Ritter J.R.R., Christensen U.R. (eds) Mantle Plumes. Springer, Berlin, Heidelberg. pp 369–378

Middlemost EAK (1994) Naming materials in the magma/igneous rock system. Earth-Science Rev 37:215–224. doi: 10.1016/0012-8252(94)90029-9

Mitchell RH (1994) The lamprophyre facies. Mineral Petrol 51:137–146. doi: 10.1007/BF01159724

Moayyed M, Moazzen M, Calagari AA, et al (2008) Geochemistry and petrogenesis of lamprophyric dykes and the associated rocks from Eslamy peninsula, NW Iran: Implications for deep-mantle metasomatism. Chemie der Erde 68:141–154. doi: 10.1016/j.chemer.2006.04.002

Moghadam HS, Ghorbani G, Khedr MZ, et al (2014) Late Miocene K-rich volcanism in the Eslamieh Peninsula (Saray), NW Iran: Implications for geodynamic evolution of the Turkish-Iranian High Plateau. Gondwana Res 26:1028–1050. doi: 10.1016/j.gr.2013.09.015

Moinvaziri H (1985) Volcanisme tertiaire et quaternaire en Iran. Paris-Sud, Orsay

Mokhtari M, Farahbod A, Lindholm C, et al (2004) An approach to a comprehensive Moho depth map and crust and upper mantle velocity model for Iran. Iran Int J Sci 5:223–244

Moore JG, Sisson TW (2008) Igneous phenocrystic origin of K-feldspar megacrysts in granitic rocks from the Sierra Nevada batholith. Geosphere 4:387. doi: 10.1130/GES00146.1

Morgan GB, London D (2003) Trace-element partitioning at conditions far from equilibrium: Ba and Cs distributions between alkali feldspar and undercooled hydrous granitic liquid at 200 MPa. Contrib to Mineral Petrol 144:722–738. doi: 10.1007/s00410-002-0425-y

Morimoto N, Farbies J, Ferguson AK, et al (1988) Nomenclature of pyroxenes. Mineral Mag 52:535–550

Morizet Y, Brooker RA, Kohn SC (2002) CO_2 in haplo-phonolite melt: Solubility, speciation and carbonate complexation. Geochim Cosmochim Acta 66:1809–1820. doi: 10.1016/S0016-7037(01)00893-6

Nardi LVS, Formoso MLL, Jarvis K, et al (2012) REE, Y, Nb, U, and Th contents and tetrad effect in zircon from a magmatic-hydrothermal F-rich system of Sn-rare metal-cryolite mineralized granites from the Pitinga Mine, Amazonia, Brazil. J South Am Earth Sci 33:34–42. doi: 10.1016/j.jsames.2011.07.004

Nardi LVS, Plá Cid J, Bitencourt MF (2007) Minette mafic microgranular enclaves and their relationship to host syenites in systems formed at mantle pressures: Major and trace element evidence from the Piquiri Syenite Massif, southernmost Brazil. Mineral Petrol 91:101–116. doi: 10.1007/s00710-007-0186-4

Němec D (1975) Barium in K-feldspar megacrysts from granitic and syenitic rocks of the Bohemian Massif. Tschermaks Mineral und Petrogr Mitteilungen 22:109–116. doi: 10.1007/BF01089111

Ni H, Keppler H (2013) Carbon in Silicate Melts. Rev Mineral Geochemistry 75:251–287. doi: 10.2138/rmg.2013.75.9

Nimis P (1999) Clinopyroxene geobarometry of magmatic rocks. Part 2. Structural geobarometers for basic to acid, tholeiitic and mildly alkaline magmatic systems. Contrib to Mineral Petrol 135:62–74. doi: 10.1007/s004100050498

Norberg N, Neusser G, Wirth R, Harlov D (2011) Microstructural evolution during experimental albitization of K-rich alkali feldspar. Contrib to Mineral Petrol 162:531–546. doi: 10.1007/s00410-011-0610-y

O'Reilly SY, Griffin WL (2000) Apatite in the mantle: Implications for metasomatic processes and high heat production in Phanerozoic mantle. Lithos 53:217–232. doi: 10.1016/S0024-4937(00)00026-8

Pang KN, Chung SL, Zarrinkoub MH, et al (2013) Iranian ultrapotassic volcanism at ~11 Ma signifies the initiation of post-collisional magmatism in the Arabia-Eurasia collision zone. Terra Nov 25:405–413. doi: 10.1111/ter.12050

Papale P (2005) Determination of total H_2O and CO_2 budgets in evolving magmas from melt inclusion data. J Geophys Res Solid Earth. doi: 10.1029/2004JB003033

Parat F, Baudouin C (2015) Crystallization of sodalite-bearing phonolite (Eifel, Germany and Saghro, Morocco): Role of volatiles (S, Cl, H_2O) and silica activity. Goldschmidt Conf 100:2308–2322

Pearce JK, Dawson GKW, Blach TP, et al (2018) Impure CO_2 reaction of feldspar, clay, and organic matter rich cap-rocks: Decreases in the fraction of accessible mesopores measured by SANS. Int J Coal Geol 185:79–90. doi: 10.1016/j.coal.2017.11.011

Pearce JK, Dawson GKW, Law ACK, et al (2016) Reactivity of micas and cap-rock in wet supercritical CO_2 with SO_2 and O_2 at CO_2 storage conditions. Appl Geochemistry 72:59–76. doi: 10.1016/j.apgeochem.2016.06.010

Perini G, Francalanci L, Davidson JP, Conticelli S (2004) Evolution and Genesis of Magmas from Vico Volcano, Central Italy: Multiple Differentiation Pathways and Variable Parental Magmas. J Petrol 45:139–182. doi: 10.1093/petrology/egg084

Perugini D, Poli G, Valentini L (2005) Strange attractors in plagioclase oscillatory zoning: Petrological implications. Contrib to Mineral Petrol 149:482–497. doi: 10.1007/s00410-005-0667-6

Petersen JS, Lofgren GE (1986) Lamellar and patchy intergrowths in feldspars: experimental crystallization of eutectic silicates. Am Mineral 71:343–355

Plá Cid J, Rios DC, Conceição H (2006) Petrogenesis of mica-amphibole-bearing lamprophyres associated with the Paleoproterozoic Morro do Afonso syenite intrusion, eastern Brazil. J South Am Earth Sci 22:98–115. doi: 10.1016/j.jsames.2006.08.002

Poli S, Schmidt MW (2002) Petrology of Subducted Slabs. Annu Rev Earth Planet Sci 30:207–235. doi: 10.1146/annurev.earth.30.091201.140550

Prelevic D, Foley SF, Cventkovic V, Romer RL (2004) Origin of Minette by Mixing of Lamproite and Dacite Magmas in Veliki Majdan, Serbia. J Petrol 45:759–792. doi: 10.1093/petrology/egg109

Price SE, Russell JK, Kopylova MG (2000) Primitive magma from the Jericho pipe, N.W.T., Canada: Constraints on primary kimberlite melt chemistry. J Petrol 41:789–808. doi: 10.1093/petrology/41.6.789

Putirka KD (2008) Thermometers and Barometers for Volcanic Systems. Rev Mineral Geochemistry 69:61–120. doi: 10.2138/rmg.2008.69.3

Putirka KD, Johnson MC, Kinzler RJ, Walker D (1996) Thermobarometry of mafic igneous rocks based on pyroxene-liquid equilibria, 0-30 kb. Contrib to Mineral Petrol 123:92–108. doi: 10.1007/s004100050145

Putirka KD, Mikaelian H, Ryerson F, Shaw H (2003) New clinopyroxene-liquid thermobarometers for mafic, evolved, and volatile-bearing lava compositions, with applications to lavas from Tibet and the Snake River Plain, Idaho. Am Mineral 88:1542–1554

Putnis A (2002) Mineral replacement reactions: from macroscopic observations to microscopic mechanisms. Mineral Mag 66:689–708. doi: 10.1180/0026461026650056

Putnis C V., Tsukamoto K, Nishimura Y (2005) Direct observations of pseudomorphism: Compositional and textural evolution at a fluid-solid interface. Am Mineral 90:1909–1912. doi: 10.2138/am.2005.1990

Renggli CJ, King PL, Henley RW, et al (2019) An experimental study of SO_2 reactions with silicate glasses and supercooled melts in the system anorthite – diopside – albite at high temperature. Contrib to Mineral Petrol 174:1–19. doi: 10.1007/s00410-018-1538-2

Richards JP, Wilkinson D, Ullrich T (2006) Geology of the Sari Gunay epithermal gold deposit, northwest Iran. Econ Geol 101:1455–1496. doi: 10.2113/gsecongeo.101.8.1455

Riley TR, Bailey DK (2003) Barium-rich sanidine megacrysts from the West Eifel (Germany). Neues Jahrb für Mineral - Monatshefte 2003:18–30. doi: 10.1127/0028-3649/2003/2003-0018

Rock NMS (1991) Lamprophyres. Springer Science & Business Media

Rock NMS (1977) The nature and origin of lamprophyres: some definitions, distinctions, and derivations. Earth Sci Rev 13:123–169. doi: 10.1016/0012-8252(77)90020-4

Rock NMS (1987) The nature and origin of lamprophyres: an overview. Geol Soc London, Spec Publ 30:191–226. doi: 10.1144/GSL.SP.1987.030.01.09

Roden MF, Smith D (1971) Field geology, chemistry, and petrology of Buell Park minette diatreme, Apache County, Arizona. In: Kimberlites, Diatremes, Diamonds: Their Geology, Petrology and Geochemistry 15:364–381. doi: 10.1029/SP015p0364

Rubatto D, Müntener O, Barnhoorn A, Gregory C (2008) Dissolution-reprecipitation of zircon at low-temperature, high-pressure conditions (Lanzo Massif, Italy). Am Mineral 93:1519–1529. doi: 10.2138/am.2008.2874

Rubin JN, Henry CD, Price JG (1989) Hydrothermal zircons and zircon overgrowths, Sierra Blanca Peaks, Texas. Am Mineral 74:865–869

Rutherford MJ (2008) Magma Ascent Rates. Rev Mineral Geochemistry 69:241–271. doi: 10.2138/rmg.2008.69.7

Scaillet B, Clemente B, Evans BW, Pichavant M (1998) Redox control of sulfur degassing in silicic magmas. J Geophys Res Solid Earth 104:23937–23949. doi: 10.1029/98jb02301

Schilling JG, Bergeron MB, Evans R (1980) Halogens in the mantle beneath the North Atlantic. Philos Trans R Soc London 297:147–178. doi: 10.1098/rsta.1980.0208

Schmincke HU (2008) Vulkane der Eifel, 2. Auflage. Springer Berlin Heidelberg. ISBN-13 : 978-3827429841

Schmincke HU (2007) The Quaternary volcanic fields of the East and West Eifel (Germany). In: Ritter J.R.R., Christensen U.R. (eds) Mantle Plumes. Springer, Berlin, Heidelberg. doi: 10.1007/978-3-540-68046-8_8

Schmitt AK, Wetzel F, Cooper KM, et al (2010) Magmatic longevity of Laacher See volcano (Eifel, Germany) indicated by U-Th dating of intrusive carbonatites. J Petrol 51:1053–1085. doi: 10.1093/petrology/egq011

Schürmann H (1960) Petrographische Untersuchung der Gleesite des Laacher Seegebietes. Beiträge zur Mineral und Petrogr 7:104–136. doi: 10.1007/BF01154326

Shannon RD (1976) Revised Effective Ionic Radii and Systematic Studies of Interatomie Distances in Halides and Chaleogenides. Acta Cryst A32:751–767

Shore M, Fowler AD (1996) Oscillatory zoning in minerals: A common phenomenon. Can Mineral 34:1111–1126

Siivola J, Schmid R (2007) List of Mineral abbreviations. IUGS Subcomm Syst Metamorph Rocks 1–14

Słaby E, Śmigielski M, Śmigielski T, et al (2011) Chaotic three-dimensional distribution of Ba, Rb, and Sr in feldspar megacrysts grown in an open magmatic system. Contrib to Mineral Petrol 162:909–927. doi: 10.1007/s00410-011-0631-6

Smith J V., Brown WL (1988) Feldspar Minerals. Springer Berlin Heidelberg

Soder C, Altherr R, Romer RL (2016) Mantle metasomatism at the edge of a retreating subduction zone: Late neogene lamprophyres from the Island of Kos, Greece. J Petrol 57:1705–1728. doi: 10.1093/petrology/egw054

Spandler C, Hermann J, Arculus R, Mavrogenes J (2004) Geochemical heterogeneity and element mobility in deeply subducted oceanic crust; insights from high-pressure mafic rocks from New Caledonia. Chem Geol 206:21–42. doi: 10.1016/j.chemgeo.2004.01.006

Spera FJ (1984) Carbon dioxide in petrogenesis III: Role of volatiles in the ascent of alkaline magma with special reference to xenolith bearing mafic lavas. Contrib to Mineral Petrol 88:217–232

Sun SS, McDonough WF (1989) Chemical and isotopic systematics of oceanic basalts: Implications for mantle composition and processes. Geol Soc Spec Publ 42:313–345. doi: 10.1144/GSL.SP.1989.042.01.19

Swanson ES (1977) Relation of nucleation and crystal-growth rate to the development of granitic textures. Am Mineral 62:966–978

Tait SR (1988) Samples from the crystallising boundary layer of a zoned magma chamber. Contrib to Mineral Petrol 100:470–483. doi: 10.1007/BF00371376

Tait SR, Wörner G, Van Den Bogaard P, Schmincke HU (1989) Cumulate nodules as evidence for convective fractionation in a phonolite magma chamber. J Volcanol Geotherm Res 37:21–37. doi: 10.1016/0377-0273(89)90111-X

Tamburello G, Pondrelli S, Chiodini G, Rouwet D (2018) Global-scale control of extensional tectonics on CO_2 earth degassing. Nat Commun 9:4608. doi: 10.1038/s41467-018-07087-z

Taylor HP (1987) Comparison of hydrothermal systems in layered gabbros and granites, and the origin of low-^{18}O magmas. In: (ed) Mysen BO. Magmat Processes. Physicochemical Princciples. The Geochemical Society. Spec. Publ. 1, pp. 338-367

Taylor HP, Frechen J, Degens ET (1967) Oxygen and carbon isotope studies of carbonatites from the Laacher See District, West Germany and the Alnö District, Sweden. Geochim Cosmochim Acta 31:407–430. doi: 10.1016/0016-7037(67)90051-8

Tomaschek F, Kennedy AK, Villa IM, et al (2003) Zircons from Syros, Cyclades, Greece--Recrystallization and Mobilization of Zircon During High-Pressure Metamorphism. J Petrol 44:1977–2002. doi: 10.1093/petrology/egg067

Tutolo BM, Luhmann AJ, Kong X, et al (2015) CO_2 sequestration in feldspar-rich sandstone: Coupled evolution of fluid chemistry, mineral reaction rates, and hydrogeochemical properties. Geochim Cosmochim Acta 160:132–154. doi: 10.1016/j.gca.2015.04.002

Tyrrell GW (1928) X. Contribution to the Petrography of the Late-Palaeozoic Igneous Suite of the West of Scotland. Trans Geol Soc Glas 18:259-294. doi: 10.1144/transglas.18.2.259

Veksler I V., Nielsen TFD, Sokolov S V. (1998) Mineralogy of crystallized melt inclusions from Gardiner and Kovdor ultramafic alkaline complexes: Implications for carbonatite genesis. J Petrol 39:2015–2031. doi: 10.1093/petroj/39.11-12.2015

Verdel C, Wernicke BP, Hassanzadeh J, Guest B (2011) A Paleogene extensional arc flare-up in Iran. Tectonics 30:. doi: 10.1029/2010TC002809

Vernon RH (1986) K-Feldspar megacrysts in granites-phenocrysts, not porphyroblasts. Earth Sci Rev 23:1–63. doi: 10.1016/0012-8252(86)90003-6

Vernon RH (2018) Microstructures of Igneous Rocks. In: A Practical Guide to Rock Microstructure. Cambridge University Press, pp 28–134. doi: 10.1017/9781108654609

Vernon RH, Paterson SR (2008) How late are K-feldspar megacrysts in granites? Lithos 104:327–336. doi: 10.1016/j.lithos.2008.01.001

Vichi G, Stoppa F, Wall F (2005) The carbonate fraction in carbonatitic Italian lamprophyres. Lithos 85:154–170. doi: 10.1016/j.lithos.2005.03.025

Wallace PJ, Plank T, Edmonds M, Hauri EH (2015) Volatiles in Magmas. In: The Encyclopedia of Volcanoes, Second Edi. Elsevier Inc., pp 163–183. doi: 10.1016/B978-0-12-385938-9.00007-9

Wass SY (1979) Fractional Crystallization in the Mantle of Late-Stage Kimberlitic Liquids - Evidence in Xenoliths from the Kiama Area, N.S.W., Australia. In. (eds) Boyd FR, Meyer HOA. The Mantle Sample: Inclusion in Kimberlites and other Volcanics. Special Publications 16:366–373. doi: 10.1029/SP016p0366

Wegner W, Wörner G, Kronz A (2005) Evolution of Taapaca Volcano, N. Chile : Evidence from major and trace elements, Sr-, Nd-, Pb-isotopes, age dating and chemical zoning in sanidine megacrysts. In: ISAG 2005. pp 795–798

Weidendorfer D, Schmidt MW, Mattsson HB (2016) Fractional crystallization of Si-undersaturated alkaline magmas leading to unmixing of carbonatites on Brava Island (Cape Verde) and a general model of carbonatite genesis in alkaline magma suites. Contrib to Mineral Petrol 171:. doi: 10.1007/s00410-016-1249-5

Wendlandt RF, Harrison WJ (1979) Rare earth partitioning between immiscible carbonate and silicate liquids and CO_2 vapor: Results and implications for the formation of light rare earth-enriched rocks. Contrib to Mineral Petrol 69:409–419. doi: 10.1007/BF00372266

Wilson L, Head JW (2007) An integrated model of kimberlite ascent and eruption. Nature 447:53–57. doi: 10.1038/nature05692

Wilson M, Downes H (1991) Tertiary - quaternary extension-related alkaline magmatism in Western and central Europe. J Petrol. doi: 10.1093/petrology/32.4.811

Wolff JA, Ellis BS, Ramos FC, et al (2015) Remelting of cumulates as a process for producing chemical zoning in silicic tuffs: A comparison of cool, wet and hot, dry rhyolitic magma systems. Lithos 236–237:275–286. doi: 10.1016/j.lithos.2015.09.002

Wörner G, Beusen JM, Duchateau N, et al (1983) Trace element abundances and mineral/melt distribution coefficients in phonolites from the Laacher See volcano (Germany). Contrib to Mineral Petrol 84:152–173. doi: 10.1007/BF00371282

Wörner G, Harmon RS, Hoefs J (1987) Stable isotope relations in an open magma system, Laacher See, Eifel (FRG). Contrib to Mineral Petrol 95:343–349. doi: 10.1007/BF00371848

Wörner G, Schmincke HU (1984a) Petrogenesis of the Laacher See tephra. J Petrol 25:836–851. doi: 10.1093/petrology/25.4.836

Wörner G, Schmincke H-U (1984b) Mineralogical and Chemical Zonation of the Laacher See Tephra Sequence (East Eifel, W. Germany). J Petrol 25:805–835. doi: 10.1093/petrology/25.4.805

Wörner G, Staudigel H, Zindler A (1985) Isotopic constraints on open system evolution of the Laacher See magma chamber (Eifel, West Germany). Earth Planet Sci Lett 75:37–49. doi: 10.1016/0012-821X(85)90048-2

Wörner G, Wright TL (1984) Evidence for magma mixing within the Laacher See magma chamber (East Eifel, Germany). J Volcanol Geotherm Res 22:301–327. doi: 10.1016/0377-0273(84)90007-6

Wu X, Liu Q, Zhu J, et al (2017) Geochemical characteristics of tight gas and gas-source correlation in the Daniudi gas field, the Ordos Basin, China. Mar Pet Geol 79:412–425. doi: 10.1016/J.MARPETGEO.2016.10.022

Yanev Y, Boev B, Tz I, et al (2010) Mineralogy of the Pliocene Trachyte and its Carbonatitic Minette Inclusions in Ostrvica, FYRO Macedonia. Proc XIX CBGA Congress, Thessaloniki, Greece. 100:287-295

Yang W Bin, Niu HC, Shan Q, et al (2014) Geochemistry of magmatic and hydrothermal zircon from the highly evolved Baerzhe alkaline granite: Implications for Zr-REE-Nb mineralization. Miner Depos 49:451–470. doi: 10.1007/s00126-013-0504-1

Yang H-J, Kinzler RJ, Grove TL (1996) Experiments and models of anhydrous, basaltic olivine-plagioclase-augite saturated melts from 0.001 to 10 kbar. Contrib to Mineral Petrol 124:1–18. doi: 10.1007/s004100050169

Yaxley GM, Green DH, Kamenetsky V (1998) Carbonatite metasomatism in the southeastern Australian lithosphere. J Petrol 39:1917–1930. doi: 10.1093/petroj/39.11-12.1917

Yeganehfar H, Ghorbani MR, Shinjo R, Ghaderi M (2013) Magmatic and geodynamic evolution of Urumieh-Dokhtar basic volcanism, Central Iran: Major, trace element, isotopic, and geochronologic implications. Int Geol Rev 55:767–786. doi: 10.1080/00206814.2012.752554

Zarasvandi A, Roshanak R, Gratzer R, et al (2019) Stable isotope geochemistry of travertines from northern Urumieh-Dokhtar volcano-plutonic belt, Iran. Carbonates and evaporites 34:869–881. doi: 10.1007/s13146-017-0405-y

Zellmer GF, Clavero JE (2006) Using trace element correlation patterns to decipher a sanidine crystal growth chronology: An example from Taapaca volcano, Central Andes. J Volcanol Geotherm Res 156:291–301. doi: 10.1016/j.jvolgeores.2006.03.004

Zhang M, Suddaby P, Thompson RN, Dungan MA (1993) Barian titanian phlogopite from potassic lavas in northeast China: chemistry, substitutions, and paragenesis. Am Mineral 78:1056–1065

Zobin VM (2012) Significant Volcano-Tectonic Earthquakes and Their Role in Volcanic Processes. In: (ed) Zobin VM. Introduction to Volcanic Seismology. Elsevier, Oxford. pp 171–196. doi: 10.1016/B978-0-444-63631-7.00010-8

Zozulya DR, Lyalina LM, Eby N, Savchenko YE (2012) Ore geochemistry, zircon mineralogy, and genesis of the Sakharjok Y-Zr deposit, Kola Peninsula, Russia. Geol Ore Depos 54:81–98. doi: 10.1134/S1075701512020079

Appendix

A-1 WHOLE-ROCK ANALYSIS

A-1A SARAY VOLCANO

Table A 1: Whole rock analyses of trachytic lavas and bombs from Saray Volcano; oxides were measured by WD-XRF; Fe^{2+}/Fe^{3+} was determined by titration; C*=total carbon by C/N analyzer; trace elements with ICP-MS

	B1	B2			B3	B4	B5	L1		L2
sample	ES37	ES 41	ES 56	ES 57	ES 113	ES 114	ES115	ES 83	ES 84	ES62
SiO_2	59.96	58.27	59.50	59.38	59.93	56.86	57.26	57.50	58.66	57.04
Al_2O_3	16.33	15.40	15.40	16.58	16.02	14.00	14.42	14.85	15.46	14.58
FeO	1.43	0.75	0.15	1.03	1.08	1.83	1.81	1.48	1.55	2.38
Fe_2O_3	3.19	4.55	5.23	4.13	2.60	4.43	4.14	5.16	4.77	4.16
MnO	0.11	0.12	0.11	0.10	0.05	0.13	0.16	0.13	0.12	0.13
MgO	1.43	1.98	2.25	1.52	1.03	4.12	2.56	2.53	1.31	2.55
CaO	2.79	4.34	4.04	3.42	3.21	5.68	5.18	5.27	3.37	5.30
Na_2O	1.73	2.63	3.11	3.06	2.04	1.55	1.14	2.24	2.65	2.22
K_2O	10.96	8.68	7.90	7.99	10.92	8.92	10.51	8.48	9.05	8.48
TiO_2	0.60	0.67	0.68	0.65	0.52	0.84	0.78	0.87	0.80	0.87
P_2O_5	0.25	0.36	0.39	0.29	0.31	0.63	0.56	0.51	0.29	0.50
LOI	0.65	1.41	1.00	1.57	3.23	1.31	0.55	1.15	1.03	0.74
Total	99.43	99.16	99.77	99.72	100.94	100.30	99.06	100.18	99.06	98.95
C*	0.09	*n.a.*	*n.a.*	*n.a.*	*n.a.*	0.19	*n.a.*	*n.a.*	0.10	0.08
(ppm)										
Ba	4468	2990	2660	2640	2370	3752	4154	2690	5350	2886
Ce	148	136	133	145	89	153	161	135	222	151
Co	8	10	12	9	5	19	13	11	9	17
Cr	16	38	62	21	48	146	< 10	< 10	< 10	< 10
Cu	36	70	180	30	40	103	82	60	40	85
Dy	5	6	6	6	4	6	6	6	8	6
Er	3	3	3	3	2	3	3	3	4	3
Eu	2	2	2	3	2	3	3	2	4	3
F	277	461	579	609	580	939	1016	453	297	823
Ga	21	17	19	19	15	18	17	19	23	17
Gd	8	8	8	9	5	10	10	9	12	9
Hf	18	14	18	15	10	19	17	13	25	16
La	78	67	65	76	44	80	84	69	114	78
Lu	0	0	0	0	0	0	0	0	0	0
Nb	57	46	53	50	34	59	65	53	94	55
Nd	58	56	55	61	39	66	67	56	87	64
Ni	5	< 20	< 20	< 20	< 20	37	10	< 20	< 20	5
Pb	32	46	163	71	29	44	243	55	115	26
Pr	16	15	15	16	10	17	18	15	25	17
Rb	328	243	297	211	282	226	415	127	248	424
Sb	0	1	2	1	7	1	1	1	2	1
Sm	11	11	11	11	7	13	13	11	16	13
Sr	2149	2610	1900	2250	920	1604	1798	1430	1650	1613
Ta	3	3	3	3	2	3	3	3	5	3
Tb	1	1	1	1	1	1	1	1	2	1
Th	43	53	69	67	32	47	44	43	99	52
Tl	8	0	0	1	3	0	1	0	1	23
Tm	0	0	0	0	0	0	0	0	1	0
U	16	12	19	10	17	7	16	14	24	22
V	135	122	69	124	97	200	282	132	155	210
W	2	3	2	5	66	4	11	< 1	< 1	2
Y	41	31	40	31	25	47	38	34	45	33
Yb	2	2	3	2	2	2	3	3	3	2
Zn	39	70	60	70	80	61	50	80	60	61
Zr	735	540	798	592	439	692	672	538	987	579

Table A 2: Whole rock analyses of mafic (M), felsic (F) minette and glimmerite (X-Gl), peridotite (X-Ol) and pyroxenite (X-Px) xenoliths from Saray Volcano; oxides were measured by WD-XRF; Fe^{2+}/Fe^{3+} was determined by titration; C*=total carbon by C/N analyzer; trace elements with ICP-MS

	F1	F2	F3	M1	M2	M3	X-Gl	X-Ol	X-Px
sample	SV-2-1	SV-4-1	SV-7-2	GV-1-5	L6	SV-2-2	GV-0-1	SV-7-1	SV-1-1
SiO_2	55.51	51.96	54.16	47.97	50.93	43.78	41.21	44.82	46.06
Al_2O_3	16.12	13.80	15.03	11.01	11.29	10.97	8.16	7.55	12.38
FeO	1.19	1.59	2.10	1.13	1.99	2.16	1.21	3.22	2.27
Fe_2O_3	3.40	4.55	3.38	6.87	6.69	7.28	7.34	4.67	7.65
MnO	0.11	0.12	0.12	0.11	0.13	0.16	0.10	0.15	0.17
MgO	1.92	2.40	2.62	7.71	7.62	9.18	14.03	12.98	7.09
CaO	3.87	7.03	4.57	9.53	9.41	12.60	14.67	14.89	12.21
Na_2O	3.98	2.53	3.65	0.81	0.77	2.08	0.46	1.70	2.44
K_2O	6.81	7.41	6.74	5.47	6.92	4.26	4.10	2.44	3.78
TiO_2	0.57	0.83	0.73	1.38	1.42	1.19	1.88	0.91	1.12
P_2O_5	0.33	0.76	0.54	1.88	1.98	1.72	4.31	1.25	1.54
LOI	6.16	6.05	5.10	4.99	2.55	5.20	1.24	3.45	3.40
Total	99.96	99.03	98.73	98.86	101.70	100.58	98.71	98.04	100.11
C*	1.24	*n.a.*	*n.a.*	0.12	0.13	*n.a.*	0.03	*n.a.*	*n.a.*
(ppm)									
Ba	2182	4311	2491	3363	3214	3484	5079	3019	3647
Ce	133	146	134	182	180	139	161	115	170
Co	47	43	32	59	52	41	59	56	39
Cr	*n.a*	30	68	194	*n.a*	*n.a*	16	1048	81
Cu	45	69	94	119	101	117	22	92	100
Dy	5	6	5	7	7	7	8	6	8
Er	2	2	2	3	3	3	3	2	3
Eu	2	3	2	3	3	3	4	2	3
F	*n.a*	1112	489	1693	*n.a*	*n.a*	2948	752	854
Ga	19	17	18	15	14	12	11	8	13
Gd	7	9	8	12	12	11	13	9	12
Hf	13	12	13	13	13	8	4	6	7
La	74	74	70	86	82	71	79	58	91
Lu	0	0	0	0	0	0	0	0	0
Nb	48	55	52	55	52	27	18	23	31
Nd	49	62	55	93	92	67	82	54	76
Ni	10	20	20	51	51	44	40	97	19
Pb	20	72	19	40	37	33	8	24	39
Pr	14	16	15	22	22	17	20	13	20
Rb	257	248	245	140	161	168	145	127	215
Sb	1	1	0	0	0	0	0	0	<0.1
Sm	9	12	11	18	17	13	16	11	14
Sr	1323	1662	1391	1232	1193	1163	708	1312	1537
Ta	2	3	3	3	3	1	1	1	2
Tb	1	1	1	1	1	1	2	1	2
Th	40	44	46	44	43	24	10	17	26
Tl	0	0	0	1	1	1	1	0	1
Tm	0	0	0	0	0	0	0	0	0
U	14	14	18	14	13	6	3	2	3
V	110	155	129	203	204	230	206	180	302
W	105	132	88	86	66	22	45	116	47
Y	26	28	27	30	30	34	32	25	36
Yb	2	2	2	2	2	2	2	2	2
Zn	63	77	69	100	75	68	42	51	58
Zr	506	484	506	502	493	303	142	236	294

A-1B LAACHER SEE VOLCANO

Table A 3: Whole rock analyses of dark and bright haüyne-sanidinite from Laacher See Volcano; oxides were measured by WD-XRF; Fe^{2+}/Fe^{3+} was determined by titration; C*=total carbon by C/N analyzer; trace elements with ICP-MS

	dark haüyne-sanidinite			bright haüyne-sanidinite							
sample	LS 211	LS 4	LS 191	IDD 11	IDD 5	IDD 58	LS 205	LS 159	LS 160	LS 170	LS 143
SiO_2	61.94	62.02	61.97	58.01	59.73	61.08	61.11	62.39	63.05	62.06	61.45
Al_2O_3	20.24	19.17	18.83	20.76	19.80	19.59	20.23	20.05	19.38	19.31	20.25
Fe_2O_3T	2.49	2.90	2.32	0.85	2.70	2.86	1.98	2.34	1.48	2.12	2.44
MnO	0.11	0.12	0.10	0.06	0.19	0.18	0.15	0.13	0.12	0.16	0.13
MgO	0.14	0.32	0.27	0.08	0.20	0.16	0.01	0.05	0.05	0.14	0.05
CaO	1.81	2.55	1.93	2.27	1.94	1.91	1.37	2.03	1.40	1.53	2.10
Na_2O	5.68	4.82	4.79	8.07	6.77	6.46	7.80	6.93	6.57	7.07	6.93
K_2O	6.32	7.40	8.04	6.67	6.76	6.44	5.81	5.46	7.09	6.28	5.58
TiO_2	0.37	0.54	0.39	0.20	0.46	0.42	0.08	0.38	0.18	0.29	0.39
P_2O_5	0.06	0.08	0.07	0.04	0.06	0.05	0.00	0.03	0.02	0.04	0.03
LOI	0.99	0.38	0.33	2.86	1.53	1.05	0.89	0.69	0.94	1.01	1.37
Total	100.15	100.30	99.04	99.87	100.14	100.21	99.43	100.48	100.29	100.01	100.72
SO_3	*n.a.*	0.13	0.11	2.10	0.96	0.76	0.20	0.47	0.57	0.38	1.21
C*	*n.a.*	*n.a.*	*n.a.*	0.11	*n.a.*	*n.a.*	*n.a.*	*n.a.*	0.08	0.08	*n.a.*
(ppm)											
Ba	202	808	704	21	*n.a.*	122	56	178	26	30	159
Ce	*n.a.*	266	74	*n.a.*	*n.a.*	117	*n.a.*	92	95	82	100
Cl	*n.a.*	1257	594	*n.a.*	*n.a.*	1006	*n.a.*	795	1522	1195	1427
Co	*n.a.*	35	7	*n.a.*	*n.a.*	7	*n.a.*	7	7	6	6
Cr	*n.a.*	-45	26	*n.a.*	*n.a.*	24	*n.a.*	40	38	33	37
F	*n.a.*	600	173	*n.a.*	*n.a.*	279	*n.a.*	146	684	395	239
Ga	*n.a.*	26	17	*n.a.*	*n.a.*	21	*n.a.*	20	19	19	26
Hf	*n.a.*	12	6	*n.a.*	*n.a.*	7	*n.a.*	7	7	8	13
La	*n.a.*	176	61	*n.a.*	*n.a.*	71	*n.a.*	60	77	71	65
Mo	*n.a.*	9	4	*n.a.*	*n.a.*	9	*n.a.*	7	8	7	13
Nb	*n.a.*	138	42	*n.a.*	*n.a.*	108	*n.a.*	111	56	65	97
Nd	*n.a.*	90	20	*n.a.*	*n.a.*	31	*n.a.*	26	18	18	12
Ni	0	9	4	5	*n.a.*	5	7	0	0	2	0
Pb	*n.a.*	20	15	*n.a.*	*n.a.*	21	*n.a.*	21	19	16	24
Rb	168	136	117	132	*n.a.*	182	224	149	174	167	151
Sr	272	802	579	42	*n.a.*	210	31	334	52	36	335
Th	*n.a.*	35	18	*n.a.*	*n.a.*	22	*n.a.*	19	22	20	31
U	*n.a.*	-6	0	*n.a.*	*n.a.*	1	*n.a.*	4	5	5	12
V	*n.a.*	230	61	*n.a.*	*n.a.*	58	*n.a.*	45	33	39	27
Y	12	23	11	20	*n.a.*	22	16	18	8	12	18
Zn	59	56	41	18	*n.a.*	108	48	83	50	58	89
Zr	273	313	165	445	*n.a.*	268	968	341	290	478	350

Table A 4: Whole rock analyses of nosean-sanidinite from Laacher See Volcano; oxides were measured by WD-XRF; Fe^{2+}/Fe^{3+} was determined by titration; C*=total carbon by C/N analyzer; trace elements of IDD64, LS57, LS64, LS88 and LS151 with ICP-MS; trace elements of LS147 and LS148 measured by XRF on pressed tablets

	nosean-sanidinite									
sample	IDD 64	LS 57	LS 59	LS 64	LS 65	LS 88	LS 147	LS 148	LS 151	LS 152
SiO_2	52.61	53.60	51.54	52.21	55.48	51.28	55.32	55.24	57.76	57.08
Al_2O_3	18.93	21.61	19.35	22.98	21.86	21.85	22.43	21.82	18.92	21.22
Fe_2O_3T	1.97	1.90	2.00	0.76	1.23	1.42	1.13	2.41	3.53	1.69
MnO	0.32	0.16	0.29	0.10	0.15	0.37	0.21	0.26	0.62	0.21
MgO	0.17	0.06	0.14	0.06	0.01	0.08	0.04	0.02	0.94	0.22
CaO	6.24	2.43	5.81	1.91	1.20	4.59	0.71	0.68	3.43	1.52
Na_2O	9.05	10.88	9.67	12.65	11.08	11.71	11.60	11.50	9.19	10.05
K_2O	4.18	5.00	4.18	4.71	4.93	4.56	5.65	4.91	2.18	5.26
TiO_2	0.11	0.10	0.10	0.05	0.08	0.09	0.08	0.16	0.17	0.10
P_2O_5	0.00	0.03	0.01	0.01	0.01	0.01	0.00	0.01	0.21	0.00
LOI	6.30	4.58	6.15	5.14	3.49	5.66	3.24	2.74	2.45	3.18
Total	99.88	100.35	99.24	100.58	99.52	101.61	100.41	99.75	99.39	100.53
SO_3	1.38	2.79	1.36	3.18	2.10	2.38	2.01	1.72	0.59	1.46
C*	*n.a.*	*n.a.*	*n.a.*	0.25	*n.a.*	1.02	*n.a.*	*n.a.*	*n.a.*	*n.a.*
(ppm)										
Ba	39	99	53	29	24	40	15	9	108	17
Ce	111	*n.a.*	288	93	110	230	*n.a.*	*n.a.*	345	*n.a.*
Cl	1598	*n.a.*	2010	2109	2321	2646	*n.a.*	*n.a.*	1027	*n.a.*
Co	7	*n.a.*	8	7	7	8	*n.a.*	*n.a.*	12	*n.a.*
Cr	39	*n.a.*	35	41	39	39	*n.a.*	*n.a.*	34	*n.a.*
F	383	*n.a.*	338	700	320	464	*n.a.*	*n.a.*	2059	*n.a.*
Ga	27	*n.a.*	22	24	26	26	*n.a.*	*n.a.*	34	*n.a.*
Hf	14	*n.a.*	17	11	13	15	*n.a.*	*n.a.*	11	*n.a.*
La	77	*n.a.*	233	63	78	190	*n.a.*	*n.a.*	347	*n.a.*
Mo	13	*n.a.*	23	23	20	22	*n.a.*	*n.a.*	9	*n.a.*
Nb	58	*n.a.*	16	61	128	115	*n.a.*	*n.a.*	100	*n.a.*
Nd	18	*n.a.*	44	17	25	36	*n.a.*	*n.a.*	53	*n.a.*
Ni	1	3	3	0	5	16	7	7	8	4
Pb	17	*n.a.*	19	13	18	20	*n.a.*	*n.a.*	18	*n.a.*
Rb	147	191	151	158	176	166	255	228	182	178
Sr	26	154	33	47	16	26	13	29	335	18
Th	28	*n.a.*	36	29	29	35	*n.a.*	*n.a.*	39	*n.a.*
U	9	*n.a.*	8	9	19	18	*n.a.*	*n.a.*	12	*n.a.*
V	27	*n.a.*	34	23	26	23	*n.a.*	*n.a.*	37	*n.a.*
Y	40	27	33	14	17	30	28	16	26	33
Zn	63	89	76	39	70	107	105	134	264	76
Zr	1329	1575	1145	688	1065	1581	1521	715	761	1324

Table A 5: Whole rock analyses of nosean-sanidinite from Laacher See Volcano; oxides were measured by WD-XRF; Fe^{2+}/Fe^{3+} was determined by titration; C*=total carbon by C/N analyzer; trace elements of LS113, LS125, LS78, LS155, IDD65 and IDD67 with ICP-MS; trace elements of LS107, LS179, LS186 and LS118 measured by XRF on pressed tablets

	nosean-sanidinite									
sample	LS 107	LS 113	LS 179	LS 186	LS 118	LS 125	LS 78	LS 144	IDD 65	IDD67
SiO_2	50.73	55.32	54.70	63.45	53.06	52.33	49.70	55.89	55.67	57.47
Al_2O_3	19.27	21.75	21.37	19.35	22.37	18.57	18.57	22.41	21.70	18.63
Fe_2O_3T	2.08	1.04	1.53	1.79	2.39	3.60	2.48	0.38	1.69	2.67
MnO	0.43	0.10	0.15	0.11	0.21	0.45	0.43	0.02	0.28	0.39
MgO	0.28	0.09	0.14	0.12	-0.03	0.01	0.02	-0.05	0.14	0.05
CaO	6.75	1.48	1.97	1.55	1.01	5.87	8.03	1.26	0.99	5.84
Na_2O	9.53	10.43	10.25	6.31	12.17	9.46	9.41	11.11	11.18	7.85
K_2O	4.15	5.64	5.62	6.44	4.58	3.46	3.52	5.17	4.80	5.70
TiO_2	0.12	0.07	0.09	0.17	0.14	0.22	0.15	0.03	0.12	0.14
P_2O_5	0.00	0.00	0.02	0.02	0.00	0.00	0.00	0.00	0.00	0.00
LOI	7.22	3.78	3.98	0.47	3.87	5.88	7.71	2.82	3.29	6.25
Total	100.56	99.70	99.82	99.78	99.78	99.86	100.02	99.04	99.86	104.99
SO_3	1.48	2.52	2.24	0.21	2.82	1.15	1.20	2.11	2.12	1.66
C*	*n.a.*	0.22	*n.a.*	*n.a.*	*n.a.*	1.23	1.71	0.09	*n.a.*	1.22
(ppm)										
Ba	31	37	79	32	39	12	29	50	27	25
Ce	*n.a.*	83	*n.a.*	*n.a.*	*n.a.*	1026	735	70	101	431
Cl	*n.a.*	1822	*n.a.*	*n.a.*	*n.a.*	1608	1736	2120	2026	1090
Co	*n.a.*	7	*n.a.*	*n.a.*	*n.a.*	8	9	7	7	9
Cr	*n.a.*	39	*n.a.*	*n.a.*	*n.a.*	34	33	38	40	33
F	*n.a.*	449	*n.a.*	*n.a.*	*n.a.*	241	14	53	395	210
Ga	*n.a.*	31	*n.a.*	*n.a.*	*n.a.*	20	20	28	28	22
Hf	*n.a.*	16	*n.a.*	*n.a.*	*n.a.*	16	21	17	15	48
La	*n.a.*	40	*n.a.*	*n.a.*	*n.a.*	1225	782	22	66	316
Mo	*n.a.*	15	*n.a.*	*n.a.*	*n.a.*	21	24	15	10	17
Nb	*n.a.*	130	*n.a.*	*n.a.*	*n.a.*	11	19	96	85	23
Nd	*n.a.*	16	*n.a.*	*n.a.*	*n.a.*	105	95	10	26	70
Ni	6	4	2	0	7	3	2	3	6	1
Pb	*n.a.*	14	*n.a.*	*n.a.*	*n.a.*	22	21	13	23	21
Rb	163	206	222	109	160	120	118	194	189	171
Sr	39	94	124	35	33	17	19	112	30	20
Th	*n.a.*	33	*n.a.*	*n.a.*	*n.a.*	53	54	28	34	40
U	*n.a.*	17	*n.a.*	*n.a.*	*n.a.*	7	13	17	11	9
V	*n.a.*	24	*n.a.*	*n.a.*	*n.a.*	46	40	20	26	39
Y	42	18	20	9	14	38	49	18	27	70
Zn	98	51	76	36	125	133	85	15	117	101
Zr	1651	1275	1027	309	870	1140	1398	1416	1194	4048

A-2 MINERAL CHEMISTRY

In the following only representative EMP-analysis are listed. The whole dataset of point measurements and transsects including detailed documentation in BSE-images can be requested by email d.assbichler@lmu.de

A-2A SARAY VOLCANO

SANIDINE

Table A 6: Representative EMP-analysis of sanidines contained in trachyte from Saray Volcano showing the composition of the different crystallization stages A-D; number of ions based on 8 oxygens

label	trachyte								
Symbol	SAN-A		SAN-B		SAN-C			SAN-D	
Colour	1	2	3	4	5	6	7	8	9
SiO_2	60.82	59.16	64.99	65.01	64.99	63.36	63.42	61.72	62.21
Al_2O_3	19.62	19.72	19.54	19.69	19.61	19.48	19.61	19.71	19.36
Fe_2O_3	0.73	0.84	0.26	0.24	0.21	0.22	0.23	0.35	0.65
CaO	0.06	0.06	0.70	0.59	0.36	0.51	0.11	0.11	0.12
BaO	4.52	5.91	0.81	0.23	0.68	1.37	1.41	3.45	2.69
SrO	0.37	0.44	0.18	0.02	0.31	0.33	0.18	0.18	0.14
Na_2O	2.88	2.32	4.77	4.57	3.93	3.72	2.26	2.21	2.11
K_2O	10.80	10.84	9.39	9.76	10.60	10.33	12.91	12.25	12.53
Total	99.80	99.29	100.63	100.11	100.69	99.31	100.12	99.97	99.81
Si	2.88	2.85	2.94	2.95	2.95	2.93	2.93	2.90	2.92
Al	1.10	1.12	1.04	1.05	1.05	1.06	1.07	1.09	1.07
Fe^{3+}	0.03	0.03	0.01	0.01	0.01	0.01	0.01	0.01	0.02
Ca	0.00	0.00	0.03	0.03	0.02	0.03	0.01	0.01	0.01
Ba	0.08	0.11	0.01	0.00	0.01	0.03	0.03	0.06	0.05
Sr	0.01	0.01	0.01	0.00	0.01	0.01	0.01	0.01	0.00
Na	0.26	0.22	0.42	0.40	0.35	0.33	0.20	0.20	0.19
K	0.65	0.67	0.54	0.56	0.61	0.61	0.76	0.74	0.75

Table A 7: Representative EMP-analysis of sanidines contained in glimmerite, felsic and mafic minette and hyalophane from wherlite from Saray Volcano; number of ions based on 8 oxygens

label	glimmerite		felsic minette				mafic minette		wherlite
Symbol	X-Gl		F1		F2		M2		X-Ol
Colour	3_1	5_1	10_7	11_4	5_A04	6_03	2_5	6_16	4_05
SiO_2	64.70	62.88	64.99	63.74	65.34	65.22	63.56	64.66	42.23
Al_2O_3	18.33	18.60	18.86	19.65	18.19	17.95	17.76	18.15	23.80
Fe_2O_3	0.16	0.19	0.47	0.37	0.47	0.63	1.06	0.94	0.07
CaO	0.12	0.04	0.89	1.22	0.10	0.25	0.64	0.10	0.06
BaO	0.00	2.13	0.06	0.21	0.11	0.03	0.33	0.36	29.70
SrO	0.00	0.00	0.00	0.00	0.00	0.00	0.00	0.00	0.00
Na_2O	0.85	1.13	4.61	3.16	2.89	3.15	0.41	3.12	0.09
K_2O	15.26	14.15	9.45	10.77	12.23	11.71	15.43	11.83	5.00
Total	99.42	99.12	99.39	99.15	99.43	99.08	99.29	99.25	100.95
Si	3.00	2.96	2.96	2.93	3.00	3.00	2.98	2.98	2.39
Al	1.00	1.03	1.01	1.07	0.98	0.97	0.98	0.99	1.59
Fe^{3+}	0.01	0.01	0.02	0.01	0.02	0.02	0.04	0.03	0.00
Ca	0.01	0.00	0.04	0.06	0.01	0.01	0.03	0.01	0.00
Ba	0.00	0.04	0.00	0.00	0.00	0.00	0.01	0.01	0.66
Sr	0.00	0.00	0.00	0.00	0.00	0.00	0.00	0.00	0.00
Na	0.08	0.10	0.41	0.28	0.26	0.28	0.04	0.28	0.01
K	0.90	0.85	0.55	0.63	0.72	0.69	0.92	0.70	0.36

Table A 8: EMP-analysis of sanidine profile of Figure 33a from B4 trachytic bomb of Saray Volcano; number of ions based on 8 oxygens

	B4 - sanidine profile (1/3)											
	C_1	C_2	C_3	C_4	C_5	C_6	C_7	C_8	C_9	C_10	C_11	C_12
distance [µm]	0	4	8	12	16	20	24	28	32	36	40	44
SiO_2	64.824	62.813	63.726	63.329	63.342	63.359	62.911	60.823	60.152	60.17	60.213	59.796
Al_2O_3	19.103	19.211	18.961	18.975	19.113	19.44	18.559	19.623	19.43	19.374	19.273	19.339
Fe_2O_3	0.416	0.468	0.445	0.52	0.557	0.488	0.867	0.732	0.984	0.984	0.966	0.927
CaO	0.047	0.049	0.053	0.036	0.036	0.083	0.022	0.056	0.068	0.033	0.061	0.077
BaO	0.619	1.757	1.054	1.386	1.789	1.635	1.268	4.522	5.114	5.099	5.22	5.517
SrO	0.19	0.24	0.202	0.144	0.208	0.148	0.081	0.366	0.312	0.193	0.223	0.355
Na_2O	1.748	2.141	2.418	2.607	2.835	2.555	2.955	2.876	2.762	2.642	2.649	2.598
K_2O	12.88	13.291	13.146	12.796	12.113	12.138	12.224	10.803	10.868	11.118	10.801	11.128
Total	99.826	99.97	100	99.792	99.994	99.845	98.886	99.8	99.688	99.613	99.406	99.735
Si	2.977	2.929	2.95	2.943	2.939	2.935	2.946	2.881	2.871	2.874	2.88	2.866
Al	1.034	1.056	1.035	1.039	1.045	1.062	1.024	1.096	1.093	1.091	1.086	1.093
Fe^{3+}	0.014	0.016	0.015	0.018	0.019	0.017	0.031	0.026	0.035	0.035	0.035	0.033
Ca	0.002	0.002	0.003	0.002	0.002	0.004	0.001	0.003	0.003	0.002	0.003	0.004
Ba	0.011	0.032	0.019	0.025	0.033	0.03	0.023	0.084	0.096	0.095	0.098	0.104
Sr	0.005	0.007	0.005	0.004	0.006	0.004	0.002	0.01	0.009	0.005	0.006	0.01
Na	0.156	0.194	0.217	0.235	0.255	0.229	0.268	0.264	0.256	0.245	0.246	0.241
K	0.755	0.791	0.777	0.759	0.717	0.717	0.73	0.653	0.662	0.677	0.659	0.681

Table A 9: EMP-analysis of sanidine profile of Figure 33a from B4 trachytic bomb of Saray Volcano; number of ions based on 8 oxygens

	B4 - sanidine profile (2/3)											
	C_13	C_14	C_15	C_16	C_17	C_18	C_19	C_20	C_21	C_22	C_23	C_24
distance [µm]	48	52	56	60	64	68	72	76	80	84	88	92
SiO_2	60.179	59.793	60.267	60.92	59.441	59.589	59.459	59.815	59.946	59.163	62.976	64.311
Al_2O_3	19.464	19.682	19.996	19.844	19.51	19.72	19.569	19.527	19.413	19.72	18.868	18.709
Fe_2O_3	0.917	0.771	0.58	0.771	0.655	0.686	0.795	0.781	0.83	0.838	0.888	0.622
CaO	0.02	0.032	0.09	0.059	0.039	0.053	0.06	0.032	0.064	0.057	0.007	0.011
BaO	5.418	5.33	4.559	5.5	5.279	5.45	5.868	5.58	5.428	5.913	2.019	1.068
SrO	0.248	0.232	0.264	0.224	0.298	0.359	0.343	0.257	0.355	0.441	0.1	0.1
Na_2O	2.35	2.191	1.602	1.942	2.152	2.063	2.026	2.126	2.278	2.322	2.585	2.971
K_2O	11.291	11.739	11.934	11.829	11.895	11.724	11.473	11.605	11.426	10.836	12.453	12.52
Total	99.887	99.77	99.292	101.09	99.268	99.643	99.594	99.723	99.74	99.29	99.896	100.31
Si	2.873	2.862	2.874	2.874	2.863	2.86	2.861	2.868	2.871	2.852	2.936	2.961
Al	1.095	1.11	1.124	1.103	1.108	1.115	1.11	1.103	1.096	1.121	1.037	1.015
Fe^{3+}	0.033	0.028	0.021	0.027	0.024	0.025	0.029	0.028	0.03	0.03	0.031	0.022
Ca	0.001	0.002	0.005	0.003	0.002	0.003	0.003	0.002	0.003	0.003	0	0.001
Ba	0.101	0.1	0.085	0.102	0.1	0.102	0.111	0.105	0.102	0.112	0.037	0.019
Sr	0.007	0.006	0.007	0.006	0.008	0.01	0.01	0.007	0.01	0.012	0.003	0.003
Na	0.218	0.203	0.148	0.178	0.201	0.192	0.189	0.198	0.212	0.217	0.234	0.265
K	0.688	0.717	0.726	0.712	0.731	0.718	0.704	0.71	0.698	0.666	0.741	0.735

Table A 10: EMP-analysis of sanidine profile of Figure 33a from B4 trachytic bomb of Saray Volcano; number of ions based on 8 oxygens

	B4 - sanidine profile (3/3)											
	C_25	C_26	C_27	C_28	C_29	C_30	C_31	C_32	C_33	C_34	C_35	C_36
distance [µm]	96	100	104	108	112	116	120	124	128	132	136	140
SiO_2	63.7	63.651	63.617	63.821	62.74	63.819	63.936	63.801	63.084	63.559	63.985	63.799
Al_2O_3	18.88	19.021	19.008	19.219	18.837	18.918	19.011	18.931	19.183	19.229	19.056	18.906
Fe_2O_3	0.486	0.522	0.517	0.477	0.543	0.529	0.469	0.479	0.508	0.434	0.412	0.392
CaO	0.025	0.012	0.016	0.041	0.017	0.042	0.032	0.013	0.088	0.068	0.049	0.057
BaO	1.771	1.861	1.878	2.03	2.073	1.47	1.259	1.347	2.022	1.517	1.18	1.034
SrO	0.169	0.154	0.156	0.216	0.211	0.248	0.137	0.252	0.331	0.258	0.207	0.121
Na_2O	3.036	3.209	3.162	3.032	2.654	3.083	2.962	2.77	2.721	2.604	2.336	2.314
K_2O	12.112	11.836	11.72	11.759	11.965	11.932	12.307	12.523	12.286	12.791	13.046	13.136
Total	100.18	100.27	100.07	100.6	99.039	100.04	100.11	100.11	100.22	100.46	100.27	99.759
Si	2.949	2.943	2.945	2.942	2.943	2.95	2.951	2.951	2.931	2.937	2.953	2.957
Al	1.03	1.037	1.037	1.044	1.041	1.031	1.034	1.032	1.05	1.047	1.036	1.033
Fe^{3+}	0.017	0.018	0.018	0.017	0.019	0.018	0.016	0.017	0.018	0.015	0.014	0.014
Ca	0.001	0.001	0.001	0.002	0.001	0.002	0.002	0.001	0.004	0.003	0.002	0.003
Ba	0.032	0.034	0.034	0.037	0.038	0.027	0.023	0.024	0.037	0.027	0.021	0.019
Sr	0.005	0.004	0.004	0.006	0.006	0.007	0.004	0.007	0.009	0.007	0.006	0.003
Na	0.272	0.288	0.284	0.271	0.241	0.276	0.265	0.248	0.245	0.233	0.209	0.208
K	0.715	0.698	0.692	0.691	0.716	0.704	0.725	0.739	0.728	0.754	0.768	0.777

Table A 11: EMP-analysis of sanidine profile of Figure 33c from B4 trachytic bomb of Saray Volcano; number of ions based on 8 oxygens

	B4 - sanidine profile (1/2)									
label	B_2	B_3	B_4	B_5	B_6	B_7	B_8	B_9	B_10	B_11
Mineral	rim	rim	rim							
distance [µm]	0	3	6	9	12	15	18	21	24	27
SiO_2	64.366	64.45	63.2	63.038	63.294	63.153	62.816	62.996	62.467	64.526
Al_2O_3	18.42	18.614	19.042	18.838	18.727	18.686	19.125	18.965	19.032	18.85
Fe_2O_3	0.606	0.693	0.712	0.625	0.665	0.578	0.577	0.542	0.652	0.415
CaO	0.039	0.156	0.189	0.157	0.172	0.098	0.149	0.174	0.121	0.06
BaO	0.199	0.205	0.536	0.447	1.134	1.645	1.703	2.418	2.688	0.841
SrO	0.001	0.184	0.227	0.219	0.368	0.253	0.241	0.191	0.136	0.176
Na_2O	1.054	1.536	1.803	1.651	2.073	2.03	1.957	2.398	2.362	2.731
K_2O	15.727	14.917	14.073	14.262	13.719	13.597	13.41	12.882	12.527	13.311
Total	100.54	100.88	100.13	99.452	100.35	100.22	100.12	100.76	100.11	101.01
Si	2.971	2.961	2.928	2.939	2.938	2.941	2.926	2.927	2.922	2.956
Al	1.002	1.008	1.04	1.035	1.025	1.026	1.05	1.038	1.049	1.018
Fe^{3+}	0.021	0.024	0.025	0.022	0.023	0.02	0.02	0.019	0.023	0.014
Ca	0.002	0.008	0.009	0.008	0.009	0.005	0.007	0.009	0.006	0.003
Ba	0.004	0.004	0.01	0.008	0.021	0.03	0.031	0.044	0.049	0.015
Sr	0	0.005	0.006	0.006	0.01	0.007	0.007	0.005	0.004	0.005
Na	0.094	0.137	0.162	0.149	0.187	0.183	0.177	0.216	0.214	0.243
K	0.926	0.874	0.832	0.848	0.812	0.808	0.797	0.764	0.747	0.778

Table A 12: EMP-analysis of sanidine profile of Figure 33c from B4 trachytic bomb of Saray Volcano; number of ions based on 8 oxygens

	B4 - sanidine profile (2/2)										
label	B_12	B_13	B_14	B_15	B_16	B_17	B_18	B_19	B_20	B_21	B_22
Mineral											
distance [µm]	30	33	36	39	42	45	48	51	54	57	60
SiO_2	64.562	64.818	64.96	64.774	65.119	64.768	64.603	64.939	65.151	64.755	64.85
Al_2O_3	18.65	18.825	18.615	18.503	18.85	18.775	18.694	18.792	18.605	18.602	18.686
Fe_2O_3	0.477	0.369	0.419	0.423	0.442	0.448	0.526	0.391	0.365	0.456	0.4
CaO	0.088	0.097	0.052	0.071	0.083	0.046	0.066	0.045	0.075	0.049	0.062
BaO	0.705	0.602	0.457	0.47	0.471	0.506	0.503	0.5	0.519	0.548	0.582
SrO	0.118	0.117	0.032	0.103	0.121	0.137	0.147	0.094	0.083	0.078	0.032
Na_2O	2.842	2.817	2.992	2.952	3.055	2.911	3.038	2.991	3.014	2.842	2.975
K_2O	13.41	13.075	13.271	12.986	13.019	12.951	12.918	13.039	13.204	13.188	12.932
Total	100.95	100.78	100.91	100.35	101.26	100.59	100.56	100.85	101.07	100.64	100.62
Si	2.959	2.965	2.968	2.973	2.963	2.966	2.962	2.966	2.972	2.968	2.968
Al	1.007	1.015	1.002	1.001	1.011	1.013	1.01	1.012	1	1.005	1.008
Fe^{3+}	0.016	0.013	0.014	0.015	0.015	0.015	0.018	0.013	0.013	0.016	0.014
Ca	0.004	0.005	0.003	0.004	0.004	0.002	0.003	0.002	0.004	0.002	0.003
Ba	0.013	0.011	0.008	0.008	0.008	0.009	0.009	0.009	0.009	0.01	0.01
Sr	0.003	0.003	0.001	0.003	0.003	0.004	0.004	0.002	0.002	0.002	0.001
Na	0.253	0.25	0.265	0.263	0.27	0.258	0.27	0.265	0.267	0.253	0.264
K	0.784	0.763	0.774	0.76	0.756	0.757	0.756	0.76	0.768	0.771	0.755

CLINOPYROXENE

Table A 13: Representative EMP-analysis of clinopyroxene in trachytes of Saray Volcano; number of ions based on 6 oxygen oxygens Note: clinopyroxenes: AC = aegirine-augite core, AR = aegirine-augite rim, AG = aegirine-augite groundmass, BDC = bright diopsidic core, DDC = dark diopsidic core, BDR = bright diopsidic rim; see Figure 37

	aegirine-augite			diopside		
	B2	B2	L1	B1	B1	B1
	AC	AR	AG	BDC	DDC	BDR
SiO_2	50.62	50.90	51.31	53.58	54.34	50.75
TiO_2	1.86	1.07	3.59	0.66	0.29	0.81
Al_2O_3	0.95	0.87	0.69	0.54	0.70	2.39
Fe_2O_3	20.77	20.79	24.14	1.86	1.53	5.27
FeO	0.05	2.72	1.34	3.36	1.73	4.62
MnO	0.52	0.59	0.29	0.19	0.10	0.37
MgO	4.29	3.22	0.98	15.58	17.59	12.02
CaO	11.43	11.32	4.90	22.98	24.28	22.44
Na_2O	8.39	8.22	11.82	0.84	0.19	1.28
K_2O	0.14	0.05	0.04	0.00	0.02	0.10
Total	99.03	99.75	99.09	99.59	100.78	100.05
Si	1.94	1.96	1.97	1.97	1.96	1.90
Ti	0.05	0.03	0.10	0.02	0.01	0.02
Al	0.04	0.04	0.03	0.02	0.03	0.11
Fe^{3+}	0.60	0.60	0.70	0.05	0.04	0.15
Fe^{2+}	0.00	0.09	0.04	0.10	0.05	0.14
Mn	0.02	0.02	0.01	0.01	0.00	0.01
Mg	0.25	0.18	0.06	0.86	0.95	0.67
Ca	0.47	0.47	0.20	0.91	0.94	0.90
Na	0.62	0.61	0.88	0.06	0.01	0.09
K	0.01	0.00	0.00	0.00	0.00	0.00

PHLOGOPITE

Table A 14: EMP-analysis of phlogopite phl-I in minette of Saray Volcano; number of ions based on 24 oxygen and F; see Figure 37

	phl-I in minette											
	M2											
label	A_29	A_30	A_31	A_32	A_33	A_34	A_35	A_36	A_37	A_38	A_39	A_40
	core											rim
SiO_2	37.99	38.58	39.00	39.26	39.03	39.13	38.89	39.09	39.08	38.23	38.90	37.46
TiO_2	3.90	3.76	3.59	3.53	3.74	3.97	4.03	3.63	3.87	3.93	5.21	5.51
Al_2O_3	12.96	13.24	13.20	13.21	13.30	13.43	13.23	13.65	13.21	13.12	13.41	13.06
Cr_2O_3	0.00	0.04	0.00	0.00	0.03	0.00	0.03	0.06	0.00	0.00	0.02	0.01
FeO	8.17	9.00	8.27	8.67	8.44	8.20	8.27	8.57	8.54	8.34	8.09	9.88
MnO	0.04	0.03	0.00	0.06	0.09	0.05	0.06	0.11	0.04	0.07	0.04	0.08
MgO	20.24	20.68	20.59	20.57	20.52	20.54	20.49	20.52	20.40	20.52	20.40	18.76
CaO	0.01	0.01	0.03	0.09	0.01	0.05	0.00	0.00	0.06	0.02	0.00	0.03
BaO	0.83	1.11	0.91	1.13	1.00	1.07	0.99	0.90	0.90	1.03	2.33	2.10
Na_2O	0.31	0.29	0.35	0.30	0.23	0.29	0.27	0.36	0.29	0.29	0.30	0.38
K_2O	9.41	9.36	9.63	9.33	9.49	9.55	9.47	9.41	9.38	9.30	8.94	8.90
F	1.08	1.09	1.13	1.07	1.06	1.10	1.19	1.18	1.04	1.12	1.01	1.61
Total	94.94	97.19	96.70	97.22	96.94	97.38	96.92	97.48	96.81	95.97	98.65	97.78
F=O	0.45	0.46	0.48	0.45	0.45	0.46	0.50	0.50	0.44	0.47	0.42	0.68
New Total	94.49	96.73	96.22	96.77	96.49	96.92	96.42	96.98	96.37	95.50	98.23	97.10
Si	5.72	5.70	5.77	5.79	5.77	5.76	5.76	5.75	5.78	5.71	5.72	5.64
Ti	0.44	0.42	0.40	0.39	0.42	0.44	0.45	0.40	0.43	0.44	0.58	0.62
Al	2.30	2.30	2.30	2.30	2.32	2.33	2.31	2.36	2.30	2.31	2.33	2.32
Cr	0.00	0.00	0.00	0.00	0.00	0.00	0.00	0.01	0.00	0.00	0.00	0.00
Fe^{2+}	1.03	1.11	1.02	1.07	1.04	1.01	1.02	1.05	1.06	1.04	1.00	1.24
Mn	0.01	0.00	0.00	0.01	0.01	0.01	0.01	0.01	0.01	0.01	0.00	0.01
Mg	4.55	4.55	4.54	4.52	4.52	4.51	4.52	4.50	4.50	4.57	4.47	4.21
Ca	0.00	0.00	0.00	0.01	0.00	0.01	0.00	0.00	0.01	0.00	0.00	0.00
Ba	0.05	0.06	0.05	0.07	0.06	0.06	0.06	0.05	0.05	0.06	0.13	0.12
Na	0.09	0.08	0.10	0.09	0.07	0.08	0.08	0.10	0.08	0.08	0.09	0.11
K	1.81	1.76	1.82	1.76	1.79	1.79	1.79	1.76	1.77	1.77	1.68	1.71
F	0.55	0.54	0.56	0.53	0.52	0.54	0.59	0.58	0.52	0.56	0.49	0.80

Table A 15: EMP-analysis of phlogopite phl-I in trachyte of Saray Volcano; number of ions based on 24 oxygen and F; see Figure 39a

	phl-I in trachyte									
	B4									
label	6_B_02	B_03	B_04	B_05	B_06	B_07	B_08	B_09	B_10	B_11
	core									rim
SiO_2	42.07	41.98	41.90	41.75	41.79	41.56	42.04	41.95	41.67	41.73
TiO_2	1.23	1.29	1.17	1.13	1.23	1.23	1.21	1.16	1.13	1.28
Al_2O_3	12.77	12.81	12.76	12.70	12.87	12.51	12.37	12.65	12.84	12.77
Cr_2O_3	0.59	0.44	0.43	0.45	0.70	0.43	0.26	0.40	0.36	0.30
FeO	3.92	3.98	4.10	3.97	4.16	4.21	4.56	4.70	5.11	5.49
MnO	0.01	0.01	0.02	0.00	0.00	0.03	0.00	0.03	0.04	0.04
MgO	24.37	24.65	24.77	24.76	24.55	24.73	24.79	24.56	24.46	24.53
CaO	0.18	0.00	0.00	0.02	0.02	0.00	0.00	0.00	0.01	0.04
BaO	0.05	0.13	0.06	0.16	0.09	0.12	0.06	0.08	0.11	0.11
Na_2O	0.39	0.34	0.46	0.50	0.57	0.55	0.59	0.58	0.54	0.42
K_2O	9.98	10.08	9.94	9.77	9.74	9.70	9.67	9.74	9.74	9.86
F	1.45	0.77	0.54	0.53	0.67	0.98	0.91	1.37	2.16	3.41
Total	97.01	96.48	96.16	95.74	96.38	96.07	96.48	97.22	98.19	99.99
F=O	0.61	0.33	0.23	0.22	0.28	0.41	0.38	0.58	0.91	1.43
New Total	96.40	96.16	95.93	95.52	96.10	95.65	96.10	96.65	97.28	98.56
Si	6.02	5.99	5.98	5.98	5.97	5.96	6.00	5.98	5.94	5.93
Ti	0.13	0.14	0.13	0.12	0.13	0.13	0.13	0.12	0.12	0.14
Al	2.15	2.16	2.15	2.14	2.16	2.12	2.08	2.13	2.16	2.14
Cr	0.07	0.05	0.05	0.05	0.08	0.05	0.03	0.05	0.04	0.03
Fe^{2+}	0.47	0.48	0.49	0.48	0.50	0.51	0.54	0.56	0.61	0.65
Mn	0.00	0.00	0.00	0.00	0.00	0.00	0.00	0.00	0.01	0.01
Mg	5.20	5.25	5.27	5.29	5.22	5.29	5.28	5.22	5.20	5.19
Ca	0.03	0.00	0.00	0.00	0.00	0.00	0.00	0.00	0.00	0.01
Ba	0.00	0.01	0.00	0.01	0.01	0.01	0.00	0.00	0.01	0.01
Na	0.11	0.09	0.13	0.14	0.16	0.15	0.16	0.16	0.15	0.12
K	1.82	1.84	1.81	1.79	1.77	1.78	1.76	1.77	1.77	1.79
F	0.70	0.37	0.26	0.26	0.32	0.48	0.44	0.66	1.03	1.60

Table A 16: Representative EMP-analysis of phlogopite phl-II in trachytic bomb (B3) and lava (L2), glimmerite (X-Gl) and mafic minette (M) of Saray Volcano; number of ions based on 24 oxygen and F

	phl-II											
	B3		L2	X-Gl		M2				M1		
label	19_3	15a_A_07	2_17	2_A_30	6_A_15	1_A_01	A_26	6_03	6_10	9_B4	9_B17	6_14
SiO_2	38.52	36.89	40.69	39.92	36.36	37.20	37.89	37.22	37.09	35.38	35.22	36.12
TiO_2	4.33	4.92	3.66	3.29	3.70	4.90	3.64	4.84	5.08	7.19	7.43	6.44
Al_2O_3	12.48	13.83	11.14	14.03	14.40	12.56	12.92	13.11	11.95	13.08	13.06	13.47
Cr_2O_3	0.00	0.02	0.00	0.00	0.08	0.00	0.01	0.11	0.02	0.00	0.00	0.00
FeO	9.26	18.21	8.62	10.45	11.60	9.91	7.92	9.86	11.46	8.14	8.09	9.19
MnO	0.23	0.25	0.33	0.09	0.11	0.09	0.07	0.06	0.16	0.07	0.06	0.16
MgO	18.87	13.84	20.15	19.73	17.35	18.14	20.58	18.39	16.76	17.82	17.83	17.84
CaO	0.47	0.00	0.06	0.74	0.00	0.27	0.00	0.05	0.03	0.00	0.00	0.00
BaO	0.00	0.79	0.07	0.46	1.66	2.35	1.00	1.55	2.46	3.95	4.24	3.40
Na_2O	0.99	0.62	0.53	0.23	0.11	0.42	0.31	0.37	0.51	0.57	0.59	0.55
K_2O	8.65	8.75	9.49	9.48	9.49	8.62	9.53	9.17	8.60	7.96	7.86	8.19
F	6.82	1.98	7.25	1.86	0.68	2.02	1.24	1.12	1.86	2.18	2.10	1.56
Total	100.62	100.09	101.99	100.28	95.54	96.48	95.11	95.85	95.98	96.34	96.48	96.92
F=O	2.87	0.83	3.05	0.78	0.29	0.85	0.52	0.47	0.78	0.92	0.88	0.66
New Total	97.75	99.26	98.94	99.50	95.25	95.63	94.59	95.38	95.20	95.42	95.60	96.26
Si	5.81	5.59	6.07	5.77	5.55	5.72	5.70	5.66	5.78	5.53	5.50	5.55
Ti	0.49	0.56	0.41	0.36	0.42	0.57	0.41	0.55	0.60	0.84	0.87	0.74
Al	2.22	2.47	1.96	2.39	2.59	2.27	2.29	2.35	2.19	2.41	2.40	2.44
Cr	0.00	0.00	0.00	0.00	0.01	0.00	0.00	0.01	0.00	0.00	0.00	0.00
Fe^{2+}	1.17	2.31	1.07	1.26	1.48	1.27	1.00	1.25	1.49	1.06	1.06	1.18
Mn	0.03	0.03	0.04	0.01	0.01	0.01	0.01	0.01	0.02	0.01	0.01	0.02
Mg	4.25	3.12	4.48	4.25	3.95	4.16	4.61	4.17	3.89	4.15	4.15	4.09
Ca	0.08	0.00	0.01	0.11	0.00	0.04	0.00	0.01	0.01	0.00	0.00	0.00
Ba	0.00	0.05	0.00	0.03	0.10	0.14	0.06	0.09	0.15	0.24	0.26	0.20
Na	0.29	0.18	0.15	0.06	0.03	0.13	0.09	0.11	0.15	0.17	0.18	0.16
K	1.67	1.69	1.80	1.75	1.85	1.69	1.83	1.78	1.71	1.59	1.57	1.61
F	3.25	0.99	3.39	0.89	0.35	1.02	0.63	0.57	0.96	1.11	1.07	0.79

Table A 17: Representative EMP-analysis of phlogopite phl-II in felsic minette (F) and wherlite xenolith (X-Ol) of Saray Volcano; number of ions based on 24 oxygen and F

	phl-II									
	F1		F2						X-Ol	
label	10_01	8_A10	13_A_01	13_A_05	13_A_07	13_A_17	7_A40	A1	1_4	2_4
SiO_2	34.74	36.03	35.99	36.24	36.13	35.29	36.35	36.33	38.20	37.36
TiO_2	4.73	3.75	5.11	4.15	4.20	4.20	5.64	5.20	3.57	3.81
Al_2O_3	13.82	13.59	13.02	13.18	13.14	13.43	12.68	13.12	10.95	11.16
Cr_2O_3	0.02	0.01	0.07	0.13	0.15	0.18	0.02	0.01	0.04	0.00
FeO	17.71	16.76	14.34	16.12	16.30	16.68	15.35	14.49	7.99	7.80
MnO	0.24	0.30	0.31	0.21	0.21	0.24	0.24	0.25	0.10	0.09
MgO	12.00	13.55	14.61	14.04	13.95	13.75	14.03	14.51	20.74	20.78
CaO	0.01	0.00	0.03	0.01	0.01	0.01	0.00	0.00	0.03	0.00
BaO	1.69	0.86	1.11	0.62	0.66	2.02	0.83	1.27	4.80	5.27
Na_2O	0.36	0.39	0.58	0.47	0.57	0.38	0.57	0.49	0.35	0.25
K_2O	8.85	8.79	8.92	9.13	8.85	8.61	8.95	8.78	8.30	8.00
F	0.36	1.86	3.12	1.32	1.75	1.03	1.71	1.96	3.74	3.61
Total	94.53	95.89	97.21	95.62	95.92	95.82	96.37	96.41	98.81	98.13
F=O	0.15	0.78	1.31	0.56	0.74	0.43	0.72	0.82	1.57	1.52
New Total	94.38	95.11	95.90	95.06	95.18	95.39	95.65	95.59	97.24	96.61
Si	5.55	5.67	5.63	5.66	5.66	5.56	5.68	5.68	5.84	5.76
Ti	0.57	0.44	0.60	0.49	0.49	0.50	0.66	0.61	0.41	0.44
Al	2.60	2.52	2.40	2.43	2.43	2.49	2.34	2.42	1.97	2.03
Cr	0.00	0.00	0.01	0.02	0.02	0.02	0.00	0.00	0.00	0.00
Fe^{2+}	2.37	2.21	1.88	2.11	2.13	2.20	2.01	1.89	1.02	1.01
Mn	0.03	0.04	0.04	0.03	0.03	0.03	0.03	0.03	0.01	0.01
Mg	2.86	3.18	3.41	3.27	3.26	3.23	3.27	3.38	4.73	4.78
Ca	0.00	0.00	0.01	0.00	0.00	0.00	0.00	0.00	0.00	0.00
Ba	0.11	0.05	0.07	0.04	0.04	0.12	0.05	0.08	0.29	0.32
Na	0.11	0.12	0.18	0.14	0.17	0.12	0.17	0.15	0.10	0.07
K	1.80	1.76	1.78	1.82	1.77	1.73	1.78	1.75	1.62	1.57
F	0.19	0.97	1.59	0.69	0.91	0.54	0.88	1.01	1.86	1.82

CARBONATE

Table A 18: Representative EMP-analysis of carbonates in trachytic bomb (B3) and felsic minette (F) of Saray Volcano; number of ions based on 3 oxygen

	B3				F1		F2			F3			
Sample	19_11	19_13	19_8	17_6	10_3	1_01b	6_05	6_09	8_2	1b_03	1b_06	4a_B02	4a_B06
SiO_2	0.79	0.07	0.36	0.02	0.23	0.12	0.04	0.07	0.09	0.07	0.04	0.01	0.02
FeO	2.43	5.51	3.05	6.44	10.45	11.17	0.03	0.04	0.00	9.51	2.60	2.18	6.79
MnO	0.37	0.39	0.89	0.30	0.69	1.00	0.03	0.01	0.00	0.63	0.44	0.29	1.61
MgO	0.85	18.69	0.45	19.04	13.55	11.10	1.21	1.04	1.83	16.30	0.31	0.29	18.21
CaO	58.65	32.75	59.36	31.31	27.85	28.14	62.56	59.82	60.53	33.25	60.50	61.22	32.91
BaO	0.06	0.00	0.04	0.01	0.04	0.01	0.00	0.00	0.01	0.00	0.00	0.04	0.00
SrO	0.00	0.00	0.00	0.00	0.00	0.00	0.00	0.00	0.00	0.00	0.00	0.00	0.00
Na_2O	0.02	0.02	0.02	0.02	0.03	0.01	0.02	0.02	0.00	0.06	0.03	0.02	0.00
K_2O	0.30	0.10	0.12	0.02	0.00	0.01	0.02	0.02	0.00	0.00	0.04	0.00	0.00
Total	63.47	57.53	64.29	57.16	52.84	51.56	63.91	61.02	62.46	59.82	63.96	64.05	59.54
Si	0.01	0.00	0.01	0.00	0.01	0.00	0.00	0.00	0.00	0.00	0.00	0.00	0.00
Fe^{2+}	0.03	0.14	0.04	0.16	0.29	0.33	0.00	0.00	0.00	0.23	0.03	0.03	0.16
Mn	0.01	0.01	0.01	0.01	0.02	0.03	0.00	0.00	0.00	0.02	0.01	0.00	0.04
Mg	0.02	0.82	0.01	0.84	0.68	0.58	0.03	0.02	0.04	0.71	0.01	0.01	0.78
Ca	0.92	1.03	0.93	0.99	1.00	1.06	0.97	0.97	0.96	1.04	0.95	0.96	1.02
Ba	0.00	0.00	0.00	0.00	0.00	0.00	0.00	0.00	0.00	0.00	0.00	0.00	0.00
Sr	0.00	0.00	0.00	0.00	0.00	0.00	0.00	0.00	0.00	0.00	0.00	0.00	0.00
Na	0.00	0.00	0.00	0.00	0.00	0.00	0.00	0.00	0.00	0.00	0.00	0.00	0.00
K	0.01	0.00	0.00	0.00	0.00	0.00	0.00	0.00	0.00	0.00	0.00	0.00	0.00

GLASS

Table A 19: Representative EMP-analysis of glass in trachytic bombs (B) and mafic minette (M) of Saray Volcano

	B1				B2		B3		B4		M1	
Label	2_4	2_13	2_14	2_16	4_2	5_4	1_4	1_7	3_15	4_G_4	4_02	4_03
SiO_2	58.44	61.455	60.399	61.389	62.923	57.548	65.965	64.518	65.9	63.727	60.43	63.28
TiO_2	0.78	0.35	0.487	0.37	0.041	0.03	0.009	0.046	0.139	0.237	0	0.17
Al_2O_3	17.406	18.894	18.628	18.594	18.01	22.013	19.759	18.537	18.243	17.727	19.36	18.41
Fe_2O_3	5.985	1.963	3.059	2.607	0.922	1.582	0.122	0.913	1.126	1.301	0.9213	0.9324
MnO	0.148	0.095	0.094	0.036	0	0	0	0	0	0	0.02	0
MgO	0.784	0.488	0.557	0.269	0	0.027	0.003	0.011	0.088	0.065	0.02	0.02
CaO	0.218	0.266	0.431	0.91	0	0.012	0.017	0.115	0.046	0.013	0.3	0.23
BaO	0.013	0.154	0.17	0.242	0.103	0	n.a.	n.a.	0.111	0.437	4.42	1.14
SrO	0	0	0	0.053	0	0	n.a.	n.a.	0	0.048	0.34	0.06
Na_2O	0.87	0.967	0.913	3.267	2.88	0.437	0.336	2.108	0.503	0.747	2.63	3.47
K_2O	13.903	14.649	13.721	11.185	13.289	16.903	14.994	11.994	13.006	15.788	9.92	10.46
Total	98.546	99.282	98.459	98.922	98.168	98.552	101.2	98.241	99.162	100.09	98.38	98.13

A-2B LAACHER SEE VOLCANO

FELDSPAR

Table A 20: Representative EMP-analysis of plagioclase in bright haüyne-sanidinite and dark haüyne-sanidinite from Laacher See Volcano; number of ions based on 8 oxygens

	bright haüyne-sanidinite						dark haüyne-sanidinite					
sample	IDD5	IDD11					IDD24					
Label	3_01	1_02	1_A_24a	2_D_15	2_D_30	4_04	3a_A_6	3a_A_7	3a_A_8	3a_A_24	3a_A_31	3a_A_34
SiO_2	64.14	64.27	64.36	64.15	64.57	64.99	62.00	61.94	61.63	62.24	62.38	61.78
Al_2O_3	21.78	21.39	21.37	21.84	21.66	21.60	23.24	23.25	23.26	22.92	22.92	23.32
Fe_2O_3	0.24	0.19	0.22	0.16	0.19	0.33	0.34	0.33	0.31	0.36	0.31	0.36
CaO	3.19	2.62	2.57	3.04	2.98	2.71	5.08	5.00	5.07	4.62	4.65	5.07
Na_2O	8.97	8.97	8.90	9.01	9.02	9.02	7.69	7.84	7.61	7.71	7.78	7.75
K_2O	1.70	2.06	2.17	1.78	1.87	2.02	1.74	1.67	1.77	1.94	1.99	1.70
Total	100.01	99.49	99.58	99.98	100.29	100.67	100.09	100.03	99.66	99.78	100.01	99.97
Si	2.85	2.87	2.87	2.85	2.86	2.87	2.76	2.76	2.76	2.78	2.78	2.76
Al	1.14	1.12	1.12	1.14	1.13	1.12	1.22	1.22	1.23	1.21	1.20	1.23
Fe^{3+}	0.01	0.01	0.01	0.01	0.01	0.01	0.01	0.01	0.01	0.01	0.01	0.01
Ca	0.15	0.13	0.12	0.14	0.14	0.13	0.24	0.24	0.24	0.22	0.22	0.24
Na	0.77	0.78	0.77	0.78	0.77	0.77	0.67	0.68	0.66	0.67	0.67	0.67
K	0.10	0.12	0.12	0.10	0.11	0.11	0.10	0.10	0.10	0.11	0.11	0.10
An	14.90	12.29	12.12	14.12	13.81	12.64	24.13	23.62	24.18	22.10	22.05	24.04
Ab	75.69	76.20	75.76	75.98	75.81	76.11	66.04	67.00	65.77	66.80	66.73	66.37
Or	9.41	11.50	12.12	9.90	10.38	11.25	9.83	9.39	10.05	11.10	11.22	9.59

Table A 21: Representative EMP-analysis of sanidine in nosean-sanidinite from Laacher See Volcano; number of ions based on 8 oxygens

	nosean-sanidinite											
Sample	LS59		LS64					LS113	LS125			
label	1_A_2	2_A_33	2a_1	1b_A_12	10_A_9	10_A_26	18_B_44	25_A_21	1_D_4	1_D_23	1_B_29	1_B_30
SiO_2	66.89	66.53	66.74	66.23	66.99	67.41	67.05	66.4	65.71	65.81	65.63	65.62
Al_2O_3	18.83	18.47	19.47	19.11	18.83	18.96	19.08	19.1	18.87	18.53	19.25	19.27
Fe_2O_3	0.138	0.134	0.108	0.185	0.079	0.179	0.156	0.128	0.067	0.125	0.141	0.141
CaO	0.049	0.068	0.4	0.107	0.043	0.121	0.216	0.103	0.245	0.077	0.091	0.094
Na_2O	5.737	6.453	9.036	6.347	5.594	6.555	7.506	6.163	4.793	5.476	5.681	5.895
K_2O	8.676	7.464	3.552	7.754	8.904	7.586	6.138	8.022	9.789	9.022	8.333	8.055
Total	100.3	99.12	99.31	99.73	100.4	100.8	100.1	99.91	99.47	99.04	99.12	99.08
Si	3	3.008	2.975	2.982	3.002	2.998	2.99	2.986	2.987	2.997	2.977	2.976
Al	0.995	0.984	1.023	1.014	0.994	0.994	1.002	1.012	1.011	0.995	1.029	1.03
Fe^{3+}	0.005	0.005	0.004	0.006	0.003	0.006	0.005	0.004	0.002	0.004	0.005	0.005
Ca	0.002	0.003	0.019	0.005	0.002	0.006	0.01	0.005	0.012	0.004	0.004	0.005
Na	0.499	0.566	0.781	0.554	0.486	0.565	0.649	0.537	0.422	0.484	0.5	0.518
K	0.496	0.43	0.202	0.445	0.509	0.43	0.349	0.46	0.568	0.524	0.482	0.466
An	0.20	0.30	1.90	0.50	0.20	0.60	0.99	0.50	1.20	0.40	0.41	0.51
Ab	50.05	56.66	77.94	55.18	48.75	56.44	64.38	53.59	42.12	47.83	50.71	52.38
Or	49.75	43.04	20.16	44.32	51.05	42.96	34.62	45.91	56.69	51.78	48.88	47.12

Table A 22: Representative EMP-analysis of sanidine in bright haüyne-sanidinite from Laacher See Volcano; number of ions based on 8 oxygens

	bright haüyne-sanidinite											
sample	IDD5			IDD11					LS160			
Label	7_A_23	3_B_04	3_B_06	1_A_04	2_A_03	3b_A_03	3b_A_06	3b_A_08	9b_C_6	16_A_6	12_A_25	14_A_46
SiO_2	66.4	66.3	66.16	65.48	66.16	66.24	66.27	66.33	65.97	66.25	66.31	66.55
Al_2O_3	19.46	19	19.33	19.38	19.66	19.33	19.26	19.15	19.52	19.46	19.4	19.64
Fe_2O_3	0.24	0.157	0.134	0.161	0.175	0.19	0.187	0.208	0.175	0.267	0.203	0.131
CaO	0.67	0.34	0.653	0.68	0.743	0.48	0.441	0.417	0.679	0.527	0.594	0.776
Na_2O	5.701	4.926	5.677	5.971	6.067	5.488	5.363	5.308	6.54	6.093	6.107	6.616
K_2O	8.26	9.651	8.378	7.772	7.854	8.712	8.966	9.044	7.165	7.726	7.803	6.938
Total	100.7	100.4	100.3	99.45	100.7	100.4	100.5	100.5	100.1	100.3	100.4	100.7
Si	2.968	2.985	2.97	2.962	2.957	2.973	2.975	2.979	2.96	2.968	2.969	2.964
Al	1.025	1.008	1.023	1.033	1.036	1.022	1.019	1.014	1.032	1.027	1.024	1.031
Fe^{3+}	0.008	0.005	0.005	0.005	0.006	0.006	0.006	0.007	0.006	0.009	0.007	0.004
Ca	0.032	0.016	0.031	0.033	0.036	0.023	0.021	0.02	0.033	0.025	0.028	0.037
Na	0.494	0.43	0.494	0.524	0.526	0.478	0.467	0.462	0.569	0.529	0.53	0.571
K	0.471	0.554	0.48	0.448	0.448	0.499	0.514	0.518	0.41	0.442	0.446	0.394
An	3.21	1.60	3.08	3.28	3.56	2.30	2.10	2.00	3.26	2.51	2.79	3.69
Ab	49.55	43.00	49.15	52.14	52.08	47.80	46.61	46.20	56.23	53.11	52.79	56.99
Or	47.24	55.40	47.76	44.58	44.36	49.90	51.30	51.80	40.51	44.38	44.42	39.32

Table A 23: Representative EMP-analysis of sanidine in dark haüyne-sanidinite from Laacher See Volcano; number of ions based on 8 oxygens

	dark haüyne-sanidinite										
sample	IDD24						LS211				
label	1b_B_5	3a_B_21	3a_B_25	3e_B_3	3e_B_17	3c_A_3	3d_1	1b_6	2a_A_13	1b_A_13	2a_B_16
SiO_2	65.21	65.38	65.6	65.03	64.85	64.71	65.62	65.43	64.87	65.42	64.91
Al_2O_3	19.36	19.46	19.55	19.21	19.22	19.35	19.58	19.01	19.47	19.74	19.77
Fe_2O_3	0.218	0.216	0.215	0.224	0.194	0.233	0	0	0	0.005	0.011
CaO	0.66	0.809	0.708	0.677	0.628	0.853	1.08	0.688	1.064	0.995	1.252
Na_2O	4.268	4.476	4.361	4.262	4.153	4.512	5.227	4.844	5.261	5.237	5.631
K_2O	10.23	9.789	10.17	10.1	10.35	9.689	8.161	9.308	8.279	8.622	7.877
Total	99.94	100.1	100.6	99.5	99.4	99.34	99.66	99.27	98.94	100	99.45
Si	2.96	2.957	2.957	2.963	2.961	2.952	2.961	2.977	2.954	2.95	2.94
Al	1.036	1.038	1.038	1.031	1.034	1.04	1.041	1.019	1.045	1.049	1.056
Fe^{3+}	0.007	0.007	0.007	0.008	0.007	0.008	0	0	0	0	0
Ca	0.032	0.039	0.034	0.033	0.031	0.042	0.052	0.034	0.052	0.048	0.061
Na	0.376	0.393	0.381	0.377	0.368	0.399	0.457	0.427	0.465	0.458	0.495
K	0.592	0.565	0.585	0.587	0.603	0.564	0.47	0.54	0.481	0.496	0.455
An	3.20	3.91	3.40	3.31	3.09	4.18	5.31	3.40	5.21	4.79	6.03
Ab	37.60	39.42	38.10	37.81	36.73	39.70	46.68	42.66	46.59	45.71	48.96
Or	59.20	56.67	58.50	58.88	60.18	56.12	48.01	53.95	48.20	49.50	45.00

HAÜYNE AND NOSEAN

Table A 24: Representative EMP-analysis of nosean in nosean-sanidinite from Laacher See Volcano; number of ions based on 21 oxygens; ** CO_2 is calculated as the difference to 2 apfu after Raman spectroscopy showed the absence of water

	nosean-sanidinite										
sample	LS125			LS64				LS113			
label	9_1	9_9	25_B_18	4_A_30	4_A_33	4_A_45	4_B_5	18_A_2	18_A_12	18_B_13	18_B_19
SiO_2	36.81	36.79	36.69	37.66	36.87	36.89	36.76	36.66	36.53	36.14	36.81
Al_2O_3	30.49	30.62	29.90	31.24	30.64	30.19	29.81	29.91	30.68	29.42	30.33
Fe_2O_3	0.19	0.16	0.14	0.43	0.29	0.48	0.25	0.22	0.13	0.22	0.17
CaO	1.46	1.53	2.27	1.16	1.15	1.18	1.70	2.41	2.54	2.80	2.25
Na_2O	22.44	22.74	22.06	20.72	22.64	21.82	21.91	21.20	21.23	21.49	21.37
K_2O	0.83	0.85	0.51	1.32	0.22	0.93	0.26	0.49	0.51	0.40	0.47
Cl	0.74	0.89	0.51	0.42	0.40	0.38	0.43	0.40	0.44	0.34	0.43
SO_3	6.75	6.46	8.79	8.00	8.03	8.28	8.60	9.43	9.73	9.34	9.21
Total	99.72	100.04	100.87	100.96	100.25	100.14	99.73	100.73	101.82	100.15	101.05
O=(F,Cl)	0.17	0.20	0.11	0.10	0.09	0.09	0.10	0.09	0.10	0.08	0.10
Total*	99.55	99.84	100.75	100.87	100.16	100.06	99.63	100.64	101.72	100.07	100.95
Si	6.05	6.04	6.10	6.04	6.04	6.07	6.10	6.09	6.02	6.09	6.07
Al	5.91	5.93	5.85	5.90	5.91	5.85	5.83	5.85	5.96	5.85	5.89
Fe^{3+}	0.02	0.02	0.02	0.05	0.04	0.06	0.03	0.03	0.02	0.03	0.02
Ca	0.26	0.27	0.40	0.20	0.20	0.21	0.30	0.43	0.45	0.51	0.40
Na	7.15	7.24	7.11	6.44	7.19	6.96	7.05	6.83	6.78	7.03	6.83
K	0.17	0.18	0.11	0.27	0.05	0.19	0.06	0.10	0.11	0.09	0.10
Cl	0.21	0.25	0.14	0.13	0.12	0.11	0.13	0.11	0.12	0.09	0.12
SO_4	0.83	0.80	1.10	0.96	0.99	1.02	1.07	1.18	1.20	1.18	1.14
CO_2**	0.96	0.95	0.76	0.91	0.89	0.86	0.80	0.71	0.68	0.73	0.74

Table A 25: Representative EMP-analysis of nosean sensu strictu in bright haüyne-sanidinite and haüyne in dark haüyne-sanidinite from Laacher See Volcano; number of ions based on 21 oxygens; ** CO_2 is calculated as the difference to 2 apfu after Raman spectroscopy showed the absence of water

	dark haüyne-sanidinite						bright haüyne-sanidinite					
sample	LS211	IDD24					LS160					
label	3b_A_23	3b_A_8	3b_A_25	1c_11	3e_A_14	3e_A_17	8_1	8_5	13_1	8_A_32	8_B_2	8_C_33
SiO_2	35.94	33.77	33.92	33.61	33.90	34.09	34.92	35.72	35.31	34.27	34.25	34.35
Al_2O_3	32.25	28.34	28.90	29.29	28.90	29.17	29.16	29.61	29.28	29.11	29.03	28.73
Fe_2O_3	0.32	0.21	0.30	0.21	0.22	0.22	0.25	0.14	0.27	0.16	0.14	0.26
CaO	7.11	7.92	8.06	8.41	8.18	8.25	6.15	5.83	5.80	5.83	5.96	5.65
Na_2O	9.07	13.47	13.66	14.23	13.56	13.83	18.67	18.99	19.26	18.89	18.93	18.93
K_2O	0.57	1.19	1.16	1.08	0.94	0.93	1.10	1.12	0.93	1.07	1.14	1.02
Cl	0.38	0.47	0.46	0.45	0.45	0.46	1.03	1.04	1.10	1.09	1.03	1.01
SO_3	15.30	13.81	13.38	13.13	13.50	13.44	9.73	9.14	9.14	9.86	9.71	10.07
Total	100.96	99.16	99.83	100.40	99.65	100.39	101.00	101.59	101.08	100.28	100.20	100.03
O=(F,Cl)	0.09	0.11	0.10	0.10	0.10	0.10	0.23	0.24	0.25	0.25	0.23	0.23
Total*	100.88	99.06	99.73	100.30	99.54	100.28	100.77	101.36	100.84	100.03	99.96	99.81
Si	5.84	6.02	5.97	5.92	5.97	5.97	6.03	6.05	6.04	5.99	5.99	6.02
Al	6.18	5.95	6.00	6.08	6.00	6.02	5.93	5.91	5.91	6.00	5.99	5.94
Fe^{3+}	0.04	0.03	0.04	0.03	0.03	0.03	0.03	0.02	0.04	0.02	0.02	0.03
Ca	1.24	1.51	1.52	1.59	1.54	1.55	1.14	1.06	1.06	1.09	1.12	1.06
Na	2.86	4.65	4.66	4.86	4.64	4.69	6.25	6.24	6.39	6.40	6.43	6.43
K	0.12	0.27	0.26	0.24	0.21	0.21	0.24	0.24	0.20	0.24	0.25	0.23
Cl	0.12	0.14	0.14	0.13	0.13	0.14	0.30	0.31	0.32	0.32	0.30	0.29
SO_4	1.87	1.85	1.77	1.74	1.79	1.76	1.26	1.16	1.17	1.29	1.28	1.33
CO_2**	0.02	0.01	0.09	0.13	0.08	0.10	0.44	0.53	0.51	0.39	0.42	0.38

CALCITE

Table A 26: Representative EMP-analysis of calcite in nosean-sanidinite from Laacher See Volcano

	calcite											
sample	LS64	LS113			LS125							
Label	4c_2	5_1	5_2	8_1	1_2	7_A_26	7_A_27	7_A_31	7_A_32	7_A_33	7_A_34	7_A_35
FeO	0.33	0.29	0.33	0.07	0.30	0.58	0.50	0.45	0.70	0.47	0.42	0.57
MnO	2.37	1.97	1.79	0.13	1.96	2.45	2.48	2.44	1.53	2.05	2.34	2.52
MgO	0.08	0.00	0.00	0.46	0.00	0.06	0.04	0.04	0.08	0.02	0.04	0.03
CaO	58.95	61.83	60.86	61.14	61.39	59.79	58.68	53.79	61.72	56.90	57.40	56.26
Na_2O	0.10	0.08	0.03	0.08	0.09	0.06	0.04	0.03	0.02	0.11	0.04	0.04
Total	61.83	64.17	63.01	61.88	63.74	62.95	61.74	56.75	64.04	59.55	60.25	59.42

CLINOPYROXENE

Table A 27: Representative EMP-analysis of clinopyroxene in dark and bright haüyne-sanidinite and in nosean-sanidinite; number of ions based on 6 oxygen

	dark haüyne-sanidinite			bright haüyne-sanidinite					nosean-sanidinite			
sample	IDD24		LS211	IDD11	LS170		160		IDD64		LS113	LS125
lable	1a_A_12	1c_7	3d_3	1a_06	14_5	11_A_10	9b_D_9	9b_F_32	8_4	8_9	12_1	8_6
SiO_2	48.08	47.61	42.41	47.09	50.13	48.72	47.07	46.99	48.71	47.97	49.61	46.49
TiO_2	0.68	1.30	2.96	0.87	0.55	0.61	0.60	0.63	1.14	0.15	0.43	1.13
Al_2O_3	2.99	4.81	4.93	4.01	2.76	3.06	3.53	3.52	1.47	0.27	1.93	1.62
Fe_2O_3	6.82	4.39	4.60	7.34	6.44	7.31	8.26	9.33	8.10	6.92	5.76	9.23
FeO	7.44	8.71	11.92	11.04	8.40	9.41	11.25	11.03	9.20	5.74	15.01	10.62
MnO	2.11	1.22	1.80	2.64	2.06	2.55	2.51	2.57	9.47	15.79	4.07	11.17
MgO	8.67	9.85	8.41	6.44	8.70	6.65	5.36	5.08	1.70	1.57	3.83	0.50
CaO	21.19	21.49	21.83	19.33	20.34	19.02	19.61	19.30	17.01	20.31	14.01	16.34
Na_2O	1.40	1.59	0.82	2.33	2.23	2.71	2.44	2.37	3.61	1.24	5.39	3.07
K_2O	0.01	0.00	0.07	0.01	0.00	0.05	0.00	0.00	0.00	0.01	0.01	0.01
Total	99.38	100.97	99.74	101.08	101.61	100.07	100.63	100.84	100.41	99.94	100.05	100.18
Si	1.85	1.78	1.64	1.80	1.87	1.86	1.81	1.81	1.92	1.94	1.90	1.87
Ti	0.02	0.04	0.09	0.03	0.02	0.02	0.02	0.02	0.03	0.00	0.01	0.03
Al	0.14	0.21	0.23	0.18	0.12	0.14	0.16	0.16	0.07	0.01	0.09	0.08
Fe^{2+}	0.22	0.14	0.15	0.23	0.20	0.23	0.27	0.30	0.27	0.23	0.19	0.31
Fe^{3+}	0.24	0.27	0.39	0.35	0.26	0.30	0.36	0.36	0.30	0.19	0.48	0.36
Mn	0.07	0.04	0.06	0.09	0.07	0.08	0.08	0.08	0.32	0.54	0.13	0.38
Mg	0.50	0.55	0.49	0.37	0.49	0.38	0.31	0.29	0.10	0.10	0.22	0.03
Ca	0.87	0.86	0.91	0.79	0.81	0.78	0.81	0.80	0.72	0.88	0.58	0.70
Na	0.10	0.12	0.06	0.17	0.16	0.20	0.18	0.18	0.28	0.10	0.40	0.24
K	0.00	0.00	0.00	0.00	0.00	0.00	0.00	0.00	0.00	0.00	0.00	0.00

MAGNETITE

Table A 28: Representative EMP-analysis of magnetite in sanidinite from Laacher See Volcano

	nosean-sanidinite				bright haüyne-sanidinite			dark haüyne-sanidinite			
sample	IDD67		LS88	LS113	IDD5	IDD11	LS160	LS211			
label	23_8	24_1	28_4	30_7	13_3	5_4	23_5	10_1	10_6	10_7	10_8
SiO_2	0.24	0.04	0.08	0.10	0.09	0.05	0.08	0.06	0.05	0.06	0.06
TiO_2	6.32	4.98	5.89	5.06	6.01	4.57	3.76	11.05	11.26	11.43	11.09
Al_2O_3	0.40	0.48	0.50	0.39	1.36	0.84	0.92	1.75	1.80	1.81	1.61
Fe_2O_3	86.14	88.86	84.96	88.72	88.26	91.84	93.21	84.09	85.27	85.43	84.57
MnO	7.19	5.83	7.64	5.74	4.35	3.36	3.51	3.16	2.79	2.82	2.87
ZnO	0.59	0.39	0.79	0.53	0.41	0.29	0.17	0.26	0.30	0.20	0.27
CaO	0.05	0.01	0.20	0.19	0.10	0.00	0.13	0.05	0.02	0.00	0.00
Total	100.92	100.58	100.05	100.73	100.57	100.96	101.77	100.41	101.49	101.76	100.47

TITANITE

Table A 29: Representative EMP-analysis of titanite in sanidinite from Laacher See Volcano

	nosean-sanidinite			haüyne-sanidinite						
	LS113			IDD5		IDD11	LS160			
Label	32_1	32_2	32_3	13_2	16_3	6_5	20_2	21_1	21_3	24_4
SiO_2	30.04	30.08	29.92	30.14	29.77	29.75	29.22	29.37	29.35	29.23
TiO_2	34.28	34.73	34.24	35.04	35.29	34.24	36.00	35.69	35.96	37.54
ZrO_2	0.32	0.34	0.32	0.80	1.03	1.43	0.97	0.75	1.16	0.60
HfO_2	0.00	0.00	0.04	0.02	0.09	0.04	0.12	0.05	0.06	0.00
ThO_2	0.02	0.00	0.03	0.02	0.03	0.02	0.03	0.01	0.00	0.01
Al_2O_3	1.81	1.37	1.77	1.45	1.29	1.16	1.48	1.39	1.27	1.05
Y_2O_3	0.08	0.03	0.08	0.11	0.10	0.09	0.09	0.11	0.11	0.12
La_2O_3	0.13	0.00	0.09	0.39	0.57	0.42	0.43	0.51	0.46	0.42
Nd_2O_3	0.22	0.12	0.22	0.31	0.35	0.22	0.25	0.22	0.33	0.32
Pr_2O_3	0.04	0.03	0.09	0.12	0.13	0.14	0.11	0.09	0.12	0.12
Sm_2O_3	0.00	0.03	0.04	0.07	0.02	0.00	0.06	0.06	0.03	0.05
Yb_2O_3	0.04	0.02	0.00	0.02	0.00	0.00	0.02	0.02	0.01	0.04
FeO	3.19	2.88	3.30	2.01	1.80	2.42	2.33	2.33	2.12	1.73
MnO	0.42	0.34	0.42	0.18	0.18	0.27	0.19	0.19	0.20	0.20
ZnO	0.02	0.01	0.02	0.03	0.01	0.00	0.01	0.02	0.00	0.00
PbO	0.00	0.04	0.00	0.00	0.02	0.00	0.00	0.00	0.00	0.00
CaO	26.63	26.97	26.64	27.19	26.86	26.99	26.38	26.51	26.50	26.77
Na_2O	0.25	0.32	0.26	0.03	0.09	0.11	0.08	0.10	0.10	0.09
P_2O_5	0.00	0.01	0.01	0.02	0.03	0.03	0.02	0.02	0.03	0.04
Nb_2O_5	1.80	2.63	1.91	1.02	2.20	1.71	1.40	1.74	2.16	1.40
Ta_2O_5	0.03	0.09	0.00	0.06	0.07	0.16	0.07	0.02	0.12	0.12
Total	99.42	100.07	99.42	99.13	99.93	99.25	99.34	99.30	100.16	99.93

APATITE

Table A 30: EMP-analysis of a transsect of apatite crystal in dark haüyne-sanidinite (see Figure 65) from Laacher See Volcano

	apatite											
	LS 211											
Label	3d_1	3d_2	3d_3	3d_4	3d_5	3d_6	3d_7	3d_8	3d_9	3d_10	3d_11	3d_12
distance [µm]	0	15	30	45	60	75	90	105	120	135	150	165
SiO_2	0.92	0.94	1.08	1.03	0.95	1.30	1.27	1.27	1.09	0.99	0.96	0.93
TiO_2	0.00	0.00	0.00	0.00	0.00	0.00	0.00	0.00	0.00	0.00	0.00	0.00
Al_2O_3	0.00	0.01	0.01	0.00	0.00	0.00	0.00	0.01	0.02	0.00	0.00	0.00
Cr_2O_3	0.00	0.00	0.00	0.01	0.00	0.00	0.01	0.00	0.00	0.00	0.09	0.00
FeO	0.10	0.19	0.16	0.08	0.15	0.15	0.17	0.15	0.17	0.10	0.20	0.16
MnO	0.28	0.23	0.22	0.23	0.20	0.28	0.25	0.23	0.25	0.23	0.23	0.23
MgO	0.05	0.04	0.06	0.03	0.08	0.06	0.06	0.09	0.05	0.06	0.05	0.05
CaO	53.09	53.50	52.76	53.80	53.45	51.61	52.76	52.72	53.25	53.51	53.57	53.40
BaO	0.00	0.00	0.04	0.00	0.09	0.00	0.04	0.00	0.05	0.00	0.06	0.05
Na_2O	0.35	0.41	0.34	0.36	0.40	0.52	0.64	0.72	0.52	0.39	0.39	0.41
K_2O	0.02	0.00	0.02	0.00	0.02	0.01	0.00	0.00	0.00	0.01	0.03	0.01
P_2O_5	42.32	41.41	41.65	41.48	41.90	39.86	40.65	40.21	41.44	41.76	41.29	41.80
Cl	0.27	0.26	0.25	0.27	0.26	0.28	0.32	0.30	0.27	0.27	0.26	0.27
F	2.06	2.04	1.92	2.05	2.00	1.79	1.93	1.96	1.96	2.01	2.06	1.86
SO_3	0.87	0.89	0.83	0.90	0.89	1.34	2.01	2.00	1.20	0.98	0.85	0.93
Total	100.33	99.92	99.34	100.24	100.39	97.20	100.11	99.66	100.27	100.31	100.04	100.10

ZIRCON

Table A 31: Representative EMP-analysis of zircon in nosean-sanidinite from Laacher See Volcano

	ZRC-1				ZRC-2					ZRC-3		
sample	LS125				LS125	IDD64	LS88	LS113	LS144	IDD67		
label	21_3	21_6	9A_3	20_6	20_1	20_7	27_4	34_4	10_8	20_2	20_8	23_8
SiO_2	31.72	31.81	31.46	31.76	32.17	32.17	31.72	32.15	32.45	32.06	32.42	31.82
TiO_2	0.03	0.02	0.00	0.02	0.04	0.03	0.04	0.07	0.00	0.02	0.00	0.00
ZrO_2	62.94	64.12	62.33	63.59	66.31	66.45	66.20	63.75	65.57	65.40	64.73	65.74
HfO_2	0.58	0.70	0.52	0.55	1.08	1.01	0.93	1.17	1.10	0.67	0.63	0.75
ThO_2	2.08	1.26	3.03	1.53	0.05	0.07	0.00	1.28	0.57	0.47	0.41	0.24
UO_2	0.16	0.06	0.21	0.05	0.00	0.00	0.00	0.00	0.00	0.00	0.00	0.00
Y_2O_3	1.00	0.88	1.22	0.84	0.16	0.04	0.00	0.38	0.31	0.23	0.55	0.42
La_2O_3	0.00	0.00	0.00	0.00	0.00	0.00	0.00	0.01	0.00	0.00	0.04	0.05
Ce_2O_3	0.16	0.09	0.11	0.17	0.00	0.04	0.00	0.19	0.11	0.04	0.02	0.01
Dy_2O_3	0.07	0.06	0.10	0.03	0.05	0.02	0.01	0.00	0.00	0.00	0.03	0.02
Er_2O_3	0.20	0.10	0.18	0.14	0.01	0.00	0.00	0.06	0.02	0.02	0.06	0.07
Gd_2O_3	0.00	0.11	0.08	0.08	0.00	0.02	0.00	0.07	0.02	0.07	0.04	0.00
Ho_2O_3	0.07	0.00	0.00	0.02	0.03	0.00	0.08	0.04	0.02	0.00	0.01	0.00
Nd_2O_3	0.02	0.04	0.06	0.00	0.00	0.01	0.00	0.05	0.00	0.05	0.04	0.01
Pr_2O_3	0.00	0.04	0.03	0.04	0.00	0.05	0.00	0.00	0.06	0.00	0.05	0.00
Sm_2O_3	0.02	0.02	0.00	0.00	0.01	0.06	0.00	0.00	0.00	0.00	0.08	0.00
Yb_2O_5	0.21	0.22	0.32	0.21	0.05	0.03	0.12	0.09	0.05	0.12	0.18	0.14
Ta_2O_5	0.12	0.00	0.07	0.07	0.00	0.07	0.00	0.00	0.00	0.00	0.00	0.02
Total	99.37	99.51	99.70	99.09	99.95	100.06	99.11	99.31	100.29	99.15	99.30	99.29

BADDELEYITE AND PYROCHLORE

Table A 32: Representative EMP-analysis of pyrochlore and baddeleyite in nosean-sanidinite from Laacher See Volcano

	pyrochlore							baddeleyite			
sample	LS88	LS113		LS125				IDD64		IDD65	
label	24_10	30_5	33_3	20_17	20_19	20_21	20_4	3_3	20_2	5_27	8_38
SiO_2	0.00	0.02	0.01	0.00	0.00	0.00	0.00	0.00	0.00	0.00	0.00
TiO_2	11.26	11.68	11.65	12.20	7.65	11.77	10.83	0.32	0.05	0.50	1.01
ZrO_2	0.76	0.76	0.52	1.23	5.43	2.31	2.93	97.17	95.59	94.07	93.56
HfO_2	0.04	0.00	0.00	0.00	0.22	0.00	0.04	1.49	1.26	1.90	0.78
ThO_2	1.48	4.26	9.31	6.04	7.42	4.23	5.67	0.00	0.00	0.04	0.00
UO_2	11.01	6.52	1.14	13.55	3.08	17.00	13.28	0.00	0.00	0.00	0.00
Y_2O_3	0.00	0.00	0.00	0.00	0.00	0.00	0.00	*n.a.*	*n.a.*	*n.a.*	*n.a.*
La_2O_3	0.55	0.42	0.51	0.70	1.09	0.66	0.77	0.00	0.00	0.00	0.00
Ce_2O_3	0.76	0.60	0.94	1.64	2.96	1.48	1.81	0.00	0.00	0.00	0.00
Dy_2O_3	0.00	0.01	0.01	0.06	0.00	0.00	0.04	*n.a.*	*n.a.*	*n.a.*	*n.a.*
Er_2O_3	0.00	0.00	0.01	0.00	0.00	0.00	0.00	*n.a.*	*n.a.*	*n.a.*	*n.a.*
Gd_2O_3	0.03	0.06	0.00	0.03	0.07	0.08	0.05	*n.a.*	*n.a.*	*n.a.*	*n.a.*
Ho_2O_3	0.00	0.00	0.00	0.00	0.00	0.09	0.02	*n.a.*	*n.a.*	*n.a.*	*n.a.*
Nd_2O_3	0.20	0.23	0.26	0.59	0.67	0.43	0.56	*n.a.*	*n.a.*	*n.a.*	*n.a.*
Pr_2O_3	0.08	0.10	0.08	0.25	0.27	0.16	0.15	*n.a.*	*n.a.*	*n.a.*	*n.a.*
Sm_2O_3	0.04	0.02	0.04	0.01	0.02	0.08	0.04	*n.a.*	*n.a.*	*n.a.*	*n.a.*
Yb_2O_3	0.00	0.00	0.00	0.02	0.00	0.02	0.00	*n.a.*	*n.a.*	*n.a.*	*n.a.*
FeO	0.29	0.31	0.46	0.69	0.92	0.70	0.75	0.26	0.34	0.36	1.03
MnO	0.22	0.29	0.54	0.58	0.52	0.41	0.48	0.07	0.39	0.30	0.57
ZnO	0.02	0.04	0.03	0.02	0.01	0.07	0.01	*n.a.*	*n.a.*	*n.a.*	*n.a.*
PbO	0.26	0.20	0.18	0.18	0.26	0.16	0.14	*n.a.*	*n.a.*	*n.a.*	*n.a.*
CaO	14.91	17.00	16.35	12.13	13.07	12.14	12.40	*n.a.*	*n.a.*	0.60	0.03
Na_2O	5.29	4.62	4.64	4.48	4.73	4.57	4.65	0.00	0.00	0.00	0.00
Nb_2O_5	50.89	51.51	52.55	40.03	47.85	41.89	43.60	0.48	2.92	1.65	3.66
Ta_2O_5	1.23	0.66	0.47	4.78	1.99	1.66	1.78	0.00	0.01	0.03	0.01
Total	99.31	99.31	99.69	99.18	98.23	99.90	100.01	99.82	100.59	99.46	100.67

GLASS

Table A 33: Representative EMP-analysis of glass in in nosean-sanidinite and bright haüyne-sanidinite from Laacher See Volcano

	nosean-sanidinite						bright haüyne-sanidinite			
sample	LS64			LS113			IDD11			
label	4d_3	1b_A_14	17_5	6_1	12_4	12_6	4_05	4_06	5_2	5_B_11
SiO_2	63.29	63.65	72.85	57.82	58.74	58.63	58.82	58.25	56.90	56.76
TiO_2	0.00	0.00	0.03	0.39	0.11	0.09	0.19	0.31	0.29	0.29
Al_2O_3	21.23	20.09	22.73	18.48	19.29	19.41	21.27	20.59	23.07	22.85
Fe_2O_3	0.25	0.20	0.32	5.34	1.66	1.79	2.28	3.23	2.72	3.12
MnO	0.18	0.10	0.02	0.35	0.32	0.26	0.56	0.72	0.45	0.55
MgO	0.00	0.00	0.00	0.01	0.12	0.09	0.09	0.14	0.14	0.25
CaO	1.13	0.73	0.12	0.66	1.47	1.27	1.46	1.38	1.06	1.22
Na_2O	5.47	6.90	0.37	7.82	7.69	7.31	4.56	4.95	5.89	5.72
K_2O	7.78	7.34	1.89	8.44	8.84	9.36	9.26	8.14	7.08	6.86
P_2O_5	0.00	0.00	0.00	0.00	0.02	0.01	0.00	0.00	0.00	0.04
SO_3	*n.a.*	*n.a.*	*n.a.*	*n.a.*	*n.a.*	*n.a.*	0.06	0.12	0.09	0.11
Cl	*n.a.*	*n.a.*	*n.a.*	*n.a.*	*n.a.*	*n.a.*	0.52	0.70	0.59	0.60
Total	99.33	99.00	98.33	99.31	98.26	98.22	99.07	98.51	98.29	98.35

Table A 34: Representative EMP-analysis of glass in bright and dark haüyne-sanidinite from Laacher See Volcano

	bright haüyne-sanidinite				dark haüyne-sanidinite						
sample	LS160		LS170		IDD24				LS211		
label	11_A_1	11_A_9	13_B_29	4_1	1c_6	1c_8	3e_A_40	3e_B_33	1b_4	1b_5	2a_A_9
SiO_2	66.70	66.04	64.95	64.61	59.14	62.14	56.61	53.85	60.73	63.70	57.21
TiO_2	0.10	0.12	0.24	0.26	0.38	0.50	0.75	0.79	1.44	0.30	0.96
Al_2O_3	21.26	21.11	20.97	20.74	20.73	21.57	16.16	16.47	19.01	19.51	18.06
Fe_2O_3	2.62	2.77	2.66	3.52	2.53	1.52	6.19	6.85	2.65	1.05	8.39
MnO	0.51	0.53	0.43	0.23	0.22	0.27	1.04	1.14	0.17	0.09	0.42
MgO	0.04	0.05	0.10	0.07	0.09	0.21	0.33	0.39	0.20	0.02	0.26
CaO	1.15	1.14	1.02	0.86	1.14	1.52	5.31	5.46	3.09	1.62	1.74
Na_2O	2.97	2.80	4.46	4.71	4.13	7.93	3.96	4.62	5.07	4.94	5.60
K_2O	4.77	4.88	5.48	5.33	10.71	3.51	8.45	8.22	7.75	8.30	6.47
P_2O_5	0.01	0.01	0.00	0.00	*n.a.*	*n.a.*	*n.a.*	*n.a.*	0.08	0.00	0.10
Total	100.13	99.44	100.32	100.33	99.08	99.19	98.79	97.79	100.18	99.52	99.20

A-3 THERMOBAROMETRY

Thermobarometric calculations were performed using diopside in equilibrium with melt thermobarometer after Putirka et al. (2003). For the calculation, rims of selected clinopyroxenes were calculated together with the respective whole rock composition, as suggested by Putirka et al. (2003). The whole rock compositions are listed in Table A1 in appendix A-1a.

Table A 35: Results of the thermobarometric calculations after Putirka et al. (2003) and used clinopyroxene compositions

					Clinopyroxene Compositions [wt%]								
	Label	T(°C)	P(kbar)	K_D(Fe-Mg)	SiO_2	TiO_2	Al_2O_3	FeOt	MnO	MgO	CaO	Na_2O	K_2O
B1	2_1	978	14	0.26	49.84	0.88	2.36	9.03	0.46	11.64	23.05	1.26	0.00
B1	4_3	985	16	0.27	50.69	0.42	1.82	9.49	0.44	11.53	23.23	0.97	0.01
B1	2_9	988	15	0.30	50.43	1.01	2.76	10.38	0.45	11.44	22.84	1.35	0.03
B1	2_8	983	14	0.15	52.21	0.78	2.08	6.64	0.23	14.68	22.70	1.22	0.03
B1	4_5	974	13	0.30	49.76	1.09	2.89	10.29	0.41	11.58	22.93	1.28	0.00
B2	4_A_10	1058	7	0.23	52.10	0.25	1.72	7.40	0.27	13.60	24.01	0.89	0.00
B2	4_A_11	1075	9	0.22	52.13	0.26	1.83	7.19	0.28	13.48	23.75	0.87	0.02
B2	4_A_12	1069	9	0.24	52.12	0.27	1.83	7.63	0.20	13.43	23.77	0.91	0.02
B2	4_A_1	1040	4	0.30	52.10	0.25	1.72	7.40	0.27	13.60	24.01	0.89	0.00
B2	1_B_2	1031	2	0.25	52.13	0.26	1.83	7.19	0.28	13.48	23.75	0.87	0.02
B2	1_B_23	1078	10	0.31	52.12	0.27	1.83	7.63	0.20	13.43	23.77	0.91	0.02
L2	2_15	1058	6	0.26	52.19	0.36	1.19	5.68	0.26	15.19	23.69	0.74	0.01
L2	B_1	1070	8	0.31	52.23	0.35	1.25	5.36	0.28	15.29	23.73	0.74	0.01
L2	B_2	1070	8	0.29	53.73	0.30	0.99	5.90	0.25	15.32	24.03	0.66	0.00
L2	B_3	1073	9	0.29	53.72	0.25	1.00	5.90	0.28	15.41	23.77	0.61	0.00
L2	B_34	1059	6	0.22	53.59	0.30	1.02	5.97	0.25	15.06	23.84	0.61	0.00
L2	B_35	1047	4	0.22	53.50	0.28	1.10	5.90	0.26	15.13	23.89	0.71	0.01
L2	2_B_41	1045	4	0.22	49.33	0.99	1.75	12.00	0.60	9.96	20.02	3.06	0.04
L2	2_B_42	1074	9	0.22	50.88	0.58	1.96	8.13	0.36	13.53	23.13	0.77	0.02
L1	1_1	990	12	0.23	50.11	1.02	1.99	12.02	0.58	9.92	20.73	2.95	0.03
B3	17_1	977	12	0.14	50.57	0.98	1.64	12.17	0.59	9.77	20.09	3.29	0.03
B3	17_2	976	13	0.22	50.38	0.85	2.36	8.94	0.40	12.27	23.46	1.16	0.07
B4	1_B_47	1124	11	0.23	50.14	0.81	2.53	9.65	0.44	11.59	23.24	1.22	0.03
B4	1_B_48	1107	9	0.23	49.25	0.83	2.76	10.43	0.57	11.07	23.30	1.18	0.00
B4	1_B_49	1104	8	0.23	50.38	0.85	2.36	8.94	0.40	12.27	23.46	1.16	0.07
B4	2_B_3	1098	7	0.30	50.14	0.81	2.53	9.65	0.44	11.59	23.24	1.22	0.03
B4	2_A_7	1136	12	0.20	49.25	0.83	2.76	10.43	0.57	11.07	23.30	1.18	0.00